Polymer Materials

Block-Copolymers,
Nanocomposites, Organic/Inorganic
Hybrids, Polymethylenes

Springer

231
Advances in Polymer Science

Advances in Polymer Science

Recently Published and Forthcoming Volumes

Polymer Materials

Block-Copolymers, Nanocomposites, Organic/Inorganic Hybrids, Polymethylenes

Volume Editors: Kwang-Sup Lee
Shiro Kobayashi

With contributions by

C.D. Han · E. Ihara · H. Kasai · J.K. Kim · A. Masuhara
H. Nakanishi · H. Oikawa · T. Onodera

Editors
Kwang-Sup Lee
Department of Advanced Materials
Hannam University
561-6 Jeonmin-Dong
Yuseong-Gu 305-811
Daejeon, South Korea
kslee@hnu.kr

Shiro Kobayashi
R & D Center for Bio-based Materials
Kyoto Institute of Technology
Matsugasaki, Sakyo-ku
Kyoto 606-8585, Japan
kobayash@kit.ac.jp

Volume Editors

Editorial Board

Advances in Polymer Sciences
Also Available Electronically

Advances in Polymer Sciences is included in Springer's eBook package *Chemistry and Materials Science*. If a library does not opt for the whole package, the book series may be bought on a subscription basis. Also, all back volumes are available electronically.

For all customers who have a standing order to the print version of *Advances in Polymer Sciences*, we offer the electronic version via SpringerLink free of charge.

If you do not have access, you can still view the table of contents of each volume and the abstract of each article by going to the SpringerLink homepage, clicking on "Browse by Online Libraries", then "Chemical Sciences", and finally choose *Advances in Polymer Science*.

You will find information about the

– Editorial Board
– Aims and Scope
– Instructions for Authors
– Sample Contribution

at springer.com using the search function by typing in *Advances in Polymer Sciences*.

Color figures are published in full color in the electronic version on SpringerLink.

Aims and Scope

The series *Advances in Polymer Science* presents critical reviews of the present and future trends in polymer and biopolymer science including chemistry, physical chemistry, physics and material science. It is addressed to all scientists at universities and in industry who wish to keep abreast of advances in the topics covered.

Review articles for the topical volumes are invited by the volume editors. As a rule, single contributions are also specially commissioned. The editors and publishers will, however, always be pleased to receive suggestions and supplementary information. Papers are accepted for *Advances in Polymer Science* in English.

In references *Advances in Polymer Sciences* is abbreviated as *Adv Polym Sci* and is cited as a journal.

Special volumes are edited by well known guest editors who invite reputed authors for the review articles in their volumes.

Impact Factor in 2009: 4.600; Section "Polymer Science": Rank 4 of 73

Publisher's Note for Volumes with Independent Contributions

This volume was not originally planned as a topical volume by the stated Volume Editors. It contains substantial review articles on interesting and valuable subjects which were invited and reviewed by the stated Editors on an independent basis and then – upon receipt – put together in one volume by the Publisher.

Marion Hertel
Executive Editor Chemistry, Springer

Contents

On the Mechanisms Leading to Exfoliated Nanocomposites Prepared by Mixing

Chang Dae Han

Abstract For most industrial applications, exfoliation is much preferred to intercalation in organoclay nanocomposites. Mechanisms leading to exfoliated nanocomposites prepared by mixing are presented with specific examples reported in the literature. It is pointed out that in the preparation, via mixing, of nanocomposites based on thermoplastic polymers or thermoplastic elastomers, exfoliation of the aggregates of layered silicate platelets requires strong attractive interactions between the clay surface (with or without chemical modification) and polymer matrix, giving rise to enhanced compatibility between the two and hence a highly dispersed (nearly exfoliated) nanocomposite. In this chapter, four different specific interactions (ionic, ion–dipole, hydrogen bonding, and coulombic) are illustrated to demonstrate the effectiveness of offering strong attractive interactions between the clay surface (with or without chemical modifications) and the polymer matrix in the preparation of exfoliated nanocomposites based on thermoplastic polymers or thermoplastic elastomers by mixing. It is pointed out further that van der Waals force is not strong enough to exfoliate the aggregates of layered silicate platelets, giving rise to intercalated nanocomposites at best.

Keywords Coulombic interaction · Exfoliation · Hydrogen bonding · Intercalation · Ion–dipole interaction · Ionic interaction · Nanocomposites

Contents

C.D. Han (✉)
Department of Polymer Engineering, The University of Akron, Akron, OH 44325, USA
e-mail:cdhan@uakron.edu

Abbreviations and Symbols

6TPy	6-(2, 2′:6′,2″-Terpyridyl-4′-oxy)hexane
CP	Cross polarization
CT	Contact time
DMF	*N*,*N*-Dimethylformamide
EVA	Poly(ethylene-*ran*-vinyl acetate)
EVAOH	Poly(ethylene-*ran*-vinyl acetate-*ran*-vinyl alcohol)
EVOH	Poly(ethylene-*ran*-vinyl alcohol)
FTIR	Fourier transform infrared
GPC	Gel permeation chromatography
HMW	High molecular weight
IS	Polyisoprene-*block*-polystyrene
ISB	Polyisoprene-*block*-polystyrene-*block*-polybutadiene
ISBOH	Polyisoprene-*block*-polystyrene-*block*-hydroxylated polybutadiene
MA	Maleic anhydride
MAS	Magic-angle spinning
MLCT	Metal-to-ligand charge transfer
MMT	Montmorillonite
MMW	Medium molecular weight
ODT	Order–disorder transition
PC	Polycarbonate
PEMA	Poly(ethylene-*co*-methacrylate)
PI	Polyisoprene
PIOH	Hydroxylated polyisoprene
POM	Polarized optical microscopy
PS	Polystyrene

PSHMW	High molecular-weight polystyrene
PSLMW	Low molecular-weight polystyrene
PVAc	Poly(vinyl acetate)
PVPh	Poly(vinylphenol)
P2VP	Poly(2-vinylpyridine)
Ru	Ruthenium
$RuCl_3$	Ruthenium chloride
S2VP	Polystyrene-*block*-poly(2-vinylpyridine)
SB	Polystyrene-*block*-polybutadiene
SBS	Polystyrene-*block*-polybutadiene-*block*-polystyrene
SEB	Polystyrene-*block*-poly(ethylene-*co*-1-butene)
SEBS	Polystyrene-*block*-poly(ethylene-*co*-1-butene)-*block*-polystyrene
SI	Polystyrene-*block*-polyisoprene
SIOH	Polystyrene-*block*-hydroxylated polyisoprene
SIOHS	Polystyrene-*block*-hydroxylated polyisoprene-*block*-polystyrene
SIS	Polystyrene-*block*-polyisoprene-*block*-polystyrene
T_{CH}	Cross polarization time
T_{cl}	Clearing temperature
TEM	Transmission electron microscopy
T_g	Glass transition temperature
THF	Tetrahydrofuran
TLCP	Thermotropic liquid-crystalline polymer
T_{ODT}	Order–disorder transition temperature
$T_{1\rho C}$	Carbon spin-lattice relaxation time in the rotating frame
$T_{1\rho H}$	Proton spin-lattice relaxation time in the rotating frame
UV-vis	Ultraviolet-visual
XRD	X-ray diffraction
χ	Flory–Huggins interaction parameter

1 Introduction

Nanocomposites are composed of a polymer matrix and layered silicate platelets having approximately 1 nm thickness and large aspect ratio. In the last two decades, nanocomposites have attracted much attention from both industry and academia, because they may offer enhanced mechanical and/or physical properties (e.g., high modulus and high heat-distortion temperature) that are not readily available from conventional particulate-filled thermoplastic polymers. One of the advantages of such nanocomposites lies in that the concentration of layered silicates required is much lower (say, less than 7 wt%) than that (e.g., 40–60 wt%) required for the conventional particulate-filled thermoplastic composites to achieve a similar property enhancement. The lower specific gravity of nanocomposites as compared to conventional thermoplastic composites can offer potential cost benefits as well.

Fig. 1 Schematic illustrating
intercalated structure and
exfoliated structure
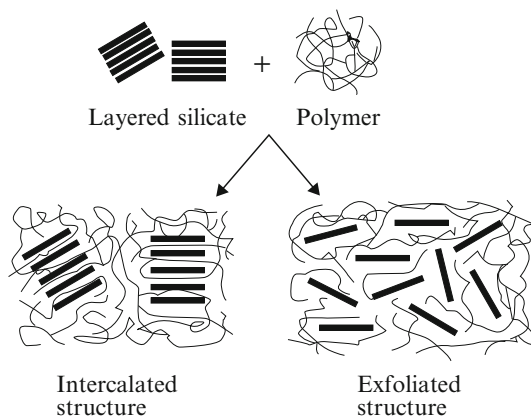
When a thermoplastic polymer is mixed with layered silicate particles, it either
intercalates or exfoliates the layered silicates, as schematically shown in Fig. 1. The
state of dispersion (intercalation vs exfoliation) of the aggregates of layered silicate
in nanocomposites is commonly assessed by X-ray diffraction (XRD) or transmis-
sion electron microscopy (TEM). Generally exfoliation is preferred to intercalation,
although exfoliation may not necessarily be required for certain industrial appli-
cations (e.g., for an enhancement of flame retardant characteristics). It should be
mentioned that the greater the extent of exfoliation of layered silicates, the larger
will be the total surface areas of the dispersed layered silicates, giving rise to en-
hanced mechanical/physical properties of the nanocomposites prepared.

Numerous research groups have reported on the preparation of organoclay
nanocomposites based on various thermoplastic polymers and there are too many
articles to cite them all here. A recent review article [1] has cited 460 articles deal-
ing with nanocomposites. In the past 10 years the number of articles dealing with
nanocomposites has increased dramatically; for instance, there are over 40,000 ar-
ticles listed under the title of "nanocomposites" in SciFinder on the Internet, which
are either published in refereed journals or documented in conference proceedings.

The extent of dispersion of organoclay aggregates depends on (1) the chemical
structure of the surfactant residing at the surface of clay particles, (2) the chemical
structure and architecture of the polymer matrix (e.g., AB-, ABA-, and ABC-type
block copolymers), (3) the molecular weight of the polymer matrix, (4) the extent
of functionality in the polymer matrix, and (5) the location(s) of the functional
groups in the polymer matrix (end-functionalization vs random functionalization).
The extent of attractive interactions between a polymer matrix and an organoclay
also depends on, besides the factors mentioned above, the gallery distance of an
organoclay. The chemistry of the surfactant that is applied to the surface of pristine
layered silicates determines the gallery distance of an organoclay. Note that layered
silicates have large active surface areas ($700–800\,m^2/g$ in the case of montmoril-
lonite, MMT) and a moderately negative surface charge (cation exchange capacity).
By replacing the hydrated metal cations from the interlayers of the pristine layered
silicates with organic cations such as alkyammonium, the layered silicates attain

a hydrophobic/organophilic character, which typically results in larger interlayer spacing. Since the negative charge originates in the layered silicate, the cationic head groups of the alkylammonium chloride molecule preferentially reside at the surface of the layered silicate (i.e., the quaternary ammonium salt of the surfactants, for example, interacts with the silicate surface), while the oligomeric tallow species, which sometimes contain polar groups, extend into the galleries. Therefore, it is very important to match the chemical affinity between the polymer matrix and an organoclay in order to achieve a very high degree of dispersion (or a high degree of exfoliation) of organoclay platelets in the polymer matrix.

There are two ways of preparing thermoplastic polymer/organoclay nanocomposites. One method is through in situ polymerization, wherein the organoclay platelets are first preintercalated with monomer. For instance, nylon 6/organoclay nanocomposites, which were prepared from in situ polymerization of ε-caprolactam in the presence of an organoclay by Toyota researchers [2, 3], gave rise to enhanced mechanical properties and a considerable increase in the heat distortion temperature. However, contrary to the impression one might get from the earlier studies of the Toyota researchers, more recently it has been shown [4] that the crystalline structure of nylon 6 and the crystallization rate of nylon 6 in the presence of an organoclay are quite different from those of pristine nylon 6. This would indicate that the experimentally observed enhancement in the mechanical properties of nylon 6/organoclay nanocomposites is not entirely due to the exfoliated clay platelets but also comes from the unique nucleation and growth mechanism of nylon 6 on the silicate layers.

The other method of preparing nanocomposites is through direct intercalation of layered silicates during melt compounding with a thermoplastic polymer. When a thermoplastic polymer does not have the necessary functional group(s) to form attractive interactions with a given organoclay, chemical modification of the polymer is necessary. In this regard, block copolymers have greater flexibility, as compared to homopolymers, in that one of the blocks in a given block copolymer can be modified (e.g., hydroxylation) to have functionality that would be compatible with the surfactant residing at the surface of an organoclay. Also, block copolymers having a functional group can be synthesized such that the functional block would have attractive interactions with the surfactant residing at the surface of an organoclay. Indeed, such approaches have been used successfully to prepare highly dispersed nanocomposites based on block copolymers [5–7].

When chemical modification of a homopolymer was not feasible, some investigators employed a third component with functional group(s) to enhance compatibility between the homopolymer and an organoclay. For example, polypropylene (PP) grafted with maleic anhydride (MA) yielding PP-*g*-MA has been used to prepare organoclay nanocomposites by melt blending with pristine PP and an organoclay [8–12]. These researchers referred to PP-*g*-MA as a "compatibilizing agent." However, the use of the words "compatibilizing agent" may *not* be warranted unless the following fundamental questions are answered satisfactorily. (1) Were the chains of PP in PP-*g*-MA mixed homogeneously during melt compounding with the chains of pristine PP in the ternary mixtures composed of pristine PP, PP-*g*-MA, and an

organoclay? (2) What role(s) did the MA in PP-*g*-MA play in dispersing the aggregates of organoclay in the ternary mixtures composed of pristine PP, PP-*g*-MA, and an organoclay? (3) What might be the mechanism that led to an enhanced dispersion of the aggregates of organoclay when PP-*g*-MA was mixed with the pristine PP and an organoclay? I believe that the PP-*g*-MA added to a mixture of pristine PP and an organoclay plays the role of a dispersing (emulsifying) agent, but not as a compatibilizing agent. It is very important to distinguish dispersing or emulsifying agent from compatibilizing agent. The distinction between the two is well described in the literature [13].

This chapter will address the mechanisms that might lead to exfoliation of organoclay nanocomposites prepared *by mixing*. Specifically, the types of specific interactions that can exist between an organoclay and a polymer matrix, which could lead to exfoliation of the aggregates of organoclay, will be summarized. This will be followed by a discussion of the mechanisms of the specific interactions that led to a very high degree of dispersion of the aggregates of organoclay in the following nanocomposite systems prepared by mixing on the basis of hydroxylated polyisoprene, polycarbonate, poly(ethylene-*ran*-vinyl acetate-*ran*-alcohol) copolymer, end-functionalized polystyrene, polystyrene-*block*-hydroxylated polyisoprene copolymer, end-functionalized polystyrene-*block*-polyisoprene copolymer, polystyrene-*block*-poly(2-vinylpyridine copolymer), and liquid-crystalline polymers having pendent pyridyl groups or side-chain azopyridine with pyridyl groups. This will also include a review of the literature that reported on *intercalated* organoclay nanocomposites prepared by mixing. In this chapter, nanocomposites prepared by in situ intercalation polymerization will not be reviewed because the process is relatively straightforward and it is easier to obtain exfoliated organoclay nanocomposites this way than by mixing, as can be found from the extensive literature [2, 3, 14–18].

2 Mechanisms Leading to Exfoliated Nanocomposites Prepared by Mixing

In general, intercalation is observed when a polymer matrix and layered silicates do not have sufficient attractive interactions, while exfoliation is observed when strong attractive interactions exist. Some effort has been made to understand better the preparation of *intercalated* nanocomposites from thermodynamic considerations [19]. It is granted that exfoliation of the aggregates of an organoclay by a very high molecular-weight thermoplastic polymer via mixing is not an easy task. This is where the challenge comes in and ingenuity is required. Thus, a fundamental issue in the preparation of *exfoliated* nanocomposites by mixing is to identify the methods that can provide the strong attractive interactions required between a polymer matrix and the layered silicates.

Conceptually, the preparation of nanocomposites by mixing is not much different from that of conventional particulate-filled polymer composites, with some

differences. One important difference between the two is the dimensions of the fillers; namely, the dimensions of layered silicates employed for nanocomposites are orders of magnitude smaller than those of particulates employed for conventional polymer composites. Due to the extremely small sizes of these layered silicates, the total surface area can become very large even at low loadings (say less than 5 wt%) when and if all the layered silicates are exfoliated.

As in the preparation of miscible polymer blends, the compatibility between the surface of layered silicates and the polymer matrix must be considered in the preparation of exfoliated nanocomposites. This then suggests that attractive interactions between the surface of layered silicates and the polymer matrix must exist in order to achieve a high degree of dispersion in organoclay nanocomposites prepared by mixing. A fundamental question may be raised about the existence of a universally acceptable criterion (or criteria) for strong or weak attractive interactions. In the literature dealing with the miscibility of polymer blends, a miscibility criterion based on polymer solution thermodynamics is invoked and often the magnitude of a negative segment-segment interaction parameter (e.g., the Flory–Huggins parameter χ) has been used to determine whether one pair of polymers is more miscible than other pairs. For instance, some investigators consider that miscible polymer blends with $\chi = -0.05$ have a very strong attractive interaction, while miscible polymer blends with $\chi = -0.01$ have a weak attractive interaction. However, such a criterion is somewhat arbitrary in that there is no theoretical guideline for a precise value of $|\chi|$, which can be used effectively to determine whether a miscible polymer blend has weak or strong attractive interactions. One may be tempted to use a similar criterion to assess whether a surfactant residing at the surface of an organoclay and a polymer matrix might have sufficiently strong attractive interactions giving rise to exfoliated nanocomposites.

A theoretical study [20] has been reported which discussed the effectiveness, in terms of $|\chi|$, of a surfactant applied to the surface of layered silicates in dispersing the aggregates of organoclay in a polymer matrix. Specifically, using numerical self-consistent field calculations, Balazs et al. [20] modeled the interactions between two closely spaced surfaces and the surrounding polymer melt. In doing so, they assumed that surfactants having short chains are terminally anchored to each of the surfaces and that the interaction between the polymer and surfactant chains anchored to each of the surfaces can be characterized by the Flory–Huggins interaction parameter χ. They also considered the effect of employing end-functionalized chains to promote the dispersion of pristine clay sheets within the polymer matrix. In doing so, they assumed that some fraction of the polymer contained "stickers" (essentially equivalent to end-functionalized groups) that were highly attractive to the surface. However, they did not elaborate on the mechanism(s) that might lead to attractive interactions between the "stickers" and the surfactant chains anchored to each of the surfaces. They employed the Flory-Huggins interaction parameter χ_{ss} between the stickers and the surface to describe the interactions between them. In their numerical calculations, they employed very large negative values of χ_{ss}, $\chi_{ss} = -75$, to construct plots of the free energy per unit area as a function of the distance between the two surfaces. Balazs et al. noted that the value of χ_{ss} must be divided by 6, the

coordination number of the cubic lattice, in order to relate χ_{ss} to experimentally relevant values. However, it is very difficult to accept such large, negative values of $\chi_{exp} = \chi_{ss}/6 = -75/5 = -12.5$ with χ_{exp} representing an experimentally relevant Flory–Huggins interaction parameter between the stickers and the surface. I am not aware of the existence of such exceedingly large, negative values of χ_{exp} determined experimentally for any pair of compounds having ever been reported in the literature.

Lee et al. [21] conducted molecular dynamics simulations of the flow of a compositionally symmetric diblock copolymer into the galleries between two silicate sheets whose surfaces were modified by grafted surfactant chains. In these simulations they assumed that block copolymers and surfactants were represented by chains of soft spheres connected by an finitely extensible nonlinear elastic potential, non-Hookean dumbbells [22], which had been employed earlier in the simulations of the dynamics of polymer blends and block copolymers by Grest et al. [23] and Murat et al. [24]. To describe the interactions among the four components, namely the surfaces, the surfactant, and two blocks, Lee et al. [21] employed a Lennard–Jones potential having the energy parameters which are associated with the type of interactions often employed for lattice systems such as in the Flory–Huggins theory.

It is fair to state that use of the Flory–Huggins theory would not be adequate to explain the strong attractive interactions present in *exfoliated* nanocomposites which were prepared by mixing. This is simply because a Lennard–Jones potential (i.e., van der Waals interaction) is very weak as compared to some specific interactions. It seems more appropriate to use, instead of the Flory–Huggins interaction parameter, intermolecular forces to determine whether a given organoclay and polymer matrix pair has weak or strong attractive interactions in terms of specific interactions. Some well-known specific interactions include (1) ionic interactions, (2) ion–dipole interactions, (3) hydrogen bonding, (4) dipole–dipole interactions, etc. Intermolecular forces have been discussed extensively in the literature [25]. Table 1 gives a summary of bond energy and relative strength of some intermolecular forces [26]. On the basis of the intermolecular forces summarized in Table 1, it is clear that among the specific interactions considered ionic interactions provide the strongest attractive interactions and van der Waals interactions provide the weakest.

A large number of organoclays can be prepared depending on the chemical structures of surfactants that may be employed to treat pristine layered silicates (e.g., MMT). However, there is only a limited number of organoclays that are commercially available. Table 2 gives a list of six commercial organoclays with their mean

Table 1 Bond energy and relative strength of different intermolecular forces [26]

Type of interactions	Bond energy (kJ/mol)	Relative strength
Ionic interactions	850–1,700	1,000
Ion–dipole interactions	170–500	500
Hydrogen bonding	50–170	100
Dipole–dipole interactions	2–8	10
van der Waals interactions	~ 1	1

Table 2 Chemical structures of surfactants residing at the surface of organoclay and the mean interlayer d-spacing of commercial organoclays produced by Southern Clay Products

Sample code	Chemical structure of surfactant[a]		d-spacing (nm)
Cloisite 6A®	H_3C—N^+—HT, with CH$_3$ up and HT down	2M2HT (90 meq/100 g)	3.51
Cloisite 30B®	H_3C—N^+—T, with CH$_2$CH$_2$OH up and CH$_2$CH$_2$OH down	MT2EtOH (90 meq/100 g)	1.85
Cloisite 10A®	H_3C—N^+—HT—(benzyl), with CH$_3$ up and HT down	2MBHT (125 meq/100 g)	1.92
Cloisite 15A®	H_3C—N^+—HT, with CH$_3$ up and HT down	2M2HT (125 meq/100 g)	3.15
Cloisite 20A®	H_3C—N^+—HT, with CH$_3$ up and HT down	2M2HT (95 meq/100 g)	2.42
Cloisite 25A®	H_3C—N^+—CH$_2$CHCH$_2$CH$_2$CH$_2$CH$_3$, with CH$_3$ up, HT down, and CH$_2$CH$_3$ branch	2MHTL8 (125 meq/100 g)	1.86

[a]T in the chemical structure of surfactant denotes tallow consisting of ca. 65% C18, ca. 30% C16, and ca. 5% C14; HT in the chemical structure of surfactant denotes hydrogenated tallow consisting of ca. 65% C18%, ca. 30% C16, and ca. 5% C14. 2M2HT is dimethyl dihydrogenated tallow quaternary ammonium ion. MT2EtOH is methyl tallow bis-2-hydroxyethyl quaternary ammonium ion. 2MBHT is dimethyl benzyl hydrogenated tallow quaternary ammonium ion. 2MHTL8 is dimethyl hydrogenated tallow 2-ethylhexyl quaternary ammonium ion

interlayer spacing of the (001) plane (d-spacing) produced by Southern Clay Products, which I have used in my research and thus I am very familiar with them. However, this list of commercial organoclays is by no means comprehensive and it is quite possible that the same or very similar results presented below could have been obtained if other commercial organoclays had been employed. Of particular note in Table 2 are the chemical structures of two surfactants, (1) MT2EtOH treated on Cloisite 30B® and (2) 2M2HT treated on Cloisite 6A® and Cloisite 15A®, respectively. Note that among the six organoclays listed in Table 2, Cloisite 30B® is the only organoclay that has a surfactant having two hydroxyl groups. Note further in Table 2 that all six surfactants have cation N^+ in the quaternary ammonium salt with T denoting tallow consisting of approximately 65% C18, 30% C16, and 5% C14, and HT denoting hydrogenated tallow also consisting of approximately 65% C18, 30% C16, and 5% C14. The cation exchange capacity of Cloisite 30B® and Cloisite 6A® is 90 meq/100 g, and for Cloisite 15A® it is 125 meq/100 g. In all the organoclays listed in Table 2, 100% of the Na^+ ions in natural clay (MMT) have been exchanged. The chemical structure of pristine clay is well documented in the literature [27–30].

The Fourier transform infrared (FTIR) spectra for two surfactants, MT2EtOH and 2M2HT, and two commercial organoclays, Cloisite 30B® and Cloisite 15A®, are given in Fig. 2 [31] in which the absorption band at about $3,360 cm^{-1}$ represents the hydroxyl (–OH) group. It is clearly seen in Fig. 2 that both MT2EtOH and Cloisite 30B® have an –OH group, and that the area under the absorption band at about $3,360 cm^{-1}$ for Cloisite 30B® is much smaller than that for the pure surfactant. This is reasonable because the amount of MT2EtOH in Cloisite 30B® is about 32%. Conversely, in Fig. 2 we observe no evidence of an –OH group present in the surfactant 2M2HT or Cloisite 15A®. The –OH groups in MT2EtOH residing at the surface of Cloisite 30B® may form hydrogen bonds with a polar group(s) in a polymer matrix, as will be shown below.
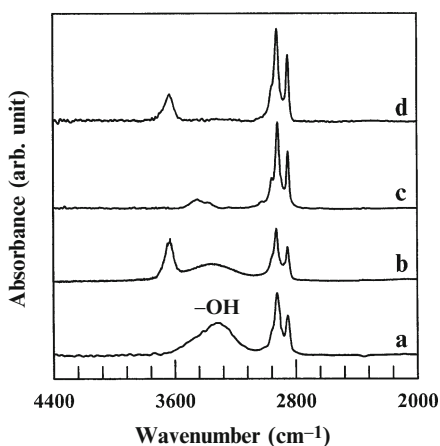
Fig. 2 FTIR spectra for (**a**) surfactant MT2EtOH, (**b**) surfactant Cloisite 30B®, (**c**) surfactant 2M2HT, and (**d**) Cloisite 15A®. (Reprinted from Lee and Han [31]. Copyright 2003, with permission from the American Chemical Society)

In the following, I will present examples of (a) hydrogen bonding that leads to highly dispersed organoclay nanocomposites based on (1) hydroxylated polyisoprene, (2) poly(ethylene-*ran*-vinyl acetate-*ran*-alcohol) copolymer, (3) polycarbonate, (4) polystyrene-*block*-hydroxylated polyisoprene copolymer, and (5) thermotropic liquid-crystalline polymer with pendent functional groups; (b) ionic interactions that lead to highly dispersed organoclay nanocomposites based on (1) end-functionalized polystyrene and (2) end-functionalized polystyrene-*block*-polyisoprene copolymer; (c) ion–dipole interactions that lead to highly dispersed organoclay nanocomposites based on polystyrene-*block*-poly(2-vinylpyridine) copolymer; (d) Coulombic interactions that lead to highly dispersed montmorillonite nanocomposites based on a ruthenium(II) complex-induced, segmented main-chain liquid-crystalline polymer having a side-chain terpyridine group.

3 Hydrogen Bonding in Exfoliated Nanocomposites Prepared by Mixing

3.1 Nanocomposites Based on Hydroxylated Polyisoprene

Polyisoprene (PI) has a very simple chemical structure having no functional groups. Thus, organoclay nanocomposites based on PI are *not* expected to give rise to exfoliation of the aggregates of organoclay. However, one can introduce hydroxyl (–OH) groups into a PI by hydroboration followed by oxidation [32] of a PI having predominantly vinyl content (3,4- and 1,2-addition microstructures).

As shown earlier by Chung et al. [33], Lee and Han [34] found that the double bond in a PI having predominantly 1,4-addition microstructure was very difficult to introduce hydroxyl groups. They first synthesized, via anionic polymerization, a nearly monodisperse PI having 34% 1,2-addition, 59% 3,4-addition, and 7% 1,4-addition in tetrahydrofuran (THF) as solvent. Subsequently, the PI was hydroborated followed by oxidation according to the procedures detailed in a paper by Lee and Han [34], yielding
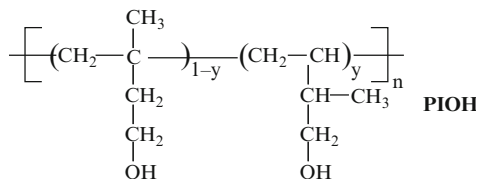
having varying degrees (30%, 50%, 75%, and 100%) of hydroxylation. Figure 3a gives the FTIR spectra for PI, PIOH-30, PIOH-50, PIOH-75, and PIOH-100, in which the numbers (30, 50, 75, and 100) refer to the percentage of hydroxylation
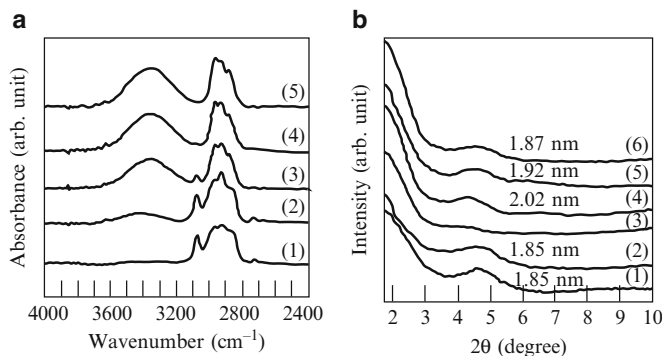
Fig. 3 (**a**) FTIR spectra for (1) PI, (2) PIOH-30, (3) PIOH-50, (4) PIOH-75, and (5) PIOH-100. (**b**) XRD patterns for (1) Cloisite 30B, (2) PI/Cloisite 30B® nanocomposite, (3) (PIOH-30)/Cloisite 30B® nanocomposite, (4) (PIOH-50)/Cloisite 30B® nanocomposite, (5) (PIOH-75)/Cloisite 30B® nanocomposite, and (6) (PIOH-100)/Cloisite 30B® nanocomposite (Reprinted from Lee and Han [31]. Copyright 2003, with permission from the American Chemical Society)

of the vinyl content in the homopolymer PI. It is seen in Fig. 3a that the area under the adsorption band at ca. $3,360 \, cm^{-1}$, representing the –OH group, increases with increasing degree of hydroxylation.

Subsequently, Lee and Han [31] prepared, via solution blending in THF, nanocomposites of Cloisite 30B® and PIOH-30, PIOH-50, PIOH-75, or PIOH-100. Figure 3b gives the XRD patterns for (1) Cloisite 30B®, (2) PI/Cloisite 30B®, (3) (PIOH-30)/Cloisite 30B®, (4) (PIOH-50)/Cloisite 30B®, (5) (PIOH-75)/Cloisite 30B®, and (6) (PIOH-100)/Cloisite 30B®, in which the concentration of Cloisite 30B® in all of the nanocomposites was 5 wt%. The following observations in Fig. 3b are worth noting. (1) The PI/Cloisite 30B® nanocomposite has a conspicuous reflection peak giving rise to a d-spacing of 1.85 nm, the same as that of Cloisite 30B®, indicating that the PI in the nanocomposite did not change the gallery distance of Cloisite 30B® and thus no attractive interactions developed between the PI and Cloisite 30B® during mixing. This observation confirms our expectation that for PI containing no functional group, there would be no attractive interactions with the hydroxyl groups in the surfactant MT2EtOH residing at the surface of Cloisite 30B®. (2) The (PIOH-30)/Cloisite 30B® nanocomposite shows a very broad, almost indistinguishable intensity peak, i.e., featureless XRD pattern, indicating that the nanocomposite has good dispersion of the aggregates of Cloisite 30®, which could only be realized if strong attractive interactions existed between the hydroxyl groups in PIOH-30 and the hydroxyl groups in the surfactant MT2EtOH residing at the surface of Cloisite 30B®. The only attractive interaction that could have existed in the (PIOH-30)/Cloisite 30B® nanocomposite would be hydrogen bonding between the hydroxyl groups in PIOH-30 and the hydroxyl groups in the surfactant MT2EtOH residing at the surface of Cloisite 30B®. Based on the experimental evidence, via FTIR spectroscopy, which will be presented below, this indeed is the case. (3) The d-spacing of the (PIOH-50)/Cloisite 30B® nanocomposite is

2.02 nm, which is slightly higher than the d-spacing (1.85 nm) of Cloisite 30B®, suggesting that the PIOH-50 intercalated slightly the aggregates of Cloisite 30B®. (4) Interestingly, the d-spacing of the other two nanocomposites decreases with increasing degree of hydroxylation from 50 to 75 and to 100%, ultimately reaching the d-spacing of Cloisite 30B®, indicating that the (PIOH-75)/Cloisite 30B® and (PIOH-100)/Cloisite 30B® nanocomposites must have had poor dispersion of the aggregates of Cloisite 30B®. The above observations indicate that there exists an optimum range of hydroxyl groups in PIOH, which gives rise to a very high degree of dispersion in the PIOH/Cloisite 30B® nanocomposites. Below I will explain the reason for the existence of an optimum range of hydroxyl groups in PIOH that would give rise to a very high degree of dispersion of the aggregates of Cloisite 30B® in the PIOH/Cloisite 30B® nanocomposites.

It is worth mentioning at this juncture that earlier Jeon et al. [35] reported a very high degree of dispersion, as determined from XRD and TEM, in a 95/5 PI/Cloisite 10A® nanocomposite, in which 95/5 refers to the weight percents of the constituent components. We were not able to reproduce their results in that their experimental results were at odd with our findings for the 95/5 PI/Cloisite 30B® nanocomposite prepared in our laboratory. Referring to Table 2, the surfactant 2MBHT residing at the surface of Cloisite 10A® does not have any functional group. In our study we synthesized, via anionic polymerization in toluene as solvent, a homopolymer PI having a weight-average molecular weight (M_w) of 36,600 and a polydispersity index (M_w/M_n) of 1.07, as determined by gel permeation chromatography (GPC) against polystyrene standards. In an effort to find a possible source(s) for the discrepancy between the two studies, we also purchased from Aldrich Chemical the same grade of PI which Jeon et al. [35] purchased earlier. Using GPC against polystyrene standards, we learned that the molecular weight and its polydispersity index of the Aldrich PI had $M_w = 58,000$ and $M_w/M_n = 4.9$, as can be seen from the GPC trace given in Fig. 4. I cannot explain why the 95/5 PI/Cloisite 10A® nanocomposites prepared by Jeon et al. [35] had a very high degree of dispersion since little or no attractive interactions between the Aldrich PI and Cloisite 10A® could have taken place during the preparation of the nanocomposite by solution blending.
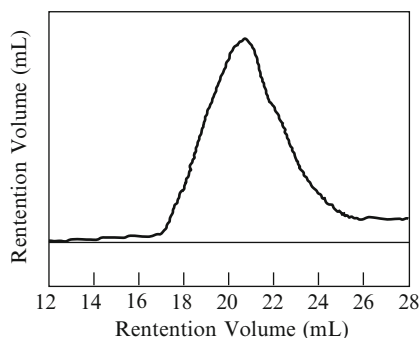
Fig. 4 GPC trace of Aldrich polyisoprene, showing that it has $M_w = 58,000$ and $M_w/M_n = 4.9$ against polystyrene standards

3.2 Nanocomposites Based on Poly(ethylene-ran-vinyl acetate-ran-alcohol) Copolymer

Lee and Han [31] prepared organoclay nanocomposites based on poly(ethylene-*ran*-vinyl acetate) copolymer (EVA), poly(ethylene-*ran*-vinyl alcohol) copolymer (EVOH), and poly(ethylene-*ran*-vinyl acetate-*ran*-vinyl alcohol) copolymer (EVAOH). The rationale behind the choice of these polymers was the following. EVA is a nonpolar random polymer, while EVOH is a *polar* random polymer that can be obtained by 100% alcoholysis (or hydrolysis) of the vinyl acetate in EVA. Lee and Han were able to control the degree of polarity by partial hydrolysis of EVA, which yielded the terpolymer EVAOH. This enabled them to investigate the dispersion characteristics of nanocomposites composed of an organoclay and a polymer matrix having a wide range of polarity from nonpolar EVA to highly polar EVOH. Since it is generally accepted that an increased polarity of the polymer matrix increases its compatibility with the polar surfaces of an organoclay, the organoclays and thermoplastic polymers chosen in their study enabled them to conduct a systematic investigation on the effects of polymer matrix/organoclay compatibility and the gallery distance of organoclay on the dispersion characteristics of the nanocomposites prepared.

Figure 5 gives FTIR spectra for EVA, EVAOH-5, EVAOH-11, and EVOH-53 specimens, in which EVAOH-5 and EVAOH-11 refer to the random terpolymer EVAOH having 5 and 11 mol% vinyl alcohol (VOH), respectively, obtained via partial hydrolysis of EVA, and EVOH-53 refers to the random copolymer EVOH having 53 mol% vinyl alcohol. The assignments of various IR absorption bands in EVAOH can be found in the literature [36]. The broad absorption band centered at approximately $3{,}360\,\mathrm{cm}^{-1}$, representing the hydroxyl (–OH) group, is the most important one. The extent of reduction of the absorption band at approximately $610\,\mathrm{cm}^{-1}$ has been used for quantitative determination of vinyl acetate (VA) content in an EVAOH [36]. It is seen in Fig. 5 that the absorption band at approximately
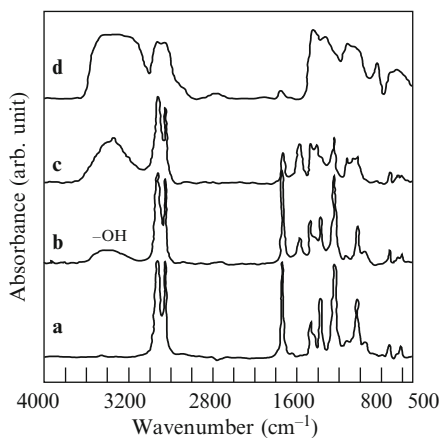
Fig. 5 FTIR spectra for (**a**) EVA, (**b**) EVAOH-5, (**c**) EVAOH-11, and (**d**) EVOH-53 taken at room temperature. (Reprinted from Lee and Han [31]. Copyright 2003, with permission from the American Chemical Society)

$3,360\,cm^{-1}$ decreases as the degree of hydrolysis of EVA is decreased from 11 mol% (EVAOH-11) to 5 mol% (EVAOH-5). According to Koopmans et al. [36], the absorption band at approximately $720\,cm^{-1}$, which remains unchanged after partial hydrolysis, may also be used to determine the VA content in an EVAOH.

Figure 6 gives XRD patterns of Cloisite 30B®, Cloisite 15A®, and six nanocomposites. Note in Fig. 6 that Cloisite 30B® has a gallery distance (d-spacing) of 1.85 nm, while Cloisite 15A® has a d-spacing of 3.15 nm. The following observations in Fig. 6 are worth noting. (1) The EVA/Cloisite 30B® nanocomposite has a d-spacing of 2.1 nm, an increase of only 0.25 nm (13.5% increase) over the d-spacing of Cloisite 30B®, while the EVA/Cloisite 15A® nanocomposite has a d-spacing of 3.84 nm, an increase of 0.69 nm (21.9% increase) over the d-spacing of Cloisite 15A®. This observation seems to suggest that the degree of intercalation of the Cloisite 15A® aggregates in EVA might be slightly higher than that of Cloisite 30B® in EVA. (2) The (EVAOH-5)/Cloisite 30B® nanocomposite does *not* exhibit a discernible intensity peak, while the (EVAOH-5)/Cloisite 15A® nanocomposite has a d-spacing of 3.80 nm, an increase of 0.65 nm (20.6% increase) over the d-spacing of Cloisite 15A®. This observation seems to suggest that Cloisite 30B® aggregates might have been reasonably well dispersed (exfoliated to a certain degree) in EVAOH-5, while the Cloisite 15A® aggregates might only have been intercalated by EVAOH-5. (3) Both (EVOH-53)/Cloisite 30B® and (EVOH-53)/Cloisite 15A® nanocomposites have the same d-spacing of 3.54 nm, indicating that the d-spacing of the (EVOH-53)/Cloisite 30B® nanocomposite has increased by 1.69 nm (91% increase) over the d-spacing of Cloisite 30B®, while the d-spacing of the (EVOH-53)/Cloisite 15A® nanocomposite has increased by 0.39 nm (12.4%
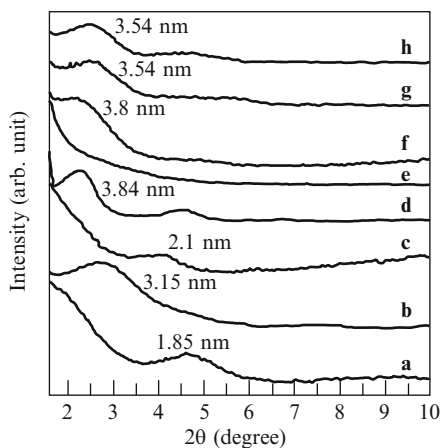
Fig. 6 XRD patterns for (**a**) Cloisite 30B®, (**b**) Cloisite 15A®, (**c**) EVA/Cloisite 30B® nanocomposite, (**d**) EVA/Cloisite 15A® nanocomposite, (**e**) (EVAOH-5)/Cloisite 30B® nanocomposite, (**f**) (EVAOH-5)/Cloisite 15A® nanocomposite, (**g**) (EVOH-53)/Cloisite 30B® nanocomposite, and (**h**) (EVOH-53)/Cloisite 15A® nanocomposite. (Reprinted from Lee and Han [31]. Copyright 2003, with permission from the American Chemical Society)

increase) over the d-spacing of Cloisite 15A$^{\circledR}$. This observation seems to suggest that the degree of intercalation of Cloisite 30B$^{\circledR}$ aggregates in EVOH-53 might be higher than that of Cloisite 15A$^{\circledR}$ aggregates in EVOH-53. (4) The difference in XRD patterns between the (EVAOH-5)/Cloisite 30B$^{\circledR}$ and (EVOH-53)/Cloisite 30B$^{\circledR}$ nanocomposites seems to indicate that EVOH-53 was not as effective as EVAOH-5 in dispersing Cloisite 30B$^{\circledR}$ aggregates. Although XRD patterns may not be regarded as being the most sensitive measure to describe the degree of intercalation or exfoliation of organoclay aggregates in a polymer matrix, they certainly are very useful for making qualitative observations.

Figure 7 gives TEM images of EVA/Cloisite 30B$^{\circledR}$, EVA/Cloisite 15A$^{\circledR}$, (EVAOH-5)/Cloisite 30B$^{\circledR}$, (EVAOH-5)/Cloisite 15A$^{\circledR}$, and (EVOH-53)/Cloisite 30B$^{\circledR}$ nanocomposites, in which the dark areas represent the clay and the gray/bright areas represent the polymer matrix. The following observations in Fig. 7 are worth noting. Within experimental uncertainties, the degree of intercalation of Cloisite 15A$^{\circledR}$ in the EVA/Cloisite 15$^{\circledR}$ nanocomposite is higher than that of Cloisite 30B$^{\circledR}$ in the EVA/Cloisite 30B$^{\circledR}$ nanocomposite. This observation is consistent with that made from the XRD patterns given in Fig. 6. It can be seen in Fig. 7 that the degree of dispersion of Cloisite 30B$^{\circledR}$ aggregates in the (EVAOH-5)/Cloisite 30B$^{\circledR}$ nanocomposite is considerably higher than that in the (EVOH-53)/Cloisite 30B$^{\circledR}$ nanocomposite. A reasonably high degree of dispersion of Cloisite 30B$^{\circledR}$ aggregates in the (EVAOH-5)/Cloisite 30B$^{\circledR}$ nanocomposite is attributable to the existence of attractive interactions, via hydrogen bonding, between the hydroxyl groups in EVAOH-5 and the hydroxyl groups
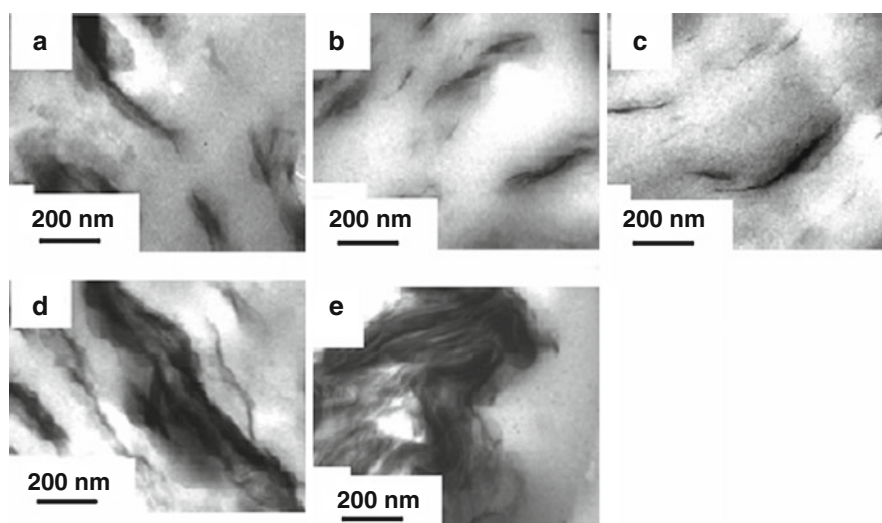
Fig. 7 TEM images of (**a**) EVA/Cloisite 30B$^{\circledR}$ nanocomposite, (**b**) EVA/Cloisite 15A$^{\circledR}$ nanocomposite, (**c**) (EVAOH-5)/Cloisite 30B$^{\circledR}$ nanocomposite, (**d**) (EVAOH-5)/Cloisite 15A$^{\circledR}$ nanocomposite, and (**e**) (EVOH-53)/Cloisite 30B$^{\circledR}$ nanocomposite. (Reprinted from Lee and Han [31]. Copyright 2003, with permission from the American Chemical Society)

in the surfactant MT2EtOH residing at the surface of Cloisite 30B$^{\circledR}$. Note in Fig. 7 that the very large Cloisite 30B$^{\circledR}$ aggregates are not well intercalated in the (EVOH-53)/Cloisite 30B$^{\circledR}$ nanocomposite, suggesting that Cloisite 30B$^{\circledR}$ and EVOH-53 had very poor compatibility (i.e., strong repulsive interactions) in spite of the fact that EVOH-53 has a very high concentration of hydroxyl groups (53 mol%). The reason is that the attractive forces within the EVOH-53 molecules are very strong, prohibiting attractive interactions between the hydroxyl groups in EVOH-53 and the hydroxyl groups in the surfactant MT2EtOH residing at the surface of Cloisite 30B$^{\circledR}$. The above observation is consistent with that made from the XRD patterns given in Fig. 6. Further, in Fig. 7 we observe that the extent of dispersion of organoclay aggregates in the (EVAOH-5)/Cloisite 30B$^{\circledR}$ nanocomposite is much higher than that in the (EVAOH-5)/Cloisite 15A$^{\circledR}$ nanocomposite. Again, this observation is consistent with that made from the XRD patterns given in Fig. 6.

To find the origin(s) of the differences in the extent of dispersion between (EVAOH-5)/Cloisite 30B$^{\circledR}$ and (EVAOH-5)/Cloisite 15A$^{\circledR}$ nanocomposites, let us look at the in situ FTIR spectra given in Fig. 8 of the two nanocomposites at temperatures ranging from 25 to 180 °C. In Fig. 8a, the absorption band for the hydrogen-bonded hydroxyl groups appears at approximately 3,330 cm^{-1}, and the area under this absorption band for the (EVAOH-5)/Cloisite 30B$^{\circledR}$ nanocomposite decreases slightly as the temperature is increased from 25 to 180 °C. The absorption band at approximately 3,330 cm^{-1} still persists at 180 °C, the highest experimental temperature employed. On the other hand, it is seen from Fig. 8b that the area under the absorption band at approximately 3,330 cm^{-1} for the (EVAOH-5)/Cloisite 15A$^{\circledR}$ nanocomposite decreases gradually with increasing temperature and disappears completely at 180 °C. Since there is no polar group in the surfactant 2M2HT residing at the surface of organoclay Cloisite 15A$^{\circledR}$, it is very reasonable to conclude that the
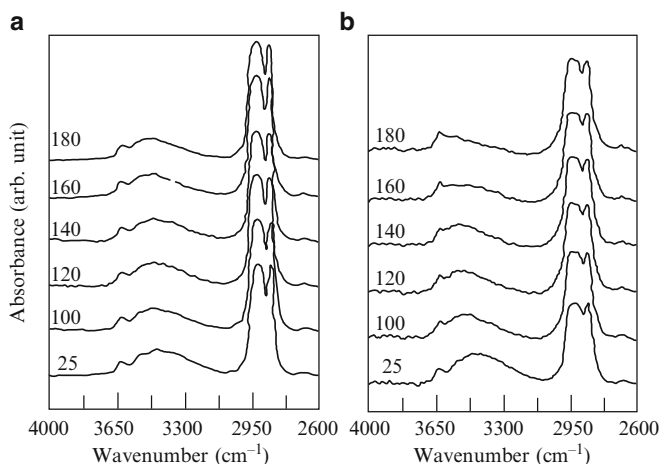
Fig. 8 In situ FTIR spectra for (**a**) (EVAOH-5)/Cloisite 30B$^{\circledR}$ nanocomposite and (**b**) (EVAOH-5)/Cloisite 15A$^{\circledR}$ nanocomposite (Reprinted from Lee and Han [31]. Copyright 2003, with permission from the American Chemical Society)

steady decrease in the area under the absorption band at approximately $3,330\,cm^{-1}$ for the (EVAOH-5)/Cloisite 15A® nanocomposite (Fig. 8b) signifies the gradual weakening of the *intramolecular* forces (due to the presence of hydroxyl groups) within the EVAOH-5 molecules themselves. It is well established that the strength of hydrogen bonds in a polymer decreases with increasing temperature [37]. This observation then leads us to conclude that the persistence of the absorption band at approximately $3,330\,cm^{-1}$ up to 180°C (Fig. 8a) is due to the presence of attractive interactions (hydrogen bonding) between the hydroxyl groups in EVAOH-5 and the hydroxyl groups in the surfactant MT2EtOH residing at the surface of organoclay Cloisite 30B®.

Lee and Han [31] noted that their attempt to determine the percentage of hydrogen bonding sites on the Cloisite 30B® surface by deconvoluting the overlapping peaks in the FTIR spectra shown in Fig. 8 was not successful because the concentration of hydroxyl groups associated with the organoclay Cloisite 30B® in the nanocomposite was very small (estimated to be less than 0.2%). They noted further that an accurate determination, via ^{1}H nuclear magnetic resonance (NMR) spectroscopy, of the amount of the hydroxyl groups in the surfactant MT2EtOH in the nanocomposite systems investigated was found to be extremely difficult due to the very complex nature of its chemical structure.

On the basis of Fig. 8 it can be concluded that the very broad, indistinguishable XRD pattern observed (see Fig. 6) for the (EVAOH-5)/Cloisite 30B® nanocomposite originated from the presence of strong attractive interactions, via hydrogen bonding, between the hydroxyl groups in EVAOH-5 and the hydroxyl groups in the surfactant MT2EtOH residing at the surface of Cloisite 30B®.

There is another factor, the gallery distance of organoclay itself, which can affect the degree of exfoliation of organoclay aggregates. The gallery distance of an organoclay depends on the chemical structure of a surfactant that is applied to the surface of the aggregates of pristine clay (MMT). It was shown in Fig. 5 that the d-spacing of Cloisite 30B® is 1.85 nm and the d-spacing of Cloisite 15A® is 3.15 nm. On the basis of the difference in the gallery distance between the two organoclays, it is reasonable to expect that the (EVAOH-5)/Cloisite 15A® nanocomposite would have a higher degree of dispersion than the (EVAOH-5)/ Cloisite 30B® nanocomposite. However, the experimental results (see Fig. 7) stand in contrast with this expectation. Note in Fig. 8 that the compatibility between EVAOH-5 and Cloisite 30B® is much greater owing to the presence of hydrogen bonding than the compatibility between EVAOH-5 and Cloisite 15A®. The above observation seems to suggest that the compatibility between the polymer matrix and an organoclay plays a predominant role over the difference in the gallery distance of two organoclays in determining the degree of dispersion of organoclay aggregates. This is quite understandable in that when strong repulsive forces exist between the polymer matrix and organoclay (i.e., when the two are incompatible), the polymer molecules will not be able to approach the surface of the layered silicates and thus they will be unable to disperse the organoclay aggregates effectively or peel away the top and bottom layers as promoted by polymer adsorption and the application of shear stress.

Intercalated organoclay nanocomposites based on EVA have also been reported by some investigators [38–40], who employed XRD and TEM to determine the morphology of the nanocomposites. Their findings are consistent with the results presented in Fig. 6. Of particular note is the study of Gelfer et al. [40] who employed Cloisite 6A® (see Table 2) and Cloisite 20A® to prepare, via melt blending, nanocomposites based on EVA. Note that Cloisite 20A® is a commercial organoclay produced by Southern Clay Products, which has the same surfactant 2M2HT as Cloisite 6A® (see Table 2), except that the concentration of 2M2HT in Cloisite 20A® is 95 meq/100 g while the concentration of 2M2HT in Cloisite 6A is 90 meq/100 g (see Table 2). It should be mentioned that, according to Southern Clays Products, after washing with methanol, Cloisite 15A® (see Table 2) will become Cloisite 20A®, i.e., Cloisite 15A® has an excess amount of surfactant 2M2HT (125 meq/100 g) as compared to Cloisite 20A®. It is now very clear why the EVA/Cloisite 20A® nanocomposites prepared by Gelfer et al. [40] had intercalation of the aggregates of Cloisite 20A®, very similar to the EVA/Cloisite 15A® nanocomposite investigated by Lee and Han [31], the results of which are presented in Figs. 6 and 7. That is, no attractive interactions exist between EVA and the surfactant 2M2HT residing at the surface of Cloisite 6A®, Cloisite 15A®, or Cloisite 20A®.

3.3 Nanocomposites Based on Polycarbonate

Lee and Han [41] investigated the dispersion characteristics of polycarbonate (PC)-based organoclay nanocomposites that were melt-blended in a twin-screw extruder. They employed Cloisite 30B® (see Table 2) as the organoclay, because they wanted to determine if hydrogen bonds formed between the carbonyl groups in PC and the hydroxyl groups in the surfactant MT2EtOH residing at the surface of Cloisite 30B® during melt blending. For comparison, they also prepared a PC-based nanocomposite using MMT.

Figure 9 gives XRD patterns of MMT, Cloisite 30B®, PC/MMT nanocomposite, and PC/Cloisite 30B® nanocomposite, in which the amount of MMT and Cloisite 30B® in the respective nanocomposites was 4.3 wt%. The XRD patterns in Fig. 9 show that Cloisite 30B® has an intensity peak at $2\theta = 4.6°$, giving rise to a d-spacing of 1.85 nm, while MMT has a d-spacing of 1.17 nm. The XRD patterns given in Fig. 9 indicate that the d-spacing of the PC/MMT nanocomposite is approximately 1.31 nm, which is slightly higher than that (1.17 nm) of MMT. On the other hand, in Fig. 9 we observe *no* sharp reflections in the XRD pattern of the PC/Cloisite 30B® nanocomposite. The lack of a discernible intensity peak in Fig. 9 for the PC/Cloisite 30B® nanocomposite indicates that very good dispersion of the aggregates of Cloisite 30B occurred during melt blending with PC and its carbonyl groups.

Figure 10 gives TEM images of (a) PC/Cloisite 30B® nanocomposite and (b) PC/MMT nanocomposite, where the dark areas represent the clay and the

Fig. 9 X-ray diffraction patterns for (**a**) MMT, (**b**) Cloisite 30B®, (**c**) PC/MMT nanocomposite, and (**d**) PC/Cloisite 30B® nanocomposite. (Reprinted from Lee and Han [41]. Copyright 2003, with permission from Elsevier)
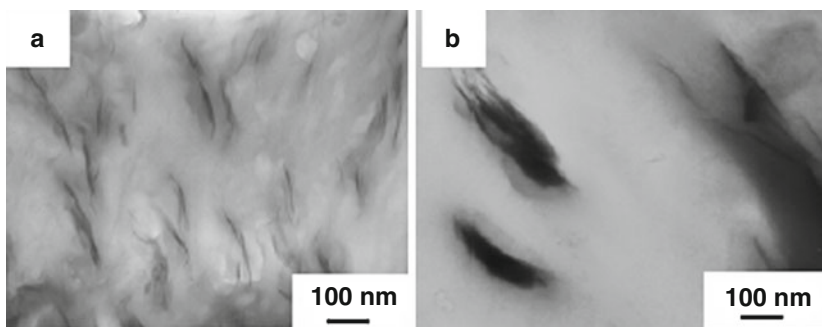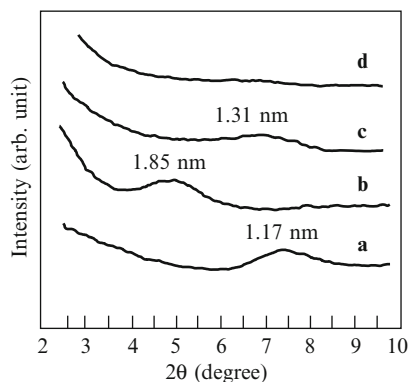
Fig. 10 TEM images of (**a**) PC/Cloisite 30B® nanocomposite and (**b**) PC/MMT nanocomposite, where the *dark areas* represent the clay and the *gray/white areas* represent the PC matrix. (Reprinted from Lee and Han [41]. Copyright 2003, with permission from Elsevier)

gray/white areas represent the PC matrix. It is clearly seen from Fig. 10 that PC in the PC/Cloisite 30B® nanocomposite has dispersed fairly well the aggregates of Cloisite 30B®, whereas PC in the PC/MMT nanocomposite has not (i.e., large aggregates of MMT are bundled together).

In an effort to find the mechanism that led to a much higher degree of dispersion of the aggregates of Cloisite 30B® as compared to the rather poor dispersion of MMT aggregates observed in Fig. 10, Lee and Han [41] conducted in situ FTIR spectroscopy experiments at various temperatures ranging from 30 to 280 °C for neat PC, PC/MMT nanocomposite, and PC/Cloisite 30B® nanocomposite, and the results are presented in Fig. 11. In Fig. 11a an absorption band for neat PC appears at approximately $1,775 \, cm^{-1}$, which represents the free carbonyl stretching vibration peak [37, 42]. Similar observation can be made in Fig. 11b for the PC/MMT nanocomposite, indicating that little attractive interaction occurred between PC and MMT. However, in Fig. 11c we observe two stretching peaks, one peak at about $1,790 \, cm^{-1}$ that is attributable to the free carbonyl stretching peak and another peak at about $1,750 \, cm^{-1}$ that is attributable to the hydrogen bonded carbonyl stretching peak in the PC/Cloisite 30B® nanocomposite. The hydrogen bonded carbonyl
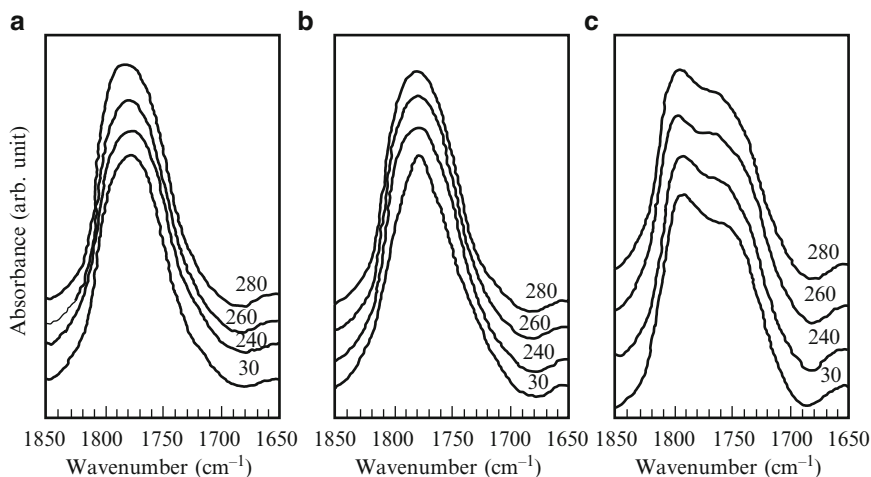
Fig. 11 FTIR spectra at various temperatures for (**a**) PC, (**b**) PC/MMT nanocomposite, and (**c**) PC/Cloisite 30B® nanocomposite. (Reprinted from Lee and Han [41]. Copyright 2003, with permission from Elsevier)

stretching peak appearing at about $1,750\,cm^{-1}$ is believed to be due to the specific interactions between the carbonyl groups in PC and the hydroxyl groups in MT2EtOH residing at the surface of Cloisite 30B® in the PC/Cloisite 30B® nanocomposite.

The presence of hydrogen bonds between the carbonyl groups in poly (vinylphenol) (PVPh) and the hydroxyl groups in poly(vinyl acetate) (PVAc) in a PVPh/PVAc blend has been demonstrated, as depicted below [43]:
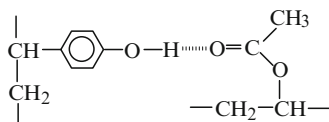
According to Coleman et al. [37] and Painter and Coleman [42], the stretching band representing free carbonyl groups in PVAc appears at $1,739\,cm^{-1}$ and the stretching band representing the PVAc acetoxy carbonyl groups hydrogen bonded to the phenolic hydroxyl group of PVPh appears at $1,714\,cm^{-1}$. They noted that the specific interactions, via hydrogen bonding, between the carbonyl groups in PVAc and the hydroxyl groups in PVPh was the reason for the PVAc/PVPh blends being miscible.

Note in Fig. 11c that the band for the hydrogen bonding (at $1,750\,cm^{-1}$) appears as a shoulder and is not well resolved. This is understandable, in that the number of hydroxyl groups in the PC/Cloisite 30B® nanocomposite is very small since the level of Cloisite 30B® in the nanocomposite is only 4.3 wt% and further Cloisite 30B® contains 32 wt% MT2EtOH, which in turn has small amounts

of hydroxyl groups (see the chemical structure of MT2EtOH given in Table 2). It is of great interest to observe in Fig. 11c that the area under the absorption band at approximately $1,750\,cm^{-1}$ for the PC/Cloisite 30B® nanocomposite remains more or less constant over the entire range of temperatures investigated from 30 to 280 °C. The above observation seems to indicate that the strength of hydrogen bonds between the carbonyl groups in PC and the hydroxyl group in MT2EtOH of Cloisite 30B® persists up to 280 °C. It can be concluded from Fig. 11 that specific interactions, via hydrogen bonding, exist between the carbonyl group in PC and the hydroxyl group in MT2EtOH residing at the surface of Cloisite 30B® in the PC/Cloisite 30B® nanocomposite, giving rise to reasonably good dispersion in the PC/Cloisite 30B®nanocomposite, as observed by XRD pattern (Fig. 9) and TEM image (Fig. 10).

Based on thermogravimetric analysis, Lee and Han [41] noted that, at 280 °C, PC had a weight loss of 0.4%, Cloisite 30B® had a weight loss of 7.8%, and PC/Cloisite 30B® nanocomposite had a weight loss of 0.6%. Since Cloisite 30B® had 32 wt% of surfactant (MT2EtOH), the net weight loss of MT2EtOH in the Cloisite 30B® at 280 °C was 24.4%. On the other hand, the net loss of MT2EtOH in the PC/Cloisite 30B® nanocomposite at 280 °C was 14.6 wt%, because the loss of 0.6 wt% in the nanocomposite includes the loss of 0.4 wt% of PC and thus the net loss of MT2EtOH alone is 0.2 wt%. Note that the amount of MT2EtOH in the PC/Cloisite 30B® nanocomposite containing 4.3 wt% Cloisite 30B® is 1.37 wt%, because Cloisite 30B® contains 32 wt% of MT2EtOH. What is most interesting from the above observations is that the net loss (14.6 wt%) of MT2EtOH in the PC/Cloisite 30B® nanocomposite is about one half the net loss (24.4 wt%) of MT2EtOH in Cloisite 30B®. The lower degree of thermal degradation of MT2EtOH observed in the PC/Cloisite 30B® nanocomposite, as compared with that in Cloisite 30B® alone, may be explained by that the PC penetrated (or diffused) into the gallery of Cloisite 30B platelets might have retarded thermal degradation and diffusion of MT2EtOH, relative to the situation where MT2EtOH is present on the surface of layered silicate aggregates without any polymers penetrated (or diffused) into the gallery. Further evidence that the extent of thermal degradation of MT2EtOH in the PC/Cloisite 30B® nanocomposite at temperatures up to 280 °C is insignificant is manifested by the FTIR spectra given in Fig. 11c, in which we observe that the area under the shoulder at the absorption band in the vicinity of $1,750\,cm^{-1}$, which represents the hydrogen bonded carbonyl stretching peak, remains virtually constant over the temperatures ranging from 30 to 280 °C. In other words, if the extent of thermal degradation of MT2EtOH had been significant, we should not have observed the same area under the shoulder at the absorption band at $1,750\,cm^{-1}$. Thus, the strength of the hydrogen bonding, which persisted even at 280 °C, in the PC/Cloisite 30B® nanocomposite as evidenced by the XRD and FTIR data shown above also must have contributed to the lower degree of thermal degradation of the surfactant MT2EtOH.

Yoon et al. [44] investigated the effect of the chemical structures residing at the surface of organoclays on the morphology and properties of nanocomposites based on PC. In the preparation of these nanocomposites using a twin-screw

extruder, they employed Cloisite 30B®, Cloisite 20A®, and ten additional experimental organoclays having various amine surfactants, and two grades of PC: a medium molecular-weight polycarbonate (MMW-PC) and a high molecular-weight polycarbonate (HMW-PC). Based on TEM images, they observed that some nanocomposites had poor dispersion of organoclay aggregates, while other nanocomposites had partial exfoliation of organoclay aggregates. However, they did not elaborate on the mechanism that led to partial exfoliation. They found that an enhancement in modulus was greater for nanocomposites based on HMW-PC than MMW-PC, which they attributed to the higher shear stresses generated during melt processing of HMW-PC.

3.4 Nanocomposites Based on Partially Hydroxylated Isoprene- or Butadiene-Containing Diblock and Triblock Copolymers

As mentioned in Introduction, block copolymers have a greater flexibility, as compared to homopolymers, to be modified chemically after polymerization or in the synthesis of block copolymers having a functional block. Here I discuss the dispersion characteristics in several organoclay nanocomposites based on (1) a polystyrene-*block*-hydroxylated polyisoprene (SIOH diblock) copolymer, (2) a polyisoprene-*block*-polystyrene-*block*-hydroxylated polybutadiene (ISBOH triblock) copolymer, and (3) a polystyrene-*block*-hydroxylated polyisoprene-*block*-polystyrene (SIOHS triblock) copolymer.

Lee and Han [6] hydroxylated the PI block of an SI diblock copolymer yielding the chemical structure
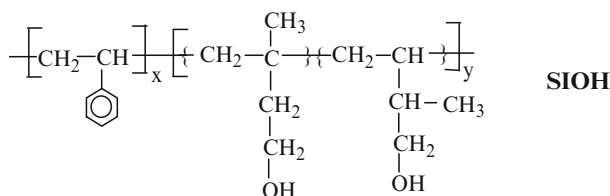
SIOH

which is polystyrene-*block*-hydroxylated polyisoprene (SIOH diblock) copolymer. Similar to the synthesis of homopolymer PIOH discussed above when presenting the organoclay nanocomposites based on PIOH, the PI block in an SI diblock copolymer must have predominantly vinyl microstructures (e.g., 34% 1,2-addition and 59% 3,4-addition), so that hydroboration/oxidation can effectively be facilitated [34].

Figure 12 gives XRD patterns of (a) Cloisite 30B®, (b) (SI-10/9)/Cloisite 30B® nanocomposite, and (c) (SI-14/3-OH)/Cloisite 30® nanocomposite, in which SI-10/9 is an SI diblock copolymer having lamellar microdomains and
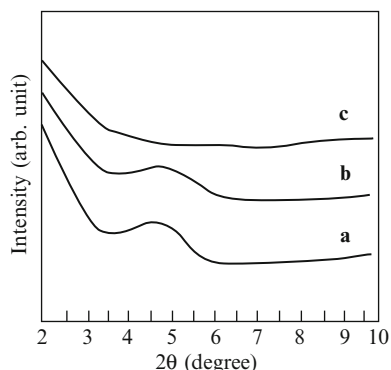
Table 3 Molecular characteristics of the SI diblock copolymers investigated by Lee and Han [6]

Sample code	M_n (g/mol)[a]	M_w/M_n [b]	PS (wt frac)[c]	Morphology[d]
SI-10/9	1.94×10^4	1.02	0.54	Lamellae
SI-14/3	1.70×10^4	1.08	0.84	Homogeneous

[a]Determined from membrane osmometry
[b]Determined from GPC
[c]Determined from ^{1}H NMR spectroscopy
[d]Determined from TEM

SI-14/3-OH is a microphase-separated diblock copolymer having hexagonally packed, cylindrical microdomains of polystyrene (PS), which was obtained by hydroxylation of a homogeneous SI diblock copolymer SI-14/3 [6]. The molecular characteristics of SI-10/9 and SI-14/3 are given in Table 3, and the weight fraction of Cloisite 30B$^{\circledR}$ in the two nanocomposites is 5 wt%. The following observations in Fig. 12 are worth noting. Cloisite 30B$^{\circledR}$ has an intensity peak at $2\theta = 4.6°$, giving rise to a d-spacing of 1.85 nm. The XRD pattern of (SI-10/9)/Cloisite 30B$^{\circledR}$ nanocomposite is little different from that of pristine Cloisite 30B$^{\circledR}$, suggesting that the block copolymer SI-10/9 and Cloisite 30B$^{\circledR}$ do not have attractive interactions and thus the aggregates of Cloisite 30B$^{\circledR}$ might not even have been intercalated by SI-10/9. This speculation is very reasonable in that neat block copolymer SI-10/9 does not have any functional group that can have attractive interactions with the hydroxyl groups in the surfactant MT2EtOH residing at the surface of Cloisite 30B$^{\circledR}$. On the other hand, the XRD pattern of (SI-14/3-OH)/Cloisite 30B$^{\circledR}$ nanocomposite has a barely discernible reflection, suggesting that a significant degree of dispersion of the aggregates of Cloisite 30B$^{\circledR}$ might have occurred by the functionalized block copolymer SI-14/3-OH.

Figure 13 gives TEM images of (a) (SI-14/3-OH)/Cloisite 30B$^{\circledR}$ nanocomposite and (b) (SI-10/9)/Cloisite 30B$^{\circledR}$ nanocomposite, where the dark areas represent the organoclay and the gray/bright areas represent the block copolymer matrix. It is clearly seen from Fig. 13 that SI-14/3-OH in the (SI-14/3-OH)/Cloisite 30B$^{\circledR}$ nanocomposite has dispersed the aggregates of Cloisite 30B$^{\circledR}$ fairly well, whereas
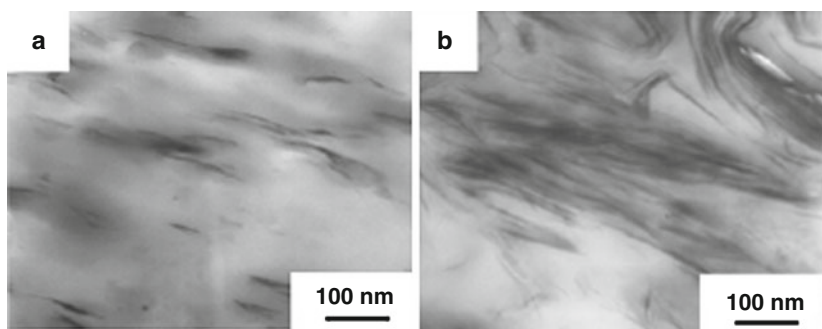
Fig. 13 TEM images of (**a**) (SI-14/3-OH)/Cloisite 30B$^{\circledR}$ nanocomposite and (**b**) (SI-10/9)/ Cloisite 30B$^{\circledR}$ nanocomposite, where the *dark areas* represent the organoclay and the *gray/white areas* represent the block copolymer matrix. (Reprinted from Lee and Han [6]. Copyright 2003, with permission from the American Chemical Society)

SI-10/9 in the (SI-10/9)/Cloisite 30B$^{\circledR}$ nanocomposite has not (i.e., large aggregates of Cloisite 30B$^{\circledR}$ are bundled together). The above observations suggest that the hydroxyl groups in SI-14/3-OH must have played the major role in dispersing the aggregates of Cloisite 30B$^{\circledR}$, leading to a significant degree of dispersion of Cloisite 30B$^{\circledR}$ aggregates. It should be mentioned that the better dispersed the Cloisite 30B$^{\circledR}$ aggregates are, the larger will be the total surface area of the layered silicates of Cloisite 30B$^{\circledR}$ that are available for interactions with the hydroxyl groups in SI-14/3-OH, which will in turn help increase the extent of dispersion of Cloisite 30B$^{\circledR}$ aggregates.

In an effort to test the hypothesis made above, Lee and Han [6] conducted in situ FTIR spectroscopy at various temperatures ranging from 30 to 240 °C for (a) neat block copolymer SI-14/3-OH, (b) (SI-14/3-OH)/Cloisite 30B$^{\circledR}$ nanocomposite, and (c) (SI-10/9)/Cloisite 30B$^{\circledR}$ nanocomposite, and the results are presented in Fig. 14. Referring to Fig. 14, hydrogen-bonded and free hydroxyl groups appear at 3,330 and 3,630 cm^{-1}, respectively. The following observations in Fig. 14 are worth noting. In Fig. 14a the area under the absorption band at 3,330 cm^{-1} for SI-14/3-OH is largest at 30 °C and then decreases as the temperature is increased. Note in Fig. 14a that the absorption band at 3,330 cm^{-1} virtually disappears at 200 °C, which is very close to the order-disorder transition temperature (T$_{ODT}$) of SI-14/3-OH [6]. The above observation indicates that the hydroxyl groups in the block copolymer SI-14/3-OH form hydrogen bonds and that their strength is weakened with increasing temperature, consistent with the general trend of the temperature dependence of hydrogen bonding [37]. In Fig. 14b we observe that at 30 °C the area under the absorption band at about 3,330 cm^{-1} for the (SI-14/3-OH)/Cloisite 30B$^{\circledR}$ nanocomposite is indeed very large compared with that for the neat block copolymer SI-14/3-OH (compare with Fig. 14a). Interestingly, the absorption band at approximately 3,330 cm^{-1} for the (SI-14/3-OH)/Cloisite 30B$^{\circledR}$ nanocomposite persists at temperatures as high as 240 °C, the highest experimental temperature employed. Note that this is *not* the case for the neat block copolymer SI-14/3-OH (compare
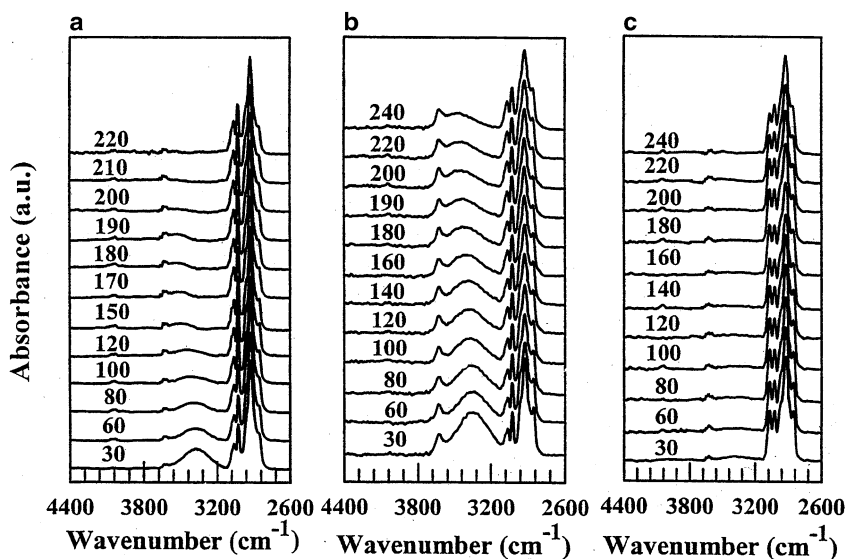
Fig. 14 FTIR spectra at varying temperatures for (**a**) SI-14/3-OH, (**b**) (SI-14/3-OH)/Cloisite 30B® nanocomposite, and (**c**) (SI-10/9)/Cloisite 30B® nanocomposite. (Reprinted from Lee and Han [6]. Copyright 2003, with permission from the American Chemical Society)

Fig. 14b with Fig. 14a). This observation suggests that very strong hydrogen bonds are formed between the hydroxyl groups in SI-14/3-OH and the hydroxyl groups in MT2EtOH of Cloisite 30B®. In contrast, in Fig. 14c we cannot find evidence that hydrogen bonds are formed between block copolymer SI-10/9 and the hydroxyl groups in the surfactant MT2EtOH residing at the surface of Cloisite 30B® in the (SI-10/9)/Cloisite 30B® nanocomposite. This should not surprise us, because SI-10/9 does not have any functional groups. Further, small amounts of hydroxyl groups present in the 5 wt% Cloisite 30B® are diluted by the 95 wt% SI-10/9 in the (SI-10/9)/Cloisite 30B® nanocomposite. It can be concluded that a high degree of dispersion of Cloisite 30B® aggregates in the (SI-14/3-OH)/Cloisite 30B® nanocomposite suggested by the XRD pattern (see Fig. 12) and shown by the TEM image (see Fig. 13a) has originated from the presence of strong attractive interactions, via hydrogen bonding, between the hydroxyl groups in SI-14/3-OH and the hydroxyl groups in the surfactant MT2EtOH residing at the surface of Cloisite 30B®.

Choi et al. [5] investigated the dispersion characteristics of organoclay nanocomposites based on ISB, ISBOH, SIS and SIOHS triblock copolymers. The objective of their investigation was to find out whether the location(s) of the functional group (endblock vs midblock) in a given triblock copolymer plays any role in the effectiveness of dispersing organoclay aggregates. To facilitate our discussion here the chemical structures of ISBOH and SIOHS triblock copolymers are given below. Note that in the ISBOH triblock copolymer the endblock PB of an ISB triblock copolymer was hydroxylated, while in the SIOHS triblock copolymer the midblock

$$\left[CH_2-\underset{\underset{CH_3}{|}}{C}=CH-CH_2\right]_x \left[CH_2-\underset{\underset{\bigcirc}{|}}{CH}\right]_y \left[CH_2-\underset{\underset{\underset{\underset{OH}{|}}{CH_2}}{\underset{|}{CH_2}}}{CH}\right]_z$$

ISBOH triblock

PI block   PS block   PBOH block

$$\left[CH_2-\underset{\underset{\bigcirc}{|}}{CH}\right]_x \left(CH_2-\underset{\underset{\underset{\underset{OH}{|}}{CH_2}}{\underset{\underset{CH_2}{|}}{CH_3}}}{C}\right)\left(CH_2-\underset{\underset{\underset{\underset{OH}{|}}{CH_2}}{\underset{|}{CH-CH_3}}}{CH}\right)_y \left[\underset{\underset{\bigcirc}{|}}{CH}-CH_2\right]_x$$

SIOHS triblock

PS block   PIOH block   PS block
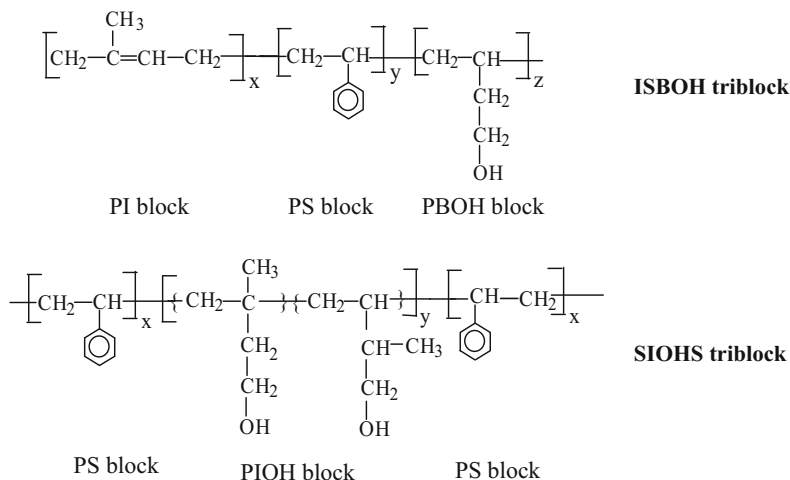
PI of an SIS triblock copolymer was hydroxylated. As will be shown below, this distinction is very important. The PBOH block in an ISBOH triblock copolymer was obtained by selective hydroxylation of 1,2-addition of the PB block of an ISB triblock copolymer. Note further that in the hydroxylation of an SIS triblock copolymer to obtain SIOHS triblock copolymer, the PI block of an SIS triblock copolymer had predominantly vinyl microstructure (34% 1,2-addition and 59% 3,4-addition) as mentioned above when an SIOH diblock copolymer was obtained, via hydroxylation, from an SI diblock copolymer. According to Choi et al. [5], all of the 1,2-addition (93%) in the PB block was hydroxylated, leaving only 1,4-addition (7%) in the remaining PB block of the resultant ISBOH triblock copolymer, and little or no 1,4-addition in the PI block of the ISB triblock copolymer was hydroxylated. It has been reported in the literature [33] that the rate of hydroxylation of 1,2-PB is much faster than that of 1,4-PB, and that the rate of hydroxylation of 1,2-PB is much faster than that of 1,2- and 3,4-PI. In the preparation of their nanocomposites, Choi et al. [5] varied the degree of hydroxylation in each triblock copolymer and employed two organoclays, Cloisite 30B® and Cloisite 15A®. Table 4 gives a summary of the molecular characteristics of ISB, ISBOH, SIS, and SIOHS triblock copolymers, and Table 5 gives a summary of the nanocomposites investigated in their study.

Figure 15 gives XRD patterns for Cloisite 15A® and its nanocomposites with ISB and ISBOH triblock copolymers with three different degrees of hydroxylation (16, 24, and 39 mol%) and Cloisite 30B® and its nanocomposites with ISB and ISBOH triblock copolymers with three different degrees of hydroxylation (16, 24, and 39 mol%). It is seen in Fig. 15 that the d-spacings of Cloisite 15A® in the ISB/Cloisite 15A® and ISBOH/Cloisite 15A® nanocomposites are very similar. This observation can be understood from the point of view that there are little or no attractive interactions between the surfactant 2M2HT residing at the surface of Cloisite 15A® and ISB or ISBOH triblock copolymers. Note in Fig. 15 that the

Table 4 Molecular characteristics of the ISB, ISBOH, SIS, and SIOHS triblock copolymers investigated by Choi et al. [5]

Sample code	M_n^a	M_w/M_n^a	w_{PS}^b	w_{PI}^b	w_{PB}^b	Degree of hydroxylation (mol%)^b
ISB	9.6×10^3	1.15	0.34	0.36	0.30	0
ISBOH-16	9.7×10^3	1.14				16
ISBOH-24	9.6×10^3	1.15				24
ISBOH-39	9.6×10^3	1.15				39
SIS	3.7×10^4	1.10	0.46	0.54		0
SIOHS-16	3.9×10^4	1.09				16
SIOHS-32	3.7×10^4	1.11				32

[a]Determined from GPC against polystyrene standards
[b]Weight fraction determined from ^{1}H NMR spectroscopy

Table 5 Sample codes of the nanocomposites^a based on ISB, ISBOH, SIS or SIOHS triblock copolymers investigated by Choi et al. [5]

Sample code	Degree of hydroxylation
(a) ISB and ISBOH nanocomposites	
ISB/Cloisite 15A®	Neat ISB triblock copolymer
ISB/Cloisite 30B®	Neat ISB triblock copolymer
(ISBOH-16)/Cloisite 15A®	16 mol% hydroxyl group in the ISBOH triblock copolymer
(ISBOH-16)/Cloisite 30B®	16 mol% hydroxyl group in the ISBOH triblock copolymer
(ISBOH-24)/Cloisite 15A®	24 mol% hydroxyl group in the ISBOH triblock copolymer
(ISBOH-24)/Cloisite 30B®	24 mol% hydroxyl group in the ISBOH triblock copolymer
(ISBOH-39)/Cloisite 15A®	39 mol% hydroxyl group in the ISBOH triblock copolymer
(ISBOH-39)/Cloisite 30B®	39 mol% hydroxyl group in the ISBOH triblock copolymer
(b) SIS and SIOHS nanocomposites	
SIS/Cloisite 15A®	Neat SIS triblock copolymer
SIS/Cloisite 30B®	Neat SIS triblock copolymer
(SIOHS-16)/Cloisite 15A®	16 mol% hydroxyl group in the SIOHS triblock copolymer
(SIOHS-32)/Cloisite 15A®	32 mol% hydroxyl group in the SIOHS triblock copolymer
(SIOHS-16)/Cloisite 30B®	16 mol% hydroxyl group in the SIOHS triblock copolymer
(SIOHS-32)/Cloisite 30B®	32 mol% hydroxyl group in the SIOHS triblock copolymer

[a]All nanocomposites have 5 wt% organoclay

d-spacing of ISB/Cloisite 30B® nanocomposite is virtually the same as that of Cloisite 30B®. Again, this experimental observation can be explained by the expectation that the surfactant MT2EtOH residing at the surface of Cloisite 30B® and ISB triblock copolymers are not compatible.

However, in Fig. 15 we observe quite different and very interesting XRD patterns in some of the ISBOH/Cloisite 30B® nanocomposites. Specifically, we cannot discern any intensity peaks in the XRD patterns for the (ISBOH-16)/Cloisite 30B® and (ISBOH-24)/Cloisite 30B® nanocomposites, while a very weak intensity peak in the XRD patterns for the (ISBOH-39)/Cloisite 30B® nanocomposite is discernible giving rise to a d-spacing of approximately 2.0 nm for the Cloisite 30B® in the nanocomposite. The very broad, indistinguishable intensity peak from
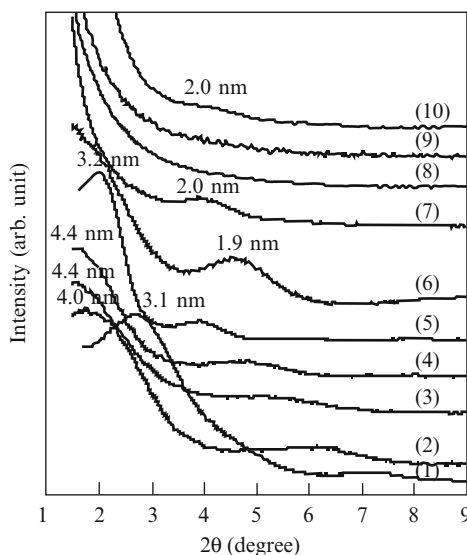
Fig. 15 XRD patterns for (1) Cloisite 15A®, (2) ISB/Cloisite 15A® nanocomposite, (3) (ISBOH-16)/Cloisite 15A® nanocomposite, (4) (ISBOH-24)/Cloisite 15A® nanocomposite, (5) (ISBOH-39)/Cloisite 15A® nanocomposite, (6) Cloisite 30B®, (7) ISB/Cloisite 30B® nanocomposite, (8) (ISBOH-16)/Cloisite 30B® nanocomposite, (9) (ISBOH-24)/Cloisite 30B® nanocomposite, and (10) (ISBOH-39)/Cloisite 30B® nanocomposite. (Reprinted from Choi et al. [5]. Copyright 2004, with permission from the American Chemical Society)

the XRD patterns for both (ISBOH-16)/Cloisite 30B® and (ISBOH-24)/Cloisite 30B® nanocomposites suggests that the Cloisite 30B® aggregates might have been very well dispersed in ISBOH-16 and ISBOH-24. Note that (ISBOH-39)/Cloisite 30B® nanocomposite has ISBOH-39 with 39 mol% hydroxyl groups, (ISBOH-16)/Cloisite 30B® nanocomposite has ISBOH-16 with 16 mol% hydroxyl groups, and (ISBOH-24)/Cloisite 30B® nanocomposite has ISBOH-24 with 24 mol% hydroxyl groups.

Figure 16 gives TEM images of (ISBOH-24)/Cloisite 15A®, (ISBOH-24)/Cloisite 30B®, and (ISBOH-39)/Cloisite 30B® nanocomposites, showing that Cloisite 30B® aggregates have a very high degree of dispersion in ISBOH-24, but a very low degree of dispersion in ISBOH-39, and Cloisite 15A® aggregates also have a very low degree of dispersion in ISBOH-24. The observations made from the TEM images given in Fig. 16 are consistent with those made from the XRD patterns given in Fig. 15.

Figure 17 gives in situ FTIR spectra for ISBOH-16, ISBOH-24, and ISBOH-39 over a wide range of temperatures. In Fig. 17a we observe that the absorption band at 3,330 cm^{-1} for ISBOH-16 persists up to 50°C and then begins to shift to a higher wave number as the temperature is increased further. Thus it can be concluded that the hydroxyl groups within ISBOH-16 molecules form hydrogen bonds, which disappear at temperatures higher than approximately 50°C. It is well documented
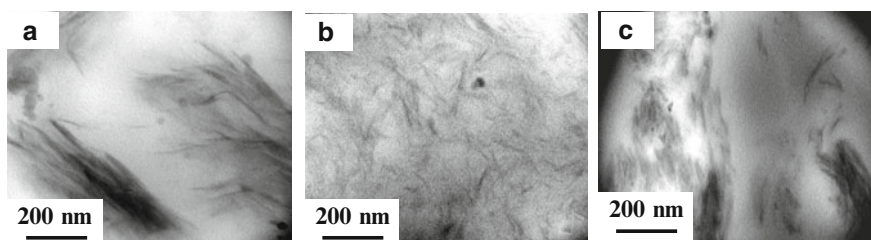
Fig. 16 TEM images of (**a**) (ISBOH-24)/Cloisite 15A® nanocomposite, (**b**) (ISBOH-24)/Cloisite 30B® nanocomposite, and (**c**) (ISBOH-39)/Cloisite 30B® nanocomposite, in which the *dark areas* represent the clay and the *gray/white areas* represent the polymer matrix. (Reprinted from Choi et al. [5]. Copyright 2004, with permission from the American Chemical Society)
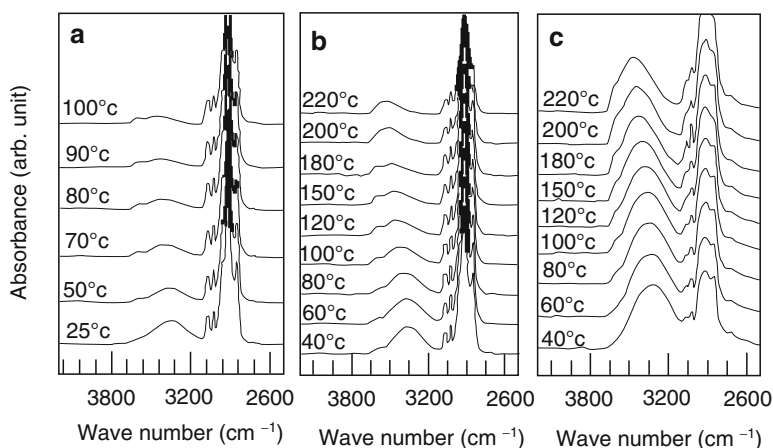
Fig. 17 In situ FTIR spectra at various temperatures for triblock copolymers: (**a**) ISBOH-16, (**b**) ISBOH-24, and (**c**) ISBOH-39. (Reprinted from Choi et al. [5]. Copyright 2004, with permission from the American Chemical Society)

in the literature [37] that the strength of hydrogen bonds decreases with increasing temperature. In the in situ FTIR spectra for ISBOH-24 given in Fig. 17b we observe that the absorption band at approximately $3,330 \, cm^{-1}$ persists up to 100°C, which is very close to the T_{ODT} of ISBOH-24 [5]. Note that the area under the absorption band at $3,330 \, cm^{-1}$ in Fig. 17b for ISBOH-24 is much larger than that in Fig. 17a for ISBOH-16. This observation is reasonable, because the number of hydroxyl groups in ISBOH-24 is greater than that in ISBOH-16. It can then be concluded that a sufficiently high degree of hydroxylation in ISBOH-24 has induced, via hydrogen bonding, order-disorder transition (ODT) from a homogeneous triblock copolymer ISB. This conclusion is consistent with that made in a previous study of Lee and Han [34] in which ODT was induced by hydroxylation of a homogeneous SI diblock copolymer yielding microphase-separated SIOH diblock copolymer. In the in situ FTIR spectra for ISBOH-39 given in Fig. 17c we observe that the absorption band at $3,330 \, cm^{-1}$ persists up to approximately 120°C, and then begins to shift to a

Fig. 18 In situ FTIR spectra at various temperatures for (**a**) (ISBOH-24)/Cloisite 30B® nanocomposite and (**b**) (ISBOH-24)/Cloisite 15A® nanocomposite. (Reprinted from Choi et al. [5]. Copyright 2004, with permission from the American Chemical Society)
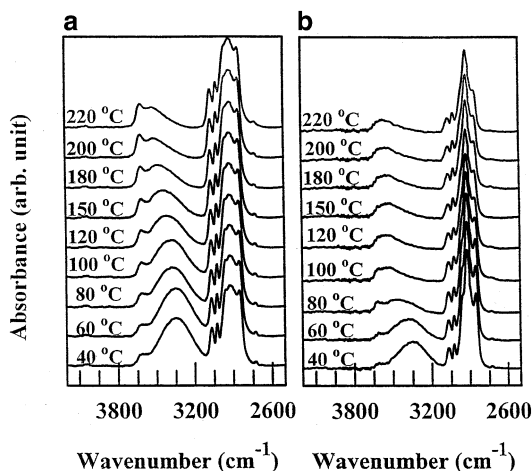
slightly higher wave number at a temperature somewhere between 120 and 150 °C. Note in Fig. 17c that the area under the absorption band at $3,330 \, cm^{-1}$ for ISBOH-39 is very large, as compared to the area under the absorption band at $3,330 \, cm^{-1}$ for ISBOH-24 (see Fig. 17b). Again, this observation is due to the much higher level of hydroxyl groups present in ISBOH-39 than in ISBOH-24. What is noteworthy in the FTIR spectra for ISBOH-39, displayed in Fig. 17c, is that the very large area of absorption band in the vicinity of $3,330 \, cm^{-1}$ persists even at 220 °C.

Figure 18 gives in situ FTIR spectra at various temperatures for (a) (ISBOH-24)/ Cloisite 30B® nanocomposite and (b) (ISBOH-24)/Cloisite 15A® nanocomposite. Comparison of Fig. 18a with Fig. 17b reveals that the area under the absorption band at $3,330 \, cm^{-1}$ is larger in the (ISBOH-24)/Cloisite 30B® nanocomposite than in neat ISBOH-24 at temperatures ranging from 60 to 150 °C. The much larger area under the absorption band at $3,330 \, cm^{-1}$ signifies the presence of the hydrogen bonds between the hydroxyl group in the surfactant MT2EtOH residing at the surface of Cloisite 30B® and the hydroxyl group in ISBOH-24. That is, attractive interactions exist between Cloisite 30B® and ISBOH-24 in the (ISBOH-24)/Cloisite 30B® nanocomposite. The in situ FTIR spectra presented above are qualitative in nature and they are intended to identify the origin of the dispersion characteristics. According to Choi et al. [5], quantitative analysis (e.g., the determination of the percentage of hydrogen bonding sites on the Cloisite 30B® surface) of the in situ FTIR spectra by deconvoluting the overlapping peaks in the FTIR spectra shown in Fig. 18 was found to be extremely difficult, because the amount of the hydroxyl groups associated with the organoclay Cloisite 30B® in the nanocomposite was so small (estimated to be less than 0.2%). In Fig. 18b we observe no evidence of the presence of hydrogen bonds between the surfactant 2M2HT residing at the surface of Cloisite 15A® and the hydroxyl group in ISBOH-24. This observation is not surprising, because the surfactant 2M2HT residing at the surface of Cloisite 15A® has no polar group that can have attractive interactions with the hydroxyl groups in ISBOH-24. Under such circumstances, one cannot expect a high degree

of dispersion of Cloisite 15A® aggregates in ISBOH-24. This indeed turns out to be the case as we have already observed from the TEM image given in Fig. 16. Comparison of Fig. 18a and Fig. 18b reveals a very large difference in FTIR spectra between the (ISBOH-24)/Cloisite 30B® and (ISBOH-24)/Cloisite 15A® nanocomposites. Such a large difference in FTIR spectra between the two nanocomposites explains why the (ISBOH-24)/Cloisite 30B® nanocomposite has good dispersion of Cloisite 30B® aggregates in ISBOH-24, while the (ISBOH-24)/Cloisite 15A® nanocomposite has poor dispersion of Cloisite 15A® aggregates in the same polymer matrix ISBOH-24 (see Fig. 16).

Figure 19 gives XRD patterns for Cloisite 15A® and its nanocomposites with SIS and SIOHS triblock copolymers having two different degrees of hydroxylation (16 and 32 mol%) and Cloisite 30B® and its nanocomposites with SIS and SIOHS triblock copolymers with two different degrees of hydroxylation (16 and 32 mol%). The following observations in Fig. 19 are worth highlighting. Note that the d-spacing (3.1 nm) of Cloisite 15A® is larger than the d-spacing (1.9 nm) of Cloisite 30B®. The d-spacing of Cloisite 15A® is increased from 3.1 to 4.0 nm in the SIS/Cloisite 15A® and SIOHS/Cloisite 15A® nanocomposites regardless of the difference in chemical structure of the block copolymers (SIS vs SIOHS triblock copolymers), and also regardless of the difference in the degree of hydroxylation (16 vs 32 mol%) in SIOHS triblock copolymer. It does not seem that a slight increase (0.9 nm) in the d-spacing of Cloisite 15A® after it was mixed with the SIS or SIOHS triblock copolymers is significant, suggesting that Cloisite 15A® has very

Fig. 19 XRD patterns for (1) Cloisite 15A®, (2) SIS/Cloisite 15A® nanocomposite, (3) (SIOHS-16)/Cloisite 15A® nanocomposite, (4) (SIOHS-32)/Cloisite 15A® nanocomposite, (5) Cloisite 30B®, (6) SIS/Cloisite 30B® nanocomposite, (7) (SIOHS-16)/Cloisite 30B® nanocomposite, and (8) (SIOHS-32)/Cloisite 30B® nanocomposite. (Reprinted from Choi et al. [5]. Copyright 2004, with permission from the American Chemical Society)
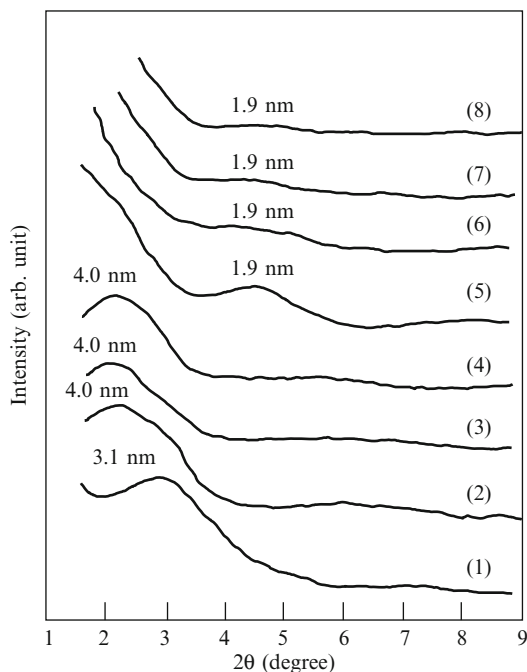
weak attractive interactions with the SIS and SIOHS triblock copolymers. Note further that the d-spacing of Cloisite 30B® remains the same before and after it was mixed with SIS or SIOHS triblock copolymers, suggesting that Cloisite 30B® also has little or very weak attractive interactions with the SIS and SIOHS triblock copolymers. The very small difference in the d-spacing between Cloisite 15A® and the SIS/Cloisite 15A®, (SIOHS-16)/Cloisite 15A®, or (SIOHS-32)/Cloisite 15A® nanocomposites, observed in Fig. 19, can be understood from the point of view that there would be little or no attractive interactions (compatibility) between the surfactant 2M2HT residing at the surface of Cloisite 15A® and the matrix of SIS or SIOHS triblock copolymers. Likewise, we can understand the reason why no difference in d-spacing between Cloisite 30B® and the SIS/Cloisite 30B® nanocomposite is observed in Fig. 19, because there is little or no compatibility between the surfactant MT2EtOH residing at the surface of Cloisite 30B® and SIS triblock copolymer. However, it seems somewhat strange (or it is unexpected at first glance) to learn from Fig. 19 that we observe no difference in d-spacing between Cloisite 30B® and the (SIOHS-16)/Cloisite 30B® or (SIOHS-32)/Cloisite 30B® nanocomposites, although the hydroxyl groups in the surfactant MT2EtOH residing at the surface of Cloisite 30B® and the hydroxyl groups in the SIOHS triblock copolymer could potentially have attractive interactions via hydrogen bonding which, however, apparently did not take place.

Figure 20 gives TEM images for (SIOHS-16)/Cloisite 15A® and (SIOHS-16)/Cloisite 30B® nanocomposites, in which we observe a low degree of dispersion of both Cloisite 15A® and Cloisite 30B® in the respective nanocomposites. This observation is consistent with that made above from the XRD patterns given in Fig. 19. In other words, in the absence of attractive interactions between the organoclay (Cloisite 30B® or Cloisite 30B®) and polymer matrix (SIS or SIOHS triblock copolymers) good dispersion of organoclay aggregates will not occur.
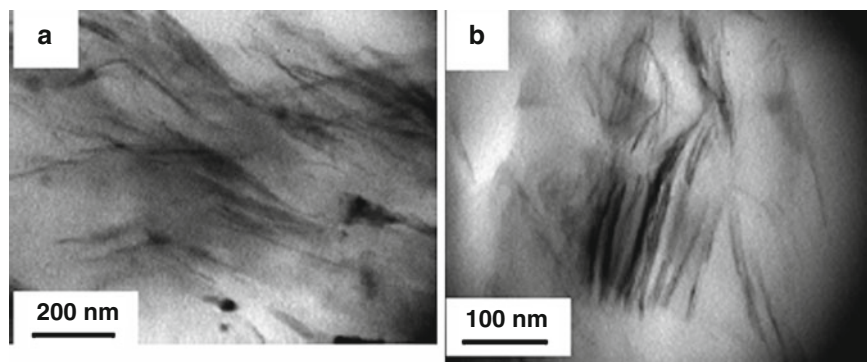
Fig. 20 TEM images of (**a**) (SIOHS-16)/Cloisite 15A® nanocomposite and (**b**) (SIOHS-16)/Cloisite 30B® nanocomposite, in which the *dark areas* represent the clay and the *gray/white areas* represent the polymer matrix. (Reprinted from Choi et al. [5]. Copyright 2004, with permission from the American Chemical Society)
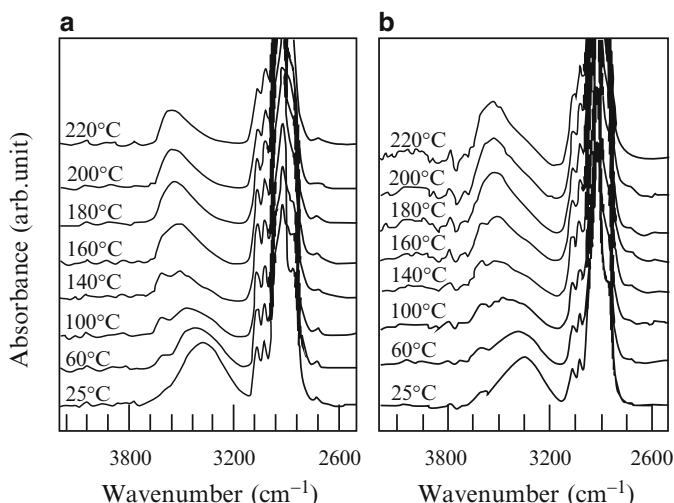
Fig. 21 In situ FTIR spectra at various temperatures for (**a**) SIOHS-16 and (**b**) (SIOHS-16)/ Cloisite 30B® nanocomposite. (Reprinted from Choi et al. [5]. Copyright 2004, with permission from the American Chemical Society)

Figure 21 compares the in situ FTIR spectra of neat triblock copolymer SIOHS-16 with the FTIR spectra of the (SIOHS-16)/Cloisite 30B® nanocomposite at temperatures ranging from 25 to 220 °C. Note that in FTIR spectroscopy the hydrogen-bonded and free hydroxyl groups appear at 3,330 and 3,630 cm^{-1}, respectively [37]. In Fig. 21 we observe a remarkable similarity in FTIR spectra between the neat block copolymer SIOHS-16 and (SIOHS-16)/Cloisite 30B® nanocomposite over the entire range of temperatures tested. Namely, the absorption band at 3,330 cm^{-1} persists up to approximately 60 °C and then begins to shift to a higher wave number at a temperature starting at approximately 100 °C. This observation suggests that the hydrogen bonds that existed within the SIOHS-16 molecules disappeared as the temperature was increased above 60 °C and that few, if any, hydrogen bonds existed between the hydroxyl groups in the surfactant MT2EtOH residing at the surface of Cloisite 30B® and the hydroxyl group in the midblock of SIOHS-16. This might have been due to less mobility of the hydroxyl groups in the midblock position of SIOHS-16 resulting in fewer and/or weaker hydrogen bonds between the hydroxyl groups in the surfactant MT2EtOH residing at the surface of Cloisite 30B® and the hydroxyl group in the midblock of SIOHS-16. This finding explains why the presence of a functional group(s) in the midblock of a triblock copolymer is *not* effective at all in dispersing the aggregates of organoclay, in contrast to the situation where a functional group(s) present at the endblock of a triblock copolymer (e.g., ISBOH) is very effective in dispersing the aggregates of organoclay (compare Fig. 20b with Fig. 16b).

Several other studies have been reported on the preparation, via mixing, of organoclay nanocomposites based on various block copolymers including SI diblock copolymers [45–48], SIS triblock copolymer [49], polystyrene-*block-*

polybutadiene (SB diblock) copolymer [50], polystyrene-*block*-polybutadiene-*block*-polystyrene (SBS triblock) copolymer [51], polystyrene-*block*-poly(ethylene-*co*-1-butene) (SEB diblock) copolymer [51, 52], and polystyrene-*block*-poly(ethylene-*co*-1-butene)-*block*-polystyrene (SEBS triblock) copolymer [51–53]. All of these studies reported only intercalation of the aggregates of the organoclays employed. On the basis of the results presented above (Figs. 12–21), we can explain why the organoclay nanocomposites reported in these studies had only intercalation, in that none of the block copolymers employed had functional groups that could possibly have had attractive interactions with the surfactants residing at the surface of the organoclays employed.

There are only a small number of studies [5–7, 54, 55] that reported on exfoliated nanocomposites which were prepared by mixing an organoclay and a block copolymer. Besides the nanocomposites based on functional block copolymers summarized above [5, 6], which had exfoliation due to the presence of hydrogen bonding, other types of specific interactions can also lead to the successful preparation, via mixing, of exfoliated organoclay nanocomposites based on block copolymers. Below, I will summarize such studies, which have reported on the successful preparation, via ionic interactions [55] and ion–dipole interactions [7], of exfoliated nanocomposites based on block copolymers. There are a few studies [56, 57], which reported on the preparation of exfoliated nanocomposites based on block copolymers using in situ polymerization in the presence of initiator-anchored MMT. As stated in Introduction, in this chapter I will not discuss the preparation of organoclay nanocomposites using in situ polymerization.

3.5 Nanocomposites Based on Functional Thermotropic Liquid-Crystalline Polymer

Thermotropic liquid-crystalline polymer (TLCP) is a class of polymers of industrial importance although only a few TLCPs have been commercialized. In general, like many thermoplastic polymers, commercial TLCPs do not have functionality and thus it is highly unlikely that exfoliation of organoclay nanocomposites would be realized, unless the TLCP has functional group(s) that would have attractive interactions with a surfactant residing at the surface of an organoclay. Huang and Han [58, 59] successfully prepared exfoliated organoclay nanocomposites based on main-chain TLCPs having a pendent pyridyl group or side-chain azopyridine with pyridyl group. Below, I will summarize their findings.

Huang and Han [58] synthesized a main-chain TLCP with a pendent pyridyl group having the chemical structure (referred to as PyHQ12), which has 12 methylene units as flexible spacer. The details of the synthesis of PyHQ12 can be found from the original paper. According to them, PyHQ12 has a glass transition temperature (T_g) of 96 °C, a clearing temperature ($T_{c\ell}$)
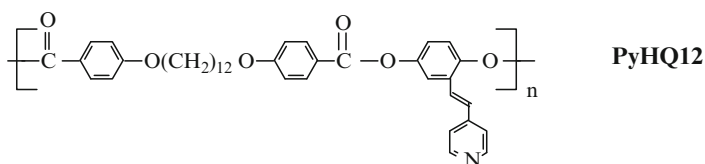
PyHQ12

of 162 °C during heating, and has Schlieren texture, as evidenced by polarizing optical microscopy (POM), which undergoes a nematic–to–isotropic (N–I) transition at temperatures between 96 and 162°C. Using PyHQ12 they prepared, via solution blending in pyridine, organoclay nanocomposites with Cloisite 30B® and Cloisite 20A®, respectively, at 5 wt% loading. For comparison, they also prepared nanocomposites based on a main-chain TCLP, PSHQ12 having no functional group, with the chemical structure
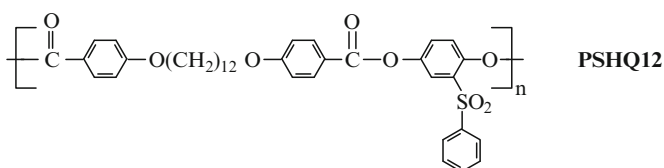
PSHQ12

Figure 22 gives XRD patterns for Cloisite 20A®, Cloisite 30B®, and organoclay nanocomposites based on PyHQ12 or PSHQ12. Note in Fig. 22 that Cloisite 30B® has a gallery distance (d-spacing) of 1.9 nm, while Cloisite 20A® has a d-spacing of 3.1 nm. The following observations in Fig. 22 are worth noting. (1) PyHQ12/Cloisite 20A® nanocomposite has a d-spacing of 3.4 nm, an increase of 0.3 nm (9.7% increase) over the d-spacing of Cloisite 20A®, suggesting that the PyHQ12
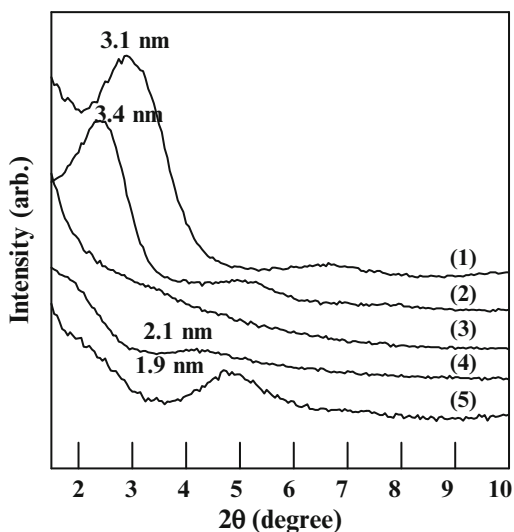
Fig. 22 XRD patterns for (1) Cloisite 20A®, (2) PyHQ12/Cloisite 20A® nanocomposite, (3) PyHQ12/Cloisite 30B® nanocomposite, (4) PSHQ12/Cloisite 30B® nanocomposite, and (5) Cloisite 30B®. (Reprinted from Huang and Han [58]. Copyright 2006, with permission from the American Chemical Society)

might have intercalated the Cloisite 20A® aggregates. (2) PyHQ12/Cloisite 30B® nanocomposite shows featureless XRD patterns. We hasten to point out that the disappearance of an XRD peak does not necessarily signify that the organoclay aggregates are highly dispersed. (3) PSHQ12/Cloisite 30B® nanocomposite has a d-spacing of 2.1 nm, an increase of 0.2 nm (10.5% increase) over the d-spacing of Cloisite 30B®, suggesting that the PSHQ12 might have intercalated the Cloisite 30B® aggregates. It is very clear from the above observations that PyHQ12/Cloisite 30B® nanocomposite has XRD patterns, which are distinctly different from the XRD patterns of the two other organoclay nanocomposites, the origin of which will be elaborated on below.

Figure 23 gives TEM images of (a) PyHQ12/Cloisite 30B® nanocomposite, (b) PyHQ12/Cloisite 20A® nanocomposite, and (c) PSHQ12/Cloisite 30B® nanocomposite, in which the dark areas represent the organoclay and the gray/bright areas represent the polymer matrix. It is clearly seen in Fig. 23 that PyHQ12/Cloisite 30B® nanocomposite has a very high degree of dispersion of Cloisite 30B® aggregates in the matrix PyHQ12, whereas PyHQ12/Cloisite 20A® and PSHQ12/Cloisite 30B® nanocomposites have poorly dispersed, large aggregates of organoclay. The XRD patterns (see Fig. 22) and the TEM images (see Fig. 23) provide consistent assessment of the state of dispersion of the functional and non-functional TLCPs nanocomposites reported by Huang and Han [58].

Figure 24 gives FTIR spectra for (a) PyHQ12, (b) PyHQ12/Cloisite 20A® nanocomposite, and (c) PSHQ12/Cloisite 30B® nanocomposite at room temperature, showing slight evidence (spectrum b) of attractive interactions between PyHQ12 and Cloisite 20A®, and no evidence (spectrum c) of attractive interactions between PSHQ12 and Cloisite 30B®. This observation is not surprising, because organoclay Cloisite 20A® does not have functional groups that can have attractive interactions with the pendent pyridyl group in PyHQ12, and PSHQ12 does not have functionality that can have attractive interactions with the hydroxyl group in the surfactant MT2EtOH residing at the surface of organoclay Cloisite 30B®, although the hydroxyl group in MT2EtOH may have attractive interactions with the carbonyl group in PSHQ12, which might have contributed
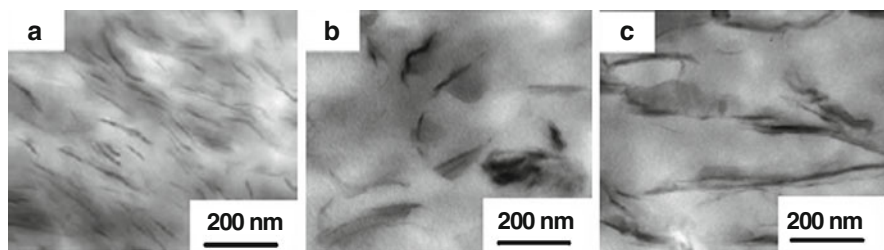
Fig. 23 TEM images of (**a**) PyHQ12/Cloisite 30B® nanocomposite, (**b**) PyHQ12/Cloisite 20A® nanocomposite, and (**c**) PSHQ12/Cloisite 30B® nanocomposite, in which the *dark areas* represent the clay and the *gray/white areas* represent the polymer matrix. (Reprinted from Huang and Han [58]. Copyright 2006, with permission from the American Chemical Society)

Fig. 24 FTIR spectra for
(**a**) PyHQ12,
(**b**) PyHQ12/Cloisite 20A®
nanocomposite,
(**c**) PSHQ12/Cloisite 30B®
nanocomposite, and in situ
FTIR spectra for
PyHQ12/Cloisite 30B®
nanocomposite at various
temperatures (°C): (1) 25, (2)
100, (3) 120, (4) 140, (5) 160,
and (6) 180. (Reprinted from
Huang and Han [58].
Copyright 2006, with
permission from the
American Chemical Society)
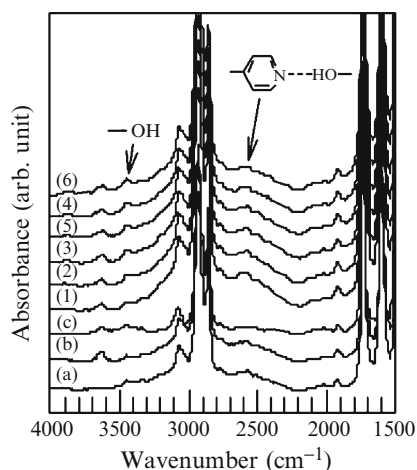
to a slight increase in d-spacing of Cloisite 30B® in the PSHQ12/Cloisite 30B® nanocomposite (Fig. 22). Also given in Fig. 24, for comparison, are in situ FTIR spectra for the PyHQ12/Cloisite 30B® nanocomposite at various temperatures ranging from 25 to 180 °C. Note in Fig. 24 that the size of the absorption peak at a wavenumber of $2{,}570\,\text{cm}^{-1}$ for the PyHQ12/Cloisite 30B® nanocomposite is larger than that for PyHQ12 although it tends to decrease, while the size of the absorption peak at a wavenumber of $3{,}460\,\text{cm}^{-1}$ for the hydroxyl group tends to increase, as the temperature is increased to 180 °C. What is interesting in the FTIR spectra for the PyHQ12/Cloisite 30B® nanocomposite displayed in Fig. 24 is that the rather strong absorption peak at a wavenumber of $2{,}570\,\text{cm}^{-1}$ persists even at a temperature as high as 180 °C. Thus, it can be concluded that attractive interactions exist (i.e., hydrogen bonds are formed) between the pendent pyridyl group in PyHQ12 and the hydroxyl group in the surfactant MT2EtOH residing at the surface of organoclay Cloisite 30B®, which contributed to the very high degree of dispersion of Cloisite 30B® aggregates in the matrix PyHQ12 (see the TEM image given in Fig. 23a). We hasten to point out that we cannot rule out the possibility of ionic interactions between the pendent pyridyl groups in PyHQ12 and N^+ ion in the surfactant 2M2HT residing at the surface of Cloisite 20A®, which could have contributed to the slight increase in d-spacing of the PyHQ12/Cloisite 20A® nanocomposite (see Fig. 22).

Figure 25 gives POM images of (a) PyHQ12, (b) PyHQ12/Cloisite 30B® nanocomposite, (c) PyHQ12/Cloisite 20A® nanocomposite, (d) PSHQ12, and (e) PSHQ12/Cloisite 30B® nanocomposite. Note that a considerable degree of liquid crystallinity in PyHQ12 is lost in the PyHQ12/Cloisite 30B® nanocomposite (compare Fig. 25b with Fig. 25a), which is attributable to the formation of hydrogen bonds between the pendent pyridyl group in PyHQ12 and the hydroxyl group in the surfactant MT2EtOH residing at the surface of Cloisite 30B®. On the other hand, the liquid crystallinity in PyHQ12 is little changed in the PyHQ12/Cloisite 20A® nanocomposite (compare Fig. 25c with Fig. 25a), and also the liquid crystallinity in
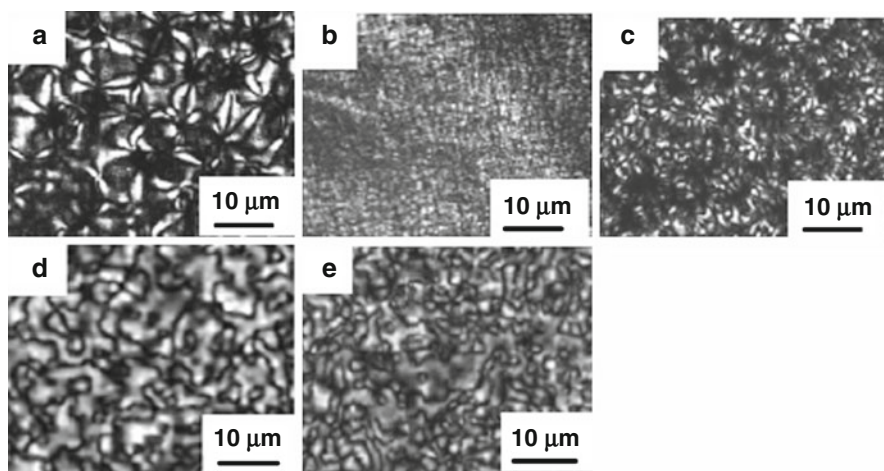
Fig. 25 POM images of (**a**) PyHQ12, (**b**) PyHQ12/Cloisite 30B® nanocomposite, (**c**) PyHQ12/Cloisite 20A® nanocomposite, (**d**) PSHQ12, and (**e**) PSHQ12/Cloisite 30B® nanocomposite at 140°C. (Reprinted from Huang and Han [58]. Copyright 2006, with permission from the American Chemical Society)

PSHQ12 is little changed in the PSHQ12/Cloisite 30B® nanocomposite (compare Fig. 25e with Fig. 25d).

The above observations support the conclusions drawn above from XRD diffraction patterns (see Fig. 22) and TEM images (see Fig. 23) that attractive interactions existed between the pendent pyridyl group in PyHQ12 and the hydroxyl group in the surfactant MT2EtOH residing at the surface of organoclay Cloisite 30B®, while little attractive interaction existed between PyHQ12 and Cloisite 20A® in the PyHQ12/Cloisite 20A® nanocomposite, and between PSHQ12 and Cloisite 30B® in the PSHQ12/Cloisite 30B® nanocomposite.

Figure 26 gives a schematic describing the state of dispersion of Cloisite 30B® aggregates in the PyHQ12/Cloisite 30B® nanocomposite, where the dark sticks represent Cloisite 30B® platelets, the thin cylinders (which denote mesogens) plus waved lines (which denote flexible spacers) represent the segmented PyHQ12 chains, and the short dashed lines represent hydrogen bonds between the pendent pyridyl group in PyHQ12 and the hydroxyl groups in the surfactant MT2EtOH residing at the surface of Cloisite 30B®. Referring to Fig. 26, the formation of hydrogen bonds between the pendent pyridyl group in PyHQ12 and the hydroxyl groups in the surfactant MT2EtOH might have restricted the mobility of PyHQ12 chains in the nanocomposite. As a result, the orientation of PyHQ12 chains in PyHQ12/Cloisite 30B® nanocomposite is severely restricted and thus the formation of a nematic mesophase having long-range order of PyHQ12 would have become very difficult. Consequently, the domain size of PyHQ12 mesophase in PyHQ12/Cloisite 30B® nanocomposite might have become very small, as shown in the POM image given in Fig. 25b.
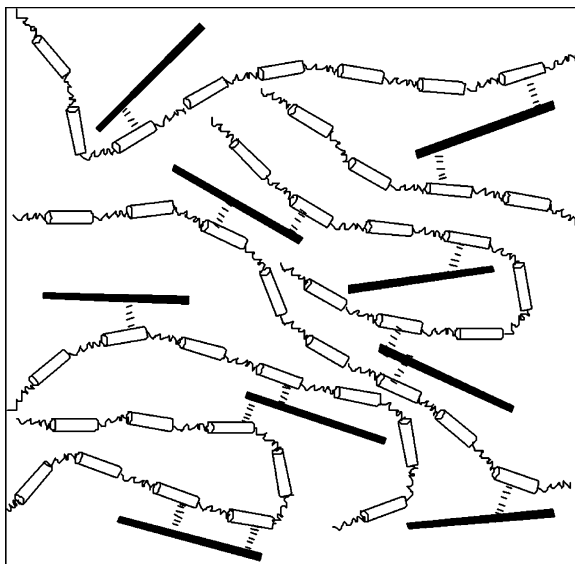
Fig. 26 Schematic describing the distributions of PyHQ12 chains and organoclay Cloisite 30B®️ in the highly dispersed PyHQ12/Cloisite 30B®️ nanocomposite, where the *dark sticks* represent Cloisite 30B®️ platelets, the *thin cylinders* (which denote mesogens) plus *waved lines* (which denote flexible spacers) represent PyHQ12 chains, and the *short dashed lines* represent hydrogen bonds between the pendent pyridyl group in PyHQ12 and the hydroxyl groups in the surfactant MT2EtOH residing at the surface of Cloisite 30B®️. (Reprinted from Huang and Han [58]. Copyright 2006, with permission from the American Chemical Society)

On the other hand, the nematic mesophase of PSHQ12 in the PSHQ12/Cloisite 30B®️ nanocomposite is virtually identical, except for the size, to that of neat PSHQ12 (compare Fig. 25e with Fig. 25d). This observation is not surprising, because little or no attractive interactions exist between PSHQ12 and Cloisite 30B®️ in the nanocomposite (see FTIR spectrum (c) in Fig. 24). Note that in the presence of Cloisite 20A®️, the nematic mesophase of PyHQ12 in the PyHQ12/Cloisite 20A®️ nanocomposite (Fig. 25c) has been modified only slightly when compared to the nematic mesophase of neat PyHQ12 (Fig. 25a). This observation is attributable to very weak interactions between the pendent pyridyl group in PyHQ12 and the positively charged N^+ ion in the surfactant 2M2HT residing at the surface of organoclay Cloisite 20A®️.

To maintain the liquid crystallinity of PyHQ12 in the PyHQ12/Cloisite 30B®️ nanocomposite, Huang and Han [59] synthesized another main-chain TLCP having side-chain azopyridine with flexible spacer (referred to as PABP), which has the chemical structure

$$\left[O(CH_2)_6O-\bigcirc-\bigcirc-O(CH_2)_6O\ \underset{\underset{(CH_2)_5}{|}}{\overset{\overset{O\ \ \ O}{||\ \ \ ||}}{C\ CHC}}\right]_x$$
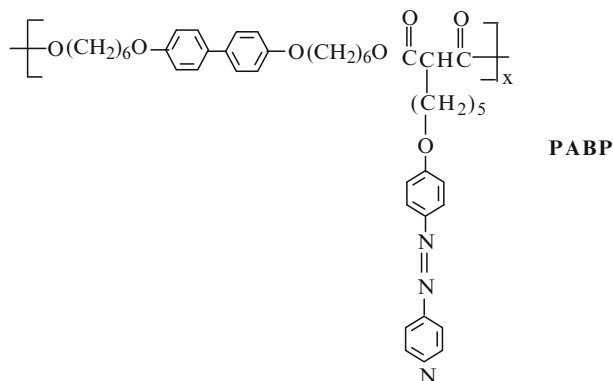
PABP

The details of the synthesis of PyHQ12 can be found in the original paper. According to Huang and Han [59], PABP is a semicrystalline TLCP having a melting temperature (T_m) of 114 °C, and a T_{cl} of 146 °C. They prepared, via solution blending in pyridine, nanocomposites based on PABP, for which MMT, Cloisite 30B®, and Cloisite 20A® were used at a 5 wt% loading, respectively.

Figure 27a gives XRD patterns for (1) Cloisite 30B® having a d-spacing of 1.9 nm, (2) MMT having a gallery distance (d-spacing) of 1.1 nm, and (3) Cloisite 20A® having a d-spacing of 3.1 nm. It is seen that chemical treatment of MMT with a surfactant has increased the gallery distance of the respective organoclays. Figure 27b gives XRD patterns for (1) neat PABP, (2) PABP/MMT nanocomposite, (3) PABP/Cloisite 20A® nanocomposite, and (4) PABP/Cloisite 30B® nanocomposite. Since PABP is a semicrystalline TLCP, the two XRD peaks at 2θ of 3.75° and 7.40° observed in Fig. 27b are attributable to the smectic layered mesophase
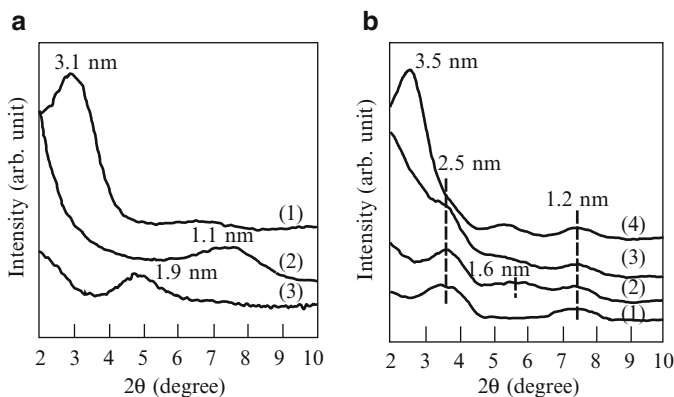
Fig. 27 XRD patterns for (**a**) (1) Cloisite 30B®, (2) MMT, and (3) Cloisite 20A®; (**b**) (1) PABP, (2) PABP/MMT nanocomposite, (3) PABP/Cloisite 20A® nanocomposite, and (4) PABP/Cloisite 30B® nanocomposite. (Reprinted from Huang and Han [59]. Copyright 2006, with permission from Elsevier)

structure of PABP. Note in Fig. 27b that the XRD peak at $2\theta = 7.40°$ appears in all three nanocomposites and the XRD peak at $2\theta = 3.75°$ also appears in the PABP/MMT nanocomposite. This observation suggests that the mesophase structure of PABP in the PABP/MMT nanocomposite might have been little affected although the d-spacing of MMT has increased by 0.5 nm. As the POM images shown below indicate, indeed little change in the mesophase structure of PABP in the PABP/MMT nanocomposite occurred.

However, the XRD peak at $2\theta = 3.75°$ due to the mesophase structure of PABP is not very discernible in Fig. 27b for the PABP/Cloisite 20A$^{®}$ and PABP/Cloisite 30B$^{®}$ nanocomposites. This observation suggests that some type of interaction between the organoclays and PABP might have occurred. Note in Fig. 27b that the d-spacing of Cloisite 20A$^{®}$ in PABP/Cloisite 20A$^{®}$ nanocomposite has increased only slightly from 3.1 nm to 3.5 nm, but interestingly the PABP/Cloisite 30B$^{®}$ nanocomposite shows virtually featureless XRD patterns. This observation suggests the presence of strong attractive interactions between PABP and Cloisite 30B$^{®}$ in the PABP/Cloisite 30B$^{®}$ nanocomposite.

Figure 28 gives TEM images of (a) PABP/MMT nanocomposite, (b) PABP/Cloisite 20A$^{®}$ nanocomposite, and (c) PABP/Cloisite 30B$^{®}$ nanocomposite. In Fig. 28 we observe (1) very poor dispersion of MMT aggregates in PABP/MMT nanocomposite, (2) intercalation, at best, of Cloisite 20A$^{®}$ aggregates in PABP/Cloisite 20A$^{®}$ nanocomposite, and (3) very high degree of dispersion of Cloisite 30B$^{®}$ aggregates in PABP/Cloisite 30B$^{®}$ nanocomposite. These observations are consistent with those made above from the XRD patterns given in Fig. 27b.

Figure 29 gives FTIR spectra for (a) neat PABP at room temperature, (b) PABP/MMT nanocomposite at room temperature, (c) PABP/Cloisite 20A$^{®}$ nanocomposite at room temperature, and (d) in situ FTIR spectra for PABP/Cloisite 30B$^{®}$ nanocomposite at various temperatures ranging from 25 to 160 °C. It can be seen in Fig. 29 that neat PABP has two absorption peaks (spectrum a), a broad peak at a wavenumber of $2,560\,cm^{-1}$ and another at a wavenumber of $1,890\,cm^{-1}$. These two absorption peaks indicate the presence of attractive interactions, though very weak, between the pyridyl group in the side-chain azopyridine and hydroxyl groups at the end of the main chain of PABP (see the chemical structure of PABP given
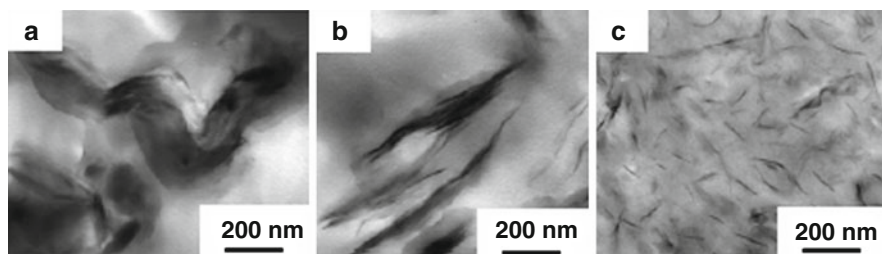
Fig. 28 TEM images of (**a**) PABP/MMT nanocomposite, (**b**) PABP/Cloisite 20A$^{®}$ nanocomposite, and (**c**) PABP/Cloisite 30B$^{®}$ nanocomposite, in which the *dark areas* represent the clay and the *gray/white areas* represent the polymer matrix. (Reprinted from Huang and Han [59]. Copyright 2006, with permission from Elsevier)

Fig. 29 FTIR spectra for (**a**) PABP, (**b**) PABP/MMT nanocomposite, (**c**) PABP/Cloisite 20A® nanocomposite, and in situ FTIR spectra for PABP/Cloisite 30B® nanocomposite at various temperatures (°C): (1) 25, (2) 100, (3) 120, (4) 140, (5) 150, and (6) 160. (Reprinted from Huang and Han [59]. Copyright 2006, with permission from Elsevier)
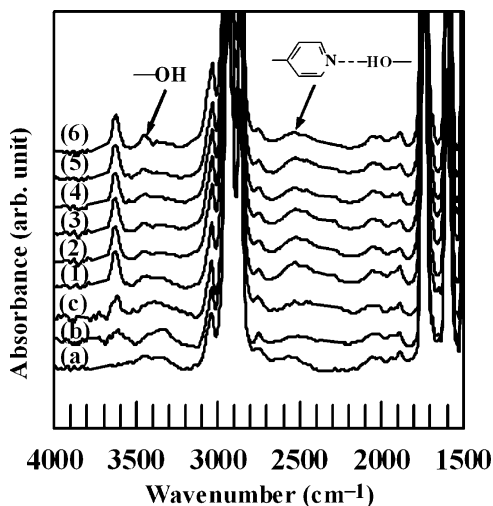
above). According to Huang and Han [59], after polymerization was completed, 50% of the terminal groups in PABP macromolecular chains could be hydroxyl groups. Thus the absorption peak at a wavenumber of $2,560\,cm^{-1}$ is believed to represent hydrogen bonds formed between the terminal hydroxyl groups at the end of the main chain of PABP and the pyridyl group in the side-chain azopyridine (i.e., self-association in PABP), while the absorption peak at a wavenumber of $1,890\,cm^{-1}$ represents Fermi resonance.

Referring to Fig. 29, little evidence can be seen of the presence of hydrogen bonds in the PABP/MMT nanocomposite (spectrum b) and a very weak interaction in PABP/Cloisite 20A® nanocomposite (spectrum c), while the in situ spectra (1–6) for PABP/Cloisite 30B® nanocomposite indicate the presence of strong attractive interactions. Note in Fig. 29 that the size (or area) of the absorption peak at $2,570\,cm^{-1}$ for the PABP/Cloisite 30B® nanocomposite is larger than that for neat PABP although it tends to decrease, while the size of the absorption peak at $3,460\,cm^{-1}$ for the hydroxyl group tends to increase, as the temperature is increased to $160\,°C$. Of particular note in the FTIR spectra for the PABP/Cloisite 30B® nanocomposite displayed in Fig. 29 is that the relatively strong absorption peak at $2,570\,cm^{-1}$ persists even at a temperature as high as $160\,°C$, which is above the clearing temperature of PABP ($146\,°C$). Thus, it can be concluded that attractive interactions exist (i.e., hydrogen bonds are formed) between the pyridyl group in the side-chain azopyridine and the hydroxyl group in the surfactant MT2EtOH residing at the surface of organoclay Cloisite 30B®. It can be concluded further that the presence of hydrogen bonding in the PABP/Cloisite 30B® nanocomposite helped achieve a very high degree of dispersion of Cloisite 30B® aggregates in the PABP matrix (see the TEM image given in Fig. 28c). Earlier, Sato et al. [60] reported on hydrogen bonding between a polymer containing pyridine group and another polymer with

hydroxyl group. The above observations can now explain the reasons for the very poor dispersion of MMT aggregates in PABP/MMT nanocomposite, some intercalation of Cloisite 20A® aggregates in PABP/Cloisite 20A® nanocomposite, and a very high degree of dispersion of Cloisite 30B® aggregates in PABP/Cloisite 30B® nanocomposite (see Fig. 28).

Figure 30 gives POM images of (a) PABP, (b) PABP/MMT nanocomposite, (c) PABP/Cloisite 20A® nanocomposite, and (d) PABP/Cloisite 30B® nanocomposite. Note in Fig. 30 that PABP has a smectic phase, and the mesophase structure of PABP/MMT nanocomposite is virtually identical to that of PABP, while the mesophase structure of PABP in the PABP/Cloisite 20A® and PABP/Cloisite 30B® nanocomposites is only slightly different from that of neat PABP. From the above observation it can be concluded that the presence of organoclay in both PABP/Cloisite 20A® and PABP/Cloisite 30B® nanocomposites has affected little the mesophase structure of PABP in the respective nanocomposites. What is significant here is that a very high degree of dispersion of Cloisite 30B® aggregates has affected little the mesophase structure (liquid crystallinity) of PABP in the PABP/Cloisite 30B® nanocomposite. This was not the case for the PyHQ12/Cloisite 30B® nanocomposite shown in Fig. 25b, in which much of the liquid crystallinity of a segmented main-chain TLCP, PyHQ12, was lost while Cloisite 30B® aggregates were dispersed very well in the matrix of PyHQ12.
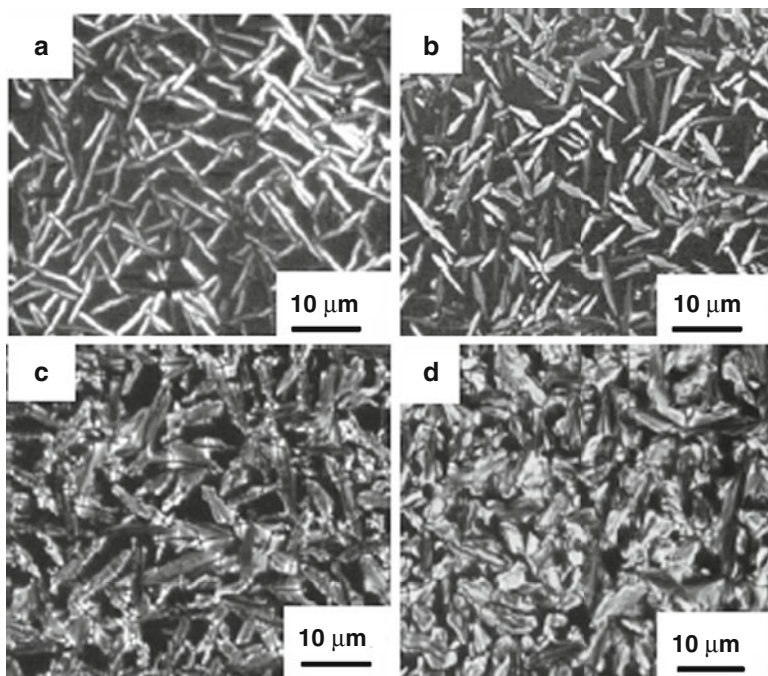
Fig. 30 POM images of (**a**) PABP, (**b**) PABP/MMT nanocomposites, (**c**) PABP/Cloisite 20A® nanocomposites, and (**d**) PABP/Cloisite 30B® nanocomposites. (Reprinted from Huang and Han [59]. Copyright 2006, with permission from Elsevier)
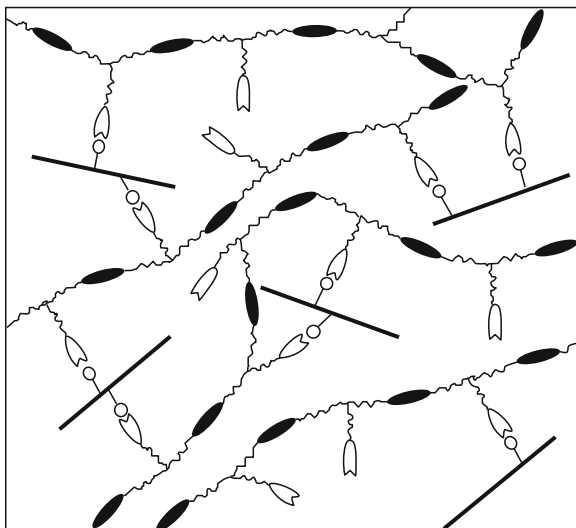
Fig. 31 Schematic describing the distributions of PABP and Cloisite 30B® in the highly dispersed PABP/Cloisite 30B® nanocomposite, where the *dark sticks* represent Cloisite 30B® platelets, the *dark ellipsoids* represent the main-chain mesogens, *waved lines* represent flexible spacers, the *empty notched ellipsoids* represent the azopyridine in the side chain of PABP, and the *empty notched ellipsoids* with "caps" represent hydrogen bonds between the pyridyl group in the side-chain azopyridine of PABP and the hydroxyl groups in the surfactant MT2EtOH residing at the surface of Cloisite 30B®. (Reprinted from Huang and Han [59]. Copyright 2006, with permission from Elsevier)

The origin of the difference between the two situations, PABP/Cloisite 30B® nanocomposite and PyHQ12/Cloisite 30B® nanocomposite, is explained using the schematic given in Fig. 31, in which the dark ellipsoidal areas represent the mesogens of the main chain interconnected by the flexible spacers (shown by thin waved lines), and the dark sticks represent Cloisite 30B® platelets that form hydrogen bonds with the pyridyl group located at the end of the side-chain azopyridyl group. Note in Fig. 31 that the side-chain azopyridyl group is connected to the main chain through five methylene units (shown by thin waved lines), i.e., the pyridyl group in the side-chain azopyridine is sufficiently far from the backbone of the main-chain of PABP. The situation depicted in Fig. 31 is quite different from that depicted in Fig. 26, in which the pendent pyridyl group was connected to the mesogenic main chain (PyHQ12, the chemical structure of which was given above) only through a vinylene unit and thus the hydrogen bonds formed between the pendent pyridyl group and the hydroxyl groups in the surfactant MT2EtOH residing at the surface of Cloisite 30B® might have interfered with the orientation of the mesogenic main chain, consequently disrupting the mesogenic structure of PyHQ12.

A few other research groups [61, 62] reported on the preparation of organoclay nanocomposites based on main-chain TLCP by melt blending. In the preparation of nanocomposites, they employed organoclays very similar to Cloisite 30B® and Cloisite 20A®. They observed large XRD peaks in 2θ scanning, suggestive of poor dispersion (or intercalation at best) of organoclay aggregates. Indeed, an intercalated

structure was observed from TEM [62]. On the basis of the experimental results of Huang and Han [58, 59] summarized above, it is now very clear why the organoclay nanocomposites based on the two TLCPs, prepared by Vaia and Giannelis [61] and Chang et al. [62], had intercalation of the aggregates of organoclays employed; no attractive interaction (no compatibility) existed between the TLCPs and organoclays employed in their studies. The above observation confirms, once again, the necessity of having specific interaction (strong attractive interaction) between a nanoclay and the polymer matrix in order to obtain exfoliated nanocomposites prepared by mixing.

4 Ionic Interactions in Exfoliated Nanocomposites Prepared by Mixing

Here I summarize a recent study of Zha et al. [55] who successfully prepared exfoliated organoclay nanocomposites based on polystyrene (PS) or SI diblock copolymer, each end-functionalized with sodium carboxylate –COONa. In their study, nanocomposites were prepared using 5 wt% Cloisite 30B$^{®}$ or Cloisite 20A$^{®}$. Zha et al. concluded, based on FTIR spectroscopy results, that ionic interactions between the negatively charged –COO$^-$ present at the chain end of a PS-t-COONa or at the chain end of the PI block of an SI-t-COONa (or at the chain end of the PS block of an IS-t-COONa) and the positively charged N$^+$ in the surfactant (MT2EtOH or 2M2HT) residing at the surface of organoclay (Cloisite 30B$^{®}$ or Cloisite 20A$^{®}$) were the driving force to exfoliate the aggregates of the organoclay. Table 6 gives the molecular characteristics of two polystyrenes (PSLMW and PSHMW) and two SI diblock copolymers (SI-1 and SI-2), which were used to prepare end-functionalized PS-t-COONa or SI-t-COONa (or IS-t-COONa), and Table 7 gives a summary of the organoclay nanocomposites prepared in the study of Zha et al. [55].

Table 6 Molecular characteristics of the polystyrenes and SI diblock copolymers synthesized for end-functionalization investigated by Zha et al. [55]

Sample code	M_w[a]	M_w/M_n[a]	w_{PS}[b]
PSLMW	2.7×10^4	1.06	
PSHMW	7.0×10^4	1.03	
SI-1	1.7×10^4	1.09	0.45
SI-2	1.9×10^4	1.07	0.47

[a]Determined from GPC
[b]Weight fraction of polystyrene block determined by ^{1}H NMR spectroscopy

Table 7 Sample codes of the nanocomposite[a] investigated by Zha et al. [55]

Sample code	Functionality
(a) End-functionalized PS/organoclay nanocomposites	
(PSLMW-t-COOH)/Cloisite 20A®	–COOH terminated low molecular weight PS
(PSLMW-t-COOH)/Cloisite 30B®	–COOH terminated low molecular weight PS
(PSLMW-t-COONa)/Cloisite 20A®	–COONa terminated low molecular weight PS
(PSLMW-t-COONa)/Cloisite 30B®	–COONa terminated low molecular weight PS
(PSHMW-t-COOH)/Cloisite 20A®	–COOH terminated high molecular weight PS
(PSHMW-t-COOH)/Cloisite 30B®	–COOH terminated high molecular weight PS
(PSHMW-t-COONa)/Cloisite 20A®	–COONa terminated high molecular weight PS
(PSHMW-t-COONa)/Cloisite 30B®	–COONa terminated high molecular weight PS
(b) End-functionalized SI diblock copolymer/organoclay nanocomposites	
(SI-t-COOH)/Cloisite 20A®	PI block in SI-1 was terminated by –COOH group
(SI-t-COOH)/Cloisite 30B®	PI block in SI-1 was terminated by –COOH group
(SI-t-COONa)/Cloisite 20A®	PI block in SI-1 was terminated by –COONa group
(SI-t-COONa)/Cloisite 30B®	PI block in SI-1 was terminated by –COONa group
(IS-t-COOH)/Cloisite 20A®	PS block in SI-2 was terminated by –COOH group
(IS-t-COOH)/Cloisite 30B®	PS block in SI-2 was terminated by –COOH group
(IS-t-COONa)/Cloisite 20A®	PS block in SI-2 was terminated by –COONa group
(IS-t-COONa)/Cloisite 30B®	PS block in SI-2 was terminated by –COONa group

[a]All nanocomposites have 5 wt% organoclay

4.1 Nanocomposites Based on End-Functionalized Polystyrene

Figure 32 gives XRD patterns of organoclay nanocomposites based on neat PSLMW and PSLMW terminated by –COOH group or –COONa group. The following observations in Fig. 32 are worth noting. The XRD patterns indicate that the d-spacing of PSLMW/Cloisite 30B® nanocomposite is 1.85 nm, which is virtually the same as that of neat Cloisite 30B®, and the d-spacing of PSLMW/Cloisite 20A® nanocomposite is 1.77 nm, which is slightly smaller than that of neat Cloisite 20A® (2.42 nm). This is not surprising, because no attractive interaction can be expected between neat PS and the surfactant residing at the surface of Cloisite 30B® or Cloisite 20A®. In Fig. 32 we still observe a broad XRD reflection peak having the d-spacing of 1.85 nm in both (PSLMW-t-COOH)/Cloisite 30B® and (PSLMW-t-COOH)/Cloisite 20A® nanocomposites, although the peak height of the XRD patterns for the two nanocomposites is much smaller than that for the PSLMW/Cloisite 30B® and PSLMW/Cloisite 20A® nanocomposites. This observation suggests that the –COOH group attached to the chain end of PSLMW might not have sufficiently strong attractive interactions with the surfactant residing at the surface of Cloisite 30B® and Cloisite 20A®, giving rise to a low degree of dispersion of organoclay aggregates in the respective nanocomposites. This can be explained by the following observations. The –COOH group present at the chain end of PSLMW-t-COOH is not expected to have any significant attractive interactions with the surfactant 2M2HT residing at the surface of Cloisite 20A®, while

Fig. 32 XRD patterns for (1)
PSLMW/Cloisite 30B
nanocomposite, (2)
PSLMW/Cloisite 20A®
nanocomposite. (3)
(PSLMW-t-COOH)/Cloisite
30B® nanocomposite, (4)
(PSLMW-t-COOH)/Cloisite
20A® nanocomposite, (5)
(PSLMW-t-COONa)/Cloisite
30B® nanocomposite, and (6)
(PSLMW-t-COONa)/Cloisite
20A® nanocomposite.
(Reprinted from Zha et al.
[55]. Copyright 2005, with
permission from the
American Chemical Society)
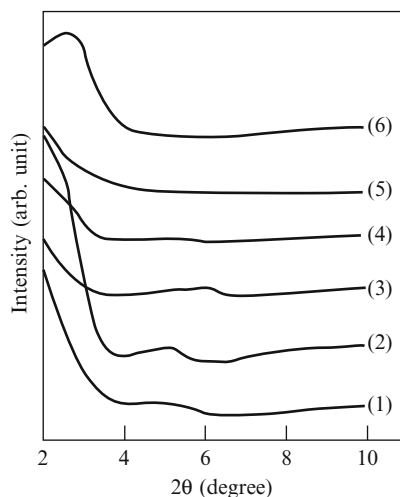
it can potentially form hydrogen bonds with the hydroxyl group in the surfactant MT2EtOH residing at the surface of Cloisite 30B®. However, only one –COOH group at the chain end of PSLMW-t-COOH would not be sufficient to form strong attractive interactions with the hydroxyl groups in the surfactant MT2EtOH residing at the surface of Cloisite 30B. The situation would be quite different if many –COOH groups had been present in the entire PSLMW molecule.

In contrast, in Fig. 32 we observe featureless XRD patterns for both (PSLMW-t-COONa)/Cloisite 20A® and (PSLMW-t-COONa)/Cloisite 30B® nanocomposites. This observation suggests that sufficiently strong attractive interactions might be present between the –COONa group at the chain end of PSLMW and the surfactant (2M2HT or MT2EtOH) residing at the surface of the nanocomposite.

Figure 33 gives TEM images of the nanocomposites based on neat PSLMW and PSLMW terminated by –COOH group or –COONa group. In Fig. 33 we observe that the degree of dispersion of organoclays, Cloisite 30B® and Cloisite 20A®, is rather poor in the matrix of neat PSLMW and PSLMW-t-COOH, while both Cloisite 30B® and Cloisite 20A® are very well dispersed in the matrix of PSLMW-t-COONa. Thus it can be concluded that the TEM images given in Fig. 33 support the observations in the XRD patterns given in Fig. 32.

Figure 34 gives FTIR spectra for (a) PSLMW-t-COONa nanocomposite, (b) Cloisite 30B®, (c) (PSLMW-t-COOH)/Cloisite 30B® nanocomposite, and (d) (PSLMW-t-COONa)/Cloisite 30B® nanocomposite. The following observations in Fig. 34 are worth noting. As expected, no absorption band appears at the wavenumber of $3,620\,cm^{-1}$ for PSLMW-t-COONa. However, two new absorption bands at the wavenumbers, 3,620 and $1,500\,cm^{-1}$, appear in Cloisite 30B®, and in the two nanocomposites. This is attributable to the presence of –OH groups in the surfactant MT2EtOH residing at the surface of Cloisite 30B®. To facilitate our discussion here, an inset is given in Fig. 34 showing the absorption bands at wavenumbers ranging from 1,200 to $1,800\,cm^{-1}$. It is clearly seen from the inset that an additional
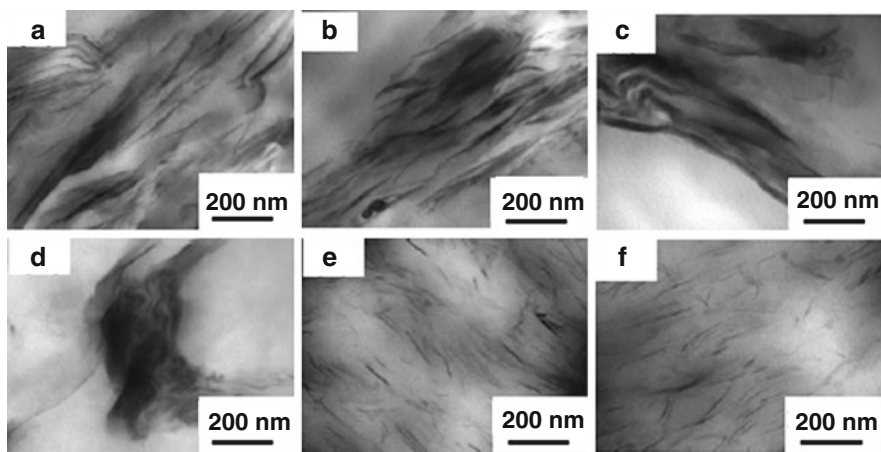
Fig. 33 TEM images of (**a**) PSLMW/Cloisite 30B$^{\circledR}$ nanocomposite, (**b**) PSLMW/Cloisite 20A$^{\circledR}$ nanocomposite, (**c**) (PSLMW-t-COOH)/Cloisite 30B$^{\circledR}$ nanocomposite, (**d**) (PSLMW-t-COOH)/Cloisite 20A$^{\circledR}$ nanocomposite, (**e**) (PSLMW-t-COONa)/Cloisite 30B$^{\circledR}$ nanocomposite, and (**f**) (PSLMW-t-COONa)/Cloisite 20A$^{\circledR}$ nanocomposite, in which the *dark areas* represent organoclay, Cloisite 30B$^{\circledR}$ or Cloisite 20A$^{\circledR}$, and the *gray/white areas* represent the polymer matrix. (Reprinted from Zha et al. [55]. Copyright 2005, with permission from the American Chemical Society)

Fig. 34 FTIR spectra for (**a**) PSLMW-t-COONa, (**b**) Cloisite 30B$^{\circledR}$, (**c**) (PSLMW-t-COOH)/Cloisite 30B$^{\circledR}$ nanocomposite, and (**d**) (PSLMW-t-COONa)/Cloisite 30B$^{\circledR}$ nanocomposite. (Reprinted from Zha et al. [55]. Copyright 2005, with permission from the American Chemical Society)
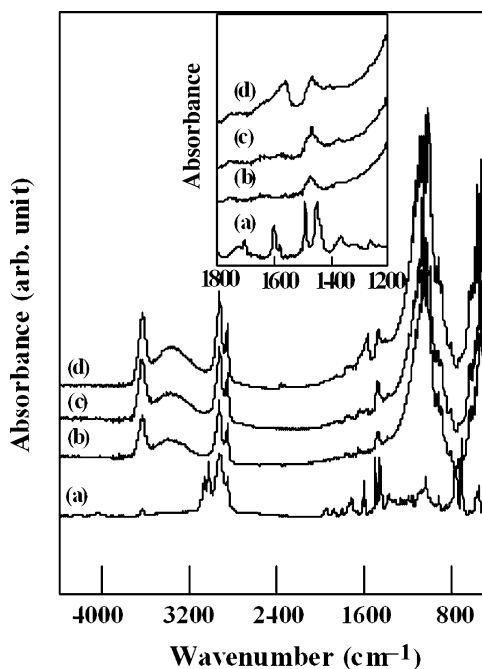
absorption band appears at $1,570\,\mathrm{cm}^{-1}$ for the (PSLMW-t-COONa)/Cloisite 30B[®] nanocomposite; otherwise the absorption bands are identical for both the (PSLMW-t-COONa)/Cloisite 30B[®] and (PSLMW-t-COOH)/Cloisite 30B[®] nanocomposites. Tachino et al. [63] and Kutsumizu et al. [64] conducted infrared spectroscopy studies of the binary blends of sodium and zinc salt ionomers of poly(ethylene-*co*-methacrylate) (PEMA) and observed the appearance of a new asymmetric carboxylate stretching band at $1,569\,\mathrm{cm}^{-1}$, which is very close to the wavelength $1,570\,\mathrm{cm}^{-1}$ observed in Fig. 34. They assigned the appearance of a stretching band at $1,569\,\mathrm{cm}^{-1}$ to carboxylate groups bridging sodium and zinc cations. Thus it can be concluded that the appearance of a new absorption peak at $1,570\,\mathrm{cm}^{-1}$ in Fig. 34 is attributable to the ionic interactions between the negatively charged $-COO^-$ at the chain end of PSLMW-t-COONa and the positively charged cation N^+ in the surfactant (2M2HT or MT2EtOH) residing at the surface of organoclay (Cloisite 20A[®] or Cloisite 30B[®]).

Figure 35 describes (a) XRD patterns and (b) TEM images of organoclay nanocomposites based on an end-functionalized high molecular-weight PSHMW-t-COONa. It can be seen in Fig. 35a that the XRD patterns of both (PSHMW-t-COONa)/Cloisite 30B[®] and (PSHMW-t-COONa)/Cloisite 20A[®] nanocomposites show a very weak and broad peak at 2θ of $4°$ to $6°$. The TEM images given in Fig. 35b for the same nanocomposites based on high molecular-weight PS support the XRD patterns given in Fig. 35a, in that the degree of exfoliation of organoclay aggregates is not so high. It should be remembered that the XRD patterns given in Fig. 32 for the (PSLMW-t-COONa)/Cloisite 30B[®] and (PSLMW-t-COONa)/Cloisite 20A[®] nanocomposites based on low molecular-weight PS are featureless and the TEM images given in Figs. 33e and 33f of the same
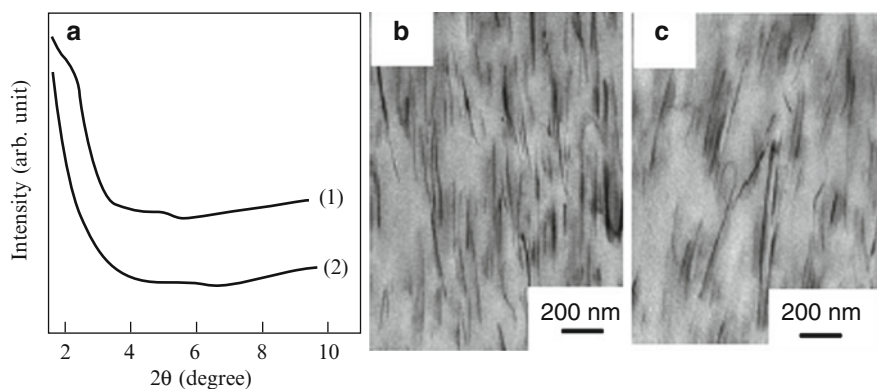
Fig. 35 (**a**) XRD patterns for (1) (PSHMW-t-COONa)/Cloisite 30B[®] nanocomposite and (2) (PSHMW-t-COONa)/Cloisite 20A[®] nanocomposite. (**b**) TEM image of (PSHMW-t-COONa)/Cloisite 30B[®] nanocomposite. (**c**) TEM image of (PSHMW-t-COONa)/Cloisite 20A[®] nanocomposite, in which the *dark areas* represent organoclay, Cloisite 30B[®] or Cloisite 20A[®], and the *gray/white areas* represent the polymer matrix. (Reprinted from Zha et al. [55]. Copyright 2005, with permission from the American Chemical Society)

nanocomposites show a very high degree of exfoliation of organoclay aggregates. The above observation indicates that the molecular weight of the polymer matrix (PSLMW vs PSHMW) has some influence on the dispersion characteristics of organoclay aggregates in nanocomposites. The above experimental observations can be interpreted as follows. The concentration of $-COO^-$ ions at the chain end of PSLMW-t-COONa is higher than that at the chain end of PSHMW-t-COONa. Specifically, for 100 g of nanocomposite containing 5 wt% of organoclay, it is estimated that 4.5 meq cations are present in the (PSLMW-t-COONa)/Cloisite 30B® nanocomposite, and 4.75 meq cations are present in the (PSLMW-t-COONa)/Cloisite 20A® nanocomposite [55]. On the other hand, it is estimated that 3.5 meq $-COO^-$ ions are present in the PSLMW ionomer, while 1.35 meq $-COO^-$ ions are present in the PSHMW ionomer (see Table 6 for the molecular weights of PSLMW and PSHMW). Therefore, the (PSLMW-t-COONa)/Cloisite 30B® nanocomposite is expected to have a higher degree of ionic interactions than the (PSHMW-t-COONa)/Cloisite 30B® nanocomposite, which would lead to an enhanced degree of organoclay dispersion in the (PSLMW-t-COONa)/Cloisite 30B® nanocomposite.

A number of research groups [65–70] reported on the preparation, via melt blending, of organoclay nanocomposites based on unmodified (non-functionalized) PS. The majority of the investigations cited above melt blended chemically modified layered silicates or mica-type layered silicates (e.g., layered silicate modified with alkylammonium, quaternary ammonium end-functionalized PS, or amine-terminated PS) with non-functionalized PS and observed *only* intercalation of the aggregates of organoclay. In their study, Lim and Park [67] melt blended a non-functionalized PS with Cloisite 6A® and observed *only* intercalation of the aggregates of Cloisite 6A®. Note that Cloisite 6A® and Cloisite 20A have the same surfactant, 2M2HT, as mentioned in a previous section, so it is no wonder that PS/Cloisite 6A® nanocomposite had intercalation of the aggregates of Cloisite 6A® (see the TEM image given in Fig. 33b). Further, they also melt blended a PS grafted with maleic anhydride (MA), yielding PS-*g*-MA, with Cloisite 6A® and observed only intercalation of the aggregates of Cloisite 6A®. This can be explained by the fact that Cloisite 6A® does not have any functional group (see Table 2) that can have attractive interaction with the MA grafted onto PS. On the basis of the experimental results presented in Figs. 32–35, it is very clear why the studies cited above reported only intercalated, as best, nanocomposites based on non-functionalized PS.

Nanocomposites based on isotactic polypropylene (i-PP) end-functionalized with an ammonium group, PP-t-NH_3^+ were reported by Wang et al. [71]. Specifically, they used PP-t-NH_3^+ to melt intercalate, under static conditions, both MMT and dioctadecylammonium-modified MMT (2C18-MMT) to yield PP-t-$NH_3^+Cl^-$/Na^+MMT and PP-t-$NH_3^+Cl^-$/2C18-MMT nanocomposites, respectively. Wang et al. observed featureless XRD patterns for both of these nanocomposites, which led them to speculate that exfoliated clay structures had formed, possibly by an ion-exchange mechanism. However, proof of the speculated ion-exchange mechanism was not provided.

4.2 Nanocomposites Based on End-Functionalized Polystyrene-block-Polyisoprene (SI Diblock) Copolymer or Polyisoprene-block-Polystyrene (IS Diblock) Copolymer

Figure 36 gives XRD patterns of organoclay nanocomposites based on an IS diblock copolymer terminated by carboxylic acid (IS-t-COOH) or an IS diblock copolymer terminated by sodium carboxylate (IS-t-COONa) nanocomposites, in which the functional group –COOH or –COONa is attached to the chain end of the PS block of an SI diblock copolymer, SI-2 (see Table 6 for the molecular weight of SI-2). The following observations in Fig. 36 are worth noting. (1) The XRD pattern of (IS-t-COOH)/Cloisite 30B® nanocomposite shows a reflection peak at $2\theta = 5.8$ (d-spacing of 1.47 nm) and the XRD pattern of (IS-t-COOH)/Cloisite 20A® nanocomposite shows a conspicuous reflection peak at $2\theta = 4.6°$ (d-spacing of 1.85 nm), suggesting that both nanocomposites would have a low degree of dispersion of organoclay aggregates. (2) The XRD pattern of (IS-t-COONa)/Cloisite 30B® nanocomposite shows a very mild reflection peak, while the XRD pattern of (IS-t-COONa)/Cloisite 20A® nanocomposite shows featureless XRD patterns over the entire range of 2θ angles investigated. The above observation seems to suggest that the (IS-t-COONa)/Cloisite 20A® nanocomposite might have a slightly higher degree of dispersion of organoclay aggregates than the (IS-t-COONa)/Cloisite 30B® nanocomposite.

Figure 37 gives TEM images of (a) neat SI diblock copolymer SI-2 (see Table 6 for the molecular characteristics of SI-2) at 90 °C, (b) end-functionalized IS-t-COONa at 90 °C, (c) (IS-t-COONa)/Cloisite 30B® nanocomposite at 90 °C, (d) (IS-t-COONa)/Cloisite 30B® nanocomposite at 150 °C, (e) (IS-t-COONa)/Cloisite 20A® nanocomposite at 90 °C, and (f) (IS-t-COONa)/Cloisite 20A® nanocomposite at 150 °C, in which SI-2, IS-t-COONa, and the block copolymer in the respective
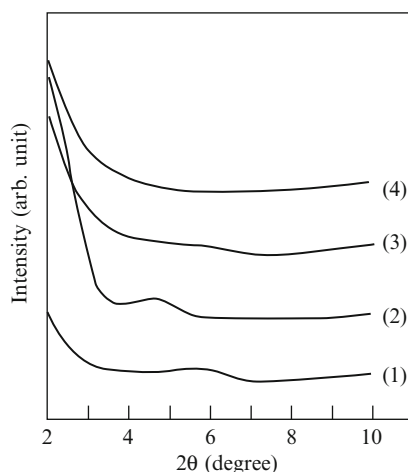
Fig. 36 XRD patterns for (1) (IS-t-COOH)/Cloisite 30B® nanocomposite, (2) (IS-t-COOH)/Cloisite 20A® nanocomposite, (3) (IS-t-COONa)/Cloisite 30B® nanocomposite, and (4) (IS-t-COONa)/Cloisite 20A® nanocomposite. (Reprinted from Zha et al. [55]. Copyright 2005, with permission from the American Chemical Society)
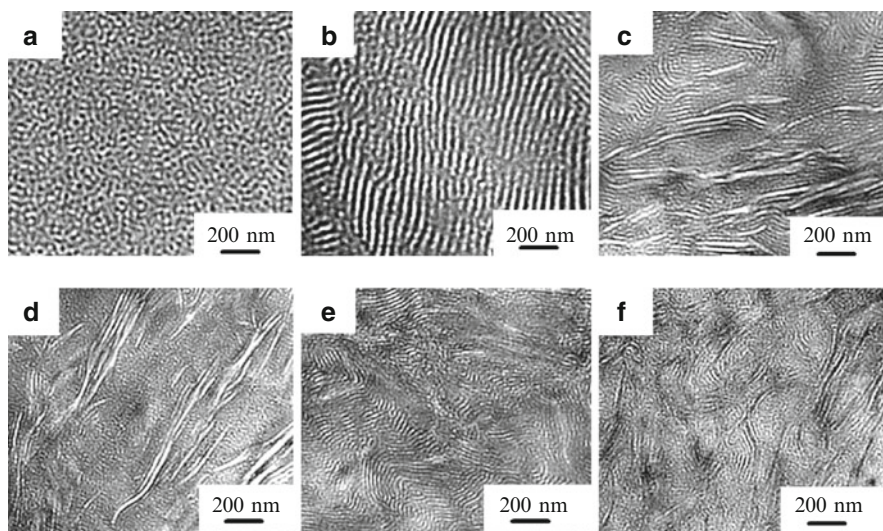
Fig. 37 TEM images of (**a**) SI-2 at 90°C, (**b**) IS-t-COONa at 90°C, (**c**) (IS-t-COONa)/Cloisite 30B nanocomposite at 90°C, (**d**) (IS-t-COONa)/Cloisite 30B nanocomposite at 150°C, (**e**) (IS-t-COONa)/Cloisite 20A nanocomposite at 90°C, and (**f**) (IS-t-COONa)/Cloisite 20A nanocomposite at 150°C, in which specimen was first annealed at 90°C for 24 h or at 150°C for 6 h and then stained with osmium tetroxide, followed by a rapid quench in ice water. (Reprinted from Zha et al. [55]. Copyright 2005, with permission from the American Chemical Society)

nanocomposites were stained with osmium tetroxide and thus the dark areas represent the PI phase. In Fig. 37 we observe that the TEM image of SI-2 at 90°C shows a structures, which resembles very much the liquidlike disordered structure of a nearly symmetric block copolymer reported by Sakamoto and Hashimoto [72]. Therefore, SI-2 having a liquidlike disordered structure can be regarded as being a disordered (homogeneous) block copolymer, which can easily be demonstrated from rheological measurements.

Figure 38 describes the temperature dependence of dynamic storage modulus G' during isochronal dynamic temperature sweep experiments for SI-2, IS-t-COONa, (IS-t-COONa)/Cloisite 30B® nanocomposite, and (IS-t-COONa)/Cloisite 20A® nanocomposite. It has been suggested by Gouinlock and Porter [73] that such plots can be used to determine the T_{ODT} of a block copolymer by identifying the temperature at which values of G' begin to drop precipitously. The following observations in Fig. 38 are worth noting. (1) Values of G' for SI-2 decrease steadily with increasing temperature over the entire range of temperatures investigated from 60 to 80°C, suggesting that SI-2 is a homogeneous block copolymer. (2) At 80°C the value of G' for the end-functionalized diblock copolymer IS-t-COONa is about three orders of magnitude larger than that for SI-2. Note further from Fig. 38 that values of G' for IS-t-COONa initially decrease slowly with increasing temperature from 70 to approximately 90°C, and then more rapidly with further increase in temperature. Choi and Han [74] reported a very large increase in G' when a homogeneous SIS
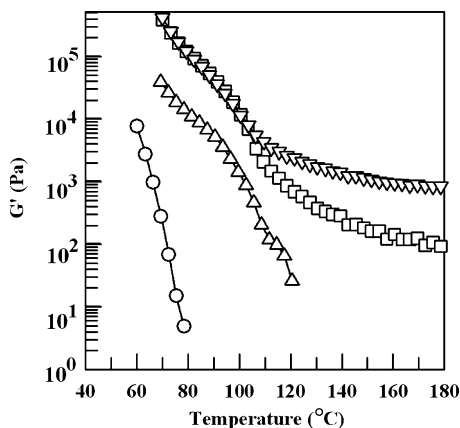
Fig. 38 Variations of dynamic storage modulus G′ with temperature during the isochronal dynamic temperature sweep experiments at ω = 0.1 rad/s for: (*open circle*) SI-2, (*open triangle*) IS-t-COONa, (*open square*) (IS-t-COONa)/Cloisite 30B® nanocomposite, and (*open inverted triangle*) (IS-t-COONa)/Cloisite 20A® nanocomposite. (Reprinted from Zha et al. [55]. Copyright 2005, with permission from the American Chemical Society)

triblock copolymer was end-functionalized with –COONa group, which then induced microphase separation in the SIS triblock copolymer. On the basis of such experimental observations it can be concluded that IS-t-COONa might have microdomains, which indeed is borne out to be the case as can be seen from Fig. 37b. (3) Values of G′ for both (IS-t-COONa)/Cloisite 30B® and (IS-t-COONa)/Cloisite 20A® nanocomposites initially decrease rapidly with increasing temperature to approximately 105 °C, and then very slowly as the temperature is increased further to approximately 180 °C. It is very interesting to observe in Fig. 38 that values of G′ for the (IS-t-COONa)/Cloisite 30B® and (IS-t-COONa)/Cloisite 20A® nanocomposites at 180 °C are still very large, suggesting the possibility that the block copolymer matrix IS-t-COONa in the respective nanocomposites might still have microdomains. Such a possibility, if it is borne out to be true, may be attributable to the formation of ionic clusters between the –COO⁻ at the chain end of PS block of SI-2 and the positively charged N⁺ in the surfactant (MT2EtOH or 2M2HT) residing at the surface of organoclay (Cloisite 30B® or Cloisite 20A®).

Returning to Fig. 37, we make the following observations. From Fig. 37b we observe that IS-t-COONa at 90 °C has lamellar microdomains, in which the dark areas represent the PI phase that was stained by osmium tetroxide and the bright areas represent the PS phase. What is significant in the TEM image of IS-t-COONa lies in that microphase separation has been induced by attaching –COONa group to the chain end of PS block of a homogeneous SI diblock copolymer, SI-2. The TEM images of (IS-t-COONa)/Cloisite 30B® and (IS-t-COONa)/Cloisite 20A® nanocomposites at 90 °C show the coexistence of the microdomains of the matrix phase IS-t-COONa and the organoclay (Cloisite 30B® or Cloisite 20A®). Of particular note is that at 150 °C the block copolymer matrix IS-t-COONa in

the (IS-t-COONa)/Cloisite 30B® and (IS-t-COONa)/Cloisite 20A® nanocomposites still retains microdomains (Figs. 37d and 37f), although they do not have perfectly aligned lamellae. In other words, the lamellar microdomain structure of IS-t-COONa (Fig. 37b) in the nanocomposite has been modified somewhat in the presence of organoclay, Cloisite 30B® or Cloisite 20A®. The presence of microdomains of the block copolymer matrix IS-t-COONa at 150 °C leads us to speculate that the ionic interactions between the –COO⁻ at the chain end of the PS block of SI-2 and the positively charged N^+ in the surfactant (MT2EtOH or 2M2HT) residing at the surface of organoclay (Cloisite 30B® or Cloisite 20A®) were sufficiently strong, so as to not allow the microdomains of IS-t-COONa to disappear at a temperature as high as 150 °C.

Figure 39 shows XRD patterns of nanocomposites based on neat SI diblock copolymer SI-1 (see Table 6 for the molecular characteristics of SI-1), SI-t-COOH, or SI-t-COONa, in which functional group, –COOH or –COONa, is attached to the chain end of PI block of SI-1. The following observations in Fig. 39 are worth noting. (1) The XRD pattern of (SI-1)/Cloisite 30B® nanocomposite shows a broad reflection peak at $2\theta = 4.6°$ (d-spacing of 1.85 nm) and the XRD pattern of (SI-1)/Cloisite 20A® nanocomposite shows a broad reflection peak at $2\theta = 4.8$ (d-spacing of 1.77 nm). Note that the shape of the XRD patterns of (SI-1)/Cloisite 30B® and (SI-1)/Cloisite 20A® nanocomposites shown in Fig. 39 is very similar to that for PSLMW/Cloisite 30B® and PSLMW/Cloisite 20A® nanocomposites (see Fig. 32). Thus it can be concluded that both (SI-1)/Cloisite 30B® and (SI-1)/Cloisite 20A® nanocomposites would have a low degree of dispersion of organoclay aggregates. This is not surprising, since no attractive interaction is expected between the SI diblock copolymer and the surfactant (MT2EtOH or 2M2HT) residing at the surface of the organoclays employed. (2) The XRD pattern of (SI-t-COOH)/Cloisite

Fig. 39 XRD patterns for (1) (SI-1)/Cloisite 30B® nanocomposite, (2) (SI-1)/Cloisite 20A® nanocomposite, (3) (SI-t-COOH)/Cloisite 30B® nanocomposite, (4) (SI-t-COOH)/Cloisite 20A® nanocomposite, (5) (SI-t-COONa)/Cloisite 30B® nanocomposite, and (6) (SI-t-COONa)/Cloisite 20A® nanocomposite. (Reprinted from Zha et al. [55]. Copyright 2005, with permission from the American Chemical Society)
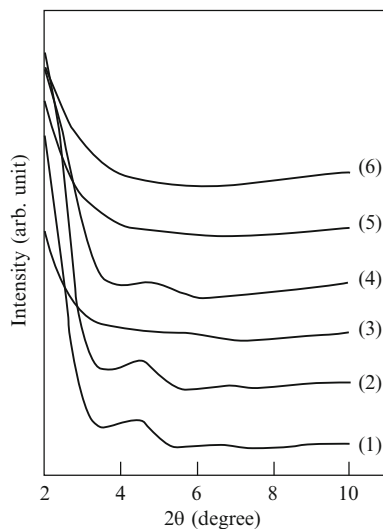
30B$^{®}$ nanocomposite shows a very mild reflection peak, while the XRD pattern of (SI-t-COOH)/Cloisite 20A$^{®}$ nanocomposite shows a conspicuous reflection peak at $2\theta = 5.0°$ (d-spacing of 1.70 nm). This observation leads us to conclude that (SI-t-COOH)/Cloisite 30B$^{®}$ nanocomposite might have a higher degree of dispersion of organoclay aggregates than (SI-t-COOH)/Cloisite 20A$^{®}$ nanocomposite. This observation is reasonable from the point of view that the –COOH group at the chain end of the PI block of SI-1 is expected to have very weak interactions, if any, with the hydroxyl groups in the surfactant MT2EtOH residing at the surface of Cloisite 30B$^{®}$, while no attractive interaction is expected between the –COOH group at the chain end of the PI block of SI-1 and the surfactant 2M2HT residing at the surface of Cloisite 20A$^{®}$. (3) Both (SI-t-COONa)/Cloisite 30B$^{®}$ and (SI-t-COONa)/Cloisite 20A$^{®}$ nanocomposites show featureless XRD patterns over the entire range of 2θ angles investigated, suggesting that a very high degree of dispersion of organoclay aggregates is expected in the matrix of SI-t-COONa for the respective nanocomposites. This observation is very similar to that made above for the (PSLMW-t-COONa)/Cloisite 30B$^{®}$ nanocomposite (see Fig. 32) and (IS-t-COONa)/Cloisite 20A$^{®}$ nanocomposite (see Fig. 36).

Figure 40 gives TEM images of the nanocomposites based on SI-1, SI-t-COOH, or SI-t-COONa, where the white/gray areas represent the block copolymer matrix phase and the dark areas represent organoclay. Note that the block copolymer in the
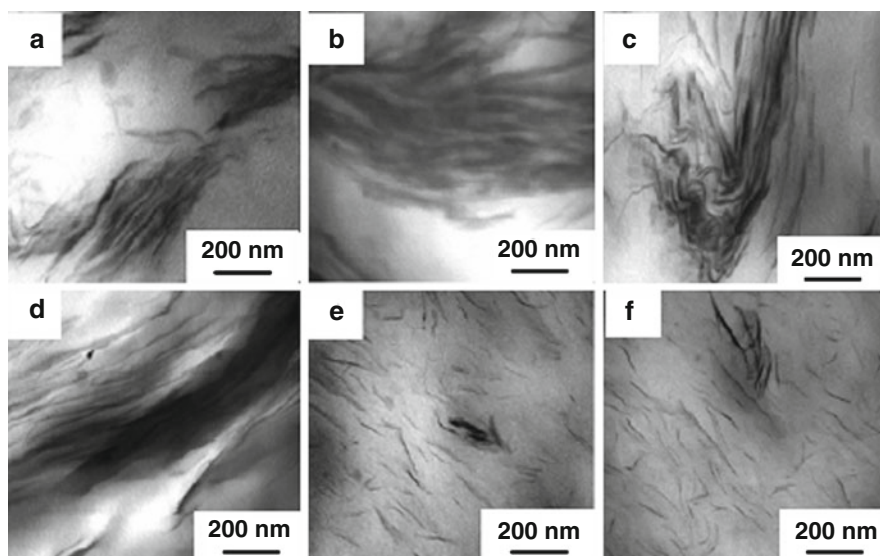
Fig. 40 TEM images at room temperature of (**a**) (SI-1)/Cloisite 30B$^{®}$ nanocomposite, (**b**) (SI-1)/ Cloisite 20A$^{®}$ nanocomposite, (**c**) (SI-t-COOH)/Cloisite 30B$^{®}$ nanocomposite, (**d**) (SI-t-COOH)/Cloisite 20A$^{®}$ nanocomposite, (**e**) (SI-t-COONa)/Cloisite 30B$^{®}$ nanocomposite, and (**f**) (SI-t-COONa)/Cloisite 20A$^{®}$ nanocomposite, in which the *dark areas* represent organoclay, Cloisite 20A$^{®}$ or Cloisite 30B$^{®}$, the *gray/white areas* represent the polymer matrix, and the specimens were not stained by osmium tetroxide. (Reprinted from Zha et al. [55]. Copyright 2005, with permission from the American Chemical Society)

respective nanocomposites was not stained with osmium tetroxide. It can be seen in Fig. 40 that the nanocomposites based on SI-1 and SI-t-COOH have very poor dispersions of organoclay aggregates, whereas the aggregates of Cloisite 30B$^{®}$ and Cloisite 20A$^{®}$ are very well dispersed in the matrix of SI-t-COONa. This observation is consistent with that made above from the XRD patterns given in Fig. 39, and is attributable to the presence of ionic interactions between the negatively charged –COO^{-} present at the chain end of the PI block of an SI-t-COONa and the positively charged N^{+} in the surfactant (MT2EtOH or 2M2HT) residing at the surface of organoclay (Cloisite 30B$^{®}$ or Cloisite 20A$^{®}$). On the other hand, the rather poor dispersion of organoclay aggregates in the matrix of SI-1 and SI-t-COOH is due to the absence (or insufficient) attractive interaction between the polymer matrix and the surfactant, MT2EtOH or 2M2HT, residing at the surface of the respective organoclays, Cloisite 30B$^{®}$ and Cloisite 20A$^{®}$.

Above, I have shown once again that the organoclay nanocomposites prepared from a non-functionalized SI diblock copolymer only yielded intercalation of the aggregates of organoclay, whereas the organoclay nanocomposites based on an SI diblock copolymer end-functionalized with sodium carboxylate yielded exfoliation of the aggregates of organoclay. The observed exfoliation is attributed to the attractive interactions, via ionic interactions, between the negatively charged carboxylic anion $-$COO^{-} present at the chain end of an SI diblock copolymer and the positively charged cation N^{+} present in the surfactant (MT2EtOH or 2H2MT) residing at the surface of organoclay (Cloisite 30B$^{®}$ or Cloisite 20A$^{®}$). What is very interesting here is the observation that as long as the surfactants had cation N^{+}, regardless of the details of their chemical structures, they underwent ionic interactions with the carboxylic anion $-$COO^{-} present at the chain end of the functionalized SI diblock copolymer. It should be remembered that an exfoliated nanocomposite was *not* obtained when an ISBOH triblock copolymer having hydroxylated PBOH block was mixed with Cloisite 15A$^{®}$, while an exfoliated nanocomposite was obtained when the same block copolymer was mixed with Cloisite 30B$^{®}$ (see Fig. 16), the reason is that the surfactant 2M2HT residing at the surface of Cloisite 15A$^{®}$ does not have hydroxyl group, while the surfactant MT2EtOH residing at the surface of Cloisite 30B$^{®}$ has hydroxyl groups (see Table 2 for the chemical structures of the two surfactants). Thus, it has been demonstrated that attractive interactions, via hydrogen bonding or ionic interactions, have led to exfoliated organoclay nanocomposites based on functionalized polystyrene homopolymer or functionalized diblock or triblock copolymers.

5 Ion–Dipole Interactions in Exfoliated Nanocomposites Based on Polystyrene-*block*-Poly(2-vinylpyridine) Copolymer Prepared by Mixing

In this section we present the recent study of Zha et al. [7], who prepared organoclay nanocomposites based on polystyrene-*block*-poly(2-vinylpyridine) (S2VP diblock)

copolymer. The uniqueness of S2VP diblock copolymer lies in that the poly(2-vinylpyridine) (P2VP) block has a very strong polar pyridine ring, which can have attractive interactions with a surfactant residing at the surface of an organoclay, potentially giving rise to exfoliated nanocomposites. Interestingly, Zha et al. indeed obtained exfoliated organoclay nanocomposites based on S2VP diblock copolymer. Using solid-state nuclear magnetic resonance (NMR) spectroscopy they demonstrated the presence of ion–dipole interactions between the positively charged N^+ ion present in a surfactant (MT2EtOH, 2MBHT, 2M2HT, or 2MHTL8) residing at the surface of an organoclay (Cloisite 30B®, Cloisite 10A®, Cloisite 15A®, or Cloisite 25A®) and the polar pyridine ring in the P2VP block of S2VP diblock copolymer.

In their study, Zha et al. [7] synthesized three S2VP diblock copolymers having different block compositions (5, 25, and 56 wt% P2VP block), the molecular characteristics of which are summarized in Table 8, and they prepared nanocomposites using four different organoclays (Cloisite 30B®, Cloisite 10A®, Cloisite 15A®, and Cloisite 25A®) with 5 wt% in each of the nanocomposites by solution blending in pyridine. The chemical structures of the surfactants residing at the surfaces of the organoclays are given in Table 2.

Figure 41 gives XRD patterns of nanocomposites based on three different S2VPs, each having a different organoclay. Also shown in Fig. 41 are, for comparison, XRD patterns of nanocomposites based on MMT. In Fig. 41a we observe that the XRD pattern of (S2VP-5)/MMT nanocomposite exhibits a broad reflection peak at $2\theta \approx 7.5$–$8.5°$, corresponding to a d-spacing of about 1 nm. That is, the d-spacing of MMT in the matrix of S2VP-5 is very close to the gallery distance of 1.1 nm for pristine MMT. This observation suggests that the dispersion characteristics of the aggregates of MMT in (S2VP-5)/MMT nanocomposite might be very poor. On the other hand, we do not observe discernible reflection peaks at 2θ angles ranging from 1.5 to $10°$ for the organoclay nanocomposites based on Cloisite 30B® or Cloisite 15A®. However, both organoclay nanocomposites show very similar XRD patterns, despite the fact that the chemical structure of the surfactant residing at the surface of each organoclay is different (see Table 2). In general, the absence of a discernible reflection peak in XRD patterns signifies good dispersion of organoclay in a polymer matrix. Thus, it can be concluded that the dispersion characteristics of both organoclay nanocomposites based on S2VP-5 would be very good.

We observe from Fig. 41b that the XRD pattern of (S2VP-25)/MMT nanocomposite shows a conspicuous reflection peak at $2\theta \approx 6°$ (d-spacing = 1.5 nm), suggesting poor dispersion of MMT aggregates in the S2VP-25 matrix, although some

Table 8 Molecular characteristics of three S2VP diblock copolymers synthesized by Zha et al. [7]

Sample code	$M^{w,a}$	M^n	$w_{PS}(wt\%)^b$	$w_{PVP}(wt\%)^b$	$T_{g,PVP}(°C)$
S2VP-5	2.29×10^4	2.14×10^4	95	5	–
S2VP-25	1.96×10^4	1.87×10^4	75	25	99.6
S2VP-56	2.41×10^4	2.13×10^4	44	56	100.0

[a]Measured against polystyrene standards using gel permeation chromatography
[b]Determined by ^1H NMR spectroscopy
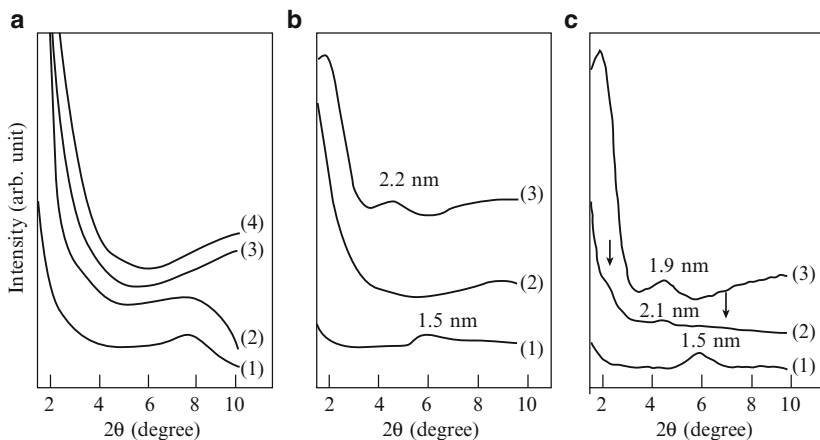
Fig. 41 XRD patterns for nanocomposites (**a**) based on S2VP-5: (1) pristine MMT (2) (S2VP-5)/ MMT nanocomposite, (3) (S2VP-5)/Cloisite 30B® nanocomposite, and (4) (S2VP-5)/Cloisite 15A® nanocomposite, (**b**) based on S2VP-25: (1) (S2VP-25)/MMT nanocomposite, (2) (S2VP-25)/Cloisite 30B® nanocomposite, (3) (S2VP-25)/Cloisite 15A® nanocomposite, and (**c**) based on S2VP-56: (1) (S2VP-56)/MMT nanocomposite, (2) (S2VP-56)/Cloisite 30B® nanocomposite, and (3) (S2VP-56)/Cloisite 15A® nanocomposite. (Reprinted from Zha et al. [7]. Copyright 2009, with permission from Elsevier)

MMT aggregates might have been intercalated. Interestingly, in Fig. 41b we observe a very broad reflection peak at $2\theta \approx 8.4°$ in the XRD pattern of (S2VP-25)/ Cloisite 30B® nanocomposite. This broad peak was not observed in the (S2VP-5)/Cloisite 30B® nanocomposite (see Fig. 41a). This observation seems to indicate that small number of Cloisite 30B® aggregates in the S2VP-25 matrix might have been poorly dispersed. Thus, the overall dispersion characteristics of Cloisite 30B® in the S2VP-25 matrix would be slightly poorer than those in the S2VP-5 matrix. From the XRD pattern given in Fig. 41b, we observe a reflection peak at $2\theta \approx 1.8°$ (d-spacing = 5.0 nm) and a conspicuous reflection peak at $2\theta \approx 4.1°$ (d-spacing = 2.2 nm) in the (S2VP-25)/Cloisite 15A® nanocomposite. Since the gallery distance of pristine Cloisite 15A® is 3.15 nm, the overall dispersion characteristics of Cloisite 15A® in the S2VP-25 matrix would be poorer than those in the S2VP-5 matrix.

From Fig. 41c we observe that the XRD pattern of (S2VP-56)/MMT nanocomposite shows a conspicuous reflection peak at $2\theta \approx 6°$ (d-spacing = 1.5 nm), very similar to that of (S2VP-25)/MMT nanocomposite (see Fig. 41b), again suggesting poor dispersion of MMT aggregates in the S2VP-56 matrix, although some intercalation might have taken place. Also, we observe that the (S2VP-56)/Cloisite 30B® nanocomposite has a small distinct reflection peak at $2\theta \approx 4.3°$ (d-spacing = 2.1 nm) and two weak reflection peaks indicated by arrows at $2\theta \approx 2.15°$ (d-spacing = 4.2 nm) and 7.3° (d-spacing = 1.24 nm). Since the gallery distance of pristine Cloisite 30B® is 1.85 nm, it appears that the (S2VP-56)/Cloisite 30B® nanocomposite has aggregates of Cloisite 30B® with varying

gallery distances. Thus, it seems reasonable to speculate that some of the Cloisite 30B® aggregates might have been dispersed well, while others might have been intercalated in the matrix of S2VP-56. However, since two reflection peaks of the (S2VP-56)/Cloisite 30B® nanocomposite are discernible at $2\theta = 2.15°$ and $7.3°$, the dispersion characteristics of Cloisite 30B® aggregates in the S2VP-56 matrix would be poorer compared with those in the S2VP-25 matrix. Further we observe that the XRD patterns of (S2VP-56)/Cloisite 15A® nanocomposite have conspicuous reflection peaks at $2\theta \approx 1.9°$ (d-spacing = 4.7 nm) and $4.4°$ (d-spacing = 1.9 nm), suggesting poor dispersion of Cloisite 15A® in the matrix of S2VP-56, although some intercalations of Cloisite 15A® aggregates might have taken place.

Figure 42 gives TEM images of the nanocomposites based on S2VP diblock copolymer with MMT and four different organoclays. The following observations can be made from Fig. 42. The dispersion characteristics of the MMT aggregates in the matrix of S2VP-5 are very poor. This is because no attractive interaction is expected between the surface of MMT and the pyridine rings in the P2VP block of the S2VP diblock copolymers. On the other hand, the dispersion characteristics of the aggregates of all four organoclays (Cloisite 30B®, Cloisite 15A®, Cloisite 10A®, and Cloisite 25A®) in the matrix of S2VP-5 are equally good, despite the fact that the chemical structures of surfactant residing at the surface of the organoclays are different (see Table 2). Figure 43 gives TEM images of nanocomposites based on different compositions of S2VP diblock copolymers. It can be seen from Fig. 43 that the dispersion characteristics of the
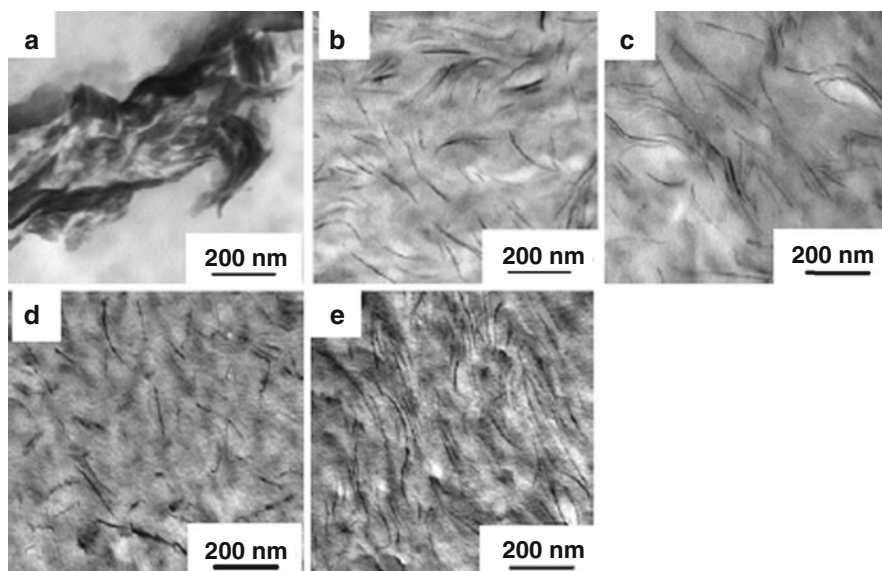
Fig. 42 TEM images of nanocomposites based on S2VP-5 (**a**) (S2VP-5)/MMT, (**b**) (S2VP-5)/Cloisite 30B®, (**c**) (S2VP-5)/Cloisite 15A®, (**d**) (S2VP-5)/Cloisite 10A®, and (**e**) (S2VP-5)/Cloisite 25A® in which specimens were not stained
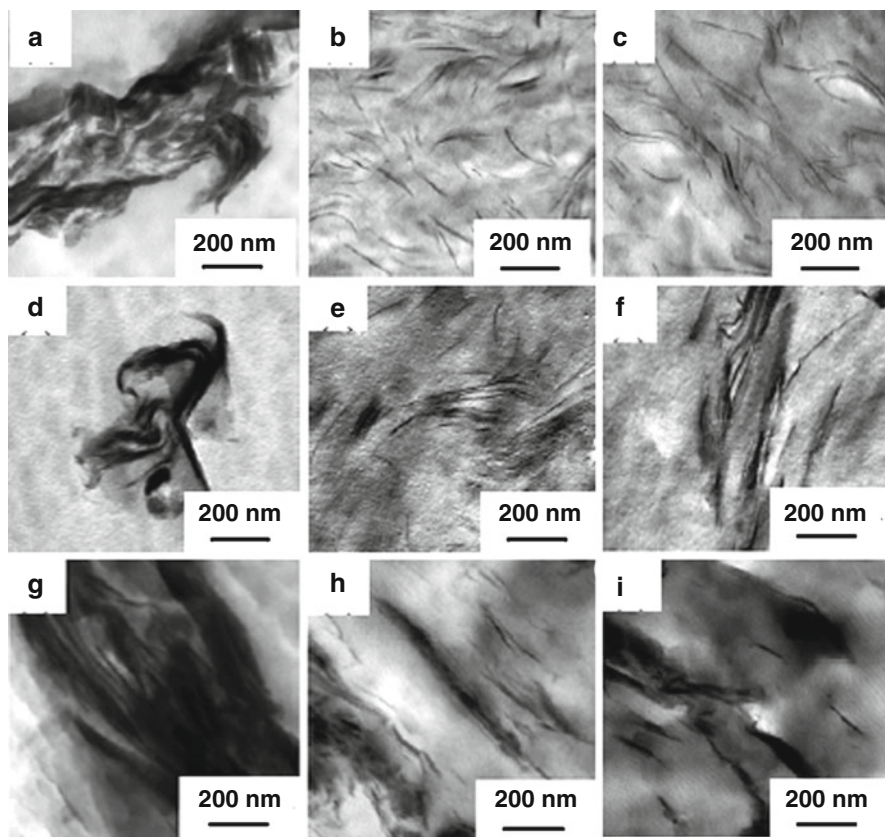
Fig. 43 TEM images of nanocomposites based on S2VP-5: (**a**) (S2VP-5)/MMT, (**b**) (S2VP-5)/Cloisite 30B®, (**c**) (S2VP-5)/Cloisite 15A®, (**d**) (S2VP-25)/MMT, (**e**) (S2VP-25)/Cloisite 30B®, (**f**) (S2VP-25)/Cloisite 15A®, (**g**) (S2VP-56)/MMT, (**h**) (S2VP-56)/Cloisite 30B®, (**i**) and (S2VP-56)/Cloisite 15A® in which specimens were not stained. (Reprinted from Zha et al. [7]. Copyright 2009, with permission from Elsevier)

aggregates of Cloisite 30B® and Cloisite 15A® become progressively poorer as the weight fraction of P2VP block in an S2VP diblock copolymer increases from 5 wt% for (S2VP-5)/Cloisite 30B® and (S2VP-5)/Cloisite 15A® nanocomposites to 25 wt% for (S2VP-25)/Cloisite 30B® and (S2VP-25)/Cloisite 15A® nanocomposites and to 56 wt% for (S2VP-56)/Cloisite 30B® and (S2VP-56)/Cloisite 15A® nanocomposites.

Figure 44 gives the TEM images of nanocomposites based on neat P2VP with MMT, Cloisite 15A®, or Cloisite 30B®. It is clearly seen from Fig. 44 that, although there are numerous pyridine groups in neat P2VP that can have attractive interactions with a surfactant (MT2EtOH or 2M2HT) residing at the surface of Cloisite 30B® or Cloisite 15A®, the dispersion characteristics of P2VP/Cloisite 30B® and P2VP/Cloisite 15A® nanocomposites are as poor as the dispersion characteristics
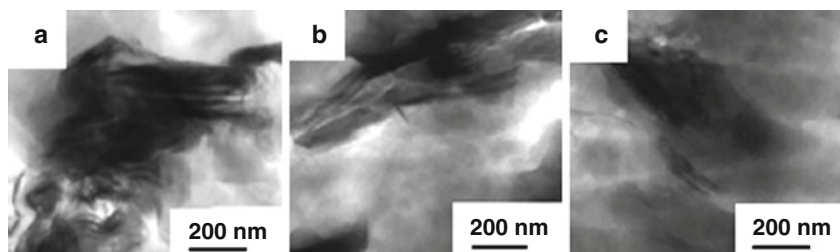
Fig. 44 TEM images of nanocomposites based on P2VP: (**a**) P2VP/MMT nanocomposite, (**b**) P2VP/Cloisite 15A® nanocomposite, and (**c**) P2VP/Cloisite 30B® nanocomposite. (Reprinted from Zha et al. [7]. Copyright 2009, with permission from Elsevier)

of P2VP/MMT nanocomposites, although some intercalations of organoclays might have taken place. This is because the pyridine rings in P2VP form self-association and thus little or no intermolecular interactions take place with a surfactant residing at the surface of an organoclay (Cloisite 30B® or Cloisite 15A®). It can then be concluded that S2VP diblock copolymers having P2VP block below a certain critical amount are far more effective than neat P2VP, in producing highly dispersed organoclay nanocomposites.

In their study, Zha et al. [7] first hypothesized that ion–dipole interactions between the polar pyridyl ring in the vinylpyridine block of S2VP-5 and the positively charged N^+ ion in the surfactant (MT2EtOH, 2MBHT, 2M2HT, or 2MHTL8) residing at the surface of an organoclay (Cloisite 30B®, Cloisite 10A®, Cloisite 15A®, or Cloisite 25A®) might have led to exfoliation of the aggregates of organoclay in the nanocomposites (see Fig. 42). In an effort to test the hypothesis of ion–dipole interactions as being the mechanism for exfoliation of organoclay aggregates in a nanocomposites based on S2VP diblock copolymer, Zha et al. employed solid-state NMR spectroscopy.

Figure 45 shows the solid state ^{13}C cross polarization/magic-angle spinning (CP/MAS) spectra of three neat S2VP diblock copolymers: (a) S2VP-5, (b) S2VP-25, and (c) S2VP-56. While the main chain (aliphatic) carbon resonances and most of the aromatic carbon resonances of both the PS and P2VP blocks overlap, a unique non-overlapping carbon resonance from the P2VP block in S2VP-56 appears at $\delta = 163.1$ ppm (see Fig. 45c), which comes from the *ipso* carbon of the pyridine ring in the P2VP block. Zha et al. used this unique signal to probe the heterogeneity of the segmental motion and interaction of the P2VP block with an organoclay. Values of the proton spin-lattice relaxation time in the rotating frame $(T_{1\rho H})$ measured for neat PS, neat P2VP, neat S2VP diblock copolymers and their nanocomposites were analyzed and they are summarized in Table 9. Due to the heterogeneous nature of the neat S2VP diblock copolymers and their nanocomposites, Zha et al. [7] averaged the values of $T_{1\rho H}$ on the timescale of the spin locking periods and thus only a single value of $T_{1\rho H}$ was measured.

Figure 46 gives stacked ^{13}C CP/MAS spectra at 15 different contact times for 3 nanocomposites: (a) (S2VP-5)/Cloisite 30B®, (b) (S2VP-25)/Cloisite 30B®, and (c) (S2VP-56)/Cloisite 30B®. Note in Fig. 46a that carbon resonance, which should

Fig. 45 ^{13}C CP/MAS spectra of (**a**) S2VP-5, (**b**) S2VP-25, and (**c**) S2VP-56, in which *asterisk* denotes the chemical shift of the carbons at positions 4, 5, 6, 7, 8, 4′, 5′, 6′, and 7′. The intensity of carbon resonance at $\delta = 163.1$ ppm from the P2VP block in S2VP-5 is so weak that it is not easily discernible. (Reprinted from Zha et al. [7]. Copyright 2009, with permission from Elsevier)
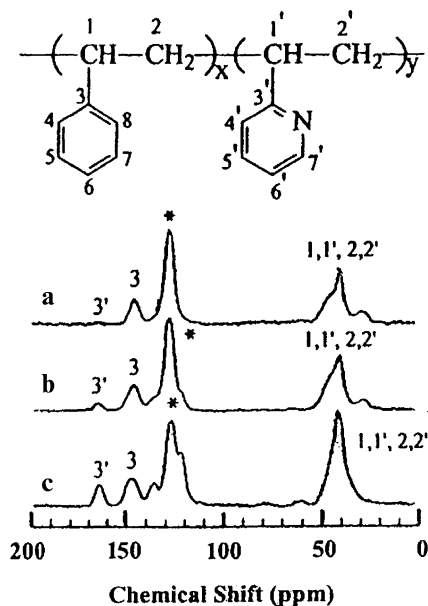
Table 9 Proton $T_{1\rho H}$ data for PS, P2VP, S2VP diblock copolymers and their nanocomposites investigated by Zha et al. [7]

| Sample code | $T_{1\rho H}$ (µs) Peak position δ (ppm) | | | | | | |
	163.09	145.78	133.85	125.00	119.81	40.57	Average
Neat PS		4,900		6,000		5,100	5,300
PS/Cloisite 30B		5,800		5,600		5,600	5,700
Neat P2VP	5,900	6,988		7,200	6,000	6,500	6,500
P2VP/Cloisite 30B	640	7,200		6,200	6,400	6,200	6,500
S2VP-5		5,300		5,700		5,300	5,500
(S2VP-5)/Cloisite 30B		5,700		5,900		5,900	5,800
S2VP-25	6,900	5,500		5,600		5,800	6,100
(S2VP-25)/Cloisite 30B	6,600	5,600		5,400		5,300	5,700
S2VP-56	5,700	5,900	6,100	5,900	6,100	5,500	5,600
(S2VP-56)/Cloisite 30B	5,700	5,400	5,900	5,700		5,600	5,800

come from the *ipso* carbon of the pyridine ring in the P2VP block of S2VP-5, in the (S2VP-5)/Cloisite 30B® nanocomposite is weak for two reasons: (1) only 5 wt% P2VP block is present in S2VP-5 and (2) the pyridine ring in P2VP has already interacted, via ion–dipole interactions, with the N$^+$ ion in the surfactant MT2EtOH residing at the surface of Cloisite 30B®. In order to help observe the carbon resonance peak in Fig. 46a that would arise from the *ipso* carbon of the pyridine ring in the P2VP block of S2VP-5, Zha et al. [7] analyzed the weak signal to determine values of ^{1}H–^{13}C cross polarization time (T_{CH}) in the (S2VP-5)/Cloisite
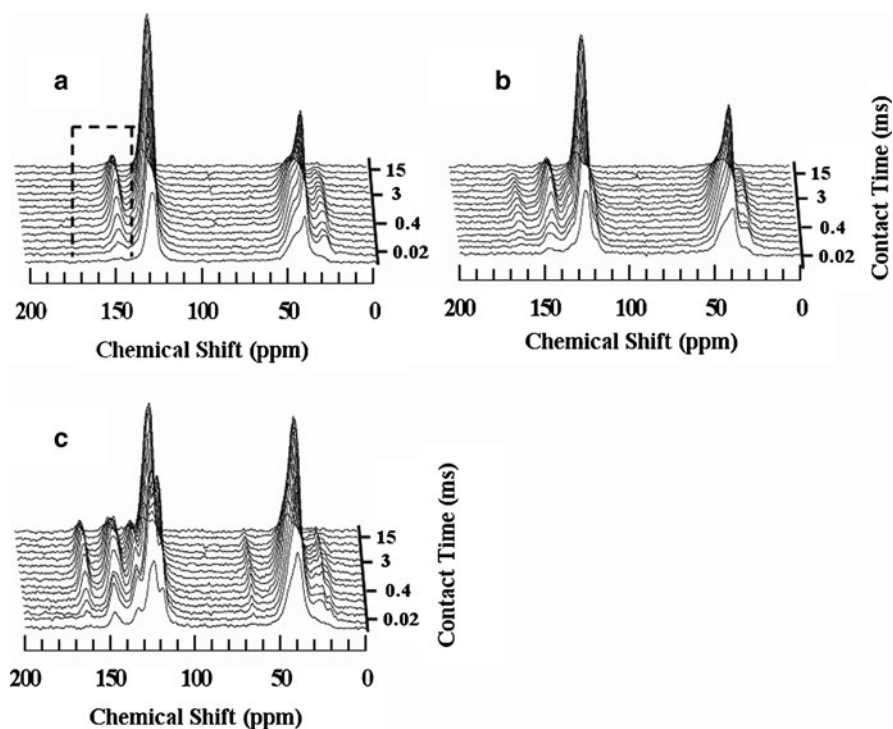
Fig. 46 Stacked ^{13}C CP/MAS spectra at 15 different contact times (ms) (0.02, 0.05, 0.1, 0.2, 0.4, 0.7, 1.0, 1.5, 2.0, 3.0, 4.0, 5.0, 7.0, 10, and 15) for (**a**) (S2VP-5)/Cloisite 30B® nanocomposite, (**b**) (S2VP-25)/Cloisite 30B® nanocomposite, and (**c**) (S2VP-56)/Cloisite 30B® nanocomposites. (Reprinted from Zha et al. [7]. Copyright 2009, with permission from Elsevier)

30B® nanocomposite. For this, by enlarging a small section covering the chemical shifts ranging from 140 to 175 ppm indicated by a dotted line in Fig. 46a, they prepared Fig. 47 describing the stacked ^{13}C CP/MAS spectra at 12 different contact times for the (S2VP-5)/Cloisite 30B® nanocomposite. In Fig. 47 one can discern a carbon resonance peak at $\delta = 163.1$ ppm arising from the *ipso* carbon of the pyridine ring in the P2VP block. Note in Fig. 47 that the carbon resonance peak at $\delta = 163.1$ ppm increases with increasing contact time. The values of T_{CH} thus determined are summarized in Table 10. The details of the procedures employed to determine the values of T_{CH} given in Table 10 can be found in the original paper [7].

The following observations on Table 10 are worth noting. While there is little or no change in the value of T_{CH} of the PS block (at $\delta = 145.8$ ppm) before and after mixing with an organoclay, the value of T_{CH} of the P2VP block (at $\delta = 163.1$ ppm) has decreased significantly from 150 to 105 ± 9 μs for the (S2VP-5)/Cloisite 30B® nanocomposite, indicating that the polar group in the P2VP segments of S2VP-5 in the nanocomposite must have interacted via ion–dipole interactions, with the positively charged N$^+$ ion in the surfactant MT2EtOH residing at the surface of Cloisite 30B®. This observation now explains why the (S2VP-5)/Cloisite

Fig. 47 Enlarged stacked
^{13}C CP/MAS spectra at
$\delta = 140$–175 ppm at 12
different contact times
increasing from 0.02 to 15 ms
for the (S2VP-5)/Cloisite
30B® nanocomposite, in
which. values of contact
times are not shown in the
figure owing to the
crowdedness of the spectra.
(Reprinted from Zha et al.
[7]. Copyright 2009, with
permission from Elsevier)
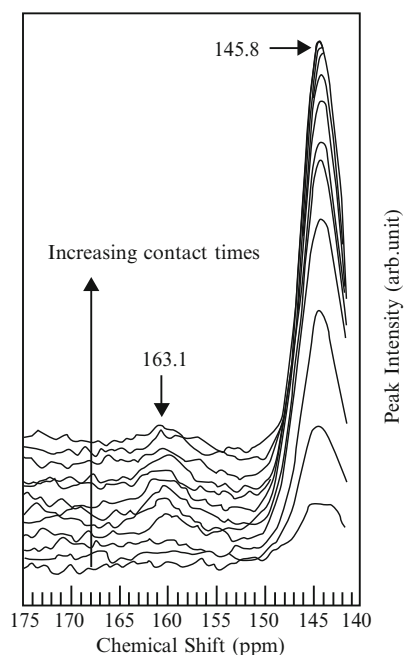
Table 10 Values of T_{CH} determined from curve fitting the variable contact time investigated by Zha et al. [7]

| | T_{CH} (μs) | | | | |
| | Peak position δ (ppm) | | | | |
Sample code	163.1	145.8	133.9	125.0	40.6
S2VP-5	150	400		136	99
(S2VP-5)/Cloisite 30B)	108 ± 9	316		85.3	70
S2VP-25	520	510		80	57
(S2VP-25)/Cloisite 30B	290 ± 20	350 ± 10		71 ± 0	59 ± 2
S2VP-56	500	140	53	66	60
(S2VP-56)/Cloisite 30B	520	210	42	59	52

Data were processed using Excel spreadsheet with the two-parameter fit protocol, and reported errors are calculated standard deviations

30B® nanocomposite has a very high degree of dispersion (near exfoliation) of the aggregates of Cloisite 30B® (see the TEM image given in Fig. 43b), supporting the hypothesis made of the presence of ion–dipole interactions in the nanocomposite. Note, however, in Table 10 that the value of T_{CH} for the P2VP block in the (S2VP-25)/Cloisite 30B® nanocomposite has decreased moderately from 520 to 290 ± 20 μs. The degree of reduction for S2VP-25 is similar to that of S2VP-5, indicating somewhat significant interaction with the Cloisite 30B®. Nevertheless, we have already observed that the (S2VP-25)/Cloisite 30B® nanocomposite has a lower degree of dispersion of the aggregates of Cloisite 30B® (see the TEM image

given in Fig. 43e). However, there is essentially no change in T_{CH} for S2VP-56 upon mixing with Cloisite 30B®, indicating that there is little or no attractive interaction between the polar pyridyl ring in the vinylpyridine block of S2VP-56 and the positively charged N^+ ion in the surfactant (MT2EtOH) residing at the surface of Cloisite 30B® in the (S2VP-56)/Cloisite 30B® nanocomposite (see the TEM image given in Fig. 43h). This observation suggests that the majority, if not all, of the polar groups in the P2VP block of S2VP-56 must have self-associated.

6 Coulombic Interactions in Exfoliated Nanocomposites Prepared by Mixing

So far I have reviewed the literature, reporting the studies where exfoliated organoclay nanocomposites were prepared by mixing an organoclay with a polymer that had been chemically modified to have a functional group(s) or with a block copolymer having a functional block. In each study reviewed, I have highlighted the experimental evidence for the presence of specific interaction (hydrogen bonding, ionic interaction, or ion–dipole interaction) between the polymer and organoclay selected to prepare nanocomposites. I have emphasized the necessity for providing (or inducing) attractive interactions (or compatibility) between the polymer and organoclay selected in order to achieve exfoliation of the aggregates of the organoclay.

Here I review a recent study of Huang and Han [75], reporting a situation where exfoliated nanocomposites were prepared by mixing pristine MMT with a ruthenium(II) complex-induced segmental, main-chain liquid-crystalline polymer having side-chain terpyridine group (PTBP-Ru-6TPy), the synthesis route for which is given in Scheme 1 below. The details of the synthesis procedures for PTBP-Ru-6TPy are available in the original paper.

Huang and Han [75] synthesized a segmented main-chain liquid-crystalline polymer having side chain terpyridine group (PTBP) (see Scheme 1) and then prepared a ruthenium metal complex [Ru(II)(PTBP)(6TPy)](PF$_6$)$_2$ (referred to as PTBP-Ru-6TPy) by mixing PTBP with a monocomplex (6TPy-RuCl$_3$), which was formed between a terpyridine (6-(2,2′ : 6′,2″-terpyridyl-4′-oxy)hexane (6TPy) and ruthenium chloride (RuCl$_3$ · 3H$_2$O). Subsequently, they prepared a (PTBP-Ru-6TPy)/MMT nanocomposite by solution blending. The MMT employed (Southern Clay Products) had Na^+ ion, the ion-exchange capacity of 92 meq/100 g, and the dimensions of about 1 nm in thickness, and approximately 100 nm in width and length. (PTBP-Ru-6TPy)/MMT nanocomposite was prepared by mixing a predetermined amount of PTBP-Ru-6TPy dissolved in a co-solvent of N,N-dimethylformamide (DMF) and H$_2$O (10:1, v/v) and MMT aggregates suspended in a mixture of DMF and H$_2$O (10:1, v/v) under vigorous stirring. The solvent in the mixture was evaporated slowly under constant stirring for 2 days at ambient temperature. When (PTBP-Ru-6TPy)/MMT nanocomposite was prepared, the exchangeable interlayer cation Na^+ was exchanged by the ruthenium complex in PTBP-Ru-6TPy and formed sodium hexafluorophosphate salt, which was still present in the final product. For
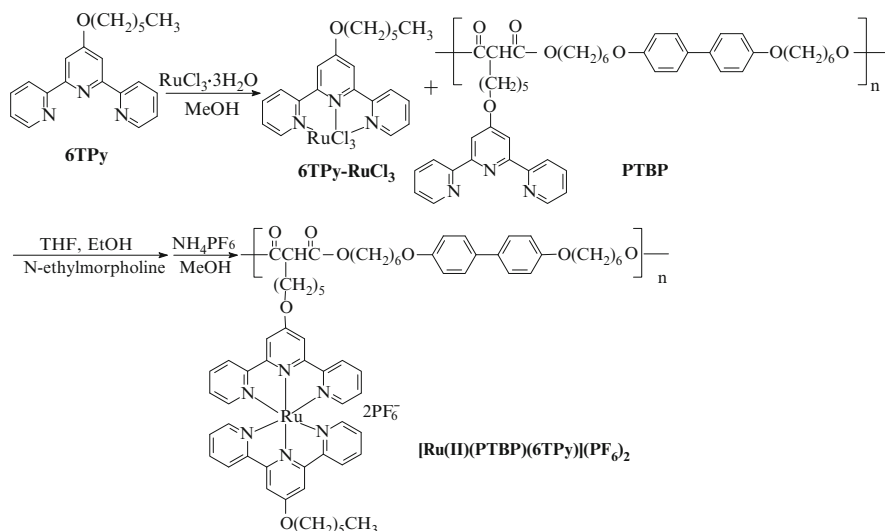
Scheme 1 Synthesis route for PTBP-Ru-6TPy

Fig. 48 XRD patterns
for (**a**) MMT,
(**b**) (PTBP-Ru-6TPy)/MMT
nanocomposite, and (**c**)
PTBP/MMT nanocomposite.
(Reprinted from Huang and
Han [75]. Copyright 2006,
with permission from the
American Chemical Society)
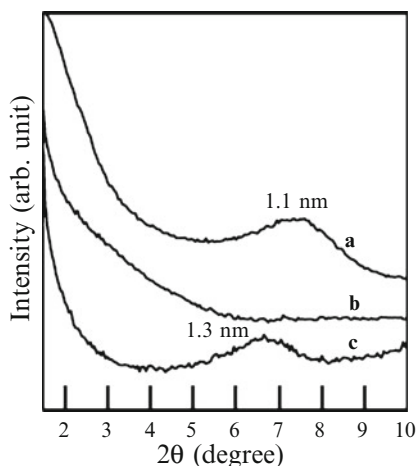
comparison, the PTBP/MMT nanocomposite was also prepared using the same procedure, except that slight heating was applied to ensure the solubility of PTBP. Nanocomposites were dried completely in a vacuum oven at $100\,^\circ$C until no weight change was detected. The amount of MMT in each nanocomposite (PTBP-Ru-6TPy)/MMT and PTBP/MMT was 3 wt%.

Figure 48 presents XRD patterns, showing that MMT has a gallery distance (d-spacing) of 1.1 nm, while the d-spacing of MMT in PTBP/MMT nanocomposite has increased only slightly from 1.1 to 1.3 nm, indicating that there would be little chance to obtain highly dispersed MMT aggregates in PTBP. Interestingly, it can be seen in Fig. 48 that (PTBP-Ru-6TPy)/MMT nanocomposite has a featureless XRD

pattern, the origin of which can be attributed to the incorporation of the ruthenium complex into PTBP which significantly improved the compatibility between the MMT and the polymer. Figure 49 gives TEM images of the (PTBP-Ru-6TPy)/MMT nanocomposite having a very high degree of dispersion of MMT aggregates in the ruthenium complex matrix, while the PTBP/MMT nanocomposite has large aggregates of MMT, indicating poor dispersion of MMT aggregates.

Tris(2,2′-bipyridine)ruthenium(II) complex has been reported to adsorb very selectively into the gallery of clay [76, 77]. The evidence of strong attractive interactions between the positively charged ruthenium center and the negatively charged clay surface is related to the red-shift of the positions of the metal-to-ligand charge-transfer (MLCT) band of tris(2,2′-bipyridine)ruthenium(II) complex and the decrease of the π–π^* band. In their study, Huang and Han [75] had an excellent ion-exchange property of ruthenium(II) complex employed to exfoliate MMT aggregates in the polymer matrix. Figure 50 shows the ultraviolet-visible
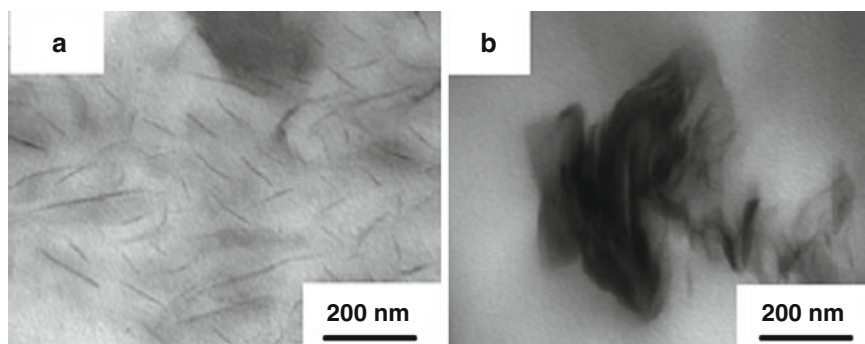
Fig. 49 TEM images of (**a**) (PTBP-Ru-6TPy)/MMT nanocomposite and (**b**) PTBP/MMT nanocomposite, in which the *dark areas* represent the clay and the *gray/white areas* represent the polymer matrix. (Reprinted from Huang and Han [75]. Copyright 2006, with permission from the American Chemical Society)
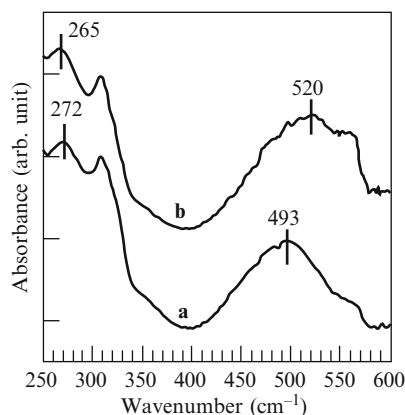
Fig. 50 UV–vis spectra of thin films for (**a**) PTBP-Ru-6TPy and (**b**) (PTBP-Ru-6TPy)/MMT nanocomposite. (Reprinted from Huang and Han [75]. Copyright 2006, with permission from the American Chemical Society)

(UV-vis) spectra of thin films of PTBP-Ru-6TPy and the (PTBP-Ru-6TPy)/MMT nanocomposite. It can be seen that the position of the MLCT band at a wavelength of about 493 nm for PTBP-Ru-6TPy has red-shifted to a wavelength of about 520 nm for the (PTBP-Ru-6TPy)/MMT nanocomposite. The π–π^* band at a wavelength of 272 nm for PTBP-Ru-6TPy has decreased to a wavelength of 265 nm for the (PTBP-Ru-6TPy)/MMT nanocomposite. The above observations are attributable to the Coulombic interactions between the positively charged ruthenium center and the negatively charged MMT surfaces, which are believed to be the driving forces that exfoliated MMT aggregates in the matrix of PTBP-Ru-6TPy.

Figure 51 gives FTIR spectra of PTBP-Ru-6TPy and the (PTBP-Ru-6TPy)/MMT nanocomposite, further confirming the presence of specific interaction, as evidenced by the increased intensity at a wavenumber of about $1,680 \, cm^{-1}$ (see the inset of Fig. 51) and the new broad absorption peak appearing at a wavenumber of about $3,420 \, cm^{-1}$ for the (PTBP-Ru-6TPy)/MMT nanocomposite. According to Huang and Han [75], when MMT was dispersed in the PTBP-Ru-6TPy complex, the hydroxyl groups on the surface of MMT formed hydrogen bonds with the terpyridine groups in the PTBP-Ru-6TPy complex. Thus, the absorption peak at $3,625 \, cm^{-1}$ for pristine MMT has been shifted to $3,420 \, cm^{-1}$ for the (PTBP-Ru-6TPy)/MMT nanocomposite (see Fig. 51). The increased intensity of the absorption peak at $1,680 \, cm^{-1}$ (see the inset of Fig. 51) is attributed to the ionization of terpyridine group and its strength is expected to increase in the (PTBP-Ru-6TPy)/MMT nanocomposite due to the Coulombic interactions between the positively charged ruthenium center and the negatively charged MMT surface.

Huang and Han [75] also prepared two additional nanocomposites with PTBP-Ru-6TPy using two organoclays, Cloisite 30B® and Cloisite 15A®, the chemical structures of which are given in Table 2. The XRD patterns, given in Fig. 52, indicate
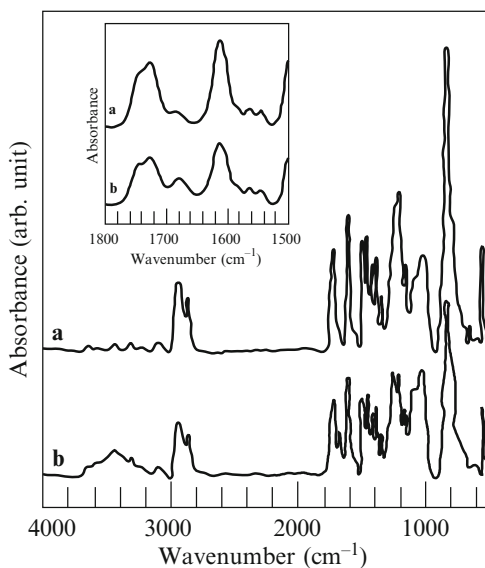
Fig. 51 FTIR spectra for (**a**) PTBP-Ru-6TPy and (**b**) (PTBP-Ru-6TPy)/MMT nanocomposite. The *inset* shows the expanded absorption band at wavenumbers ranging from 1,500 to $1,800 \, cm^{-1}$. (Reprinted from Huang and Han [75]. Copyright 2006, with permission from the American Chemical Society)
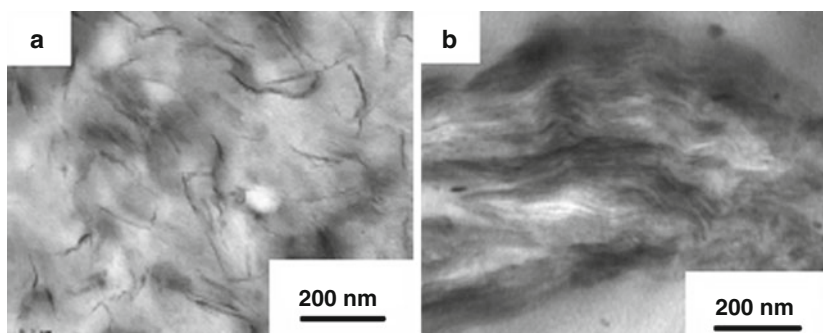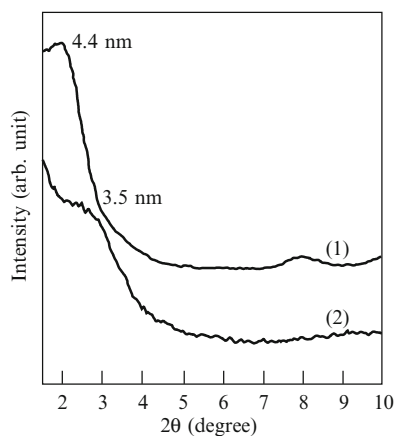
Fig. 53 TEM images of (**a**) (PTBP-Ru-6TPy)/Cloisite 30B® nanocomposite and (**b**) (PTBP-Ru-6TPy)/Cloisite 15A® nanocomposites. (Reprinted from Huang and Han [75]. Copyright 2006, with permission from the American Chemical Society)

that the d-spacing of Cloisite 30B® aggregates in the (PTBP-Ru-6TPy)/Cloisite 30B® nanocomposite has only increased from 1.85 to 4.4 nm, and the d-spacing of Cloisite 15A® aggregates in the (PTBP-Ru-6TPy)/Cloisite 15A® nanocomposite has only slightly increased from 3.15 to 3.5 nm. Note that Fig. 6 shows d-spacing of Cloisite 30B® and Cloisite 15A®, respectively. Correspondingly, the (PTBP-Ru-6TPy)/Cloisite 30B® nanocomposite has a flocculated dispersion, while (PTBP-Ru-6TPy)/Cloisite 15A® nanocomposite exhibits an intercalated structure, as can be observed from the TEM images given in Fig. 53. This observation suggests that the chance of direct interactions between the positively charged ruthenium center and the negatively charged MMT surfaces has been largely diminished, because of the shielding effect of the positively charged surfactants. It should be mentioned that the (PTBP-Ru-6TPy)/Cloisite 30B® and (PTBP-Ru-6TPy)/Cloisite 15A® nanocomposites were prepared by a simple mixing process.

In conclusion, here I have presented an experimental observation, in which the ruthenium(II) complex in a functional liquid-crystalline polymer has exfoliated pristine MMT aggregates through the Coulombic interactions between the positively charged ruthenium center and the negatively charged MMT surfaces. This observation provides a new concept for molecular design to achieve a very high degree of dispersion of the aggregates of natural clay in a polymer matrix without the need to treat the natural clay with surfactant, and may pave a new way for preparing nanocomposites based on natural clay.

7 Concluding Remarks

In this chapter I have reviewed some experimental results of highly dispersed (nearly exfoliated) nanocomposites, prepared by mixing, based on thermoplastic polymers, block copolymers, and liquid-crystalline polymers. In this chapter I have presented the experimental results mostly from my own publications during the past 5 years, because I know very well how the experimental results were obtained and I have confidence in the accuracy of the experimental results. This does not imply that the experimental results reported in the literature by other investigators are less important than mine. However, the readers are reminded that the primary objective of this chapter is to summarize the importance (or necessity) of having strong attractive interactions, via specific interaction, between the polymer matrix and the surface of clay, pristine or chemically modified, in order to obtain exfoliated nanocomposites.

In the majority of situations when thermoplastic nanocomposites are prepared, chemically modified clays, instead of pristine clay, are used to obtain exfoliated nanocomposites. This is because many commercial polymers do not have functional groups. In this chapter I have presented an example of a nanocomposite based on a ruthenium metal complex formed with a liquid-crystalline polymer having a side-chain terpyridine group, which exhibits exfoliation, via Coulombic interaction, when pristine clay was employed. In other words, chemical modification of the clay is not always necessary when the polymer matrix has a certain chemical structure that would form specific interaction with pristine clay. Along this line of logic, here I present, at least conceptually, another example of preparing exfoliated nanocomposites, by mixing a thermoplastic polymer and pristine clay. Namely, since the surface of pristine clay has negatively charged ions, any ionomers having positively charged ions would have ionic interactions with pristine clay, thus yielding highly dispersed (nearly exfoliated) nanocomposites. This concept suggests that the introduction of cations into a thermoplastic polymer would be a very effective method of preparing highly dispersed (nearly exfoliated) nanocomposites with pristine clay. The readers are reminded that among the several specific interactions, ionic interactions have the highest bond energy.

An important issue that must be addressed in future research efforts on the preparation of exfoliated nanocomposites is mathematical modeling. Within the spirit of this chapter that deals with how exfoliation of nanocomposites can be achieved,

there are two aspects of mathematical modeling that are needed. One aspect of mathematical modeling is to be able to predict the conditions, chemical or physical, which would lead to exfoliation of the aggregates of layered silicates without or with chemical modifications. This area of mathematical modeling, when successful, will be extremely helpful in selecting, without resorting to a trial-end-error approach, the appropriate chemical structures of surfactant and/or polymer matrix for a specifically targeted nanocomposite, hence minimizing time and money that would otherwise be wasted. Another aspect of mathematical modeling is to be able to predict the rheological and/or mechanical properties of exfoliated nanocomposites based on layered silicates without or with chemical modifications. Since it has been amply demonstrated in this chapter that strong attractive interaction is necessary to achieve, during mixing, exfoliation of the aggregates of layered silicate, the mathematical modeling effort must include specific interaction (e.g., ionic interaction; hydrogen bonding; ion–dipole interaction; Coulombic interaction). In this regard, a mathematical exercise that does not include specific interaction in modeling the rheological and/or mechanical properties of exfoliated nanocomposites must be avoided. Use of simple modification of existing constitutive equations that are based on continuum approach would not be able to yield meaningful results predicting accurately the rheological and/or mechanical properties of exfoliated nanocomposites. Further, I hasten to point out that layered silicates commonly used in the preparation of exfoliated nanocomposites are not spherical or ellipsoidal particles; rather they are platelets having the thickness of about 1 nm and a very large aspect ratio (about 100). I think that a simplification of the geometry of layered silicates, strictly for mathematical convenience, with spherical or ellipsoidal particles is grossly inaccurate! Granted the problems at hand are not trivial, but these are the challenges requiring the ingenuity and creativity of future researchers.

References

1. Ray SS, Okamoto M (2003) Polymer/layered silicate nanocomposites: a review from preparation to processing. Prog Polym Sci 28:1539–1641
2. Kojima Y, Usuki A, Kawasumi M, Okada A, Kurauchi T, Kamigaito O (1993) Synthesis of nylon 6-clay hybrid by montmorillonite intercalated with ε-caprolactam. J Polym Sci Polym Chem Ed 31:983–986
3. Usuki A, Kawasumi M, Kojima Y, Fukushima Y, Okada A, Kurauchi T, Kamigaito O (1993) Swelling behavior of montmorillonite cation exchanged for ω-amino acids by ε-caprolactam. J Mater Res 8:1174–1178
4. Maiti P, Okamoto M (2003) Crystallization controlled by silicate surfaces in nylon 6-clay nanocomposites. Macromol Mater Eng 288:440–445
5. Choi S, Lee KM, Han CD (2004) Effects of triblock copolymer architecture and the degree of functionalization on the organoclay dispersion and rheology of nanocomposites. Macromolecules 37:7649–7662

6. Lee KM, Han CD (2003) Linear dynamic viscoelastic properties of functionalized block copolymer/organoclay nanocomposites. Macromolecules 36:804–815
7. Zha W, Han CD, Han SH, Lee DH, Kim JK, Guo M, Rinaldi PL (2009) Ion–dipole interactions in the dispersion of organoclay nanocomposites based on polystyrene-*block*-poly(2-vinylpyridine) copolymer. Polymer 50:2411–2423
8. Galgali G, Ramesh C, Lele A (2001) A rheological study on the kinetics of hybrid formation in polypropylene nanocomposites. Macromolecules 34:852–858
9. Kawasumi M, Hasegawa N, Kato M, Usuki A, Okada A (1997) Preparation and mechanical properties of polypropylene-clay hybrids. Macromolecules 30:6333–6338
10. Nam PH, Maiti P, Okamoto M, Kotaka T, Hasegawa N, Usuki A (2001) A hierarchical structure and properties of intercalated polypropylene/clay nanocomposites. Polymer 42:9633–9640
11. Reichert P, Hoffmann B, Bock T, Thomann R, Mülhaupt R, Fredrich C (2001) Morphological stability of polypropylene nanocomposites. Macromol Rapid Commun 22:519–523
12. Solomon MJ, Almusallam AS, Seefeldt KF, Somwangthanaroj A, Varadan P (2001) Rheology of polypropylene/clay hybrid materials. Macromolecules 34:1864–1872
13. Han CD (2007) Rheology and processing polymeric materials. Vol 2: Polymer processing Oxford University Press, New York, chap 4
14. Akelah A, Moet A (1996) Polymer-clay nanocomposites: free-radical grafting of polystyrene on to organophilic montmorillonite interlayers. J Mater Sci 31:3589–3596
15. Heinemann J, Reichert P, Thomson R, Mülhaupt R (1999) Polyolefin nanocomposites formed by melt compounding and transition metal catalyzed ethene homo- and copolymerization in the presence of layered silicates. Macromol Rapid Commun 20:423–430
16. Hoffmann B, Kressler J, Stöpelmann G, Friedrich C, Kim GM (2000) Rheology of nanocomposites based on layered silicates and polyamide-12. Colloid Polym Sci 278:629–639
17. Messersmith PB, Giannelis EP (1995) Synthesis and barrier properties of poly(ε–caprolactone)-layered silicate nanocomposites. J Polym Sci Polym Chem Ed 33:1047–1057
18. Yano K, Usuki A, Okada A, Kurauchi T, Kamigaito O (1993) Synthesis and properties of polyimide-clay hybrid. J Polym Sci Polym Chem Ed 31:2493–2498
19. Vaia RA, Giannelis EP (1997) Lattice model of polymer melt intercalation in organically-modified layered silicates. Macromolecules 30:7990–7999
20. Balazs AC, Singh C, Zhulina E (1998) Modeling the intercalations between polymers and clay surface through self-consistent field theory. Macromolecules 31:8370–8381
21. Lee JY, Baljon ARC, Sogan DY, Loring RF (2000) Molecular dynamics study of the intercalation of diblock copolymers into layered silicates. J Chem Phys 112:9112–9119
22. Bird RB, Curtiss CF, Armstrong RC, Hassager O (1987) Dynamics of polymeric liquids. Vol 2: Kinetic theory, 2nd edn. Wiley, New York
23. Grest GS, Lacasse MD, Kremer K, Gupta AM (1996) Efficient continuum model for simulating polymer blends and copolymers. J Chem Phys 105:10583–10594
24. Murat M, Grest GS, Kremer K (1999) Statics and dynamics of symmetric diblock copolymers: a molecular dynamics simulation. Macromolecules 32:595–609
25. Israelachvili JN (1991) Intermolecular and surface forces, 2nd edn. Academic, New York
26. Yang Z, Han CD (2008) Rheology of miscible polymer blends with hydrogen bonding. Macromolecules 41:2104–2118
27. Bennett RH, Hulber MH (1986) Clay microstructure. International Human Resources Development, Boston
28. Grim RE (1968) Clay minerology, 2nd edn. McGraw Hill, New York
29. Theng BK (1974) The chemistry of clay-organic reactions. Wiley, New York
30. van Olphen H (1977) Clay colloid chemistry, 2nd edn. Wiley, New York
31. Lee KM, Han CD (2003) Rheology of organoclay nanocomposites: effects of polymer matrix/organoclay compatibility and the gallery distance of organoclay. Macromolecules 36:7165–7178
32. Brown HC (1962) Hydroboration. Benjamin, New York
33. Chung TC, Raate M, Berluche E, Schulz DN (1988) Synthesis of functional hydrocarbon polymer with well-defined molecular structures. Macromolecules 21:1903–1907

34. Lee KM, Han CD (2002) Order-disorder transition induced by the hydroxylation of homoge-neous polystyrene-*block*-polyisoprene copolymer. Macromolecules 35:760–769
35. Jeon HS, Rameshwaram JK, Kim G, Weinkauf DH (2003) Characterization of polyisoprene-clay nanocomposites prepared by solution blending. Polymer 44:5749–5758
36. Koopmans RJ, van der Linden R, Vansant EF (1980) The characterization of newly developed and promising hydrolyzed ethylene vinyl acetate copolymers. J Adhesion 11:191–202
37. Coleman MM, Graf JF, Painter PC (1991) Specific interactions and the miscibility of polymer blends. Technomic, Lancaster, Pennsylvania
38. Alexandre M, Beyer G, Henrist C, Cloots R, Rulmont A, Jérôme R, Dubois P (2001) Prepa-ration and properties of layered silicate nanocomposites based on ethylene vinyl acetate copolymers. Macromol Rapid Commun 22:643–646
39. Alexandre M, Beyer G, Henrist C, Cloots R, Rulmont A, Jérôme R, Dubois P (2001) One-pot preparation of polymer/clay nanocomposites starting from Na$^+$ montmorillonite. 1. Intercala-tion of ethylene-vinyl acetate polymer. Chem Mater 13:3830–3832
40. Gelfer MY, Burger C, Chu B, Hsiao BS, Drozdov AD, Si M, Rafailovich M, Sauer BB, Gilman JW (2005) Relationships between structure and rheology in model nanocomposites of ethylene-vinyl based copolymers and organoclays. Macromolecules 38:3765–3775
41. Lee KM, Han CD (2003) Effect of hydrogen bonding on the rheology of polycarbon-ate/organoclay nanocomposites. Polymer 44:4573–4588
42. Painter PC, Coleman MM (1997) Fundamentals of polymer science, 2nd edn. Technomic, Lancaster, Pennsylvania
43. Abbate M, Martuschelli E, Musto P, Ragosta G, Scarinzi G (1984) Toughening of a highly cross-linked epoxy resin by reactive blending with bisphenol A polycarbonate. I. FTIR spec-troscopy. J Polym Sci Polym Phys Ed 32:395–408
44. Yoon PJ, Hunter DL, Paul DR (2003) Polycarbonate nanocomposites. Part 1. Effect of organ-oclay structure on morphology and properties. Polymer 44:5323–5339
45. Chen H, Schmidt DF, Pitsikalis M, Hadjichristidis N, Zhang Y, Wiesner U, Giannelis IP (2003) Poly(styrene-*block*-isoprene) nanocomposites: kinetics of intercalation and effects of copoly-mer on intercalation behavior. J Polym Sci Polym Phys Ed 41:3264–3271
46. Mitchell CA, Krishnamoorti R (2002) Rheological properties of diblock copolymer/layered-silicate nanocomposites. J Polym Sci Polym Phys Ed 40:1434–1443
47. Ren J, Silva AS, Krishnamoorti R (2000) Linear viscoelasticity of disordered polystyrene-polyisoprene block copolymer based on layered-silicate nanocomposites. Macromolecules 33:3739–3746
48. Ren J, Krishnamoorti R (2003) Nonlinear viscoelastic properties of layered-silicate-based in-tercalated nanocomposites. Macromolecules 36:4443–4451
49. Ha YH, Thomas EL (2002) Deformation behavior of a roll-cast layered-silicate/lamellar tri-block copolymer nanocomposite. Macromolecules 35:4419–4428
50. Liao M, Zhu J, Xu H, Li Y, Shan W (2004) Preparation and structure and mechanical properties of poly(styrene-*block*-butadiene)/clay nanocomposites. J Appl Polym Sci 92:3430–3434
51. Silva AS, Mitchell CA, Tse MF, Wang HC, Krishnamoorti R (2001) Templating of cylin-drical and spherical block copolymer microdomains by layered silicates. J Chem Phys 115:7166–7174
52. Krishnamoorti R, Silva AS, Mitchell CA (2001) Effect of silicate layer anisotropy on cylin-drical and spherical microdomain ordering in block copolymer nanocomposites. J Chem Phys 115:7175–7181
53. Hasegawa N, Usuki A (2003) Arranged microdomain structures induced by clay silicate layers in block copolymer-clay nanocomposites. Polym Bull 51:77–83
54. Ha YH, Kwon Y, Breiner T, Chan EP, Tzianetopoulou T, Cohen RE, Boyce MC, Thomas EL (2005) An orientationally ordered hierarchical exfoliated clay-block copolymer nanocompos-ite. Macromolecule 38:5170–5179
55. Zha W, Choi S, Lee KM, Han CD (2005) Dispersion characteristics of organoclay in nanocom-posites based on end-functionalized homopolymer and block copolymer. Macromolecules 38:8418–8429

56. Zhao H, Shipp DA (2003) Preparation of poly(styrene-butylacrylate) block copolymer-silicate nanocomoposites. Chem Mater 15:2693–2695
57. Di J, Sogah DY (2006) Intergallery living polymerization using silicate-anchored photoinifer-ter: a versatile preparatory method for exfoliated silicate nanocomposites. Macromolecules 39:1020–1028
58. Huang W, Han CD (2006) Dispersion characteristics and rheology of organoclay nanocomposites based on a segmented main-chain liquid-crystalline polymer having pendent pyridyl group. Macromolecules 39:257–267
59. Huang W, Han CD (2006) Dispersion characteristics and rheology of organoclay nanocomposites based on a segmented main-chain liquid crystalline polymer having side-chain azopyridine with flexible spacers. Polymer 47:4400–4410
60. Sato A, Kato T, Uryu T (1996) Hydrogen-bonded liquid-crystalline polymer blends formed from a thermotropic polyester containing a lateral pyridyl groups and poly(4-vinylphenol). J Polym Sci Polym Chem Ed 34:503–505
61. Vaia RA, Giannelis EP (2001) Liquid crystal polymer nanocomposites: direct intercalation of thermotropic liquid crystalline polymers into layered silicates. Polymer 42:1281–1285
62. Chang JH, Seo BS, Hwang SH (2002) An exfoliation of organoclay in thermotropic liquid crystalline polyester nanocomposite. Polymer 43:2969–2974
63. Tachino H, Hara H, Hirasawa E, Kutsumizu S, Yano S (1994) Structure and properties of ethylene ionomers neutralized with binary metal cations. Macromolecules 27:372–378
64. Kutsumizu S, Hara H, Tachino H, Shimabayashi K, Yano S (1999) Infrared spectroscopic study of the binary blends of sodium and zinc salt ionomers produced from poly(ethylene-*co*-methacrylic acid). Macromolecules 32:6340–6347
65. Beyer FL, Beck Tan NC, Dasgupta A, Galvin ME (2002) Polymer-layered silicate nanocomposites from model surfactants. Chem Mater 14:2983–2988
66. Hoffmann B, Dietrich C, Thomann R, Friedrich C, Mülhaupt R (2000) Morphology and rheology of polystyrene nanocomposites based upon organoclay. Macromol Rapid Commun 21:57–61
67. Lim YT, Park OO (2001) Phase morphology and rheological behavior of polymer/layered silicate nanocomposites. Rheol Acta 40:220–229
68. Sikka M, Cerini LN, Ghosh SS, Winey KI (1996) Melt intercalation of polystyrene in layered silicate. J Polym Sci Polym Phys Ed 34:1443–1449
69. Vaia RA, Ishii H, Giannelis EP (1993) Synthesis and properties of two-dimensional nanostructures by direct intercalation of polymer matrix in layered silicates. Chem Mater 5:1694–1696
70. Vaia RA, Giannelis EP (1997) Polymer melt intercalation in organically modified layered silicates: model prediction and experiment. Macromolecules 30:8000–8008
71. Wang ZM, Nakajima H, Manias E, Chung T (2003) Exfoliated PP/clay nanocomposites using ammonium terminated PP as the organic modification for montmorillonite. Macromolecules 36:8919–8922
72. Sakamoto N, Hashimoto T (1998) Ordering dynamics of a symmetric polystyrene-block-polyisoprene. 1. Ordering mechanism from the disordered state. Macromolecules 31:3292–3302
73. Gouinlock EV, Porter RS (1977) Linear dynamic mechanical properties of an SBS block copolymer. Polym Eng Sci 17:535–543
74. Choi S, Han CD (2003) Phase transition in end-functionalized polystyrene-*block*-polyisoprene-*block*-polystyrene copolymers. Macromolecules 36:6220–6228
75. Huang W, Han CD (2006) Ruthenium(II) complex-induced dispersion of montmorillonite in a segmented main-chain liquid-crystalline polymer having side-chain terpyridine group. Macromolecules 39:8207–8209
76. Joshi V, Kotkar D, Ghosh PK (1986) On the interaction of poly(pyridine)ruthenium (II) optical antipodes intercalated in montmorillonite clay. J Am Chem Soc 108:4650–4651
77. Schoonheydt RA, Pauw PD, Vliers D, Schrijver FCD (1984) Luminescence of tris(2,2′-bispyridine) ruthenium(II) in aqueous clay minerals suspensions. J Phys Chem 88:5113–5118

Editor: K.-S. Lee

Phase Behavior and Phase Transitions in AB- and ABA-type Microphase-Separated Block Copolymers

Jin Kon Kim and Chang Dae Han

Abstract Currently held mean-field theories for microphase-separation in AB-type diblock and ABA-type triblock copolymers are reviewed and their limitations are highlighted. Numerical predictions, based on these theories, for the design of such block copolymers are also presented. It is emphasized that the use of a numerical algorithm leading to successful design and synthesis of block copolymers in terms of order–disorder transition temperature (T_{ODT}) is critically dependent upon the accuracy of the temperature-dependent interaction parameter. Specifically, the available temperature-dependent interaction parameters are often obtained using the molecular weights which are much lower than the molecular weights of the constituent blocks, in spite of the fact that the interaction parameters are molecular weight dependent. Two as yet unresolved issues, finite molecular weight effect and the phase behavior and phase transitions in highly asymmetric block copolymers, are discussed. These issues are fundamental enough to require a fresh look, particularly from a theoretical point of view, because the currently held mean-field theory cannot explain every conceivable phase behavior and phase transitions experimentally observed in block copolymers.

Keywords Block copolymer · Disordered micelles · Fluctuation effect · Order–disorder transition · Self-consistent mean-field theory

J.K. Kim (✉)
National Creative Research Initiative Center for Block Copolymer Self-Assembly
and Department of Chemical Engineering, Pohang University of Science and Technology,
Pohang, Kyungbuk 790–784, P.O. Box 125 Republic of Korea
email: jkkim@postech.ac.kr

C.D. Han (✉)
Department of Polymer Engineering, The University of Akron, Akron, OH 44325, USA
email: cdhan@uakron.edu

Contents

Abbreviations and Symbols

a_T	Temperature-dependent shift factor
b_k	Kuhn length for component k
B_∞	Equilibrium birefringence
D	Microdomain spacing
DOT	Disorder–order transition
DMT	Demicellization/micellization transition
F–H	Fredrickson–Helfand
ΔG_m	Free energy difference
G'	Dynamic storage modulus
G''	Dynamic loss modulus
H–W	Helfand–Wasserman
$I(q)$	Scattering intensity
k_B	Boltzmann constant
LCDOT	Lower critical disorder–order transition
LDOT	Lattice disorder–order transition

M–O	Mayes–Olvera de la Cruz
n_c^t	Total number of block copolymer chains
N_i	Degree of polymerization for component i
NIA	Narrow interphase approximation
ODT	Order–disorder transition
OOT	Order–order transition
q	Wave vector
$R_{g,k}$	Radius of gyration of component k
SANS	Small-angle neutron scattering
SAXS	Small-angle X-ray scattering
SB	Polystyrene-*block*-polybutadiene
SBS	Polystyrene-*block*-polybutadiene-*block*-polystyrene
SI	Polystyrene-*block*-polyisoprene
SIS	Polystyrene-*block*-polyioprene-*block*-polystyrene
SSL	Strong segregation limit
TEM	Transmission electron microscopy
T_g	Glass transition temperature
T_{DMT}	Demicellization/micellization transition temperature
T_{LDOT}	Lattice disorder–order transition temperature
T_{ODT}	Order–disorder transition temperature
T_{OOT}	Order–order transition temperature
UCODT	Upper critical order–disorder transition
$\bar{v}_{o,k}$	Monomeric molar volume of component k
V_c	Molecular volume of one block copolymer chain
V_{ref}	Molar volume of a reference component
V–W	Vavasour–Whitmore
WSL	Weak segregation limit
W_ξ	Mean-field potential
Z	Partition function
α	Interaction parameter $\left(\mathrm{mol/cm^3}\right)$
χ	Flory–Huggins interaction parameter (dimensionless)
χN	Segregation power
γ	Interfacial tension
φ_i	Local volume fraction of component i
λ_I	Interfacial thickness

1 Introduction

It seems quite appropriate to point out at the beginning of this chapter the correct nomenclature for block copolymers, polyA-*block*-polyB. This nomenclature was recommended by the Commission on Macromolecular Nomenclature of the International Union of Pure and Applied Chemistry, and subsequently the Commission's recommendations entitled Source-Based Nomenclature for Copolymers were published in Pure Applied Chemistry **57**, 1427–1440 (1985). The above nomenclature

makes perfect sense, because a block copolymer consists of two long macro-molecules. During the past two decades, since the publication of the above article, numerous researchers have used the nomenclature, e.g., poly(A-*block*-B), which implies that a block copolymer is formed by the two blocks of monomers *A* and *B*. This does not make sense at all, because two monomers do not form a block. On the other hand, such nomenclature makes perfect sense, as given in the above cited reference, for random copolymers with poly(A–*ran*–B) and for alternating copolymer with poly(A–*alt*–B). We strongly urge that the researchers in the block copolymer community use the correct nomenclature in their future publications.

Since the earliest successful synthesis of block copolymers in seminal investigation of living anionic polymerization by Szwarc [1, 2], diene-based block copolymers, such as polystyrene-*block*-polybutadiene (SB diblock), polystyrene-*block*-polyisoprene (SI diblock), polystyrene-*block*-polybutadiene-*block*-polystyrene (SBS triblock), and polystyrene-*block*-polyisoprene-*block*-polystyrene (SIS triblock) copolymers have been widely used in the thermoplastic elastomer industry due to their unique physical properties not attainable with the constituent homopolymers alone.

Many different molecular structures of block copolymers can be synthesized by anionic polymerization, as shown in Fig. 1. It is well established today that at low temperatures most block copolymers have an ordered equilibrium microdomain structure, which depends on the composition of the block copolymer. As schematically shown in Fig. 2, with increasing amount of *A* block in an AB-type diblock copolymer, the microdomain structure changes from body-centered-cubic (bcc), commonly referred to as spheres, to hexagonally packed cylinders to gyroids to lamellae. Such equilibrium microdomain structures in block copolymers have been confirmed using transmission electron microscopy (TEM) in the 1970s and 1980s by Kawai et al. [3], Sadron and Gallot [4], and Hashimoto et al. [5], and gyroids much later by Hajduk et al. [6]. Theoretical studies by Helfand [7] and Helfand and Wasserman [8–12], Leibler [13], Matsen and Schick [14] confirmed the experimentally observed microdomains.

It should be mentioned that the microdomains in block copolymers are on the order of 10–100 nm, which is smaller than the wavelength of light and makes them
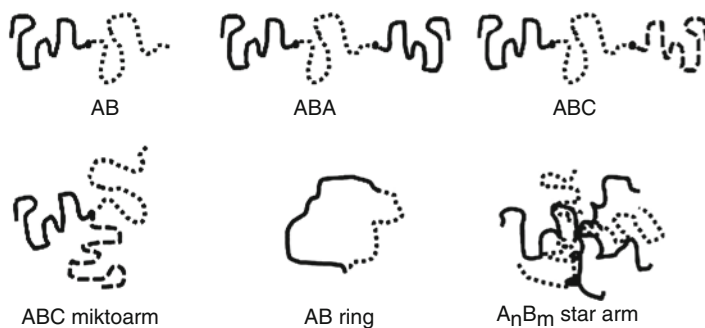
Fig. 1 Schematic describing various molecular architectures of block copolymers
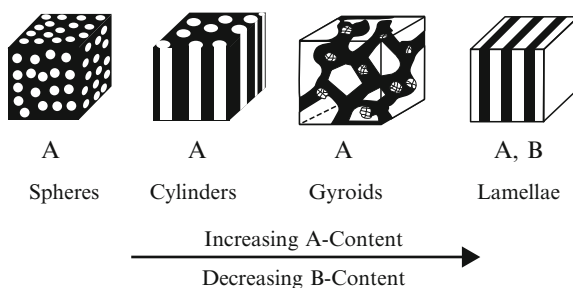
Fig. 2 Schematic describing the composition dependence of the microdomain structures: spheres (S), cylinders (C), gyroids (G), and lamellae (L), in AB-type diblock copolymers. (Reprinted from Han [31]. Copyright © 2007, with permission from Oxford University Press)
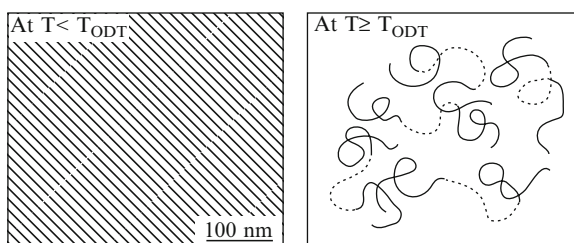
Fig. 3 **a** TEM image of a lamella-forming SIS triblock copolymer at $T < T_{ODT}$. **b** Schematic describing the flexible chains of PS and PI blocks connected in the block copolymer when it is heated to the disordered state at $T \geq T_{ODT}$. (Reprinted from Han [31]. Copyright © 2007, with permission from Oxford University Press)

look transparent to the naked eye. In contrast, the phase separated domain size of polymer blends is on the order of micrometers, which is larger than the wavelength of light and makes them appear opaque. As the temperature is raised above a certain critical value, commonly referred to as the order–disorder transition (ODT) temperature (T_{ODT}), the microdomains in a block copolymer disappear completely, giving rise to the disordered phase, as schematically shown in Fig. 3. During the past three decades numerous research groups have reported on such experimental observations and there are too many references to cite them here. Below we will cite some representative studies when we summarize experimental methods for determining the T_{ODT} of block copolymers.

From a rheological point of view, microphase-separated block copolymers (i.e., at temperatures below T_{ODT}) have very high viscosities and they behave very much like particulate filled molten polymers or vulcanized rubbers. However, as the temperature is increased above T_{ODT}, block copolymers behave like many ordinary molten homopolymers. In this regard, T_{ODT} can be regarded as being a very important processing variable. It should be mentioned that, while the majority of the literature reported on the phase transition in block copolymers exhibiting the upper critical solution temperature (UCST) behavior with increasing temperature,

some investigators [15–22] reported on the phase transition in block copolymers exhibiting lower critical solution temperature (LCST) behavior with increasing temperature, giving rise to disorder–order transition (DOT) temperature (T_{DOT}). Precisely stated, the phase transition in the former-type block copolymers should be referred to as upper critical order–disorder transition (UCODT) and the phase transition in the latter-type block copolymers should be referred to as lower critical disorder–order transition (LCDOT). In this chapter we only discuss the phase behavior and phase transition in block copolymers exhibiting UCODT and thus, for simplicity, we will use the nomenclatures ODT and T_{ODT}.

From a theoretical point of view, T_{ODT} is related to the microdomain structure of a block copolymer and it is a fundamental thermorheological parameter that is of interest to equilibrium and non-equilibrium statistical physics in the condensed state. In order to predict the T_{ODT} of a block copolymer, theories developed for the cooperative phenomena in atomic or small molecular systems have to be generalized to take into account properly the connectivity between similar and dissimilar monomer units, i.e., the connectivity of monomers A in block A (or monomers B in block B) sequences and the connectivity between the sequences A and B at their ends. The T_{ODT} of a block copolymer depends, among many factors, on the extent of miscibility between the constituent blocks, block molecular weights, and block composition. In the past, several research groups [8–14, 23–27] developed theories to investigate ODT and microdomain structures of block copolymers, which many experimental studies were able to confirm using small-angle X-ray scattering (SAXS), small-angle neutron scattering (SANS), rheology, and/or TEM. There are too many papers to cite them all here. The interested readers are referred to earlier review articles [28, 29] and monographs by Hamley [30] and Han [31].

A theory which can predict the T_{ODT} of a block copolymer accurately is of particular importance to be able to design block copolymers as an effective compatibilizing agent for two immiscible homopolymers or random copolymers [32]. This chapter is motivated primarily by the desire to present currently held mean-field theories of block copolymers from the point of view of molecular design and then to compare theory with experiment. In so doing, we will critically review the literature and highlight the area in need of greater attention from experimentalists who wish to use currently held mean-field theories of block copolymers. The organization of this chapter is as follows. We will first summarize currently held theories of block copolymers in the literature: (1) self-consistent mean-field theory of Helfand and Wasserman [8–12], (2) mean-field theory of Leibler [13] who used random phase approximation, (3) fluctuation correction of the Leibler theory by Fredrickson and Helfand [33], (4) self-consistent mean-field theory of Vavasour and Whitmore [26, 27], and (5) self-consistent mean-field theory of Matsen and Schick [14]. Next, we will summarize (1) experimental methods for investigating the phase behavior and phase transitions in microphase-separated block copolymers, and (2) some as yet unresolved issues on the phase behavior and phase transitions in microphase-separated block copolymers.

2 Theory of Microphase-Separation Transition in AB- and ABA-Type Block Copolymers

The T_{ODT} depends on the volume fraction of one block (f), the degree of polymerization (N), the segmental interaction described by the Flory–Huggins interaction parameter (χ), and the conformational asymmetry of each block. Based on the segregation power (χN), in the literature two cases are emphasized: strong segregation limit (SSL) $(\chi N \gg 10)$ and weak segregation limit (WSL) $(\chi N \sim 10)$. The free energy difference (ΔG_m) between the ordered state (microphase-separated state) and disordered (homogeneous) state in a block copolymer is expressed by enthalpic (ΔH_m) and entropic (ΔS_m) terms [34]:

$$\Delta G_m = G_{micro} - G_{homo} = \Delta H_m - T\Delta S_m \tag{1}$$

where G_{micro} and G_{homo} are the free energies of a block copolymer in the microphase-separated state and in the homogeneous state, respectively, and T is the absolute temperature. The T_{ODT} is defined by the temperature at which ΔG_m in (1) is equal to zero. At a given temperature, a block copolymer is in the homogeneous state when $\Delta G_m > 0$, while it is in the microphase-separated state when $\Delta G_m < 0$.

ΔH_m and ΔS_m in (1) are given by

$$\Delta H_m = H_{int} - H_{homo} \tag{2a}$$
$$\Delta S_m = \Delta S_c + \Delta S_p \tag{2b}$$

Here, H_{int} is the unfavorable interaction arising from the presence of two incompatible blocks at the interface and it is proportional to the interfacial thickness (λ_I). Thus, H_{int} decreases with increase in segregation power χN (or the microdomain spacing D) because of the decrease in λ_I. On the other hand, H_{homo} is the enthalpic penalty in the homogeneous state where two immiscible blocks coexist. Under such a situation, because the unfavorable interaction between two blocks is expected to exist in the entire volume, H_{homo} is proportional to the size of the microdomains. Since $D > \lambda_I$, a positive value of H_{homo} becomes larger than H_{int}. Therefore, ΔH_m is always negative. Namely, from the enthalpic point of view, a microphase-separated state is always preferred to the disordered state.

However, the negative contribution of ΔH_m to ΔG_m is counterbalanced by the increase of two negative entropic terms [34]. (1) One is the confinement entropy loss (ΔS_c) resulting from the chains of each block being located at its own microdomain with stretched conformation. Since the number of the maximum allowable block chain conformations in the microdomain should be smaller than that in the ideal Gaussian chain in the homogeneous state due to the extended coils, we have $\Delta S_c < 0$. (2) The other is the placement entropy loss (ΔS_p), due to the block junction being located at the interfacial region of the two blocks. This term also becomes negative (i.e., $\Delta S_p < 0$), since in the homogeneous state the junction point should be located anywhere within the microdomains. According to (2b), these two terms make

$\Delta S_m < 0$ and hence the entropy penalty term, $-T\Delta S_m$, appearing on the right-hand side of (1), becomes dominant over the negative value of the enthalpy terms, ΔH_m; thus ΔG_m becomes positive with increasing temperature. Under such circumstances, the disordered state is favored. On the other hand, ΔG_m will become negative with decreasing temperature due to the smaller positive value of $-T\Delta S_m$; thus the ordered state will be preferred. Below we summarize the currently held mean-field theories, which describe the phase behavior and phase transitions in microphase-separated block copolymer.

2.1 Self-Consistent Mean-Field Theory of Helfand and Wasserman

A self-consistent mean-field theory was developed by Helfand and Wasserman [8–12], who used a statistical thermodynamic approach by taking into account the incompressibility constraint. They formulated a modified diffusion equation

$$\frac{\partial Q_k(\mathbf{r},t|\mathbf{r}_o)}{\partial t} = \frac{b_k^2}{6}\nabla^2 Q_k(\mathbf{r},t|\mathbf{r}_o) - \{\chi[\varphi_{k'}(\mathbf{r})]^2 + W_\xi(\mathbf{r})\}Q_k(\mathbf{r},t|\mathbf{r}_o) \quad (3)$$

in terms of $Q_k(\mathbf{r},t;\mathbf{r}_o)$, which is proportional to the probability of the density of block k of t repeat units with one end at $\mathbf{r}_o$ and the other end at $\mathbf{r}$. In (3), b_k is the Kuhn length for component k with $k' = B$ when $k = A$ and $k' = A$ when $k = B$, $\varphi_{k'}(\mathbf{r})$ denotes the local volume fraction, and $W_\xi(\mathbf{r})$ is the mean-field potential given by

$$W_\xi(\mathbf{r}) = \frac{\varphi_A(\mathbf{r}) + \varphi_B(\mathbf{r}) - 1}{\kappa k_B T} \quad (4)$$

in which κ is the compressibility of the block copolymer, which approaches zero for an incompressible polymeric melt. Then, for $\kappa \to 0$, $\varphi_A(\mathbf{r}) + \varphi_B(\mathbf{r})$ must be unity to have a finite value of $W_\xi(\mathbf{r})$ which satisfies $\int W_\xi(\mathbf{r})d\mathbf{r} = 0$. The boundary and initial conditions, respectively, for (3) are given by

$$\left.\frac{\partial Q_k(\mathbf{r},t|\mathbf{r}_o)}{\partial \mathbf{r}}\right|_{r=D/2} = 0 \quad (5)$$

$$Q_k(\mathbf{r},0;\mathbf{r}_o) = \delta(\mathbf{r} - \mathbf{r}_o) \quad (6)$$

Once $Q_k(\mathbf{r},t;\mathbf{r}_o)$ is calculated from the solution of (3)–(6), the interfacial concentration profiles of components A and B, $\varphi_A(\mathbf{r})$ and $\varphi_B(\mathbf{r})$, can be determined from the following expression [8–12]:

$$\varphi_k(\mathbf{r}) = \frac{n_c^t}{VQ_c}\int_0^{N_k} dt \int_V d\mathbf{r}_k d\mathbf{r}_J d\mathbf{r}_{k'} Q_k(\mathbf{r}_k,N_k-t|\mathbf{r})Q_k(\mathbf{r},t|\mathbf{r}_J)Q_{k'}(\mathbf{r}_J,N_{k'}|\mathbf{r}_{k'}) \quad (7)$$

where n_c^t is the total number of block copolymer chains, N_k is the degree of poly-merization for component k ($k = $ A, B) and V is the volume of the system given by $n_c^t V_c$ (in which V_c is the molecular volume of one block copolymer chain), and Q_c is given by

$$Q_c = \frac{1}{V} \int_V dr_A dr_J dr_B Q_A (r_A, N_A | r_J) Q_B (r_J, N_B | r_B) \tag{8}$$

in which r_J is the position of the connectivity of block A and block B. Thus, Q_c describes the probability of the density of the AB-type diblock copolymer chain with N_A being the degree of polymerization of block A and N_B being the degree of polymerization of block B, which are covalently bonded, in a unit volume. In order to determine Q_c from (8) we need information on Q_A and Q_B, which requires the solution of (3). However, the solution of (3) in turn requires information on $\varphi_A(r)$ and $\varphi_B(r)$ defined by (7). Thus, one must solve (3) and (7) iteratively, with the aid of (4), for $\varphi_A(r)$, $\varphi_B(r)$, Q_A, and Q_B. Note that $W_\xi(r)$ defined by (4) also depends on as yet undetermined $\varphi_A(r)$ and $\varphi_B(r)$, which must satisfy $\int W_\xi(r) dr = 0$. This type of calculation method is called the "self-consistent method", and the $W_\xi(r)$ thus determined is referred to as the self-consistent mean-field potential.

According to Helfand and Wasserman [8], the free energy difference (ΔG_m) can be expressed as (see Appendix A):

$$\frac{\Delta G_m}{k_B T \, n_c^t} = -\ln Q_c - \frac{1}{n_c^t} \int dr W_\xi(r) - \frac{\alpha (N_A \bar{v}_{0A})(N_B \bar{v}_{0B})}{[(N_A \bar{v}_{0A}) + (N_B \bar{v}_{0B})]} \tag{9}$$

where $\alpha = \chi / V_{\text{ref}}$ in which V_{ref} is the molar volume of a reference component and $\bar{v}_{0,k}$ is the monomeric molar volume of component k. Note that the last term in (9) describes the Flory–Huggins interaction energy density for the homogeneous state.

In principle, Q_c appearing in (9) must be obtained from the solution of (8). Owing to the practical difficulty Helfand and Wasserman [8] had in calculating Q_c rigor-ously from (9), they applied the 'Narrow Interphase Approximation' (NIA) method to calculate Q_c. Note that the NIA method is only valid for the situations where the interfacial thickness λ_I between block A and block B is very small compared to the domain spacing D, i.e., $\lambda_I/D \ll 1$. Specifically, in place of (9), based on the NIA method Helfand and Wasserman employed the following expression to calculate Q_c:

$$Q_c \approx \frac{1}{V} \int_V dr_A dr_J Q_A (r_A, N_A | r_J) \times \frac{1}{V} \int_V dr_B dr_J Q_B (r_B, N_B | r_J) \times$$
$$\times \frac{1}{V} \int_V dr_J dr_A dr_B Q_A (r_J, N_A | r_A) Q_B (r_J, N_B | r_B) = Q_A Q_B Q_I \tag{10}$$

Namely, Q_c is divided into three parts: Q_A and Q_B describing the probabilities of the densities of the chains of block A and block B, in a unit volume, and Q_I describing the probability of the density of the junction point of the block copolymer in a unit volume. Applying NIA to the lamellar microdomains having the domain spacing of D, Helfand and Wasserman obtained the following expression for Q_I:

$$
\begin{aligned}
Q_I &= \frac{1}{V} \int_V \mathrm{d}\mathbf{r}_J \mathrm{d}\mathbf{r}_A \mathrm{d}\mathbf{r}_B Q_A^I \left(\mathbf{r}_J, N_A | \mathbf{r}_A \right) Q_B^I \left(\mathbf{r}_J, N_B | \mathbf{r}_B \right) \\
&= \frac{1}{(D/2)} \int_{-D/4}^{D/4} \mathrm{d}x_J q_A^I \left(x_J, N_A \right) q_B^I \left(x_J, N_A \right) \\
&= \frac{a_J}{D/2}
\end{aligned}
\tag{11}
$$

in which $Q_A^I \left(\mathbf{r}_j, N_A | \mathbf{r}_A \right)$ and $Q_B^I \left(\mathbf{r}_j, N_B | \mathbf{r}_B \right)$ appearing in the first term of (11) are replaced by

$$
q_k^I \left(x_J, N_k \right) = \int \mathrm{d}x_0 Q_k \left(x_J, N_k | x_0 \right)
\tag{12}
$$

and superscript I denotes that the parameters are obtained using NIA. It should be mentioned that the representation given by (12) is tantamount to the assumption that the interphase is composed of a randomly distributed mixture of two homopolymers A and B. Under such a scenario, $q_k^I \left(x_J, N_k \right)$ defined by (12) becomes independent of N_k as the molecular weights of homopolymers A and B become very large and they are given by [8]

$$
q_k^I \left(x_J, N_k \right) = q_k^I \left(x_J \right) = \left[1 + \exp \left[2 \left(6\chi \right)^{1/2} x_J / b_k \right) \right]^{-1/2} = q_{k'}^I \left(-x_J \right)
\tag{13}
$$

For $b_A = b_B = b$, the substitution of (13) into (11) gives

$$
a_J = \left(\pi/2 \right) \left(6\chi \right)^{-1/2} b
\tag{14}
$$

in which $\chi = \alpha / V_{\mathrm{ref}}$. Note that the dependence of a_J on b and χ given by (14) is the same as that of the interfacial thickness, $2b \left(6\chi \right)^{-1/2}$, of immiscible blends of two homopolymers A and B [35] with the only difference between the two in the numerical values of the coefficients. Therefore, hereafter we regard a_J as representing the interfacial thickness between block A and block B.

On the other hand, for $\beta_A \neq \beta_B$ with $\beta_k = \left(1/6\bar{v}_{0k} \right)^{1/2} b_k$, a_J is given by [10]

$$
a_J = \beta_G \alpha^{-1/2} E \left(\beta_G / \beta_S \right)
\tag{15}
$$

and E is the elliptic integral of the second kind with β_G and β_S being taken as the larger and the smaller values between β_A and β_B.

Thus, according to (11), Q_I represents the ratio of the interfacial thickness $\left(a_J \right)$ to half of the domain spacing $\left(D/2 \right)$. Note that we used $D/2$, because there is only one interface between block A and block B in $D/2$ (see Fig. 4). The physical meaning of Q_I may be restated as being the ratio of the probability that the junction point of the block copolymer chains is located only at the interface in the microdomains and the probability that the junction point is located anywhere within the entire microdomains. Note that $-\ln Q_I$ corresponds to ΔS_p appearing in (2b), and ΔS_p becomes negative due to $\lambda_I / D \ll 1$ (see (11) and (14)). Note that ΔS_p is the entropy loss due to the confinement of the junction point of block copolymer chains at the interface.
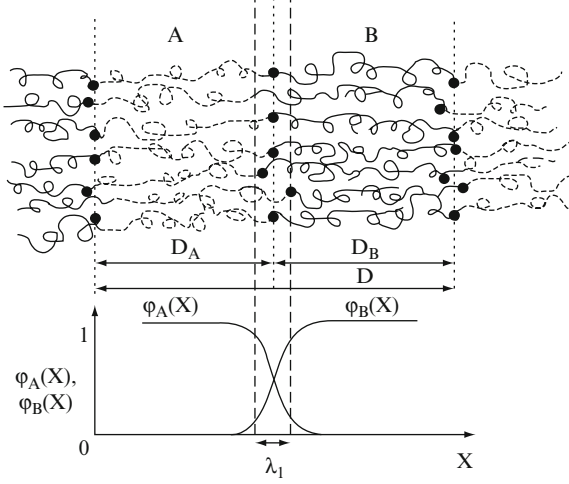
Fig. 4 *The upper panel* describes schematically the chain configuration of an AB-type diblock copolymer, in which D_A and D_B denote the domain widths of block A and block B, respectively, with D being the periodicity distance, and the *lower panel* describes schematically the concentration profiles, in which φ_A and φ_B denote the local concentration profiles for block A and block B, respectively, and λ_I denotes the interphase thickness

Helfand and Wasserman [8] obtained Q_k ($k = A$ or B), via curve fitting, from the following semi-empirical expression:

$$-\ln Q_k = c\left[(D_k/2)/R_{g,k}\right]^m = c\left\{(D_k/2)/\left[\left(b_k N_k^{1/2}\right)/\sqrt{6}\right]\right\}^m \quad (16)$$

in which $R_{g,k}$ is the radius of gyration of the chain for block k, and the relationship for a Gaussian chain, $R_{g,k} = b_k N_k^{1/2}/\sqrt{6}$ is used. Also, c appearing in (16) is a positive numerical constant (0.085 for the lamellar microdomain) and $m = 2.5$ for a block copolymer with lamellar microdomains in the regions where $D_k \leq 2b_k N_k^{1/2}$ is valid. Bates and Fredrickson [28] showed that the exponent m in (16) would be 2.0 if the axis of $D_k/b_k N_k^{1/2}$ is extended to very large values when calculating Q_k. According to (16), $-\ln Q_k$ is proportional to the ratio of half of the domain spacing of block k ($D_k/2$) to the radius of gyration $(R_{g,k})$ of the block k chain in Gaussian conformation. Following (10), we have $-\ln Q_c = -\ln Q_A - \ln Q_B - \ln Q_I$. Above, referring to (11) we have shown that Q_I is proportional to the ratio of the interfacial thickness (a_I) of two blocks to half of the domain spacing $(D/2)$. We regard the term $-\ln Q_I$ appearing in the expression for $-\ln Q_c$ to represent the placement entropy loss (ΔS_p) appearing in (2b). Now, we consider the remaining two terms, $-\ln Q_A$ and $-\ln Q_B$, appearing in the expression for $-\ln Q_c$, to represent the confinement entropy loss (ΔS_c) also appearing in (2b). Thus we conclude that the term $-\ln Q_c$ appearing on the right-hand side of (9) represents the conformational contributions consisting of the placement entropy loss and confinement entropy loss to

the free energy difference (ΔG_m) between the microphase-separated and homogeneous states of an AB-type diblock copolymer. The same argument also applies to ABA-type triblock copolymers [10].

The second term on the right-hand side of (9) is the enthalpy gain due to the presence of the interface, and this term is represented by [8]

$$\frac{\gamma}{k_{\mathrm{B}} T n_{\mathrm{c}}^t} S = -\frac{1}{n_{\mathrm{c}}^t} \int d\mathbf{r} \, W_{\xi}^I(\mathbf{r}) \tag{17}$$

in which γ is the interfacial tension, S is the area of the interface, and $W_{\xi}^I(\mathbf{r})$ is the mean-field potential with NIA. For an AB-type diblock copolymer having $b_A \neq b_B$, $\gamma/k_{\mathrm{B}}T$ appearing on the left-hand side of (17) is given by [36]

$$\frac{\gamma}{k_{\mathrm{B}} T} = \alpha^{1/2} \left\{ \left(\frac{\beta_A + \beta_B}{2} \right) + \frac{1}{6} \frac{(\beta_A - \beta_B)^2}{(\beta_A + \beta_A)} \right\} \tag{18}$$

From (9)–(18), one obtains the following expression (see Appendix B):

$$\frac{\Delta G_m}{k_{\mathrm{B}} T n_{\mathrm{c}}^t} = \frac{2\gamma}{k_{\mathrm{B}} T} (N_A \bar{v}_{0A} + N_B \bar{v}_{0B}) \frac{1}{D} + \ln(D/2a_J) + 0.141$$
$$\times \frac{\left(N_A^{1/2} \bar{v}_{0A}/b_A \right)^{2.5} + \left(N_B^{1/2} \bar{v}_{0B}/b_B \right)^{2.5}}{(N_A \bar{v}_{0A} + N_B \bar{v}_{0B})^{2.5}} D^{2.5} - \frac{\alpha (N_A \bar{v}_{0A}) (N_B \bar{v}_{0B})}{[(N_A \bar{v}_{0A}) + (N_B \bar{v}_{0B})]} \tag{19}$$

in which use was made of the following relationships:

$$S/n_{\mathrm{c}}^t = 2 (N_A \bar{v}_{0A} + N_B \bar{v}_{0B}) / D$$
$$D/ (N_A \bar{v}_{0A} + N_B \bar{v}_{0B}) = D_A/N_A \bar{v}_{0A} = D_B/N_B \bar{v}_{0B} \tag{20}$$

where D_A and D_B are the sizes of lamellar microdomains of block A and block B, respectively. Note that in reference to the right-hand side of (19) the first term describes the surface contribution, the second term describes the joint contribution, and the third term describes the domain contribution to the free energy difference ΔG_{m}.

The equilibrium domain size (D_{eq}) can be obtained by differentiating (19) with respect to D. Since α (or χ) and γ in (19) depend on temperature, one could obtain T_{ODT} of a block copolymer by taking the derivative of ΔG_m with respect to D at $D = D_{\mathrm{eq}}$, at which $[\mathrm{d}(\Delta G_m/k_{\mathrm{B}} T \, n_{\mathrm{c}}^t)/\mathrm{d}D]_{D_{\mathrm{eq}}} = 0$. A block copolymer is in the disordered state at a given temperature when the value of ΔG_m at $D = D_{\mathrm{eq}}$ is larger than zero. In reference to (19), the free energy difference corresponding to the first term (describing the interfacial energy) is inversely proportional to D, the magnitude of the second term (describing the free energy difference of the system due to the entropy loss resulting from the chains located at the interface) increases logarithmically with D, the third term (describing the free energy difference due to the entropy loss resulting from the chain confinements of each block at its own microdomain) is proportional to $D^{2.5}$, and the free energy corresponding to the homogeneous state (the last term) is independent of D.
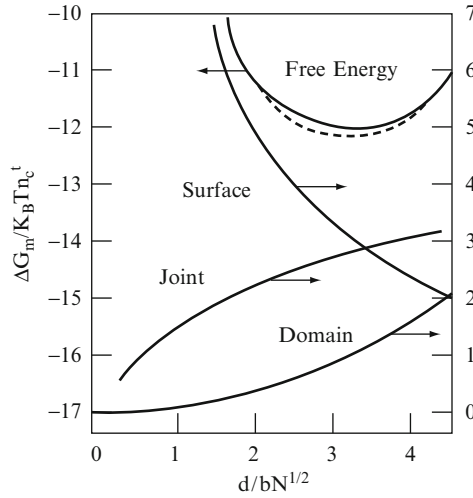
Fig. 5 Free energy per molecule as a function of periodicity distance D for an AB-type diblock copolymer having a χN of 37. On the abscissa D denotes the periodicity distance, b denotes the Kuhn length, and N denotes the degree of polymerization of the block copolymer. The components of the free energy labeled surface, joint, and domain are, respectively, the first three terms on the right-hand side of (19). The *dotted curve* is the prediction without making narrow interphase approximation. (Reprinted from Helfand and Wassermann [8]. Copyright © 1976, with permission from the American Chemical Society)

For $\chi N = 37$, the contribution of each term appearing in (19) is summarized in Fig. 5 [8], and D_{eq} obtained from $[\mathrm{d}\,(\Delta G_m/k_B T n_c^t)\,/\mathrm{d}D]_{D_{eq}} = 0$ for an AB-type diblock copolymer having lamellar microdomains is given by $D_{eq} \cong 3bN^{1/2}$. It should be remembered that the NIA method employed in the derivation of (19) is only valid for large values of χN (e.g., $\chi N \gg 10$). According to Helfand and Wasserman [8], for an AB-type diblock copolymer at $\chi N \sim 10$ the concentration profiles near the interface predicted without NIA are quite different from those predicted with NIA. For a symmetric diblock copolymer ($N_A = N_B = N$; $b_A = b_B$; $\bar{v}_{0A} = \bar{v}_{0B}$) with high molecular weight where $D/\left(b_k N_k^{1/2}\right) \gg 1$ is applicable, the third term in (19) becomes dominant over the second term. In this situation, it can be shown easily that D_{eq} is given by

$$D_{eq} \sim N^{9/14}\alpha^{1/7} \tag{21}$$

However, when use is made of $m = 2$ in (16), the following expression is obtained:

$$D_{eq} \sim N^{2/3}\alpha^{1/6} \tag{22}$$

Equation (22) was first derived by Meier [34] who employed the confined chain model.

Note that the difference between the exponent 9/14 appearing on N in (21) and the exponent 2/3 appearing on N in (22) is very small, 1/42. This small difference is

attributed to the fact that ΔS_c is proportional to D^2 in the Meier theory [34, 37], while it is proportional to $D^{2.5}$ in the Helfand–Wasserman (H–W) theory (see (16)). Experimentally, D_{eq} was observed to be proportional to $M^{2/3}/T^{1/3}$ [38]. Thus, although the agreement in the exponent appearing on molecular weight M between theory and experiment is reasonably good, the temperature dependence between the two is still unresolved, because it is well established experimentally that χ is inversely proportional to T.

Helfand and Wasserman [12] suggested use of the following expression for the free energy difference, in place of (19), which then enables one to determine the T_{ODT} of AB-type diblock copolymers having lamellar, cylindrical, and spherical microdomains:

$$
\begin{aligned}
\frac{\Delta G_m}{k_B T n_c^t} =\; & Sh\,(N_A \bar{v}_{0A}) \left(\frac{\gamma}{k_B T} \right) \frac{1}{D} + \ln \left(\frac{D T_1}{Sh\, a_J} \right) + \left[\eta_{A1} \left(C_2 D^2 + \eta_{A2}{}^2 \right)^{\eta_{A3}/2} \right. \\
& \left. - \eta_{A1} \left(\eta_{A2} \right)^{\eta_{A3}} \right] + \left\{ \eta_{B1} \left(C_6 D^2 + \eta_{B2}{}^2 \right)^{\eta_{B3}/2} - \eta_{B1} \left(\eta_{B2} \right)^{\eta_{B3}} \right\} \\
& - \frac{\alpha\,(N_A \bar{v}_{0A})\,(N_B \bar{v}_{0B})}{[(N_A \bar{v}_{0A}) + (N_B \bar{v}_{0B})]}
\end{aligned}
\tag{23}
$$

where

$$
C_2 = 6/N_A b_A{}^2; \quad C_6 = 6/N_B b_B{}^2 \xi^2
\tag{24}
$$

with

$$
1/\xi = \left(\frac{N_A \bar{v}_{0A}}{N_B \bar{v}_{0B}} + 1 \right)^{1/Sh} - 1
\tag{25}
$$

in which Sh is a shape factor (1 for lamellar structure, 2 for cylindrical structure, and 3 for spherical structure); N_A and N_B are the degrees of polymerization for components A and B, respectively, while N_B must be replaced by $N_B/2$ for ABA-type triblock copolymers; D is the domain size; T_1 is related to Sh and, also, to N_A and N_B; (see the computer programs given in the Supplementary Material for the values of T_1 for AB-, ABA-, and BAB-type block copolymers) η_{A_1}, η_{A2}, η_{A3}, η_{B1}, η_{B2}, η_{B3} are parameters which depend on the microdomain structure of the block copolymer. Table 1 gives a summary of the numerical values of the parameters (η_{A1}, η_{A2}, η_{A3}, η_{B1}, η_{B2}, η_{B3}) for both AB-type diblock and ABA-type triblock copolymers, which were obtained by curve fitting, after applying NIA, to the computer simulations. Thus, (23) was not obtained from a rigorous analysis. One of the drawbacks of the H–W theory is that the self-consistent field, $W_\xi(\mathbf{r})$ given by (4), could not be obtained from the molecular parameters even when the volume fractions of two block components ($\varphi_A(\mathrm{r})$, $\varphi_B(\mathrm{r})$) are known. As will be summarized below, later more rigorous self-consistent mean-field theories were developed by other investigators to overcome this drawback of the H–W theory.

For illustration, the phase behavior predicted by the H–W theory for an SI diblock copolymer at 150°C is given in Fig. 6. In obtaining Fig. 6 we used the following expressions for an interaction parameter α having the units of mol/cm^3 given by [39]:

$$
\alpha = -0.00118 + 0.839/T
\tag{26}
$$

Table 1 Numerical values for the parameters appearing in the Helfand-Wasserman theory

Parameter	Lamellar domain	Cylindrical domain	Spherical domain
AB-type diblock copolymers			
η_{A1}	0.061	0.0166	0.0081
η_{A2}	0.838	1.051	1.07
η_{A3}	2.64	2.86	2.87
η_{B1}	0.0766	$0.0792 + 0.0412/\xi$	$0.0852 + 0.0744/\xi$
η_{B2}	0.531	$0.539 - 0.206/\xi$	$0.348 + 0.220/\xi$
η_{B3}	2.57	$2.53 - 0.152/\xi$	$0.248 - 0.123/\xi$
ABA-type triblock copolymers			
η_{A1}	0.0766	0.0274	0.0123
η_{A2}	0.531	0.202	0.348
η_{A3}	2.57	2.605	2.680
η_{B1}	0.061	$0.0659 + 0.0357/\xi$	$0.0705 + 0.0578/\xi$
η_{B2}	0.838	$0.757 - 0.132/\xi$	$0.596 + 0.599/\xi$
η_{B3}	2.64	$2.590 - 0.147/\xi$	$2.550 - 0.132/\xi$

ξ is defined by (25)

Fig. 6 Phase diagram of an SI diblock copolymer in terms of molecular weight vs weight fraction of PS block at 150°C predicted from the Helfand–Wasserman theory, in which *S* denotes spherical microdomains, *C* denotes hexagonally packed cylindrical microdomains, *L* denotes lamellar microdomains, and *H* denotes the disordered (homogeneous) phase
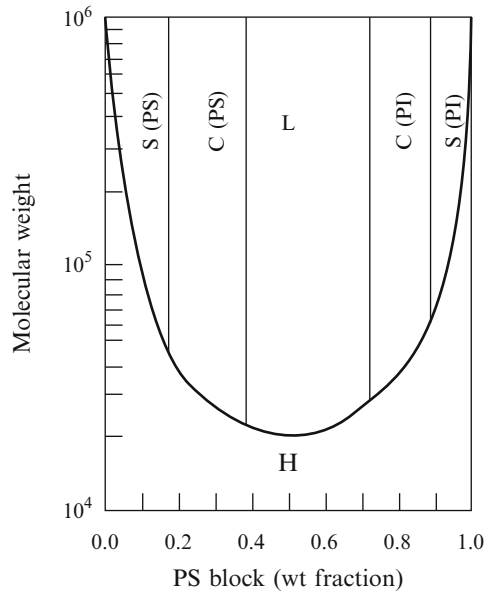
the specific volume having the units of cm^3/g for polystyrene (PS) given by [40]

$$v_{PS} = 0.9199 + 5.098 \times 10^{-4} (T - 273) + 2.354 \times 10^{-7} (T - 273)^2$$
$$+ [32.46 + 0.1017 (T - 273)] / M_{w,PS} \tag{27a}$$

in which $M_{w,PS}$ is the molecular weight of PS, and the specific volume for polyisoprene (PI) given by [41]

$$v_{PI} = 1.0771 + 7.22 \times 10^{-4}(T-273) + 2.46 \times 10^{-7}(T-273)^2 \qquad (27b)$$

Also used in obtaining Fig. 6 were the Kuhn length of PS, $b_{PS} = 0.68$ nm, and the Kuhn length of PI, $b_{PI} = 0.63$ nm. It is seen in Fig. 6 that, with increasing weight fraction of PS block, the microdomains of PS block change from bcc lattice in sphere to hexagonally packed cylinders to alternating lamellae.

In the Supplementary Material we have included Fortran computer programs for predicting the T_{ODT} of AB-type diblock copolymers based on the H–W theory. During the past two decades we have used these computer programs very effectively to determine the molecular weight of a block copolymer based on a predetermined block composition and target T_{ODT} before initiating the synthesis of the block copolymer. In this way we were able to save considerable time and resources in the synthesis of target block copolymers. It should be mentioned that the accuracy of predicted T_{ODT} depends very much on the specific expression(s) for the temperature dependence of $\alpha(T)$ or $\chi(T)$. That is, different values of predicted T_{ODT} may be obtained for different expressions for $\alpha(T)$ or $\chi(T)$. As will be discussed later in this chapter, there is a great deal of uncertainty in the experimental determination of $\alpha(T)$ or $\chi(T)$.

For the sake of comparing the predicted T_{ODT}s of the same block copolymer using two different expressions for $\chi(T)$, and later for comparison of the predicted T_{ODT}s of the same block copolymer using different theories, here we present some representative predictions. For an SI diblock copolymer having block molecular weights: $M_w = 8,000$ for PS block and $M_w = 8,000$ for PI block using the expression for $\alpha(T)$ given by (26), the H–W theory predicts a T_{ODT} of 120°C for the SI diblock copolymer. For the same block copolymer using the following expression for $\chi(T)$ given by [42]:

$$\chi = -0.0937 + 66/T \qquad (28)$$

the H–W theory predicts a T_{ODT} of 94°C. That is, the predicted T_{ODT} of the same SI diblock copolymer is different depending on which expression for $\alpha(T)$ or $\chi(T)$ was employed. This is a serious issue which the block copolymer community must address in the future.

The H–W theory can also be used to predict the T_{ODT} of ABA-type triblock copolymers. The Fortran computer program for predicting the T_{ODT} of ABA-type triblock copolymers is also included in the Supplementary Material. For an SIS triblock copolymer having block molecular weights, $M_w = 1.3 \times 10^4$ for one PS endblock and $M_w = 1.14 \times 10^5$ for the PI midblock, using the $\alpha(T)$ given by (26) the H–W theory predicts a T_{ODT} of 248°C.

2.2 Mean-Field Theory of Leibler Based on Random Phase Approximation

Leibler [13] developed a statistical thermodynamic theory for the microphase separation of an AB-type diblock copolymer on the basis of random phase approximation (RPA) [43]. The Leibler theory predicts the spinodal temperature (T_s) and T_{ODT} of microphase-separated AB-type diblock copolymers, as well as the type of microdomain structure (body-centered cubic, hexagonally packed cylinders or lamellae). This theory is believed to be valid for WSL, whereas the H–W theory is only valid for SSL due to its use of NIA.

Leibler obtained the free energy difference between the microphase-separated and homogenous states using the order parameter ($\psi(\mathbf{r})$):

$$\psi(\mathbf{r}) = \langle (1 - f)\,\varphi_A(\mathbf{r}) - f\,\varphi_B(\mathbf{r}) \rangle \tag{29}$$

in which f is the volume fraction of block A, and $\varphi_A(\mathbf{r})$ and $\varphi_B(\mathbf{r})$ are the local volume fractions at position $\mathbf{r}$ for block A and block B, respectively, and the bracket $<P>$ denotes the equilibrium ensemble average of the variable P. Since $\varphi_A(\mathbf{r}) + \varphi_B(\mathbf{r}) = 1$ for all $\mathbf{r}$ due to the condition of incompressibility, (29) becomes

$$\psi(\mathbf{r}) = \langle \varphi_A(\mathbf{r}) - f \rangle \tag{30}$$

Then, the density–density correlation function $\tilde{S}(\mathbf{r} - \mathbf{r}')$ is represented in terms of the order parameter as follows:

$$\tilde{S}(\mathbf{r} - \mathbf{r}') = \frac{1}{k_B T}\,\psi(\mathbf{r})\,\psi(\mathbf{r}') \tag{31}$$

The Fourier transform of $\tilde{S}(\mathbf{r} - \mathbf{r}')$ becomes the correlation function $\tilde{S}(q)$ which is directly proportional to the scattering intensity, ($I(q)$):

$$I(q) \sim (a_A - a_B)^2\,\tilde{S}(q) \tag{32}$$

with a_A and a_B being the scattering power of monomers A and B, respectively.

Leibler [13] obtained the free energy difference between microphase-separated and homogenous states ($\Delta G_m = G_{\text{micro}} - G_{\text{homo}}$) as a function of the order parameter

$$\Delta G_m = k_B T \sum_{n=2}^{\infty} \frac{1}{V^n} \sum_{q_n} \Gamma_n (q_1 \cdots q_n)\,\psi(q_1) \cdots \psi(q_n) \tag{33}$$

where V is the volume of the system, Γ_n is the vertex function which is related to the correlation function, and $q = (4\pi/\lambda)\sin\theta$ is the absolute value of wave vector $\mathbf{q}$ with λ being the wavelength of the incident radiation and θ being equal to half of the

scattering angle in the medium. According to Leibler, ΔG_m for most microdomains (bcc spheres, hexagonally packed cylinders, and lamellae) can be expressed by the fourth-order expansion of the order parameter (that is, n up to 4 in (33)). On the other hand, the stability limit of the system is simply given by the consideration of only the second-order expansion of the order parameter $\Gamma_2(q_1, q_2) = (1/\tilde{S}(q))$. Using RPA, Leibler derived the following expression for the composition correlation function $\tilde{S}(q)$ for an AB-type diblock copolymer (see Appendix C):

$$\tilde{S}(q) = W(q)/[S(q) - 2\chi W(q)] \tag{34}$$

and calculated $S(q)$ and $W(q)$ from the following expressions:

$$S(q) = S_{AA}(q) + S_{BB}(q) + 2S_{AB}(q) \tag{35}$$

$$W(q) = S_{AA}(q)S_{BB}(q) - S_{AB}{}^2(q) \tag{36}$$

where $S_{ij}(q)$ are the elements of the matrix $\|S(q)\|$, which is the Fourier transform of the composition correlation functions for ideal Gaussian copolymer chains, and they are given by (see Appendix C)

$$S_{AA}(q) = Ng(f, x) \tag{37}$$
$$S_{BB}(q) = Ng(1 - f, x) \tag{38}$$
$$S_{AB}(q) = (N/2)[g(1, x) - g(f, x) - g(1 - f, x)] \tag{39}$$

where N is the degree of polymerization of the block copolymer, and $g(f, x)$ is the Debye function defined as

$$g(f, x) = (2/x^2)[fx + \exp(-fx) - 1] \tag{40}$$

and x is defined by
$$x = q^2Nb^2/6 = q^2R_g{}^2 \tag{41}$$

with b being the Kuhn length of the chain for blocks A and B (assumed to be identical), and R_g is the radius of gyration of an ideal chain. Use of (35)–(39) in (34) gives

$$\tilde{S}(q) = N/[F(f, x) - 2\chi N] \tag{42}$$

where

$$F(f, x) = g(1, x)/\{g(f, x)g(1 - f, x) - (1/4)[g(1, x) - g(f, x) - g(1 - f, x)]^2\} \tag{43}$$

Leibler also predicted phase transitions between three different microdomains (from the disordered phase to spherical microdomains, from spherical to cylindrical microdomains, and from cylindrical to lamellar microdomains) using the fourth-order expansion of the vertex function in terms of the order parameter. Figure 7 displays
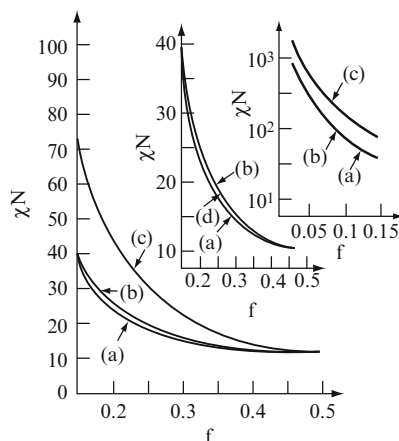
Fig. 7 Phase diagrams of an AB-type diblock copolymer in terms of χN vs the volume fraction (f) of block A, predicted from the Leibler theory, in which curve (a) denotes the phase transition from the disordered state to spherical microdomains, curve (b) denotes the phase transition from spherical microdomains to cylindrical microdomains, curve (c) denotes the phase transition from cylindrical microdomains to lamellar microdomains, and curve (d) denotes the spinodal curve $(\chi N)_s$. (Reprinted from Han et al. [41]. Copyright © 1989, with permission from the American Chemical Society)

relationships between the transition temperatures in terms of N and f for an AB-type diblock copolymer with different microdomain structures. In reference to Fig. 7, the differences between curves (b) and (d) in the middle panel are not discernible and the differences between curves (a) and (b) in the right-side panel are not discernible, because the size of the original drawing was reduced so much. To see Fig. 7 in more detail the readers are referred to Fig. 3 of the original paper [41]. According to Fig. 7, a transition from the disordered phase to lamellar microdomain structure at $f = 0.2$, for instance, by decreasing the temperature, passes first through the spherical microdomain structure and then through the cylindrical microdomain structure.

One can now obtain a relationship between $(\chi N)_s$, at which spinodal decomposition occurs, and f, by finding values of x^* (or q^*) that make $\tilde{S}(q)$ a maximum. Curve (d) in Fig. 7 represents the thermodynamic stability limit, in which the region below the curve represents the thermodynamically stable and metastable phases, while the region above the curve represents the mesophase or microphase-separation phase [13]. Note in Fig. 7 that $(\chi N)_s$ depends on the composition f and χ, which is inversely proportional to temperature, and therefore, at a given value of f, with information on N, the spinodal decomposition temperature (T_s) can be determined from the value of $(\chi N)_s$.

In the Supplementary Material we have included a Fortran computer program for predicting the T_{ODT} of AB-type diblock copolymers based on the Leibler theory. For the same SI diblock copolymer considered above when predicting its T_{ODT} based on the H–W theory, using (26), the Leibler theory predicts a T_{ODT} of 197°C, which is much higher than the $T_{ODT} = 120$°C predicted from the H–W theory.

Fig. 8 Plots of χN vs f for AB-type diblock copolymer, in which curve 1 was predicted from the Leibler theory and curve 2 was predicted from the Helfand–Wasserman theory. (Reprinted from Choi et al. [126]. Copyright © 2003, with permission from the American Chemical Society)
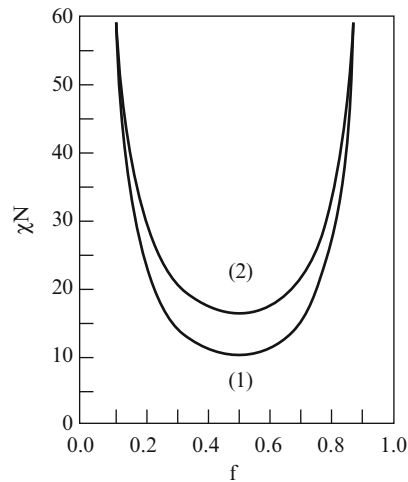
Figure 8 gives phase diagrams, plots of segregation power χN vs volume fraction f of block A, for AB-type diblock copolymers from the Leibler theory (curve 1) and from the H–W theory (curve 2). The following observations are worth noting in Fig. 8. (1) For nearly symmetric AB-type diblock copolymers, the Leibler theory has lower χN than the H–W theory, suggesting that the Leibler theory predicts higher T_{ODT} than the H–W theory. It should be remembered that χ is inversely proportional to temperature as indicted by (26) and (28). (2) As the volume fraction f decreases from 0.5 (i.e., moving towards the compositionally asymmetric diblock copolymer), the difference in χN between the two theories decreases steadily, suggesting that both theories predict virtually the identical T_{ODT} for highly asymmetric AB-type block copolymers.

It should be mentioned that the Leibler theory can easily be extended to the prediction of $(\chi N)_s$ for a multicomponent system and complex structure such as multi-arm or ring-type block copolymers. Indeed, such efforts were made by several research groups [24, 44–51]. For instance, $(\chi N)_s$ for an ABA-type triblock copolymer can easily be obtained when S_{AA}, S_{BB}, and S_{AB} in (37)–(39) are modified as follows:

$$S_{AA}(q) = N\left[g(f_1,x) + g(f_2,x) + g(f_3,x) + g(1,x) - g(1-f_3,x)\right.$$
$$\left. - g(1-f_1,x)\right] \tag{44}$$

$$S_{BB}(q) = N g(f_2,x) \tag{45}$$

$$S_{AB}(q) = \frac{N}{2}\left[g(1-f_1,x) + g(1-f_3,N) - g(f_1,x) - g(f_3,x)\right.$$
$$\left. - 2g(f_2,x)\right] \tag{46}$$

in which f_1, f_2, and f_3 are the volume fractions of the first endblock A, the midblock B, and the last endblock A.

A phase diagram for ABA-type triblock copolymers including the transitions between microdomain structures was obtained by Mayes and Olvera de la Cruz [24], who evaluated the Γ_2, Γ_3, and Γ_4 terms of the vertex function appearing in (33) for the most general situation of a multi-arm block copolymer $((AB)_m)$ and then for ABA-type triblock copolymers as a special case which corresponds to $m = 2$.

In the Supplementary Material we have given a Fortran computer program for the Mayes–Olvera de la Cruz (M–O) theory. Using this computer program we predicted the T_{ODT} of the same SIS triblock copolymer having $f = 0.157$, which was considered above when predicting its T_{ODT} based on the H–W theory. The M–O theory predicts a T_{ODT} of 262°C for the SIS triblock, which is only approximately 14°C higher than the T_{ODT} predicted from the H–W theory. The small difference in the predicted T_{ODT} between the M–O theory and H–W theory can be explained by a comparison of the two phase diagrams given in Fig. 9, in which curve 1 is the prediction from the M–O theory and curve 2 is the prediction from the H–W theory. It is seen in Fig. 9 that the difference in χN between the two theories decreases with decreasing f, suggesting that the predicted difference in the T_{ODT} of an ABA-type triblock copolymer between the two theories is expected to be very small as the value of f approaches about 0.1. This observation explains the reason why the difference in the T_{ODT} of the SIS triblock copolymer having $f = 0.157$ predicted from the two theories is small.

It is appropriate to mention at this juncture that the Leibler theory used the one-wave-number approximation for the calculation of the order parameter, while the M–O theory used higher order harmonics by extending the Leibler theory. Barrat and Fredrickson [52] also extended the Leibler theory within the spirit of a self-consistent one-loop approximation without making an assumption about the wave vector dependence of the correlation functions. This allowed them to calculate the shift in the peak of the fluctuation spectrum observed experimentally in small-angle neutron scattering experiments.
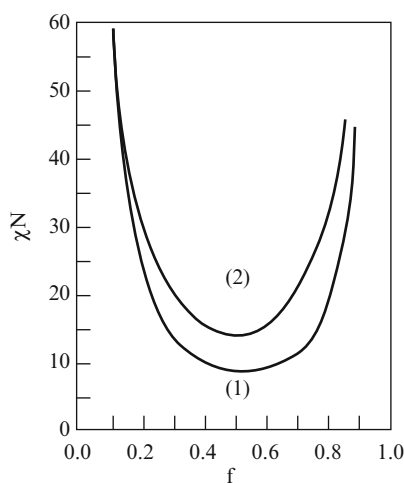
Fig. 9 Plots of χN vs f for ABA-type triblock copolymer, in which curve 1 was predicted from the Mayes–Olvera de la Cruz theory and curve 2 was predicted from the Helfand–Wasserman theory. (Reprinted from Choi et al. [126]. Copyright © 2003, with permission from the American Chemical Society)

Many research groups [53–63] have observed experimentally the order–order transition (OOT) between different microdomains in some block copolymers when temperature was changed. For instance, using SAXS and TEM Sakurai et al. [63] observed a thermally-induced OOT from cylindrical to spherical microdomains in an SI diblock copolymer and Sakamoto et al. [62] observed an OOT from cylindrical to spherical microdomains in an SIS triblock copolymer. The above experimental observations are consistent with the prediction made by the Leibler theory.

2.3 Fluctuation Correction of the Leibler Theory by Fredrickson and Helfand

By including composition fluctuations which were neglected in the Leibler theory [13], Fredrickson and Helfand [33] developed a theory predicting the effect of composition fluctuations on the ODT of AB-type diblock copolymers with finite molecular weight. They found that the T_{ODT} of a diblock copolymer with finite molecular weight is always lower than that of a diblock copolymer with infinite molecular weight as considered in the Leibler theory. Using the Hartree approximation for a finite-sized diblock copolymer, the Fredrickson–Helfand (F–H) analysis took into account composition fluctuations and improved the Landau-type mean-field prediction. Specifically, the F–H analysis considered fluctuation corrections to the vertex functions appearing in the Leibler theory. In doing so, the F–H analysis used the Hartree approximation, employed previously by Brazovskii [64], to obtain a thermodynamic potential from the Ohta–Kawasaki Hamiltonian functional [25].

The F–H analysis obtained a set of equations from the Hartree approximation for the thermodynamic potential, which depends on the three variables, f, χN, and N, whereas the Leibler analysis depends on only two variables, f and χN. The location of the ODT in the presence of composition fluctuations, $(\chi N)_t$, obtained from the F–H analysis is given by (see Appendix D)

$$(\chi N)_t = (\chi N)_s - (1/2)\,c^2 \tau^* \,(\mathrm{d}\lambda)^{2/3}\,\tilde{N}^{-1/3} \tag{47}$$

where $(\chi N)_s$ refers to the microphase transition at spinodal and $\tilde{N}$ is given by

$$\tilde{N} = N\left[\left(b_A{}^6/\bar{v}_{oA}{}^2\right)\left(b_B{}^6/\bar{v}_{oB}{}^2\right)\right]^{1/2} \tag{48}$$

Other constants appearing in (47) are given by

$$\tau^* = \left[\frac{F(f,x^*) - 2\chi N}{c^2}\right](\mathrm{d}\lambda)^{-2/3}\,\tilde{N}^{1/3}; \quad c = \left[\frac{x}{3}\frac{\partial^2 F(f,x)}{\partial x^2}\right]^{1/2}_{x=x^*};$$

$$d = \frac{3x^*}{2\pi}; \quad \lambda = \frac{\Gamma_4(0,0)}{c^4} \tag{49}$$

Note that $F(f,x)$ is defined by (43) and $\Gamma_4(0,0)$ is the parameter of the fourth-order vertex function (see (33)). In reference to (47), τ^* is equal to -2.0308 for lamellar microdomain, but this value depends on f and $\tilde{N}$ for cylindrical or spherical microdomains. The above analysis gives (see Appendix D)

$$(\chi N)_t = 10.495 + 41.022/\tilde{N}^{1/3} \tag{50}$$

for $f = 0.5$. It is clear from (50) that the presence of the second term, $41.022/\tilde{N}^{1/3}$, will lower the predicted value of T_{ODT} below the value based on the first term alone, which is the prediction from the Leibler theory [13].

The F–H analysis opens up the 'windows' of the phase diagram predicted earlier by Leibler [13], and it predicts that the system can pass directly from the disordered phase to lamellar or to cylindrical microdomains. It turns out that the F–H analysis predicts a first-order transition at $f = 0.5$, which is in contrast to a second-order transition predicted from the Leibler theory. Thus, the F–H analysis goes beyond the mean-field approximation of Leibler. However, according to Fredrickson and Helfand [33] their analysis is only valid for very large values of $\tilde{N}$, say $\tilde{N} > 10^4$, because it fails to predict the existence of spherical microdomains for $\tilde{N} \leq 10^4$.

Although Burger et al. [65] showed that the polydispersity effect can extend the validity of the F–H analysis to values of $\tilde{N}$ lower than 10^4, the fluctuation contribution to the total χN would be unacceptably very large for most SI and SB diblock copolymers, for instance, which have $\tilde{N} \sim 10^3$ [66, 67].

In the past, some research groups [68–73] used (50) to obtain expressions for a temperature-dependent interaction parameter, χ (T), in the presence of concentration fluctuations for relatively small values of $\tilde{N}$, say $\tilde{N} < 2000$. We wrote our own computer codes based on the F–H analysis (see Supplementary Material) to determine the upper limit of $\tilde{N}$ below which the F–H analysis fails to predict the presence of spherical microdomains. Table 2 gives some calculated results from the computer program based on the F–H analysis for (a) $\tilde{N} = 10^4$, (b) $\tilde{N} = 4 \times 10^4$, (c) $\tilde{N} = 5 \times 10^4$, and (d) $\tilde{N} = 10^5$. It is clearly seen in Table 2 that the F–H analysis does not predict the presence of spherical microdomains in the AB-type diblock copolymer having $\tilde{N} = 10^4$, and begins to predict the presence of spherical microdomains at $f = 0.15$ for $\tilde{N} = 4 \times 10^4$. The above observations lead us to conclude that use of the F–H analysis to obtain expressions for $\chi(T)$ for block copolymers having relatively low molecular weights (say $\tilde{N} < 4 \times 10^4$) is not warranted.

2.4 Self-Consistent Mean-Field Theory of Vavasour and Whitmore

Hong and Noolandi [74, 75] extended the approach taken by Helfand and Wasserman [8–11] to formulate a system of equations, via functional integral formalism, for multicomponent systems containing a solvent, and then solved the self-consistent system equations with the incompressibility constraint using a Lagrangian multiplier. Note that earlier Helfand and Wassermann used the incom-

Table 2 Some representative computational results from the Fredrickson–Helfand fluctuation theory

f	$(\chi N)_s$	$(\chi N)_t$	$(\chi N)_{13}$	$(\chi N)_{36}$
(a) For $\tilde{N} = 10^4$				
0.100	0.74331×10^2	0.11404×10^3	0.17695×10^3	Not predicted
0.125	0.51069×10^2	0.72978×10^2	0.11645×10^3	Not predicted
0.150	0.38038×10^2	0.51571×10^2	0.83402×10^2	Not predicted
0.175	0.29968×10^2	0.39019×10^2	0.63228×10^2	Not predicted
0.200	0.24613×10^2	0.31044×10^2	0.49913×10^2	Not predicted
0.225	0.20876×10^2	0.25677×10^2	0.40591×10^2	Not predicted
0.250	0.18172×10^2	0.21911×10^2	0.33753×10^2	Not predicted
0.275	0.16160×10^2	0.19189×10^2	0.28545×10^2	Not predicted
0.300	0.14635×10^2	0.17183×10^2	0.24455×10^2	Not predicted
0.325	0.13464×10^2	0.15692×10^2	0.21269×10^2	Not predicted
0.350	0.12562×10^2	0.14586×10^2	0.18492×10^2	Not predicted
0.375	0.11868×10^2	0.13758×10^2	0.16314×10^2	Not predicted
0.400	0.11344×10^2	0.13240×10^2	0.14586×10^2	Not predicted
0.425	0.10960×10^2	0.12925×10^2	0.13323×10^2	Not predicted
0.450	0.10698×10^2	0.12701×10^2	Not predicted	Not predicted
0.475	0.10545×10^2	0.12473×10^2	Not predicted	Not predicted
0.500	0.10498×10^2	0.12399×10^2	Not predicted	Not predicted
(b) For $\tilde{N} = 4 \times 10^4$				
0.100	0.74331×10^2	0.95054×10^2	0.16869×10^3	Not predicted
0.125	0.51069×10^2	0.62322×10^2	0.11197×10^3	Not predicted
0.150	0.38038×10^2	0.44788×10^2	0.80662×10^2	0.45052×10^2
0.175	0.29968×10^2	0.34370×10^2	0.61407×10^2	0.37411×10^2
0.200	0.24613×10^2	0.27678×10^2	0.48624×10^2	0.28015×10^2
0.225	0.20876×10^2	0.23134×10^2	0.39631×10^2	0.23434×10^2
0.250	0.18172×10^2	0.19922×10^2	0.33005×10^2	0.20168×10^2
0.275	0.16160×10^2	0.17586×10^2	0.27939×10^2	0.17772×10^2
0.300	0.14635×10^2	0.15857×10^2	0.23943×10^2	0.15979×10^2
0.325	0.13464×10^2	0.14566×10^2	0.20719×10^2	0.14623×10^2
0.350	0.12562×10^2	0.13604×10^2	0.18077×10^2	Not predicted
0.375	0.11868×10^2	0.12880×10^2	0.15909×10^2	Not predicted
0.400	0.11344×10^2	0.12372×10^2	0.14162×10^2	Not predicted
0.425	0.10960×10^2	0.12056×10^2	0.12834×10^2	Not predicted
0.450	0.10698×10^2	0.11933×10^2	0.11987×10^2	Not predicted
0.475	0.10545×10^2	0.11760×10^2	Not predicted	Not predicted
0.500	0.10498×10^2	0.11694×10^2	Not predicted	Not predicted
(c) For $\tilde{N} = 5 \times 10^4$				
0.100	0.74331×10^2	0.92888×10^2	0.16782×10^3	Not predicted
0.125	0.51069×10^2	0.60996×10^2	0.11150×10^3	0.61283×10^2
0.150	0.38038×10^2	0.43962×10^2	0.80372×10^2	0.44422×10^2
0.175	0.29968×10^2	0.33815×10^2	0.61215×10^2	0.34291×10^2
0.200	0.24613×10^2	0.27283×10^2	0.48488×10^2	0.27718×10^2
0.225	0.20876×10^2	0.22838×10^2	0.39529×10^2	0.23213×10^2
0.250	0.18172×10^2	0.19692×10^2	0.32927×10^2	0.19996×10^2
0.275	0.16160×10^2	0.17400×10^2	0.27875×10^2	0.17633×10^0

<div align="right">(continued)</div>

Table 2 (continued)

f	$(\chi N)_s$	$(\chi \mathbf{N})_t$	$(\chi N)_{13}$	$(\chi N)_{36}$
0.300	0.14635×10^2	0.15700×10^2	0.23889×10^2	0.15861×10^2
0.325	0.13464×10^2	0.14299×10^2	0.20671×10^2	0.14519×10^2
0.350	0.12562×10^2	0.13484×10^2	0.18033×10^2	0.13504×10^2
0.375	0.11868×10^2	0.12777×10^2	0.15866×10^2	Not predicted
0.400	0.11344×10^2	0.22272×10^2	0.14117×10^2	Not predicted
0.425	0.10960×10^2	0.11956×10^2	0.12782×10^2	Not predicted
0.450	0.10689×10^2	0.11836×10^2	0.11917×10^2	Not predicted
0.475	0.10545×10^2	0.11673×10^2	Not predicted	Not predicted
0.500	0.10498×10^2	0.11608×10^2	Not predicted	Not predicted
(d) For $\tilde{N} = 10^5$				
0.100	0.74331×10^2	0.86933×10^2	0.16566×10^3	0.87970×10^2
0.125	0.51069×10^2	0.57620×10^2	0.11033×10^3	0.58721×10^2
0.150	0.38038×10^2	0.41871×10^2	0.79654×10^2	0.43855×10^2
0.175	0.29968×10^2	0.32411×10^2	0.60737×10^2	0.33249×10^2
0.200	0.24613×10^2	0.26282×10^2	0.48150×10^2	0.26981×10^2
0.225	0.20876×10^2	0.22090×10^2	0.39277×10^2	0.22663×10^2
0.250	0.18172×10^2	0.19108×10^2	0.32731×10^2	0.19568×10^2
0.275	0.16160×10^2	0.16928×10^2	0.27716×10^2	0.17386×10^2
0.300	0.14635×10^2	0.15304×10^2	0.23756×10^2	0.15568×10^2
0.325	0.13464×10^2	0.14085×10^2	0.20553×10^2	0.14262×10^2
0.350	0.12562×10^2	0.13172×10^2	0.17924×10^2	0.13267×10^2
0.375	0.11868×10^2	0.12502×10^2	0.15760×10^2	0.12522×10^2
0.400	0.11344×10^2	0.12014×10^2	0.14006×10^2	Not predicted
0.425	0.10960×10^2	0.11694×10^2	0.12654×10^2	Not predicted
0.450	0.10689×10^2	0.11546×10^2	0.11745×10^2	Not predicted
0.475	0.10545×10^2	0.11440×10^2	Not predicted	Not predicted
0.500	0.10498×10^2	0.11378×10^2	Not predicted	Not predicted

f = volume fraction; $(\chi N)_s$ = the critical value of χN at which spinodal decomposition occurs at a certain composition; $(\chi N)_t$ = microphase-separation temperature in the presence of fluctuations; $(\chi N)_{13}$ = the value of χN at which hexagonal cylinder–lamella transition occurs; $(\chi N)_{36}$ = the value of χN at which bcc lattice–hexagonal cylinder transition occurs

pressibility constraint on an ad hoc basis. Subsequently, Vavasour and Whitmore [26, 27] took the formalism of Hong and Noolandi to solve a set of self-consistent mean-field equations for an AB-type diblock copolymer without a solvent. Here we summarize the Vavasour–Whitmore (V–W) analysis.

The V–W analysis is based on the following expression for the free energy difference between the microphase-separated and homogeneous states, ΔG_m:

$$
\frac{\Delta G_m}{\rho_o k_{\mathrm{B}} T V} = \frac{1}{V} \int_V \mathrm{d}\mathbf{r} \, \chi \left[\varphi_A(\mathbf{r}) \varphi_B(\mathbf{r}) - \varphi_{Ao} \varphi_{Bo} \right] - \frac{\rho_{oA}}{\rho_o} \omega_A(\mathbf{r}) \varphi_A(\mathbf{r})
$$
$$
- \frac{\rho_{oB}}{\rho_o} \omega_B(\mathbf{r}) \varphi_B(\mathbf{r}) - \frac{1}{r_c} \ln \frac{Q_c}{V} \tag{51}
$$

in which $\omega_k(\mathbf{r})$ is the self-consistent mean-field potential given by

$$\omega_k(\mathbf{r}) = \frac{\rho_o}{\rho_{ok}} \left[\chi \left(\varphi_{k'}(\mathbf{r}) - \varphi_{k'o} \right) + \frac{\sigma^2}{2} \left(\nabla^2 \varphi_{k'}(\mathbf{r}) - \nabla^2 \varphi_{k'o} + \frac{\eta(\mathbf{r})}{\rho_o} \right) \right] \qquad (52)$$

where $k' = B$ for $k = A$ and $k' = A$ for $k = B$, and $\eta(\mathbf{r})$ is an as yet undermined parameter. Using the following initial guess for $\eta(\mathbf{r})$,

$$\eta(\mathbf{r}) = \frac{1}{2} \left[\rho_{oA} \omega_A(\mathbf{r}) + \rho_{oB} \omega_B(\mathbf{r}) \right] \qquad (53)$$

Vavasour and Whitmore solved (51)–(53) self-consistently. They also obtained an equilibrium phase diagram which enabled them to predict which of the microdomain structures is most stable for given values of f and χ. Note in (51) that φ_{A0} corresponds to f and φ_{B0} corresponds to $1 - f$, and Q_c depends on the type of microdomain structure.

A summary of the predictions from the V–W analysis is given in Fig. 10, in which the predictions from the V–W theory are close to those from the Leibler theory for $\chi N \approx 10$ in the WSL, while the predictions from the V–W theory are consistent with the H–W theory for $\chi N \gg 10$ in the SSL.

The difference in the predictions between the V–W theory and the Leibler theory for large χN is attributable to the fact that the Leibler theory expresses the free energy difference up to the fourth order of the order parameter, which is certainly not valid for the SSL because a single sine (or cosine) function is not adequate to accurately describe the interfacial concentration in the SSL.
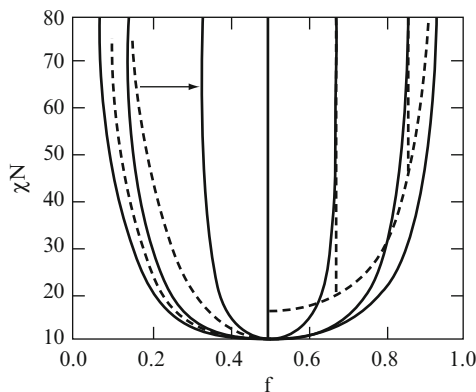
Fig. 10 Comparison between the SSL theory and the WSL theory with the self-consistent mean-field theory (SCMFT) of Whitmore and Vavasour. *Solid curves* were calculated by SCMFT, *dashed curves* at the left side were calculated from the Leibler theory, and the *dashed curves* at the right side were calculated from the Helfand–Wasserman theory. (Reprinted from Vavasour and Whitmore [26]. Copyright © 1992, with permission from the American Chemical Society)

On the other hand, the H–W analysis was developed based on the NIA, i.e., the interfacial thickness of a block copolymer is the same as that of an immiscible polymer blend. Thus, the H–W analysis is applicable only to the SSL, but near $\chi N \approx 10$ the interfacial thickness would be much larger than that for an immiscible polymer blend. Furthermore, in the H–W analysis the mean-field potential $\omega_k(\mathbf{r})$ was treated on an ad hoc basis and thus the H–W analysis is applicable to very large values of χN. The phase boundary between the lamellar and cylindrical microdomains predicted by the V–W theory is the same as that predicted by the H–W analysis when $\chi N \geq \sim 50$. Also, the phase boundary between the cylindrical and spherical microdomains predicted by both theories is the same when $\chi N \geq \sim 70$. However, even when χN is approximately 80, the phase boundary between the spherical microdomain and homogeneous state predicted by both theories is quite different. Helfand and Wasserman [12] reported that for $\chi N > 40$ the interfacial concentration profiles for lamellar microdomains obtained with NIA are essentially the same as those obtained by numerical simulation. However, it is expected that for cylindrical or spherical microdomains, NIA is valid for values of χN much larger than about 40. The main result of the V–W analysis is that for $\chi N > 70$, the order–order transitions are almost independent of χN and the transition between lamellar and cylindrical microdomains occurs at $f \approx 0.67$ and the transition between cylindrical and spherical microdomains occurs at $f \approx 0.85$.

2.5 Self-Consistent Mean-Field Theory of Matsen and Schick

Matsen and Schick [14] solved a set of self-consistent mean-field equations using the reciprocal space method. They started with the following form of the partition function Z for an AB-type diblock copolymer:

$$Z = \int \prod_{\alpha=1}^{n} \tilde{D}(\mathbf{r}_\alpha)\, \delta\left[1 - \hat{\phi}_A(\mathbf{r}) - \hat{\phi}_B(\mathbf{r})\right] \exp\left\{-\chi \rho_o \int d\mathbf{r}\, \hat{\phi}_A(\mathbf{r})\, \hat{\phi}_B(\mathbf{r})\right\} \quad (54)$$

where $\widehat{D\mathbf{r}_\alpha} \equiv D\mathbf{r}_\alpha P[\mathbf{r}_\alpha; 0, 1]$ with $D\mathbf{r}_\alpha$ denoting a functional integral and $P[\mathbf{r}_\alpha; s_1, s_2]$ denoting a weighting function, commonly referred to as Wiener measure with $\mathbf{r}_\alpha(s)$ being functions which specify the space curve occupied by the α-th copolymer, χ is the Flory–Huggins interaction parameter, ρ_o is the density of pure component, and $\hat{\phi}_A(\mathbf{r})$ and $\hat{\phi}_B(\mathbf{r})$ are the density operators for monomer A and monomer B, respectively, defined by

$$\hat{\phi}_A(\mathbf{r}) = \frac{N}{\rho_o} \sum_{\alpha=1}^{n} \int_0^f ds\, \delta[\mathbf{r} - \mathbf{r}_\alpha(s)]; \; \hat{\phi}_B(\mathbf{r}) = \frac{N}{\rho_o} \sum_{\alpha=1}^{n} \int_f^1 ds\, \delta[\mathbf{r} - \mathbf{r}_\alpha(s)]; \quad (55)$$

Inserting the following identities:

$$1 = \int D\Phi_A \delta\left(\Phi_A - \hat{\phi}_A\right); \quad 1 = \int D\Phi_B \delta\left(\Phi_B - \hat{\phi}_B\right) \quad (56)$$

into (54) one obtains

$$Z = \int \prod_{\alpha=1}^{n} \tilde{D}\mathbf{r}_\alpha D\Phi_A D\Phi_B \delta \left(\Phi_A - \hat{\phi}_A\right) \delta \left(\Phi_B - \hat{\phi}_B\right)$$

$$\times \delta \left[1 - \hat{\phi}_A(\mathbf{r}) - \hat{\phi}_B(\mathbf{r})\right] \exp\left\{-\chi\rho_o \int d\mathbf{r}\hat{\phi}_A(\mathbf{r})\hat{\phi}_B(\mathbf{r})\right\} \quad (57)$$

Replacing the δ-functional in (57) by the standard integral representations, (57) can be rewritten as

$$Z = N \int D[\Phi_A] D[\Phi_B] D[W_A] D[W_B] D[\Xi] \exp[-F(\Phi_A,\Phi_B,W_A,W_B,\Xi)/k_BT] \quad (58)$$

where N is a normalization constant and $F(\Phi_A,\Phi_B,W_A,W_B,\Xi)/nk_BT$ is defined by

$$F(\Phi_A,\Phi_B,W_A,W_B,\Xi)/nk_BT = -\ln\tilde{Q}(-iW_A,-iW_B) + \frac{1}{V}\int d\mathbf{r}[\chi N\Phi_A\Phi_B - iW_A\Phi_A$$
$$- iW_B\Phi_B - i\Xi(1-\Phi_A-\Phi_B)] \quad (59)$$

with

$$\tilde{Q}(-iW_A,-iW_B) \equiv \int \tilde{D}(\mathbf{r}_\alpha)\exp\left\{-i\left[\int_0^f dsW_A(\mathbf{r}_\alpha(s)) + \int_f^1 dsW_B(\mathbf{r}_\alpha(s))\right]\right\} \quad (60)$$

In obtaining Eqs. (58)–(60), the following standard delta functionals defined by

$$\delta\left(\Phi_A(\mathbf{r}) - \hat{\phi}_A(\mathbf{r})\right) = \int DW_A \exp\left\{i\frac{n}{V}\int d\mathbf{r}W_A(\mathbf{r})\left[\Phi_A(\mathbf{r}) - \hat{\phi}_A(\mathbf{r})\right]\right\} \quad (61a)$$

$$\delta\left(\Phi_B(\mathbf{r}) - \hat{\phi}_B(\mathbf{r})\right) = \int DW_B \exp\left\{i\frac{n}{V}\int d\mathbf{r}W_B(\mathbf{r})\left[\Phi_B(\mathbf{r}) - \hat{\phi}_B(\mathbf{r})\right]\right\} \quad (61b)$$

$$\delta\left(1 - \hat{\phi}_A(\mathbf{r}) - \hat{\phi}_B(\mathbf{r})\right) = \int D[\Xi] \exp\left\{i\frac{n}{V}\int d\mathbf{r}\Xi(\mathbf{r})\left[1 - \hat{\phi}_A(\mathbf{r}) - \hat{\phi}_B(\mathbf{r})\right]\right\} \quad (62)$$

were introduced. Hence, $F(\Phi_A,\Phi_B,W_A,W_B,\Xi)$ defined by Eq. (59) is a 'complex' variable. Note that for the definitions of the delta functionals given above the limits of integration of the functionals must be taken from $-i\infty$ to $+i\infty$. On the other hand, the following definition of the delta functional, for instance,

$$\delta\left(1 - \hat{\phi}_A(\mathbf{r}) - \hat{\phi}_B(\mathbf{r})\right) \propto \int D[\Xi] \exp\left\{\frac{n}{V}\int d\mathbf{r}\Xi(\mathbf{r})\left[1 - \hat{\phi}_A(\mathbf{r}) - \hat{\phi}_B(\mathbf{r})\right]\right\} \quad (63)$$

yields the expression,

$$F/nk_BT = -\ln Q(W_A,W_B) + \frac{1}{V}\int d\mathbf{r}[\chi N\Phi_A\Phi_B - W_A\Phi_A - W_B\Phi_B - \Xi(1-\Phi_A-\Phi_B)] \quad (64)$$

with

$$Q(W_A, W_B) \equiv \int \tilde{D}(\mathbf{r}_\alpha) \exp \left\{ -\int_0^f ds W_A(\mathbf{r}_A(s)) - \int_f^1 ds W_B(\mathbf{r}_B(s)) \right\} \qquad (65)$$

Note that $Q(W_A, W_B)$ defined by (65) is a 'real' variable, and thus F/nk_BT defined by (64) is regarded as being the free energy.

Since the functional integral in (64) cannot be evaluated exactly, in the SCMFT this integral was approximated by taking a saddle point approximation of $F(\Phi_A, \Phi_B, W_A, W_B, \Xi)$, defined by (64), resulting in the following expressions for the two fields, $w_A(\mathbf{r})$ and $w_B(\mathbf{r})$:

$$w_A(\mathbf{r}) = \chi N \varphi_B(\mathbf{r}) + \xi(\mathbf{r}) \qquad (66)$$

$$w_B(\mathbf{r}) = \chi N \varphi_A(\mathbf{r}) + \xi(\mathbf{r}) \qquad (67)$$

in which $\varphi_A(\mathbf{r}), \varphi_B(\mathbf{r}), w_A(\mathbf{r}), w_B(\mathbf{r})$, and $\xi(\mathbf{r})$ are the functions for which $F[\varphi_A, \varphi_B, w_A, w_B, \xi]$ attains its extreme. Since (66) and (67) contain five functions, three additional equations

$$\varphi_A(\mathbf{r}) + \varphi_B(\mathbf{r}) = 1 \qquad (68)$$

$$\varphi_A(\mathbf{r}) = -\frac{V}{Q} \frac{\delta Q}{\delta w_A} \qquad (69)$$

$$\varphi_B(\mathbf{r}) = -\frac{V}{Q} \frac{\delta Q}{\delta w_B} \qquad (70)$$

were introduced, so that $\varphi_A(\mathbf{r}), \varphi_B(\mathbf{r}), w_A(\mathbf{r}), w_B(\mathbf{r})$, and $\xi(\mathbf{r})$ could be determined in a self-consistent manner. This approach neglects the functional integrals, $\int D\phi_A, \int D\phi_B, \int DW_A, \int DW_B, \int D\Xi$, appearing in (58). In order to solve (66)–(70) for $\varphi_A(\mathbf{r}), \varphi_B(\mathbf{r}), \omega_A(\mathbf{r}), \omega_B(\mathbf{r})$, and $\xi(\mathbf{r})$, one must have information on $Q(W_A, W_B)$, defined by (65), which is related to the solution of the modified diffusion equation

$$\frac{\partial q(\mathbf{r},s)}{\partial s} = \begin{cases} \frac{Nb^2}{6}\nabla^2 q(\mathbf{r},s) - w_A(\mathbf{r}) q(\mathbf{r},s) & \text{for } s < f \\ \frac{Nb^2}{6}\nabla^2 q(\mathbf{r},s) - w_B(\mathbf{r}) q(\mathbf{r},s) & \text{for } s > f \end{cases} \qquad (71)$$

Matsen and Schick [14] were the first to use the reciprocal phase approach to solve (71). Briefly stated, the solution of (71) was obtained by first expanding $q(\mathbf{r}, s)$ as

$$q(\mathbf{r},s) = \sum_i q_i(s) f_i(\mathbf{r}) \quad (i = 1, 2, 3, \ldots) \qquad (72)$$

in terms of orthonormal basis functions $\{f_i(\mathbf{r})\}$ (i. e., $(1/V) \int f_i(\mathbf{r}) f_j(\mathbf{r}) d\mathbf{r} = \delta_{ij}$) that possess the symmetry of the phases being considered, and then choosing $\{f_i(\mathbf{r})\}$ to be eigenfunctions of the Laplacian operator

$$\nabla^2 f_i(\mathbf{r}) = -\lambda_i D^{-2} f_i(\mathbf{r}) \quad (i = 1, 2, 3, \ldots) \qquad (73)$$

in which λ_i are the eigenvalues corresponding to orthonormal basis functions $\{f_i(\mathbf{r})\}$ that possess the symmetry of the phases being considered, and D corresponds to a length scale of the phase. Note that $\{f_i(\mathbf{r})\}$ can be arranged in such a way, that $f_1(\mathbf{r}) = 1$ corresponding to $\lambda_1 = 0$ and λ_i is a nondecreasing series. Substituting (72) into (71) with the aid of (73), we obtain

$$\frac{\mathrm{d}q_m(s)}{\mathrm{d}s} = \begin{cases} \sum_k A_{mk} q_k(s) & \text{if } s < f \\ \sum_k B_{mk} q_k(s) & \text{if } s > f \end{cases} \tag{74}$$

with

$$A_{mk} = -\alpha_A \lambda_m \delta_{mk} - \frac{1}{V} \sum_n \int \mathrm{d}\mathbf{r} \, w_{A,n}(\mathbf{r}) \, f_m(\mathbf{r}) \, f_k(\mathbf{r}) f_n(\mathbf{r}) \tag{75}$$

$$B_{mk} = -\alpha_B \lambda_m \delta_{mk} - \frac{1}{V} \sum_n \int \mathrm{d}\mathbf{r} \, w_{B,n}(\mathbf{r}) \, f_m(\mathbf{r}) \, f_k(\mathbf{r}) f_n(\mathbf{r}) \tag{76}$$

where $\alpha_A = Nb_A{}^2/6D^2$ and $\alpha_B = Nb_B{}^2/6D^2$. The solution of (74) can be written as

$$q_m(s) = \begin{cases} \left[e^{\mathbf{A}s} \right]_{m1} & \text{if } s < f \\ \sum_k \left[e^{\mathbf{B}(s-f)} \right]_{mk} \left[e^{\mathbf{A}f} \right]_{k1} & \text{if } s > f \end{cases} \tag{77}$$

where suffix $m1$ refers to the $(m,1)$ element of the corresponding matrix. Since analytical solutions for (66)–(70) cannot be obtained, Matsen and Schick numerically solved these equations in a self-consistent manner. Note that Q appearing in (69) and (70) can be calculated from

$$Q = \int \mathrm{d}\mathbf{r} \, q(\mathbf{r}, 1) \tag{78}$$

Matsen and Schick [14] found that there exists a gyroid microdomain structure, which occurs between cylindrical and lamellar microdomains. The region of stability for the gyroid (bicontinuous Ia$\bar{3}$d cubic) phase increases as the number of arms in a star block copolymer increases. Matsen and Bates [76] generalized the SCMFT, and obtained the phase behavior for an AB-type diblock copolymer as given in Fig. 11. It is seen from Fig. 11 that, with increasing f, the microdomains change from closed-packed spheres (cps) such as face-centered-cubic (fcc) or hexagonally closed-packed-cubic (hpc), passing through body-centered-cubic (bcc) spheres (Im$\bar{3}$m), hexagonally packed cylinders (H) and bicontinuous gyroid (Ia$\bar{3}$d), to lamellae (L) at lower values of χN. In reference to Fig. 11, it should be mentioned that there is an additional curve representing the disordered phase just outside the curve representing CPS. However, the two curves lie very close to each other and thus they are not discernible in the scale of the drawing given in Fig. 11. An enlarged drawing
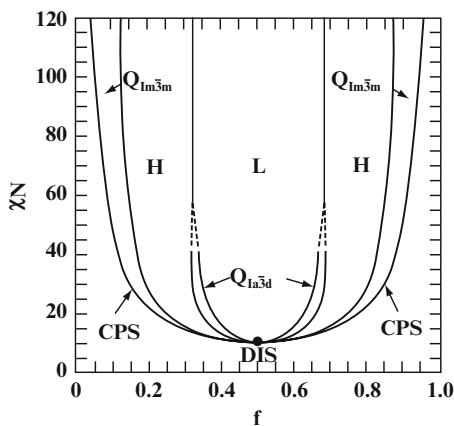
Fig. 11 Phase diagram for a conformationally symmetric AB-type diblock copolymer predicted from the self-consistent mean-field theory, in which L denotes a lamellar phase, H denotes a hexagonally packed cylindrical phase, $Q_{Ia\bar{3}d}$ denotes a bicontinuous $Ia\bar{3}d$ cubic, $Q_{Im\bar{3}m}$ denotes bcc spheres, CPS denotes close-packed spheres, and DIS denotes a disordered phase. *Dashed lines* denotes extrapolated phase boundaries, and the *dot* denotes the mean-field critical point. (Reprinted from Matsen and Bates [76]. Copyright © 1996, with permission from the American Chemical Society)

of a small section of Fig. 11, showing the region between CPS and the disordered phase, is given in Fig. 5 of the original paper [76]. We conducted our own numerical simulations based on the SCMFT and confirmed the accuracy of the phase diagram given in Fig. 11. Comparison of Fig. 11 with Fig. 7 reveals that the SCMFT predicts the presence of an additional mesophase, gyroid, between the hexagonally packed cylinders and lamellae over a very narrow range of f, while the Leibler theory does not. Some research groups [6, 77, 78] confirmed experimentally the presence of a gyroid microphase in some block copolymers. Although the bicontinuous gyroid phase is unstable compared with hexagonally cylinders or lamellae at higher χN, a modified version of SCMFT by Cochran et al. [79] shows that the bicontinuous gyroid microphase is stable even at higher χN. However, they found that the bicontinuous double diamond microphase structure is not stable for all χN.

3 Experimental Methods for Investigating Phase Behavior and Phase Transitions in Microphase-Separated Block Copolymers

3.1 Radiation Scattering Methods

One of the most powerful experimental methods to investigate the phase behavior, microdomain structure, and the T_{ODT} of microphase-separated block copolymers is radiation scattering, namely small-angle X-ray scattering (SAXS) and small-angle neutron scattering (SANS). During the past three decades numerous research groups

used SAXS and/or SANS to investigate the phase behavior and phase transitions in block copolymers. There are too many papers to cite them all here. The readers are referred to some seminal studies reported in the 1980s [38, 42, 80–89]. The characteristic length (L) of the microdomains observed by SAXS and SANS is given by $\lambda/(2\sin\theta)$ in which λ is the wavelength of the incident radiation and θ is a half of the scattering angle in the medium. For SAXS, λ is about 0.15 nm, and 2θ becomes $0.17-2.7°$ for L being 5–50 nm. Although the microdomain structures of microphase-separated block copolymers are easily detected by transmission electron microscopy (TEM), in most cases they can only be observed at room temperature. Furthermore, selective staining of a specimen is required prior to being able to observe the microdomains of a block copolymer using TEM. For polystyrene-*block*-polydiene copolymers, polydiene blocks are readily stained by osmium tetroxide (OsO_4), while polystyrene blocks are stained effectively by ruthenium tetroxide (RuO_4). In using SAXS and/or SANS to investigate the phase behavior and phase transitions in block copolymers, a contrast between two blocks must exist. In SAXS the contrast comes from the difference in electron density of each monomer (the same as a_A and a_B in (32)), while in SANS the contrast comes from the difference in neutron coherence length of each monomer [90].

The specific microdomain structure in a block copolymer is easily determined by the ratios of the positions (q_m) of the scattering peaks to the maximum scattering peak position (q^*), in which q is the scattering vector defined by $q = (4\pi/\lambda)\sin\theta$, as summarized in Table 3. Furthermore, from the SAXS measurements of the intensity $I(q)$, the interfacial thickness (λ_I) between two block chains can be calculated using

Table 3 Types of microdomains in block copolymers determined by SAXS (or SANS)

Type of microdomains		Domain size of block A (L for the lamellae and the radius (R) for cylindrical or spherical micrdomains)[a]	Relative peak positions of the high ordered peaks $(q^*, q_2, q_3, q_4, q_5)$
Lamellae		$L = fD$	1, 2, 3, 4, 5
Hexagonally packed cylinders		$R = D\left(\frac{2f}{\sqrt{3}\pi}\right)^{1/2}$	$1, \sqrt{3}, \sqrt{4}, \sqrt{7}, \sqrt{9}$
Spheres	Simple cubic lattice	$R = D\left(\frac{3f}{4\pi}\right)^{1/3}$	$1, \sqrt{2}, \sqrt{3}, \sqrt{4}, \sqrt{5}$
	Body-centered-cubic lattice	$R = D\left(\frac{3f}{\sqrt{8}\pi}\right)^{1/3}$	$1, \sqrt{2}, \sqrt{3}, \sqrt{4}, \sqrt{5}$
	Face-centered-cubic lattice	$R = D\left(\frac{27f}{16\sqrt{3}\pi}\right)^{1/3}$	$1, \sqrt{(4/3)}, \sqrt{(8/3)}, \sqrt{(11/3)}, \sqrt{(12/3)}$
Gyroids			$1, \sqrt{(8/6)}, \sqrt{(14/6)}, \sqrt{(16/6)}, \sqrt{(20/6)}$

[a] $D = 2\pi/q^*$ and f is the volume fraction of block A
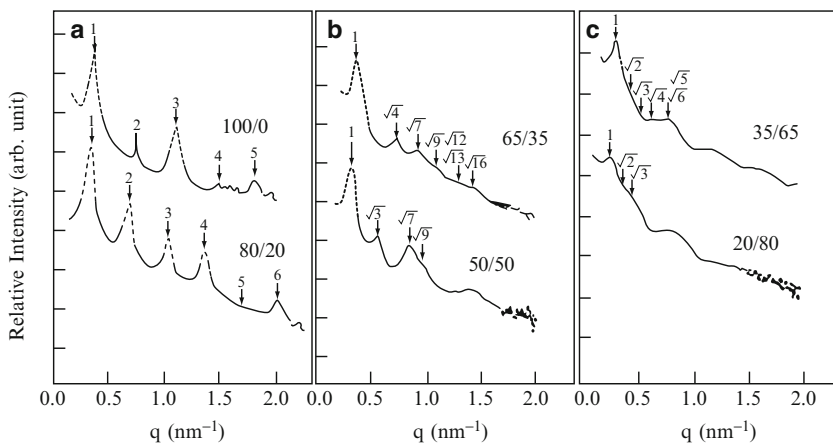
Fig. 12 SAXS profiles for SI diblock copolymer/homopolymer polystyrene (hPS) mixtures having different blend ratios (w/w). (**a**) Neat SI diblock copolymer and 80/20 SI/hPS mixture having lamellar microdomains. (**b**) 65/35 SI/hPS and 50/50 SI/hPS mixtures having cylindrical microdomains. (**c**) 35/65 SI/hPS and 20/80 SI/hPS mixtures having spherical microdomains. (Reprinted from Tanaka et al. [92]. Copyright © 1991, with permission from the American Chemical Society)

the relationship $I(q) \sim q^{-2}\left[\sin^2(q\lambda_{\mathrm{I}}/2)/(q\lambda_{\mathrm{I}}/2)^2\right]$ at higher q regimes for lamellar microdomains [91], in which it was assumed that the local volume fraction of block A, $\varphi_A(\mathbf{r})$, could be expressed by a step function across λ_{I}. For very small values of λ_{I}, the above expression reduces to $I(q) \sim q^{-2}\left[1-\left(\lambda_{\mathrm{I}}^2/12\right)q^2\right)\right]$. Thus, the negative slope of a plot of $I(q)q^2$ vs q^2 becomes $\lambda_{\mathrm{I}}^2/12$, from which λ_{I} can be determined.

Figure 12 gives SAXS profiles ($I(q)$ vs q plots) at room temperature for mixtures of SI diblock copolymer and homopolymer PS (hPS) [92]. The following observations are worth noting in Fig. 12. (1) When the weight fraction of hPS in the mixture is below 0.35, higher order SAXS peaks were observed at relative peak positions of 1, 2, 3, and 4, indicating that the mixtures had formed lamellar microdomains (see Table 3). (2) For values of the weight fraction of hPS between 0.35 and 0.5, the mixtures formed hexagonally packed cylindrical microdomains having the relative peak positions: $1, \sqrt{3}, \sqrt{4}$, and $\sqrt{7}$. (3) At higher weight fractions of hPS, the mixture formed spherical microdomains. According to Table 3, simple cubic lattice and bcc lattice have the same relative peak positions: $1, \sqrt{2}, \sqrt{3}$, and $\sqrt{4}$. However, the radius (R) of the spherical microdomains for the simple cubic lattice structure and the bcc lattice structure is distinctly different from each other, as given in Table 3. Thus, once the value of the volume fraction of block A is known, R can be calculated from Table 3. On the other hand, R can also be obtained experimentally from the form factor of spheres in SAXS profiles [90]. It should be pointed out that the spherical microdomain structure in neat block copolymers reported in the literature is bcc lattice, and not simple cubic lattice. Thus, above we have demonstrated that SAXS

Fig. 13 SAXS profiles of a compositionally symmetric SI diblock copolymer ($M_n = 8.5 \times 10^3$ and $M_w/M_n = 1.25$) in the disordered state obtained at various temperatures (°C): (1) 45, (2) 60, (3) 80, (4) 100, (5) 110, (6) 120, and (7) 140. (Reprinted from Mori et al. [42]. Copyright ©1985, with permission from the Society of Polymer Science, Japan)
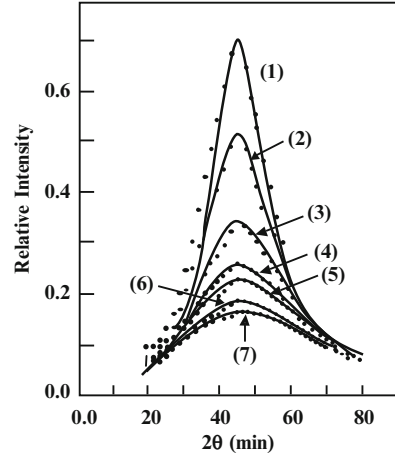
(likewise SANS) is a very powerful tool to investigate the microdomain structures of block copolymers either in the bulk state or in solution.

Figure 13 gives SAXS profiles of a low molecular weight compositionally symmetric SI diblock copolymer ($M_n = 8.5 \times 10^3$ and $M_w/M_n = 1.25$) in the disordered state obtained at various temperatures ranging from 45 to 140°C [42]. The readers are reminded that, according to (32), the scattering intensity $I(q)$ is proportional to the correlation function $\tilde{S}(q)$, commonly referred to as the structure factor. Thus, from (32) and (42) we have

$$I(q^*)^{-1} \sim F(x^*)/N - 2\chi \tag{79}$$

in which $F(x^*)$ is defined by (43) with x^* being given by (41). The solid lines in Fig. 13 were obtained by curve fitting SAXS profiles to (79) using the adjustable parameter χ. It is seen in Fig. 13 that the Leibler theory describes the experimental results very well. It should be mentioned that in the use of (32) and (34) or (42), the absolute scattering intensity, and not the relative scattering intensity, should be obtained from SAXS or SANS experiments. The measurement of the absolute scattering intensity by SAXS is a rather time-consuming process compared with that for SANS which gives directly the absolute scattering intensity.

When the following empirical relationship between χ and T:

$$\chi = a + b/T \tag{80}$$

is substituted into (79), we obtain

$$I(q^*)^{-1} \sim F(x^*)/N - 2a - 2b/T \tag{81}$$

where a and b are constants which are characteristic of the chemical structure of the block copolymer. According to (81), plots of $1/I_m$ vs $1/T$ are expected to be linear

Fig. 14 Plots of $1/I_m$ vs $1/T$ for a compositionally symmetric SI diblock copolymer ($M_n = 8.5 \times 10^3$ and $M_w/M_n = 1.25$). (Reprinted from Mori et al. [42]. Copyright © 1985, with permission from the Society of Polymer Science, Japan)
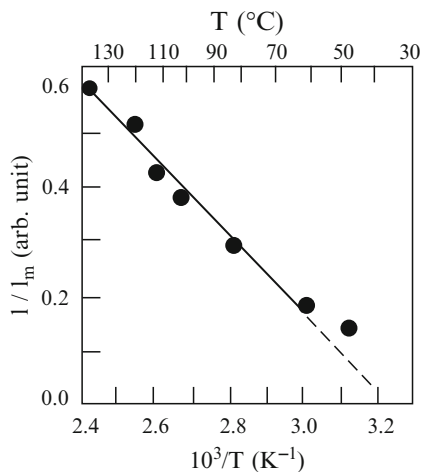
if the Leibler theory coupled with (80) is valid, in which, for simplicity, the notation I_m was used in place of $I(q^*)$. Indeed, this has turned out to be the case, as shown in Fig. 14. According to Mori et al. [42], the deviation of the data point at 45 °C, appearing in Fig. 14, from linearity is attributable to the fact that this temperature is very close to the glass transition temperature (T_g) of the polystyrene block of the SI diblock copolymer. Once information on the values of χ at different temperatures is available, determined from curve fitting SAXS (or SANS) profiles to the Leibler theory, one can prepare a plot of χ vs $1/T$ to determine the coefficients, a and b, appearing in (80). One such plot is given in Fig. 15 for the SI diblock copolymer, the SAXS profiles of which are given in Fig. 13. The resulting expression for the temperature dependence of $\chi(T)$ is given by (28). In the past a number of research groups [38, 42, 72, 80, 83, 84, 88, 89, 93–98] reported on a linear relationship between $1/I_m$ vs $1/T$ from SAXS or SANS experiments and subsequently obtained $\chi(T)$ for various block copolymers.

Above we have illustrated how one can determine $\chi(T)$ for block copolymers using the SAXS (or SANS) profiles obtained in the disordered state and how useful the Leibler theory is. Below we will illustrate how one can determine the T_{ODT} of microphase-separated block copolymers using SAXS or SANS.

Figure 16 gives SAXS profiles for three SI diblock copolymers, SI-Z ($f = 0.303$), SI-X ($f = 0.461$), and SI-L ($f = 0.811$) [94]. The molecular characteristics of the SI diblock copolymers are summarized in Table 4. The following observations are worth noting in Fig. 16. (1) The SAXS profiles of SI-Z given in Fig. 16a indicate that as the temperature is increased from 30 to 90 °C the first-order peak becomes very sharp, and at 90 °C (profile 6) the higher order scattering maximum appears at the scattering vectors q of 1, $\sqrt{3}$, and $\sqrt{7}$ relative to the position of the first-order scattering maximum, indicating that this block copolymer forms hexagonally packed cylindrical microdomains of PS in the PI matrix. (2) The SAXS profiles of SI-X given in Fig. 16b indicate that this block copolymer forms

Fig. 15 Plots of χ vs $1/T$ for a compositionally symmetric SI diblock copolymer ($M_n = 8.5 \times 10^3$ and $M_w/M_n = 1.25$). (Reprinted from Mori et al. [42]. Copyright © 1985, with permission from the Society of Polymer Science, Japan)
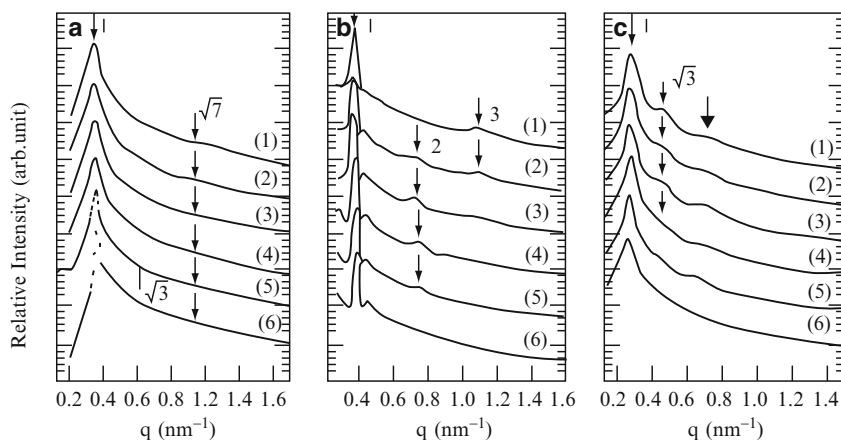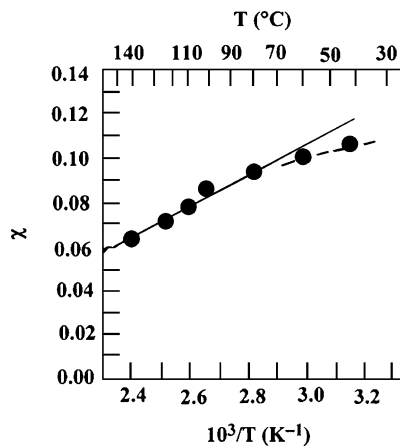
Fig. 16 SAXS profiles of three SI diblock copolymers having different block length ratios. (**a**) SI-Z ($M_w = 1.93 \times 10^4$; $w_{PS} = 0.336$; $f_{PS} = 0.30$) at various temperatures (°C): (1) 30, (2) 50, (3) 60, (4) 70, (5) 80, and (6) 90. (**b**) SI-X ($M_w = 1.79 \times 10^4$; $w_{PS} = 0.50$; $f_{PS} = 0.46$) at various temperatures (°C): (1) 25, (2) 50, (3) 70, (4) 90, (5) 100, and (6) 110. (**c**) SI-L ($M_w = 4.10 \times 10^4$; $w_{PS} = 0.833$; $f_{PS} = 0.81$) at various temperatures (°C): (1) 26, (2) 50, (3) 70, (4) 90, (5) 110, and (6) 130. (Reprinted from Ogawa et al. [94]. Copyright © 1996, with permission from the American Chemical Society)

lamellar microdomains of alternating layers of PS and PI lamellae as judged from the positions of higher order scattering maxima at the scattering vectors q of integer multiples relative to the position of the first-order scattering maximum. (3) The SAXS profiles of SI-L given in Fig. 16c indicate that this block copolymer forms either spherical or hexagonally packed cylindrical microdomains of PI in the PS matrix as judged from the positions of higher order scattering maxima at the scattering vectors q of 1 and $\sqrt{3}$ relative to the position of the first-order scattering peak maximum. Note in Table 4 that SI-L has a 0.189 volume fraction of PI.

Table 4 Molecular characteristics of the SI diblock copolymers synthesized by Han et al. [67]

Sample code	Block molecular weight (Mw)	M_w/M_n	PS block (wt frac)	f^a	N^b	$T_{g,PS}{}^c$
SI-Z	6500PS–*block*–12800PI	1.09	0.336	0.30	235	63
SI-X	8950PS–*block*–8950PI	1.07	0.500	0.46	213	66
SI-L	34200PS–*block*–6800PI	1.05	0.833	0.81	462	94

[a] f is the volume fraction of PS block in the SI diblock copolymer at 25 °C

[b] N is the total number of statistical segments at 25 °C, defined by $N = \left(M_{W,PS}v_{PS} + M_{W,PI}v_{PI}\right)/V_{ref}$, where $M_{W,PS}$ and $M_{W,PI}$ are the molecular weights of the PS and PI blocks, respectively, in the SI diblock copolymer, v_{PS} and v_{PI} are the specific volumes of PS and PI, respectively, and V_{ref} is the molar volume of a reference component

[c] After the specimens were aged for 8 months

An independent study with TEM has indicated that SI-L has hexagonally packed cylindrical microdomains [67]. A broad scattering peak at $q \cong 0.77\,\mathrm{nm}^{-1}$ appearing in Fig. 16c is attributable to the form factor of isolated particles. Again, we have demonstrated that SAXS is very powerful to identify the microdomain structures of the three SI diblock copolymers.

SAXS and SANS have been used to determine the T_{ODT} of microphase-separated block copolymers, by identifying the temperature at which the linearity of a plot of $1/I_m$ vs $1/T$ begins to show a discontinuity as the measurement temperature is increased from an ordered state or decreased from the disordered state [29, 84, 94, 96, 99–101]. Also, Stühn et al. [102] and Ehlich et al. [103] first introduced the concept of using the square of half width at the half maximum $\left(\sigma_q{}^2\right)$ of the first-order scattering maximum in SAXS experiments to determine the T_{ODT} of microphase-separated block copolymers. Later, Hashimoto and coworkers [94, 96, 99–101] used plots of $\sigma_q{}^2$ vs $1/T$ to determine the T_{ODT} of a microphase-separated block copolymer by identifying a temperature at which values of $\sigma_q{}^2$ begin to show discontinuity. Such plots have a theoretical basis in the mean-field theory [94].

Figure 17 gives plots of $1/I_m$ vs $1/T$ and plots of $\sigma_q{}^2$ vs $1/T$ for the three SI diblock copolymers, the SAXS profiles of which are given in Fig. 16. The following observations are worth noting in Fig. 17. (1) It is seen from Fig. 17a that plots of $1/I_m$ vs $1/T$ and plots of $\sigma_q{}^2$ vs $1/T$ show a sharp discontinuity over a narrow range of temperatures between 89 and 91 °C, indicating that the T_{ODT} of SI-Z is 90 ± 1 °C. (2) It is seen from Fig. 17b that plots of $1/I_m$ vs $1/T$ and plots of $\sigma_q{}^2$ vs $1/T$ show a sharp discontinuity at temperatures between 111 and 112 °C, indicating that the T_{ODT} of SI-X is 111 ± 0.5 °C. (3) Interestingly, however, in Fig. 17c no clear discontinuity is seen in the plots of $\sigma_q{}^2$ vs $1/T$ for SI-L. As will be discussed later, a similar observation has been made from an independent rheological investigation [67]. Based on the $\sigma_q{}^2$ vs $1/T$ plot given in Fig. 17c, we can only conclude that the T_{ODT} of SI-L lies between 130 and 150 °C. Such a very broad range for the phase transition temperature has seldom been observed in microphase-separated block copolymer. Later we will return to this issue when we discuss the T_{ODT} of SI-L determined from a rheological method.
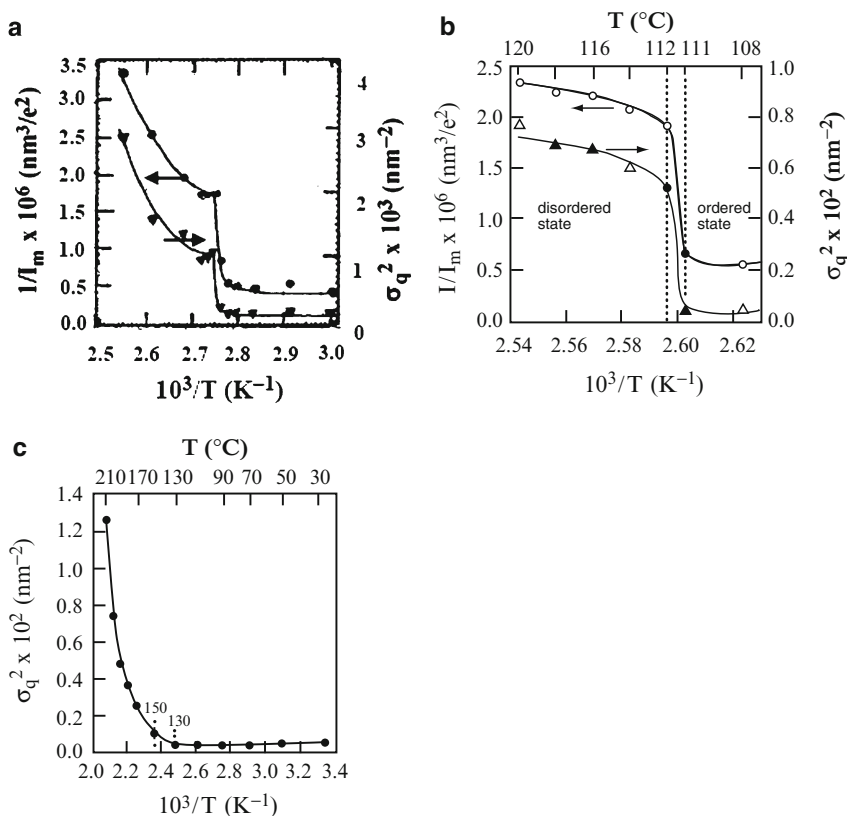
Fig. 17 Plots of $1/I_m$ vs $1/T$ and σ_q^2 vs $1/T$ for three SI diblock copolymers having different block length ratios. (**a**) SI-Z ($M_w = 1.93 \times 10^4$; $w_{PS} = 0.336$; $f_{PS} = 0.30$). (**b**) SI-X ($M_w = 1.79 \times 10^4$; $w_{PS} = 0.50$; $f_{PS} = 0.46$). (**c**) SI-L ($M_w = 4.10 \times 10^4$; $w_{PS} = 0.833$; $f_{PS} = 0.81$). (Reprinted from Ogawa et al. [94]. Copyright © 1996, with permission from the American Chemical Society)

3.2 Rheological Methods

Here we review different rheological methods for determining the T_{ODT} of microphase-separated block copolymers. For such purposes, we consider the linear dynamic viscoelasticity of the two SI diblock copolymers, SI-X and SI-L, the SAXS profiles of which were presented in Fig. 16. In Fig. 18, the left-side panel gives logarithmic plots of dynamic storage modulus (G') vs angular frequency (ω) and logarithmic plots of dynamic loss modulus (G'') vs ω at various temperatures for lamella-forming SI-X, and the right-side panel of Fig. 18 gives logarithmic plots of G' vs G'' at various temperatures for the same block copolymer. In reference to Fig. 18, some of the symbols are not so clearly distinguishable, because the size of the original drawing was reduced very much. To see Fig. 18 in more detail the readers are referred to the original paper [67].
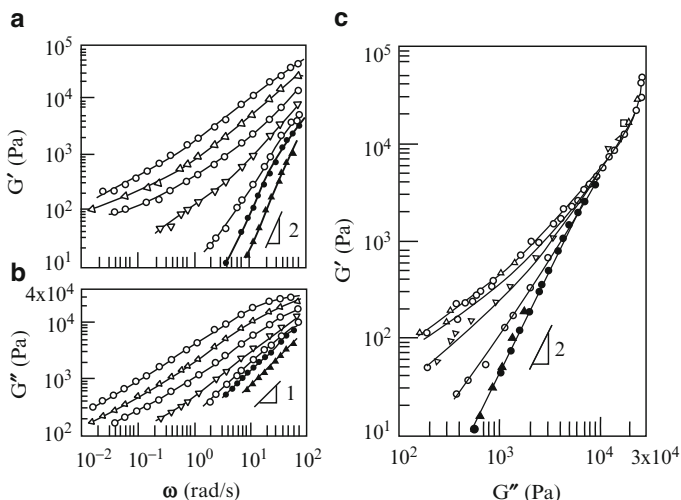
Fig. 18 Plots of (**a**) log G' vs log ω, (**b**) log G'' vs log ω, and (**c**) plots of log G' vs log G'' for SI-X ($M_w = 1.79 \times 10^4$; $w_{PS} = 0.50$; $f_{PS} = 0.464$) at various temperatures (°C): (○)100, (△)105, (□)110, (▽)115, (◇)117, (●)120, and (▲)125. (Reprinted from Han et al. [67]. Copyright © 1995, with permission from the American Chemical Society)

In the past, time-temperature superposition (TTS) has successfully been applied to linear dynamic viscoelastic properties of homopolymers to obtain temperature-independent reduced plots, sometimes referred to as master plots. In applying TTS, log G' vs log ω (or log G'' vs log ω) plots are often shifted along the ω-axis to a plot at an arbitrarily chosen reference temperature with an expectation that the plots at various temperatures would overlap with the plot at a reference temperature, yielding a single temperature-independent master plot. The degree of shift made along the ω-axis would produce, if successful, a temperature-dependent shift factor $a_T(T)$ from which one will be able to prepare master plots, log G' vs log $a_T\omega$ plots and log G'' vs log $a_T\omega$ plots. However, the expectation for obtaining master plots can be realized only when log G' vs log ω plots (or log G'' vs log ω plots) at various temperatures have the same or nearly the same shape along the ω-axis.

Upon visual inspection of the log G' vs log ω and log G'' vs log ω plots given on the left-side panel of Fig. 18, it is very obvious that master plots will not be obtained and hence application of TTS would fail. There is a more compelling, fundamental reason why TTS would fail for microphase-separated block copolymers which consist of two chemically dissimilar, thermodynamically incompatible blocks. For the details of this subject, the readers are referred to the recent monograph by Han [31].

In the past three decades numerous research groups [72, 104–122] have erroneously applied TTS to microphase-separated block copolymers in attempts to determine T_{ODT} by constructing master plots, log G' vs log $a_T\omega$ plots, from the values of a_T obtained by shifting log G' vs log ω plots along the ω-axis or by calculating a_T using the Williams–Landel–Ferry (WLF) equation [123]. On the basis of the comments made above, such an approach is *not* warranted.

An alternative approach to determine the T_{ODT} of microphase-separated block copolymers using the experimental data obtained from linear dynamic viscoelasticity measurements has been used very successfully by preparing log G' vs log G'' plots as given, for instance, on the right-side panel of Fig. 18. Such plots can be prepared directly from log G' vs log ω and log G'' vs log ω plots without having to manipulate raw experimental data. According to the rheological criterion introduced by Han and coworkers [39, 41, 124], the T_{ODT} of a microphase-separated block copolymer can be determined by identifying the lowest temperature, during heating, at which log G' vs log G'' plot begins to be independent of temperature. The theoretical basis of this rheological criterion is well documented, the details of which can be found in the recent monograph by Han [31]. Hence, by applying the rheological criterion described above to the right-side panel of Fig. 18 we determine the T_{ODT} of SI-X to be about 120 °C, which is reasonably close, within experimental uncertainties, to the value of T_{ODT} determined from SAXS experiment (see Fig. 17b).

The left-side panel of Fig. 19 gives log G' vs log ω and log G'' vs log ω plots at various temperatures, and the right-side panel of Fig. 19 gives log G' vs log G'' plots at various temperatures for cylinder-forming SI-L, in which PI cylinders are in the PS matrix. In reference to Fig. 19, some of the symbols are not so clearly distinguishable, because the size of the original drawing was reduced so much. To see Fig. 19 in more detail the readers are referred to the original paper [67]. It is clear from the left-side panel of Fig. 19 that TTS would fail. By applying the rheological criterion described above to the log G' vs log G'' plots given on the right-side panel of Fig. 19, we determined the T_{ODT} of SI-L to be about 170 °C, which is 20–40 °C
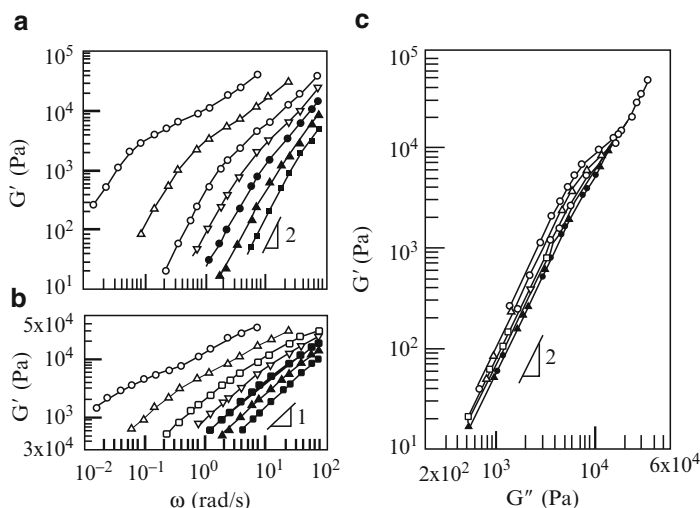
Fig. 19 Plots of (**a**) log G' vs log ω, (**b**) log G'' vs log ω, and (**c**) plots of log G' vs log G'' for SI-L ($M_w = 4.10 \times 10^4$; $w_{PS} = 0.833$; $f_{PS} = 0.81$) at various temperatures (°C): (○)140, (Δ)150, (□)160, (∇)165, (●)170, (▲)175, and (■)180. (Reprinted from Han et al. [67]. Copyright © 1995, with permission from the American Chemical Society)

higher than the value of T_{ODT} determined from SAXS experiment (see Fig. 17c). In the absence of a sharp discontinuity in the plot of σ_q^2 vs $1/T$ given in Fig. 17c, it is fair to state that the value of T_{ODT} determined from the log G' vs log G'' plots given on the right-side panel of Fig. 19 is more reliable than that determined from Fig. 17c. However, it is worth pointing out a very unusual feature of the log G' vs log G'' plots for SI-L given on the right-side panel of Fig. 19 in that the log G' vs log G'' plots at all measurement temperatures employed are parallel to each other until reaching 170 °C, at which point they begin to overlap with each other as the temperature is increased further to 175 and 180 °C. Such a parallel shift of log G' vs log G'' plots with increasing temperature until reaching a certain critical temperature was *not* seen from Fig. 18c for SI-X. The only difference between SI-L and SI-X from a morphological point of view is that SI-L is a highly asymmetric SI diblock copolymer having a 0.189 volume fraction of PI block, in which PI cylindrical microdomains are in the PS matrix, whereas SI-X is a nearly symmetric SI diblock copolymer having microdomains of alternating layers of PS and PI lamellae. We hasten to point out that a parallel shift of log G' vs log G'' plots with increasing temperature until reaching a certain critical temperature has also been observed in highly asymmetric SI diblock and SIS triblock copolymers in which PS spherical microdomains are in the PI matrix [62, 125–127] and in a highly asymmetric polystyrene-*block*-poly(ethylene-*co*-1-butene)-*block*-polystyrene copolymer in which PS spherical microdomains are in the poly(ethylene-*co*-1-butene) matrix [128]. The origin of such experimental observations will be elaborated on later in this chapter.

Another rheological method for determining the T_{ODT} of a microphase-separated block copolymer is to conduct isochronal dynamic temperature sweep experiments. Figure 20 gives the temperature dependence of G' for (a) SI-X and (b) SI-L which was obtained from isochronal dynamic temperature sweep experiments. According to the rheological criterion advocated by Gouinlock and Porter [113], the T_{ODT} of a microphase-separated block copolymer may be determined by identifying the temperature at which values of G' begin to drop precipitously.

Using this rheological criterion, from Fig. 20a we determine the T_{ODT} of SI-X to be 115 ± 3 °C which is reasonably close, within experimental uncertainties, to that (120 °C) determined from log G' vs log G'' plots (see Fig. 18c). However, from Fig. 20b we cannot find a temperature at which values of G' begin to drop precipitously for SI-L, although we observe an initial change in slope of the plot of log G' vs T at about 150 °C and a second change in slope at about 170 °C, which is very close to the T_{ODT} of SI-L determined from log G' vs log G'' plots (see Fig. 19b). Thus we conclude that the isochronal dynamic temperature sweep experiment is not as effective as the method of using log G' vs log G'' plot to determine the T_{ODT} of a highly asymmetric SI diblock copolymer having cylinder- (or sphere-) forming PI microdomains in the PS matrix.

Table 5 compares experimentally determined T_{ODT}s of three SI diblock copolymers, SI-Z, SI-X, and SI-L, with predictions from the H–W theory and Leibler theory, respectively, which were presented in a previous section. It is seen in Table 5 that the predicted T_{ODT}s from the Leibler theory are much higher than those from

a   **b**
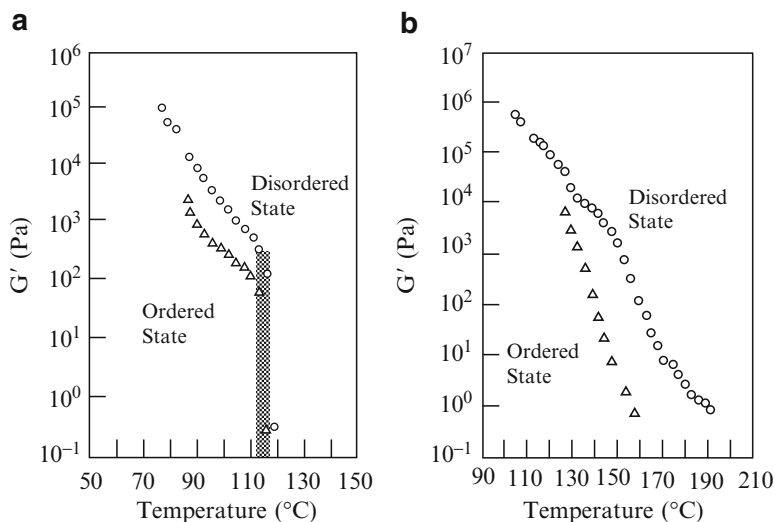
Fig. 20 Variation of G' with temperature obtained at $\omega = 0.5 (\bigcirc)$ and $\omega = 0.10$ rad s^{-1}($\triangle$) for: (**a**) SI-X ($M_w = 1.79 \times 10^4$; $w_{PS} = 0.50$; $f_{PS} = 0.46$), from which the T_{ODT} of this block copolymer is determined to be about 115°C; (**b**) SI-L ($M_w = 4.10 \times 10^4$; $w_{PS} = 0.833$; $f_{PS} = 0.81$), in which no sudden drop in G' is discernible and thus it is not possible to determine the T_{ODT} of this block copolymer from this plot. (Reprinted from Han et al. [67]. Copyright © 1995, with permission from the American Chemical Society)

Table 5 Comparison of measured T_{ODT} with prediction for the SI diblock copolymers synthesized by Han et al. [67]

Sample code	Measured T_{ODT} (°C)	Equations employed	Predicted T_{ODT} (°C)	
			H–W theory	**Leibler theory**
SI-Z	90	(26)	113	182
		(28)	87	150
SI-X	120	(26)	142	216
		(28)	113	181
SI-L	170	(26)	161	195
		(28)	131	161

the H–W theory, as compared with the experimentally measured T_{ODT}s. We wish to point out that the prediction of the T_{ODT} of SI-L using the mean-field theories may not be warranted for the reason mentioned above when log G' vs log G'' plots were presented in Fig. 19c. Namely, SI-L exhibits a parallel shift in log G' vs log G'' plot in the ordered state until reaching a certain critical temperature. This rheological behavior has only been observed for highly asymmetric block copolymers. Below we will discuss the physical origin(s) of the parallel shift in log G' vs log G'' plots with temperature for highly asymmetric block copolymers.

Table 6 Summary of computed $(\chi N)_t$ and coefficients associated with (47) for the SI diblock copolymers synthesized by Han et al. [67]

Sample code	c	τ^*	d	λ	$\tilde{N}$	$(\chi N)_s$	$(\chi N)_t$	T_{ODT} (°C)
SI-Z	1.205	−1.695	1.927	234.3	854	14.6	22.3	11
SI-X	1.106	−2.031	1.812	110.5	742	10.6	15.3	68
SI-L	1.409	−1.636	2.163	629.0	1505	26.3	43.4	9

Table 6 summarizes numerical values for the parameters c, τ^*, λ, and $\tilde{N}$ appearing in (47) for three SI diblock copolymers SI-Z, SI-X, and SI-L. It is seen in Table 6 that the calculated values of $(\chi N)_t$ are much higher than those of $(\chi N)_s$, which is the prediction from the Leibler theory. This observation clearly indicates that the fluctuation correction of the Leibler theory by the F–H fluctuation theory would underpredict the T_{ODT} of the three SI diblock copolymers, because the larger the value of $(\chi N)_t$ the smaller the value of predicted T_{ODT}. This indeed turns to be the case as it is shown in Table 6 that the calculated T_{ODT}s from $(\chi N)_t$ are 11 °C for SI-Z, 68 °C for SI-X, and 9 °C for SI-L. These values are much lower than the experimentally measured T_{ODT}s of the three SI diblock copolymers, given in Table 5. The above observation is not surprising in that the values of $\tilde{N}$ for the three SI diblock copolymers given in Table 6 are an order of magnitude smaller than the values of $\tilde{N}\left(>10^4\right)$ at which use of the F–H fluctuation theory is warranted, as discussed in a previous section.

3.3 Birefringence Method

Besides SAXS (or SANS) and rheological methods, the T_{ODT} of a block copolymer can also be determined from plots of temporal change in birefringence. A distinct birefringence is observed in the ordered state, due to optical anisotropy within the ordered microdomains. On the other hand, the disordered state does not exhibit any birefringence due to its isotropic nature. Thus, with increasing temperature, the birefringence (or depolarizing light scattering intensity) drops precipitously at the T_{ODT} of a block copolymer. This method is relatively simple compared with scattering or rheological methods, and the required sample size is relatively small.

Due to the anisotropic nature of birefringence, the microdomain structure should be lamellar or cylindrical to determine the T_{ODT} by this method. Therefore, for block copolymers having spherical microdomains or double gyroids in the ordered state, no birefringence is expected. Figure 21 shows the changes in birefringence (B_∞) and G' (at $\omega = 10$ rad s^{-1}) with temperature for a 50.8/49.2 (w/w) SI/bis(2-ethylhexyl) phthalate solution [129]. It is seen from Fig. 21 that a distinct birefringence is observed at lower temperatures, which drops precipitously at 77 ± 2 °C, the T_{ODT} of this polymer solution. The T_{ODT} measured by birefringence was found to be consistent with that determined by the isochronal dynamic temperature sweep experiment of G', as also shown in Fig. 21.
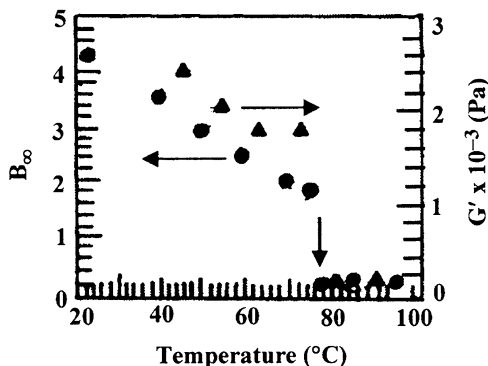
Fig. 21 Variation of birefringence (B_∞) (●) and G' (▲) at $\omega = 10$ rad s^{-1} with temperature for a 50.8/49.2 (w/w) SI diblock copolymer/bis(2-ethylhexyl)phthalate solution. (Reprinted from Balsara et al. [129]. Copyright © 1992, with permission from the American Chemical Society)

It should be pointed out that there is no way of knowing whether the T_{ODT} or T_{OOT} measured by the above-mentioned methods (radiation scattering, rheology, or birefringence) is a first-order or second-order thermodynamic transition, since none of the measured properties is a thermodynamic parameter. Thus, when first-order thermodynamic properties such as volume and entropy of a block copolymer are measured, one can easily determine whether T_{ODT} and T_{OOT} are first-order transitions. When either an exothermic or endothermic peak is observed in a differential scanning calorimetry thermogram at a certain critical temperature, except at a peak corresponding to an enthalpy relaxation near the T_g, such a transition is considered to be a first-order transition. Also, when volume is measured via dilatometry and a discontinuity in volume changes is observed at a certain critical temperature, that temperature can be regarded as signifying the onset of a first-order transition. Some research groups [57, 130–132] observed an endothermic peak occurring at T_{ODT} for lamella-forming SI diblock copolymers, although the size of the peak was small. Kim et al. [57] observed that the T_{OOT} between hexagonally-packed cylinders and bcc lattice in an SIS triblock copolymer having a 0.183 weight fraction of PS block was a first-order transition. Kasten and Stühn [130] observed a discontinuity in volume changes occurring at T_{ODT} for a lamella-forming SI diblock copolymer, while Ryu et al. [133] observed a similar behavior for a lamella-forming PS-*block*-poly (*n*-pentyl methacrylate) copolymer.

4 Some Unresolved Issues on Phase Behavior and Phase Transitions in Microphase-Separated Block Copolymers

There are several unresolved issues in having a better understanding of phase behavior and phase transitions in block copolymers. Owing to the space limitation here,

below we will address only two issues along the lines of the material presented above.

4.1 Finite Molecular Weight Effect

All of the mean-field theories summarized in the previous sections do not consider the effect of compositional fluctuations on microphase-separation transitions in block copolymers. In principle, the compositional fluctuation effect becomes negligible for block copolymers having infinitely high molecular weight. The F–H theory includes the compositional fluctuation effect on the ODT of an AB-type diblock copolymers with finite molecular weights. However, as pointed out in a previous section, the F–H theory cannot predict the T_{ODT} of AB-type diblock copolymers having spherical microdomains unless their molecular weights are very high (i.e., for $\tilde{N} > 4 \times 10^4$), while the molecular weights of many diblock block copolymers commonly used in experiments are on the order of up to about $\tilde{N} = 10^3$. This is because one cannot achieve the disordered state in a block copolymer without encountering thermal degradation when its molecular weight is exceedingly high (say, values of $\tilde{N}$ as high as 10^4). Therefore, we have a very compelling need for the development of a better theory that can adequately describe the phase behavior and phase transitions in microphase-separated block copolymers having the lower molecular weights commonly encountered in experiment.

Above we have shown that the currently held mean-field theories of block copolymers require information on the segment-segment interaction parameter χ (or α), which in principle would depend not only on temperature but also on the molecular weight and block length ratio (composition) of a block copolymer. But thus far, we have only discussed the temperature-dependent expressions for χ (or α) (see, for example, (26) and (28)). The fundamental question that remains to be resolved is the effect of molecular weight, in particular, on χ (or α), as we have already demonstrated that the molecular weight of a block copolymer greatly influences its T_{ODT}. Therefore, it is of fundamental importance to understand the accuracy of the predicted T_{ODT} of a block copolymer, based on an expression for χ (or α) which has included the effect of molecular weight.

Extending the lattice cluster theory [134, 135] Freed and Dudowicz [136] and Dudowicz and Freed [137] obtained the following expression for χ:

$$\chi = (a + b/N) + (c + d/N)/T \tag{82}$$

in which N denotes the degree of polymerization, and a, b, c, and d are constants characteristic of the polymer. Note that (82) reduces to (80) for very large values of N (see (26) and (28)). However, it is very difficult to obtain experimentally the molecular weight dependent χ, and thus values of b and d appearing in (82), for the practical reason that a block copolymer having high molecular weight usually undergoes thermal degradation before reaching its disordered state (since the T_{ODT}

of a block copolymer increases with molecular weight). Therefore, in practice one is forced to use expressions for χ, which were determined for block copolymers having relatively low molecular weights, to predict the phase behavior and the T_{ODT} of block copolymers having molecular weights much higher than those employed for obtaining the expression for χ (or α). Owing to the practical difficulty in obtaining χ values for reasonably high molecular weight block copolymers, as often encountered in research, it is highly desirable to develop a molecular approach which will enable one to estimate values of the constants b and d appearing in (82).

There are two ways of determining experimentally expressions for the segment-segment interaction parameter $\chi(T)$ (or $\alpha(T)$): one method is to obtain a structure factor for AB-type diblock copolymers using the Leibler theory [13] and another method is to construct equilibrium phase diagrams for binary pairs of homopolymers A and B using the Flory–Huggins theory. A fundamental question to ask is whether it is possible to obtain a common $\chi(T)$ (or $\alpha(T)$) from the two different experimental methods. Earlier, Maurer et al. [138] posed the same question and conducted SANS experiments using mixtures of polyethylene (PE) and poly(ethylene propylene) (PEP) of equal molecular weight, and PE-*block*-PEP copolymers. They concluded that a common $\chi(T)$ (or $\alpha(T)$) could not be determined from their experiments and suggested that a more sophisticated block copolymer theory be developed that can take into account chain polarization and stretching in the vicinity of the T_{ODT} of a block copolymer.

Interestingly, the H–W theory predicts χN of about 17 for AB-type lamella-forming ($f = 0.5$) diblock copolymers (see Fig. 8), which is close to the experimentally determined value. It has been our experience over the years that the predicted T_{ODT} of AB-type diblock copolymers from the H–W theory are often closer to the experimentally determined values [39, 41, 67, 98] than the values predicted from the Leibler theory or SCMFT. It should be remembered that all three theories do not include the effect of composition fluctuations. On the other hand, as pointed out above, at present the use of the Leibler theory with the fluctuation correction due to Fredrickson and Helfand [33] is not warranted for relatively low molecular weight (say $\tilde{N} < 2000$) diblock copolymers, as is often used in experimental investigations.

Therefore we suggest that a new theory for block copolymers, which takes into account the fluctuation effect, be developed such that it can help accurately predict the phase behavior and the T_{ODT} of relatively low molecular weight, microphase-separated block copolymers having values of $\tilde{N}$ in the range from 500 to 2000, as are often encountered in many experimental investigations. Such theoretical capability will greatly help synthetic polymer chemists who wish to design and synthesize block copolymers having a specific microdomain structure and T_{ODT}. We are of the opinion that future theoretical development for predicting the phase behavior and phase transitions in microphase-separated block copolymers should go far beyond the traditional concept of mean-field theory. Namely, although one may argue that the average force in a given block copolymer chain may be assumed not to change much from one position to another, the interaction (or repulsion) between the two blocks of a given diblock copolymer chain might be position-dependent. Due to the presence of connectivity (i.e., junction point) of a block copolymer chain, the force

near the junction point of a block copolymer chain can be quite different from the average over the whole space. In other words, one may have to depart from the concept of traditional mean-field theory in the development of a new block copolymer theory.

4.2 Phase Transitions in Highly Asymmetric Block Copolymers

It is well established today that during heating, lamella-forming symmetric block copolymers lose long-range order at a critical temperature T_{ODT} and transform into the disordered phase with thermally-induced composition fluctuations. However, the readers are reminded of the different temperature dependencies of log G' vs log G'' plots between SI-X and SI-L, shown in Fig. 18c and Fig. 19c, as each of the two block copolymers was heated from a low temperature in an ordered state. It is very clear from Figs. 18c and 19c that the temperature dependence of log G' vs log G'' plots of the highly asymmetric SI-L is conspicuously different from that of the symmetric SI-X, suggesting that the mechanism associated with the phase transition in a highly asymmetric block copolymer might be quite different from that in a symmetric (or nearly symmetric) block copolymer. The central question one must answer is whether a highly asymmetric block copolymer undergoes the same phase transition as a symmetric (or nearly symmetric) block copolymer. This is, among others, one of the as yet unresolved issues in block copolymer research. Since we consider that this issue is important enough to warrant serious investigations in the future, below we will elaborate on this issue in order to set the stage for future investigation.

To facilitate our discussion, in Fig. 22 we have plots of log G' vs log G'' plots for a *highly asymmetric* solvent-cast SIS triblock copolymer (SIS-110) having a 0.16 weight fraction of PS block and $M_n = 1.06 \times 10^5$ at various temperatures, during heating, ranging from 140 to 214°C [126]. It is seen in Fig. 22 that the log G' vs log G'' plot begins to exhibit a parallel shift at 164°C, which continues until reaching about 200°C, above which they virtually overlap each other. Parallel shift in log G' vs log G'' plots has also been observed in a highly asymmetric commercial SIS triblock copolymer (Vector 4111, Dexco Polymers Co.) [62], in a highly asymmetric SI diblock copolymer [127], and in a highly asymmetric polystyrene-*block*-poly(ethylene-*co*-1-butene)-*block*-polystyrene (SEBS diblock) copolymer [128]. Since the data points at temperatures above 180°C given in Fig. 22 are very crowded on the plot, an enlarged section of the log G' vs log G'' plots given in Fig. 22 for the values of G' ranging from 10^2 to 10^3 Pa and G'' ranging from 6×10^2 to 3×10^3 Pa is shown in Fig. 23, in which the dynamic frequency sweep data were taken a temperature interval of 2°C from 200 to 214°C. The following observations are worth noting in Figs. 22 and 23. SIS-110 loses long-range order at a critical temperature corresponding to the lattice disorder–order transition (LDOT) temperature (T_{LDOT}) at approximately 166°C and transforms into disordered micelles with short-range order exhibiting liquidlike behavior in the terminal region. Upon
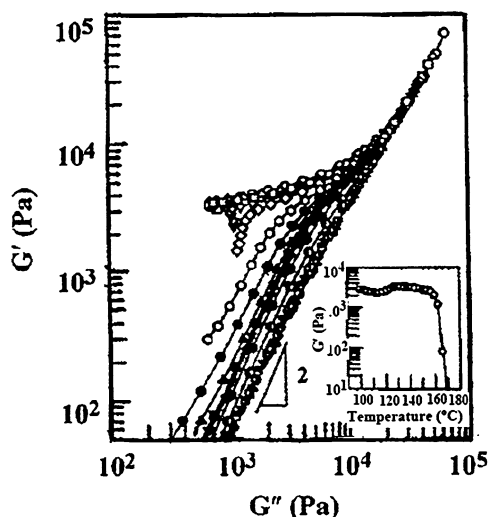
Fig. 22 Log G' vs log G'' plots for a highly asymmetric solvent-cast SIS triblock copolymer (SIS-110) ($M_w = 1.06 \times 10^5$; $w_{PS} = 0.16$; $f_{PS} = 0.16$) during heating at various temperatures (°C): (○)140, (△)151, (□)155, (▽)160, (◇)162, (◎)164, (●)166, (▲)168, (■)170, (▼)172, (◆)174, (●)180, (◐)190, (▲)200, (▥)202, (▼)204, (◓)206, (◑)208, (△)210, (▤)212, and (▼)214. Prior to the rheological measurements, the specimen was annealed at 110°C for 3 days. The *inset* describes the temperature dependence of G' obtained from the isochronal dynamic temperature sweep experiment at $\omega = 0.01$ rad s^{-1} during heating. (Reprinted from Choi et al. [126]. Copyright © 2003, with permission from the American Chemical Society)

further heating, the log G' vs log G'' plot having a slope of 2 in the terminal region becomes virtually independent of temperature and the disordered micelles transform into the micelle-free disordered phase with thermally-induced composition fluctuations at another critical temperature corresponding to the demicellization–micellization transition (DMT) temperature (T_{DMT}) at approximately 208°C. That is, SIS-110 attains a micelle-free disordered phase with thermally-induced fluctuations at $T \geq 208$°C. According to Sakamoto et al. [62] and Han et al. [127], LDOT in a highly asymmetric block copolymer is a first-order transition like ODT in a lamella-forming block copolymer, but the distinction between LDOT and ODT is necessary because LDOT is followed by another phase transition, DMT, at a higher temperature at which point the disordered micelles disappear completely.

Also, given in the inset of Fig. 22 are plots of isochronal dynamic temperature sweep experiments for SIS-110. It is seen in the inset of Fig. 22 that values of G' go through a minimum at about 120°C, which corresponds to T_{OOT} from hexagonally packed cylindrical microdomains to spherical mircodomains in a bcc lattice, followed by a very slight maximum, and then start to decrease precipitously at about 165°C, which corresponds to T_{LDOT} It should be pointed out that the T_{DMT} of SIS-110 cannot be determined from the isochronal dynamic temperature sweep experiments.
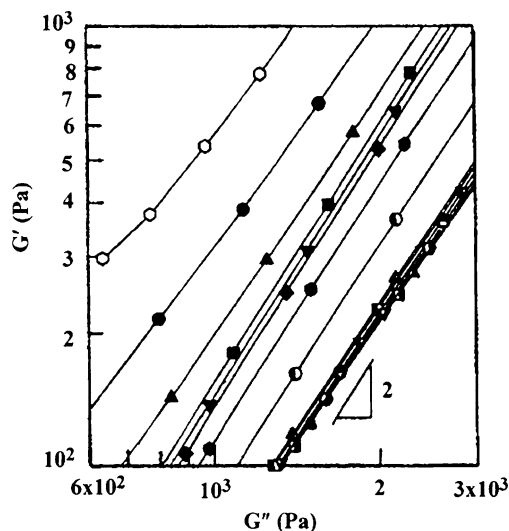
Fig. 23 Enlarged section of log G' vs log G'' plots for the highly asymmetric SIS-110 given in Fig. 22, for the values of G' ranging from 10^2 to 10^3 Pa and G'' ranging from 6×10^2 to 3×10^3 Pa at various temperatures (°C): (○)164, (●)166, (▲)168, (■)170, (▼)172, (◆)174, (●)180, (◐)190, (▲)200, (▥)202, (▼)204, (◗)206, (◑)208, (△)210, (▯)212, and (▽)214. Prior to the rheological measurements, the specimen was annealed at 110°C for 3 days. (Reprinted from Choi et al. [126]. Copyright © 2003, with permission from the American Chemical Society)

Interestingly, Rosedale and Bates [118] also observed a parallel shift in the log G' vs log G'' plots of a *nearly symmetric* poly(ethylene propylene) (PEP)-*block*-poly(ethylethylene) (PEE) copolymer. They attributed this observation to the thermally-induced composition fluctuations near the T_{ODT}. However, to date no investigation has ever reported a parallel shift in log G' vs log G'' plots for *nearly symmetric* SI diblock copolymers [67, 127] (see Fig. 18c, for example) and SIS triblock copolymers [126]. If indeed the assertion made by Rosedale and Bates [118] was valid, one is led to conclude that symmetric (or nearly symmetric) SI diblock and SIS triblock copolymers would not be susceptible to the thermally-induced composition fluctuations near the T_{ODT}. On the other hand, there is no reason why one should observe the thermally-induced composition fluctuations near the T_{ODT} for only nearly symmetric PEP-*block*-PEE copolymer but not for nearly symmetric SI diblock and SIS triblock copolymers if a parallel shift in log G' vs log G'' plots for lamella-forming block copolymers was a common attribute for all symmetric (or nearly symmetric) block copolymers. Thus, we are of the opinion that the assertion made by Rosedale and Bates on the origin of a parallel shift observed in the log G' vs log G'' plots with increasing temperature of a nearly symmetric PEP-*block*-PEE copolymer is not warranted [31].

The existence of the disordered micelles in SIS-110 are easily detected by SAXS measurements, as shown in Fig. 24 [126]. The following observations are worth noting in Fig. 24. SIS-110 has hexagonally packed cylindrical microdomains at lower
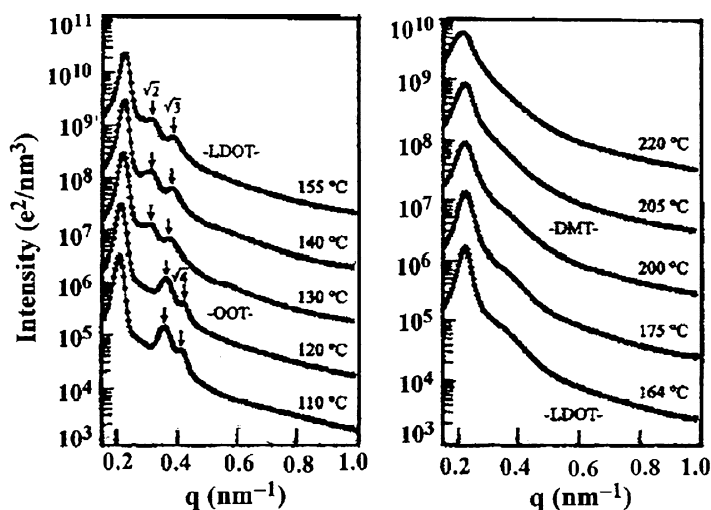
Fig. 24 SAXS profiles for the highly asymmetric SIS-110 during the heating process at various temperatures as indicated on the plot. Prior to the SAXS experiment, the specimen was annealed at 110°C for 3 days. (Reprinted from Choi et al. [126]. Copyright © 2003, with permission from the American Chemical Society)

temperature, and spherical microdomains in a bcc lattice of PS are formed between 120 and 130°C. The spherical microdomains in a bcc lattice with characteristic peak positions of 1, $\sqrt{2}, \sqrt{3}$, relative to the first order peak (see Table 3), are observed until reaching about 155°C. However, at 164°C, these peaks are not distinct and become very broadly shouldered. Interestingly, this shoulder disappears at $T > 205$°C. Thus, Choi et al. concluded from the SAXS profiles that T_{LDOT} lies between 155 and 164°C, and T_{DMT} lies between 200 and 205°C, the observation of which is consistent with that made above from the rheological experiments as shown in Figs. 22 and 23. Sakamoto and Hashimoto [101] also observed, via SAXS, the presence of disordered micelles in a highly asymmetric commercial SIS triblock copolymer (Vector 4111, Dexco Polymers Co.).

The existence of disordered micelles in SIS-110 at temperatures between T_{LDOT} (ca. 165°C) and T_{DMT} (ca. 205°C) can directly be observed from the TEM images given in Fig. 25. According to Choi et al. [126], the specimens used for the TEM images were solvent cast followed by annealing in a vacuum oven at 110°C for 3 days to completely remove the solvent. The TEM images given in Fig. 25 had the following thermal histories: the image (a) was obtained after further annealing at 110°C for 1 h followed by rapid quenching in ice water, the image (b) was obtained after further annealing at 140°C for 1 h followed by rapid quenching in ice water, and the image (c) was obtained after further annealing at 175°C for 1 h followed by rapid quenching in ice water. The following observations are worth noting in Fig. 25. SIS-110 has hexagonally packed cylindrical microdomains of PS at 110°C. As the temperature is increased to 140°C, SIS-110 has spherical microdomains in a bcc lattice of PS. As the temperature is increased further to 175°C, the spherical
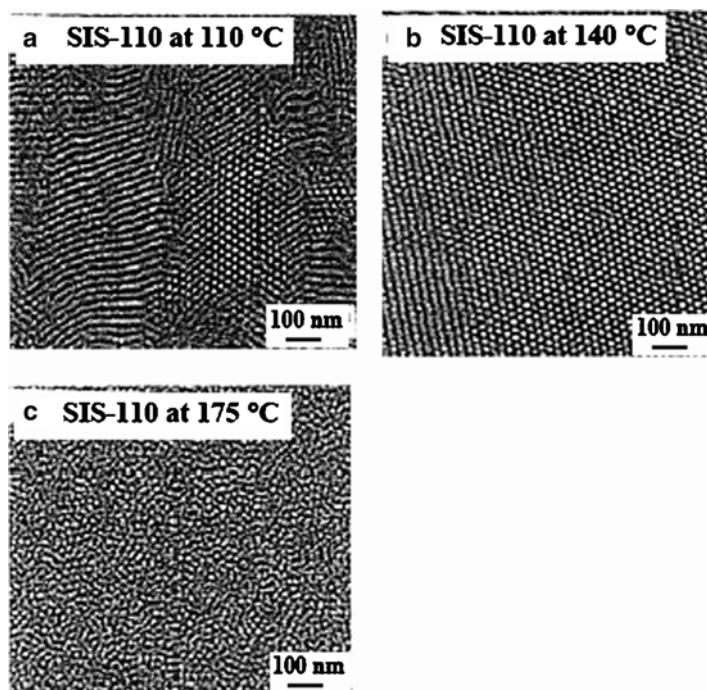
Fig. 25 TEM images of the highly asymmetric SIS-110, which had been annealed at 110°C for 3 days and then annealed further at: (**a**) 110°C for 1 h followed by a rapid quench in ice water; (**b**) 140°C for 1 h followed by a rapid quench in ice water; (**c**) 175°C for 1 h followed by a rapid quench in ice water. (Reprinted from Choi et al. [126]. Copyright © 2003, with permission from the American Chemical Society)

microdomains of SIS-110 have lost long-range order, giving rise to disordered micelles. Note in Fig. 25c that the disordered micelles at 175°C have a *very distinct interface*, which is in the region where log G' vs log G'' plots have a parallel feature (see Figs. 22 and 23) exhibiting liquidlike behavior. Note that 175°C is about 10°C higher than the temperature at which values of G' begin to drop precipitously in the isochronal dynamic temperature sweep experiments (see the inset of Fig. 22). Since the disordered micelles at 175°C, shown in Fig. 25c, have a very sharp interface which cannot be regarded as being part of frozen composition fluctuations [139], the T_{LDOT} of SIS-110 must be distinguished from the T_{ODT} commonly observed in symmetric (or nearly symmetric) block copolymers. It should be mentioned that disordered micelles have also been observed in highly asymmetric SI diblock copolymer [127], commercial SIS triblock copolymer (Vector 4111, Dexco Polymers Co.) [62, 101], SEBS triblock copolymer [128], and polystyrene-*block*-poly(2-vinyl pyridine) (PS-*block*-P2VP) copolymer [140]. More recently, Abuzaina et al. [141] reported that, with increasing temperature, hexagonally packed cylindrical microdomains in an SI diblock copolymer having a 0.18 volume fraction of PS were first transformed into the disordered micelles *before* reaching the micelle-free

disordered state. However, with a higher volume fraction of PS of 0.23, hexagonally packed cylindrical microdomains were directly transformed into the micelle-free disordered state.

We are of the opinion that a parallel shift observed in the log G' vs log G'' plots of highly asymmetric block copolymers at temperatures between T_{LDOT} and T_{DMT} is closely related to the presence of disordered micelles having a very sharp interface in the same temperature range. That is, the liquidlike rheological behavior observed at $T_{LDOT} \leq T < T_{DMT}$ in the terminal region of the log G' vs log G'' plots, shown in Figs. 22 and 23, has originated from the presence of disordered micelles in the same temperature range. Thus, the disordered micelles observed, via SAXS (see Fig. 24) and TEM (see Fig. 25), at $T_{LDOT} \leq T < T_{DMT}$ should not be regarded as being part of the disordered phase associated with thermally-induced concentration fluctuations, commonly observed in symmetric (or nearly symmetric) block copolymers near the T_{ODT}. If disordered micelles were part of the disordered phase like homogeneous polymers, one would *not* expect to observe any shift in log G' vs log G'' plots with increasing temperature at $T_{LDOT} \leq T < T_{DMT}$. There is ample, unambiguous experimental evidence showing that log G' vs log G'' plots for homogenous polymers are independent of temperature [123, 143], which is supported by theoretical consideration [143, 144]. Further, if a shift in log G' vs log G'' plots observed in Figs. 22 and 23 were caused by the thermally-induced composition fluctuations near the T_{ODT}, such a regularly spaced shift in log G' vs log G'' plots with increasing temperature at $T_{LDOT} \leq T < T_{DMT}$ (see Fig. 23) would not be observed.

The differences in phase transition mechanism between symmetric (or nearly symmetric) block copolymers and highly asymmetric block copolymers are summarized schematically in Fig. 26 [101, 127], in which LDOT in highly asymmetric block copolymers is distinguished from ODT in symmetric (or nearly symmetric) block copolymers. According to the experimental studies of Sakamoto et al. [62], Choi et al. [126], and Han et al. [127], who recognized that LDOT is a first order transition, T_{DMT} is as much as approximately 40°C higher than T_{LDOT}. By the definition of ODT, there should not be another phase transition, DMT, above ODT. If LDOT in a highly asymmetric block copolymer is called ODT, then we are faced with a dilemma in that ODT is followed by another phase transition, DMT, at a higher temperature (T_{DMT}), at which point disordered micelles disappear, transforming into the micelle-free disordered phase with thermally-induced fluctuations.

There are some investigators who regard disordered micelles as being part of the disordered phase. Using a mean-field approach, Dormindontova and Lodge [145] predicted the existence of disordered micelles in a highly asymmetric block copolymer at temperatures above T_{ODT} (using their terminology), which corresponds to T_{LDOT} defined above [62, 127]. Interestingly, Dormindontova and Lodge identified a so-called critical micelle temperature (T_{CMT}), which is equivalent to T_{DMT} defined above [127]. Their predicted value of T_{CMT} was found to be much higher than T_{ODT} (using their terminology), very similar to the experimental findings by Choi et al. [126] and Han et al. [127]. However, Dormindontova and Lodge regarded disordered micelles as being part of the disordered phase associated with thermally-induced composition fluctuations. In his review paper on SCMFT presented in a previous
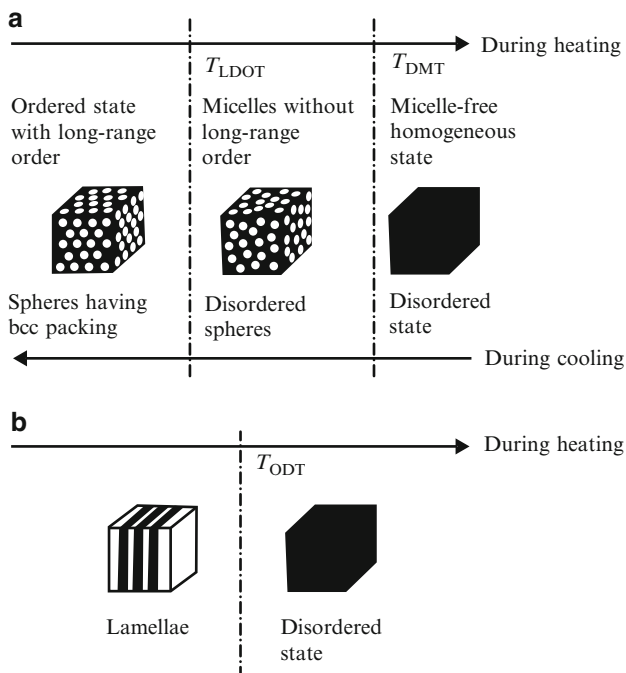
Fig. 26 (**a**) Schematic showing the phase disordering and ordering processes in highly asymmetric sphere-forming block copolymers: namely, the phase transition path, during heating, from spheres with long-range order to disordered spheres (micelles) without long-range order and to the micelle-free disordered state, also the phase transition path, during cooling, from the micelle-free disordered state to disordered micelles without long-range order and to spheres with long-range order. (**b**) Schematic showing the phase disordering process in symmetric or nearly symmetric block copolymers during heating, from lamellae to the disordered state, and upon cooling from the disordered phase, where the block copolymer exhibits a disorder–order transition since the phase transition is thermally reversible. (Reprinted from Han et al. [127]. Copyright © 2000, with permission from the American Chemical Society)

section, Matsen [146] also regarded disordered micelles as being part of disordered phase associated with thermally-induced composition fluctuations. Based on SCMF calculation, Wang et al. [147] also concluded that disordered micelles are part of the disordered phase associated with thermally-induced composition fluctuations. We are of the opinion that this is where a limitation of the mean-field approach may lie. We suggest that in the future a new theory for block copolymers be developed by departing from the traditional mean-field approach in order to determine whether DMT may be regarded as being a phase transition. There is no reason why one should expect that mean-field approach can explain every conceivable phase transitions in microphase-separated block copolymers, although currently held mean-field theories have been found to be very useful to understand *some* phase transitions in microphase-separated block copolymers. This issue is important enough to deserve greater attention by future theorists.

5   Concluding Remarks

In this chapter, we first reviewed the currently held mean-field theories predict-ing the phase behavior and phase transitions in AB- and ABA-type microphase-separated block copolymers. As a supplement to this discussion, in the Appendix we have provided detailed derivations of some of the very complicated mathematical expressions from these theories, which we hope will be helpful in providing a better understanding the origins of such complicated expressions.

We then compared predictions of T_{ODT} with experimental results for both AB- and ABA-type block copolymers. The ability to predict accurately the T_{ODT} of a block copolymer is very important to the synthesis of block copolymers, with re-spect to efficient use of time and resources. We believe strongly that this is one of the areas where a successful block copolymer theory can be put into practice. In the Supplementary Material we have provided five Fortran computer programs, which we have used over the past two decades to predict the T_{ODT}s of AB- and ABA-type block copolymers (e.g., SI, SB, SIS, and SBS) based on the currently held mean-field theories summarized in this chapter. Although the predicted values of T_{ODT} were approximate, we have found that the computer programs were very helpful in saving time and resources for synthesis.

While comparing the predictions of T_{ODT} with experimental results, we have pointed out the importance of having an accurate expression for the interaction pa-rameter α or χ, which is expected to depend not only on temperature but also on molecular weight, as indicated by (82). Unfortunately, almost all the expressions for α or χ reported to date have not included a dependence on molecular weight. Moreover, the values of α or χ reported to date have been based on relatively low molecular weights, which are far below the molecular weights of the block copoly-mers that have been employed for the investigations of the phase behavior and phase transitions. In this regard, a meaningful comparison of the predictions of T_{ODT} and experiment is questionable. We are well aware of the practical experimental dif-ficulty in determining the dependence of α or χ on molecular weight due to the thermal degradation of high molecular weight block copolymers at temperatures even below their T_{ODT}. Thus we have suggested that a molecular approach be de-veloped, which will enable one to predict the effect of molecular weight on α or χ, i.e., to determine the constants b and d, appearing in (82), in terms of the chemical structure of a block copolymer.

There are several areas where the ability to predict accurately the T_{ODT} of a block copolymer can be put into use to solve some significant practical problems. Let us mention here two such areas. One area of need is to be able to determine the desired molecular weight for a block copolymer that can be used as a compatibilizer for blends of two immiscible homopolymers. For this, there are two requirements for a block copolymer to become an effective compatibilizer [32]. One is a thermody-namic requirement in that miscibility (or compatibility in a qualitative sense) must exist between the two immiscible homopolymers and the block copolymer. This requirement is very obvious and thus is easily understood. The other requirement, which is much less obvious, is that the viscosity of a block copolymer chosen for

melt blending with two immiscible homopolymers must be sufficiently low. Readers are reminded that the melt viscosity of a microphase-separated block copolymer is much higher than that in the disordered state [31]. This then suggests that melt blending of two immiscible homopolymers and a block copolymer must be conducted at a temperature above the T_{ODT} of the block copolymer chosen. Since the T_{ODT} of a block copolymer depends on its molecular weight and block length ratio as discussed in this chapter, one must determine the molecular weight and block length ratio for a given chemical structure of block copolymer, which is to be employed as a compatibilizer for two immiscible homopolymers, such that the T_{ODT} of the block copolymer lies below the intended melt processing temperature. This is where accurate prediction of the T_{ODT} of a block copolymer in terms of its molecular weight and block length ratio is needed. This concept has amply been demonstrated [32]. We wish to add that most commercial block copolymers have very high molecular weight and thus they are not suitable for use as an effective compatibilizer for immiscible homopolymers. Another area where block copolymers have long been used is the formulation of pressure-sensitive adhesives (PSA) and hot melt adhesives. In the preparation of a PSA, asymmetric SIS or SBS triblock copolymers, in which the PS endblock forms either spherical or cylindrical microdomains, are typically used. Their unique combination of elasticity and thermoplasticity makes them suitable for use in PSA and hot melt adhesives. Since the block copolymer alone is not sufficient to give rise to the desired level of adhesion and tackiness, one usually adds low molecular weight resin in order to improve its ability to wet the substrate surfaces sufficiently and to form a bond of measurable strength upon contact. Such low molecular weight material is referred to as a "tackifying resin." Tackifying resins come in a variety of chemical structures (e.g., aliphatic or aromatic hydrocarbons, and polyterpenes) and physical properties. While a PSA is prepared in solution, hot melt adhesives are prepared using melt processing where the T_{ODT} of a block copolymer plays a significant role as mentioned above.

In this chapter we have discussed two as yet unresolved issues, finite molecular weight effect and the phase behavior and phase transitions in highly asymmetric block copolymers. We believe that these issues are fundamental enough to require a fresh look, particularly from a theoretical point of view. We do not think that the currently held mean-field theory can explain every conceivable phase behavior and phase transitions experimentally observed in block copolymers. Additionally, most if not all of the physical theories in the literature are based on certain assumptions which were made, more often than not, for the reason of mathematical simplicity. We have suggested that a new theory for phase behavior and phase transitions in block copolymers be developed by relaxing the assumptions made in the formulation of the currently held mean-field theories.

In this chapter we have limited our review to the phase behavior and phase transitions in AB- and ABA-type block copolymers, although we are well aware of the fact that other subjects are equally important. While preparing this chapter, two subjects drew our attention, in particular (1) phase behavior and phase transitions in mixtures of a block copolymer and a homopolymer and (2) phase behavior and phase transitions in ABC-type triblock copolymers. The first subject is closely

related to the preparation of compatibilized immiscible polymer blends with the aid of a block copolymer and the formulation of pressure-sensitive adhesives, briefly mentioned above. However, we have concluded that a review of this subject is premature for the reason that at present we do not have a comprehensive theory, which allows for the construction of binodal curves for blends of a block copolymer and a homopolymer, which include the variations of microdomain structure in the presence of the added homopolymer, and there is a lack of systematic experimental studies reported in the literature. Regarding the second subject mentioned above, at present we do not have a comprehensive theory which can predict the T_{ODT} of an ABC-type triblock copolymer. We wish to point out that the prediction of spinodal temperature alone is not sufficient to have a complete understanding of the phase behavior and phase transitions in ABC-type triblock copolymers. Thus we have concluded that we will have to wait for a future opportunity to review such subjects.

When we first began to prepare this chapter, we also planned to review some applications of block copolymers (e.g., pressure-sensitive adhesives; block polymer micelles; block copolymer thin films and lithography). However, we did not pursue this for the reason of the space limitation in that we have estimated that the total number of pages of this chapter would exceed well over 100 pages. Thus we have concluded that we will have to wait for a future opportunity to review such subjects.

Supplementary Material There are five Fortran computer programs, which can be run using Compaq Visual Fortran or any other Fortran compiler. They are Helfanddi.f, Helfandtri.f, Leibler.f, Mayestri.f, and Fredkim.f. This material is available free of charge via the Internet at http://springer.org.

Appendix A Derivation of (9)

According to Helfand [7], the free energy difference between the microphase-separated and homogeneous states is given by

$$
\frac{\Delta G_m}{V k_B T} = \frac{1}{V k_B T} \int d\mathbf{r} \left\{ \Delta f^* \left(\varphi_A \left(\mathbf{r} \right), \varphi_B \left(\mathbf{r} \right) \right) - \varphi_A \left(\mathbf{r} \right) \frac{\partial \Delta f^*}{\partial \varphi_A \left(\mathbf{r} \right)} - \varphi_B \left(\mathbf{r} \right) \frac{\partial \Delta f^*}{\partial \varphi_B \left(\mathbf{r} \right)} \right\}
$$
$$
- \frac{n_c^t}{V} \ln Q_c - \frac{\alpha \left(N_A \bar{v}_{0A} \right) \left(N_B \bar{v}_{0B} \right)}{\left[\left(N_A \bar{v}_{0A} \right) + \left(N_B \bar{v}_{0B} \right) \right]^2} \tag{A1}
$$

in which Δf^* appearing inside the bracket of the first term on the right-hand side is the free energy density of a mixture having the *local* volume fractions $\varphi_A(\mathbf{r})$ and $\varphi_B(\mathbf{r})$ at position $\mathbf{r}$, which are different from the *average* volume fractions of A and B blocks in the homogeneous state. The second term on the right-hand side of (A1) represents the conformational entropy contribution, $S = -k_B \ln(Q_c)^{n_c^t}$, and the last term on the right-hand side represents the Flory–Huggins interaction energy density in the homogeneous state, $G_o = \alpha f(1-f)$ in which α (having the units of mol/cm^3) is the interaction parameter which is related to the Flory–Huggins interaction parameter χ by $\alpha = \chi/V_{ref}$ with V_{ref} being the molar volume of a reference component and f is the average volume fractions of block A defined by $N_A \bar{v}_{0A}/(N_A \bar{v}_{0A} + N_B \bar{v}_{0B})$ with N_k being the degree of polymerization of component k ($k = A$ or B) and $\bar{v}_{ok}$ being the monomeric molar volume of component k ($k = A$ or B).

By defining the first term inside the bracket on the right-hand side of (A1) as $W_\xi(\mathbf{r})$,

$$-W_\xi(\mathbf{r}) = \frac{1}{k_B T}\Delta f^*(\varphi_A(\mathbf{r}), \varphi_B(\mathbf{r})) - \varphi_A(\mathbf{r})\frac{\partial \Delta f^*}{\partial \varphi_A(\mathbf{r})} - \varphi_B(\mathbf{r})\frac{\partial \Delta f^*}{\partial \varphi_B(\mathbf{r})} \quad (A2)$$

we have

$$\frac{\Delta G_m}{V k_B T} = -\frac{1}{V}\int d\mathbf{r}\, W_\xi(\mathbf{r}) - \frac{n_c^t}{V}\ln Q_c - \frac{\alpha(N_A\bar{v}_{0A})(N_B\bar{v}_{0B})}{[(N_A\bar{v}_{oA}) + (N_B\bar{v}_{oB})]^2}$$

or

$$\frac{\Delta G_m}{k_B T\, n_c^t} = -\frac{1}{n_c^t}\int d\mathbf{r}\, W_\xi(\mathbf{r}) - \ln Q_c - \frac{V}{n_c^t}\frac{\alpha(N_A\bar{v}_{0A})(N_B\bar{v}_{0B})}{[(N_A\bar{v}_{0A}) + (N_B\bar{v}_{0B})]^2}$$

$$= -\frac{1}{n_c^t}\int d\mathbf{r}\, W_\xi(\mathbf{r}) - \ln Q_c - \frac{\alpha(N_A\bar{v}_{0A})(N_B\bar{v}_{0B})}{[(N_A\bar{v}_{0A}) + (N_B\bar{v}_{0B})]} \quad (9)$$

in which use was made of $V_c = N_A\bar{v}_{0A} + N_B\bar{v}_{0B}$ and $V = n_c^t V_c$.

Appendix B Derivation of (19)

NIA assumes that the interfacial thickness (λ_I) of a block copolymer is much smaller than its domain sizes, D_A and D_B (i.e., $\lambda_I \ll D_A + D_B$) and thus $D = D_A + D_B$. Then we have

$$\frac{D}{N_A\bar{v}_{0A} + N_B\bar{v}_{0B}} = \frac{D_A}{N_A\bar{v}_{0A}} = \frac{D_B}{N_B\bar{v}_{0B}} \quad (B1)$$

yielding

$$D_A = \frac{N_A\bar{v}_{0A}D}{N_A\bar{v}_{0A} + N_B\bar{v}_{0B}}; \quad D_B = \frac{N_B\bar{v}_{0B}D}{N_A\bar{v}_{0A} + N_B\bar{v}_{0B}} \quad (B2)$$

where N_A and N_B are the degrees of polymerization of block chain A and block chain B, respectively, and $\bar{v}_{0A}$ and $\bar{v}_{0B}$ are the monomeric molar volumes of block chain A and block chain B, respectively.

Now, the area of the interface, S, is defined by [34]

$$S = V/(D/2) = 2n_c^t V_c/D = 2n_c^t \left(N_A \bar{v}_{0A} + N_A \bar{v}_{0B}\right)/D \tag{B3}$$

in which V is the volume of the system, D denotes the size of the microdomains, n_c^t is the total number of block copolymer chains, and V_c is the molecular volume of one block copolymer chain. In (B3) the following relationships are used: (i) $V = n_c^t V_c$ and (ii) $V_c = N_A \bar{v}_{0A} + N_B \bar{v}_{0B}$. Thus, from (B3) we have

$$S/n_c^t = 2\left(N_A \bar{v}_{0A} + N_B v_{0B}\right)/D \tag{B4}$$

Substitution of (B4) into the left-hand side of (17) gives

$$\frac{2\gamma}{k_B T}\left(N_A \bar{v}_{0A} + N_B \bar{v}_{0B}\right)/D = -\frac{1}{n_c^t}\int d\mathbf{r} W_\xi^I(\mathbf{r}) \tag{B5}$$

From (16) with $m = 2.5$ and $c = 0.085$, we have

$$-\ln Q_k = 0.085\left[D_k/2R_{g,k}\right]^{2.5} = 0.085\left(6^{1/2}/2\right)^{2.5}\left(\frac{D_k}{b_k N_k^{1/2}}\right)^{2.5} \tag{B6}$$

in which use was made of the definition, $R_{g,k} = b_k N_k^{1/2}/6^{1/2}$. Substitution of (B2) into (B6) gives

$$-\ln Q_A - \ln Q_B = 0.141\frac{\left(N_A^{1/2}\bar{v}_{0A}/b_A\right)^{2.5} + \left(N_B^{1/2}\bar{v}_{0B}/b_B\right)^{2.5}}{\left(N_A \bar{v}_{0A} + N_B \bar{v}_{0B}\right)^{2.5}}D^{2.5} \tag{B7}$$

Finally, substitution of (10), with the aid of (11) and (B7), and (B5) into (9) gives (19).

Appendix C Derivation of (34) and (37)–(39)

C.1 Derivation of (34)

According to the RPA, we have

$$\psi_i(q) = -\beta \tilde{S}_{ij}(q) U_j(q) = -\beta S_{ij}(q) U_j^{eff}(q) \tag{C1}$$

where $i = A$ and B, $j = A$ and B for a diblock copolymer, $\beta = 1/k_B T$, and $U_j^{eff}(q)$ is given by

$$U_j^{eff}(q) = U_j(q) + \phi_{jm}\psi_m(q) + \Theta \tag{C2}$$

in which Θ is the self-consistent potential acting on all monomers of blocks A and B, and

$$\phi_{jm} = (1/\beta)\chi_{jm} \tag{C3}$$

From (C2) we have

$$\begin{aligned}
U_A^{eff}(q) - U_B^{eff}(q) &= U_A(q) - U_B(q) + (\phi_{AA} - \phi_{AB})\psi_A(q) + (\phi_{BA} - \phi_{BB})\psi_B(q) \\
&= U_A(q) - U_B(q) - (2/\beta)\chi\psi_A(q)
\end{aligned} \tag{C4}$$

in which use was made of $\chi_{AB} = \chi_{BA} = \chi$, $\chi_{AA} = \chi_{BB} = 0$, and $\psi_A(q) = -\psi_B(q)$. Also, from (C1), we have

$$\psi_A(q) + \psi_B(q) = 0 = -\beta\left(S_{AA}(q)U_A^{eff}(q) + S_{AB}(q)U_B^{eff}(q)\right.$$

$$\left. + S_{BA}(q)U_A^{eff}(q) + S_{BB}(q)U_B^{eff}(q)\right) \tag{C5}$$

Rearrangement of (C5) with the aid of the relationship $S_{AB}(q) = S_{BA}(q)$ gives

$$U_B^{eff}(q)/U_A^{eff}(q) = -\left(S_{AA}(q) + S_{AB}(q)\right)/\left(S_{AB}(q) + S_{BB}(q)\right) \tag{C6}$$

On the other hand, from (C1) and $\psi_A(q) = -\psi_B(q)$, we have

$$\tilde{S}_{AA}(q) = \tilde{S}_{BB}(q) = -\tilde{S}_{AB}(q) = -\tilde{S}_{BA}(q) = \tilde{S}(q) \tag{C7}$$

Using (C7) and (C1), we have

$$\tilde{S}(q)\left(U_A(q) - U_B(q)\right) = S_{AA}(q)U_A^{eff}(q) + S_{AB}(q)U_B^{eff}(q) \tag{C8}$$

Also, from (C1), we have

$$\psi_A(q) = -\beta\tilde{S}(q)\left(U_A(q) - U_B(q)\right) \tag{C9}$$

From (C4) and (C9) we have

$$U_A^{eff} - U_B^{eff}(q) = \left(1 + 2\chi\tilde{S}(q)\right)\left(U_A(q) - U_B(q)\right) \tag{C10}$$

and from (C7) and (C10) we have

$$U_A^{eff} - U_B^{eff}(q) = \left(1 + 2\chi\tilde{S}(q)\right)\left(S_{AA}(q)U_A^{eff}(q) + S_{AB}(q)U_B^{eff}(q)\right)/\tilde{S}(q) \tag{C11}$$

Finally, from (C6) and (C11) we have

$$1/\tilde{S}(q) = \left(S_{AA}(q) + 2S_{AB}(q) + S_{BB}(q)\right) / \left(S_{AA}(q)S_{BB}(q) - S_{AB}^{2}(q)\right) - 2\chi \quad (34)$$

C.2 Derivation of (37) and (39)

$S_{AA}(q)$ can be expressed by

$$
\begin{aligned}
S_{AA}(q) &= \frac{1}{N}\int_{0}^{fN}\int_{0}^{fN}\exp\left(-y|i-j|\right)\mathrm{d}j\mathrm{d}i = \frac{2}{N}\int_{0}^{fN}\int_{0}^{i}\exp\left(-y(i-j)\right)\mathrm{d}j\mathrm{d}i \\
&= \frac{2}{N}\int_{0}^{fN}\exp\left(-yi\right)(1/y)\left(\exp\left(yi\right)-1\right)\mathrm{d}i = \frac{2}{yN}\int_{0}^{fN}\left(1-\exp\left(-yi\right)\right)\mathrm{d}i \\
&= \frac{2}{yN}\left(fN + \frac{\exp\left(-fNy\right)-1}{y}\right) = \frac{2}{y^{2}N}\left(fNy + \exp\left(-fNy\right) - 1\right) \\
&= \frac{2N}{(yN)^{2}}\left(fNy + \exp\left(-fNy\right) - 1\right) = \frac{2N}{x^{2}}\left(fx + \exp\left(-fx\right) - 1\right) = Ng\left(f,x\right)
\end{aligned}
$$

$$(37)$$

in which $y = q^{2}b^{2}/6$ and $x = yN = q^{2}Nb^{2}/6$ are used. $S_{BB}(q)$ can be obtained from (37) by changing the integration range from fN to $(1-f)N$. Further, $S_{AB}(q)$ can be expressed by

$$
\begin{aligned}
S_{AB}(q) &= \frac{1}{N}\int_{fN}^{N}\int_{0}^{fN}\exp(-y(i-j)\,\mathrm{d}j\mathrm{d}i = \frac{1}{N}\left[\int_{fN}^{N}\exp\left(-yi\right)\mathrm{d}i\right]\left[\int_{0}^{fN}\exp\left(yj\right)\mathrm{d}j\right] \\
&= \frac{1}{N}\left[\frac{-\exp\left(-Ny\right)+\exp\left(-fNy\right)}{y}\right]\left[\frac{\exp\left(fNy\right)-1}{y}\right] \\
&= \frac{1}{y^{2}N}\left[-\exp\left(-(1-f)Ny\right)+\exp\left(-Ny\right)+1-\exp\left(-fNy\right)\right] \\
&= \frac{N}{2(yN)^{2}}\left[\begin{array}{l}2\left\{Ny+\exp\left(-Ny\right)-1\right\}-2\left\{fNy+\exp\left(-fNy\right)-1\right\}\\-2\left\{(1-f)Ny+\exp\left(-(1-f)Ny\right)-1\right\}\end{array}\right] \\
&= \frac{N}{2}\left[g\left(1,x\right) - g\left(f,x\right) - g\left(1-f,x\right)\right]
\end{aligned}
$$

$$(39)$$

Appendix D Derivation of (50)

The difference in free energy density $(\Phi)\,(=\Delta G_{m}/k_{B}T)$ between the microphase-separated and disordered states is given by [33]

$$\Phi\left[\varphi\right] = \frac{1}{2\lambda}\left(r_{n}^{2} - r_{0}^{2}\right) + \frac{d}{\tilde{N}^{1/2}}\left(r_{n}^{1/2} - r_{0}^{1/2}\right) - \frac{2}{3}n\theta_{n}a_{n}^{3} + \frac{1}{2}n\eta_{n}a_{n}^{4} \quad (\text{D1})$$

in which $\tilde{N}$ is defined by (48), λ and d are defined in (49), n describes the type of microdomain structure (i.e., $n = 1$ for lamellar microdomains, $n = 3$ for cylindrical microdomains, and $n = 6$ for body-centered-cubic (bcc) lattice), and θ_n and η_n depend on the type of microdomain structure; namely (i) $\theta_1 = 0$ and $\eta_1 = -\lambda/2$ for $n = 1$, (ii) $\theta_3 = \mu$ and $\eta_3 = -\lambda/2$ for $n = 3$, and (iii) $\theta_6 = -2\mu$ and $\eta_6 = 3\lambda/2$ for $n = 6$ in which $\mu = N\Gamma_3/c^3$ with N being the degree of polymerization, Γ_3 being the third-order vertex function (see (33)), and c being defined in (49). In reference to (D1), r_n and r_o are the inverse susceptibilities of the microphase-separated and disordered states, respectively, and they are given by

$$r_0 = \tau + d\lambda / \left(r_0 \tilde{N}\right)^{1/2} \tag{D2}$$

and

$$r_n = \tau + d\lambda / \left(r_n \tilde{N}\right)^{1/2} + n\lambda a_n^2 \tag{D3}$$

and a_n is the amplitude of the concentration of block A and is related to the order parameter ψ in the Leibler theory [13]. Also, r_n can be expressed in term of a_n by [33]

$$r_n = \theta_n a_n - \eta_n a_n^2 \tag{D4}$$

τ appearing in (D2) and (D3) is defined by

$$\tau = \left[\frac{2(\chi N)_s - 2\chi N}{c^2}\right] = \left[\frac{F(x^*, f) - 2\chi N}{c^2}\right] \tag{D5}$$

which is a measure of the distance from the spinodal, where use was made of $(\chi N)_s = F(x^*, f)/2$ with x^* (or q^*) being the value of x (or q) at which $\tilde{S}(q)$ defined by (42) becomes a maximum.

Let us now calculate τ for $n = 1$ (lamellar microdomains). From (D3) and (D4) we obtain

$$\tau = -r_1 \left[1 + d\lambda / \left(r_1^{3/2} \tilde{N}^{1/2}\right)\right] \tag{D6}$$

On the other hand, a rearrangement of (D2) gives

$$\tau = r_0 \left[1 - d\lambda / \left(r_0^{3/2} \tilde{N}^{1/2}\right)\right] \tag{D7}$$

From the point of view of dimensional analysis, the second term inside the bracket of both (D6) and (D7) should be dimensionless and thus we have

$$r_1 = k_1 (d\lambda)^{2/3} \tilde{N}^{-1/3}; r_0 = k_0 (d\lambda)^{2/3} \tilde{N}^{-1/3} \tag{D8}$$

in which k_1 and k_0 are constants. From (D6)–(D8) we have

$$-k_1 \left(1 + k_1^{-3/2}\right) = k_0 \left(1 - k_0^{-3/2}\right)$$

or

$$\left(k_1^{1/2} - k_0^{1/2}\right) = (k_1 + k_0)(k_1 k_0)^{1/2} \tag{D9}$$

Note that at a transition temperature $\Phi = 0$ (see (D1) for the definition of Φ). Substitution of (D8) into (D1), with the aid of (D4), gives

$$\Phi[\phi] = \mathrm{d}^{4/3} \lambda^{1/3} \tilde{N}^{-2/3} \left[(1/2)\left(k_1^2 - k_0^2\right) + \left(k_1^{1/2} - k_0^{1/2}\right) - k_1^2 \right] = 0$$

or

$$\left(k_1^{1/2} - k_0^{1/2}\right) = \left(k_1^2 + k_0^2\right)/2 \tag{D10}$$

From (D9) and (D10) we have

$$(k_1 + k_0)(k_1 k_0)^{1/2} = \left(k_1^2 + k_0^2\right)/2$$

or

$$\sqrt{R}(R+1) = (R^2+1)/2 \tag{D11}$$

with $R = k_1/k_0$, yielding $R = 5.27451$. Also, from (D10) we have

$$k_0^{1/2}\left(R^{1/2} - 1\right) = k_0^2\left(R^2+1\right)/2 \tag{D12}$$

yielding $k_0 = 0.200801$. Then, we obtain $k_1 = 1.059138$. Finally, from (D6) we have

$$\tau = -\left(k_1 + k_1^{-1/2}\right)(\mathrm{d}\lambda)^{2/3}\tilde{N}^{-1/3} = -2.0308\,(\mathrm{d}\lambda)^{2/3}\tilde{N}^{-1/3} \tag{D13}$$

Rearrangement of (D5) gives

$$(\chi N)_t = (\chi N)_s - (1/2)\,c^2\tau \tag{D14}$$

Substituting values of c, d and λ for $f = 0.5$ into (D14), we obtain

$$(\chi N)_t = 10.495 + 41.022/\tilde{N}^{1/3} \tag{50}$$

for which use was made of the numerical values: $x^* = 3.7852, \partial^2 F(f,x)/\partial x^2|_{x^*} = 0.9624$, and $\lambda = 106.18$ given in Table 1 of Fredrickson and Helfand [33].

References

1. Szwarc M (1956) Living polymers. Nature 178:1168–1169
2. Szwarc M (1968) Carbanions, living polymers and electron transfer process. Interscience, New York

3. Kawai H, Soen T, Inoue T, Ono T, Uchida T (1972) Domain formation mechanisms of block and graft copolymers from solution. Prog Polym Sci Jpn 4:145–221, Kodansha, Tokyo

4. Sadron C, Gallot B (1973) Heterophases in block-copolymer/solvent systems in the liquid and in the solid state. Macromol Chem 164:301–332

5. Hashimoto T, Shibayama M, Fujimura M, Kawai H (1983) Microphase separation and the polymer-polymer interphase in block copolymers. In: Meier DJ (ed) Block copolymers science and technology. MMI Press, Symp Series, vol 3. Harwood Academic, New York, pp 63–108

6. Hajduk DA, Harper PE, Gruner SM, Honeker CC, Kim G, Thomas EL, Fetters LJ (1994) The gyroid: a new equilibrium morphology in weakly segregated diblock copolymers. Macromolecules 27:4063–4073

7. Helfand E (1975) Block copolymer theory. III. Statistical mechanics of the microdomain structure. Macromolecules 8:552–556

8. Helfand E, Wasserman ZR (1976) Block copolymer theory. 4. Narrow interphase approximation. Macromolecules 9:879–889

9. Helfand E, Wasserman ZR (1977) Statistical thermodynamics of microdomain structures in block copolymer systems. Polym Eng Sci 17:582–586

10. Helfand, E, Wasserman ZR (1978) Block copolymer theory. 5. Spherical microdomains. Macromolecules 11:960–966

11. Helfand E, Wasserman ZR (1980) Block copolymer theory. 6. Cylindrical microdomains. Macromolecules 13:994–998

12. Helfand E, Wasserman ZR (1982) Microdomain structure and the interface in block copolymers. In: Goodman I (ed) Developments in block copolymers–1. Applied Science, New York, Chap 4

13. Leibler L (1980) Theory of microphase separation in block copolymers. Macromolecules 13:1602–1617

14. Matsen MW, Schick M (1994) Stable and unstable phases of a diblock copolymer melt. Phys Rev Lett 72:2660–2663

15. Hasegawa H, Sakamoto N, Takeno H, Jinnai H, Hashimoto T, Schwahn D, Frielinghaus H, Janssen S, Imai M, Mortensen K (1999) Small-angle neutron scattering studies on phase behavior of block copolymers. Phys Chem Solids 60:1307–1312

16. Karis TE, Russell TP, Gallot Y, Mayes AM (1995) Rheology of the lower critical ordering transition. Macromolecules 28:1129–1134

17. Pollard M, Russell TP, Ruzette AVG, Mayes AM, Gallot Y (1998) The effect of hydrostatic pressure on the lower critical ordering transition in diblock copolymers. Macromolecules 31:6493–6498

18. Russell TP, Karis TE, Gallot Y, Mayes AM (1994) A lower critical ordering transition in a diblock copolymer melt. Nature 368:729–731

19. Ruzette AVG, Benerjee P, Mayes AM, Pollard M, Russell TP, Jerome R, Slawecki T, Hjelm R, Thiyagarajan P (1988) Phase behavior of diblock copolymers between styrene and *n*-alkyl methacrylate. Macromolecules 31:8509–8516

20. Ryu DY, Jeong U, Lee DH, Kim J, Youn HS, Kim JK (2003) Phase behavior of deuterated polystyrene-*block*-poly(*n*-penyl methacrylate) copolymers. Macromolecules 36:2894–2902

21. Weidisch R, Stamm M, Schubert DW, Arnold M, Budde H, Horring S (1999) Correlation between phase behavior and tensile properties of diblock copolymers. Macromolecules 32:3405–3411

22. Weidisch R, Schreyeck G, Ensslen M, Michler GM, Stamm M, Schubert DW, Budde H, Horing S, Jerome R (2000) Deformation behavior of weakly segregated block copolymers. 2. Correlation between phase behavior and deformation mechanisms of diblock copolymers. Macromolecules 33:5495–5504

23. Kawasaki K, Ohta T, Kohrogui M (1988) Equilibrium morphology of block copolymer melts. 2. Macromolecules 21:2972–2980

24. Mayes AM, Olvera de la Cruz M (1989) Microphase separation in multiblock copolymer melt. J Chem Phys 91:7228–7235

25. Ohta T, Kawasaki K (1986) Equilibrium morphology of block copolymer melts. Macromolecules 19:2621–2632
26. Vavasour JD, Whitmore MD (1992) Self-consistent mean field theory of the microphases of diblock copolymers. Macromolecules 25:5477–5486
27. Vavasour JD, Whitmore MD (1993) Self-consistent field theory of block copolymers with conformational asymmetry. Macromolecules 26:7070–7076
28. Bates FS, Fredrickson GH (1990) Block copolymer thermodynamics: theory and experiment. Annu Rev Phys Chem 41:525–557
29. Hashimoto T (1996) Order–disorder transition in block copolymers. In: Holden G, Legge NR, Quirk R, Schroeder HE (eds) Thermoplastic elastomers, 2nd edn. Hanser, Munich, Chap 15A
30. Hamley IW (1998) The physics of block copolymers. Oxford University Press, Oxford
31. Han CD (2007) Rheology and processing of polymeric materials. Vol 1. Polymer rheology. Oxford University Press, Oxford, Chap 8
32. Han CD (2007) Rheology and processing of polymeric materials. Vol 2 Polymer processing. Oxford University Press, Oxford, Chap 4
33. Fredrickson GH, Helfand E (1987) Fluctuation effects in the theory of microphase separation in block copolymers. J Chem Phys 87:697–706
34. Meier DJ (1987) Theoretical aspects of block copolymers. In: Legge NR Holden G Schroeder HE (eds) Thermoplastic elastomers Hanser Munich, Chap 11
35. Helfand E, Tagami Y (1972) Theory of the interface between immiscible polymers. II. J Chem Phys 56:3592–3601
36. Helfand E, Sapse AM (1975) Theory of unsymmetric polymer-polymer interfaces. J Chem Phys 62:1327–1311
37. Meier DJ (1969) Theory of block copolymers. I. Domain formation in A–B block copolymers. J Polym Sci Part C 26:81–98
38. Hashimoto T, Shibayama M, Kawai H (1983) Ordered structure in block copolymer solutions. 4. Scaling rules on size of fluctuations with block molecular weight, concentration, and temperature in segregation and homogeneous regimes. Macromolecules 16:1093–1101
39. Han CD, Baek DM, Kim JK (1990) Effect of microdomain structure on the order–disorder transition temperature of polystyrene-*block*-polyisoprene-*block* polystyrene copolymers Macromolecules 23:561–570
40. Richardson MJ, Savill NG (1977) Volumetric properties of polystyrene: influence of temperature, molecular weight and thermal treatment. Polymer 18:3–9
41. Han CD, Kim J, Kim JK (1989) Determination of order–disorder transition temperature of block copolymers. Macromolecules 22:383–394
42. Mori K, Hasegawa H, Hashimoto T (1985) Small-angle scattering from bulk block copolymers in disordered state. Estimation of χ-values from accidental thermal fluctuations. Polym J 17:799–806
43. De Gennes PG (1979) Scaling concepts in polymer physics Cornell University Press, Ithaca
44. Benoit H, Wu W, Benmouna M, Mozer B, Bauer B, Lapp A (1985) Elastic coherent scattering from multicomponent systems: applications to homopolymer mixtures and copolymers. Macromolecules 18:986–993
45. Kim JK (1995) Compatibilization effect of a block copolymer in two random copolymer blends. Polymer 36:1243–1252
46. Kim JK, Kimishima K, Hashimoto T (1993) Random-phase approximation calculation of the scattering function for multicomponent polymer systems. Macromolecules 26:125–136
47. Mayes AM, Olvera de la Cruz M (1991) Equilibrium domain spacing in weakly segregated block copolymers. Macromolecules 24:3975–3976
48. Mori K, Tanaka H, Hashimoto T (1987) Scattering function for disordered two-component polymer systems including block copolymers. Macromolecules 20:381–393
49. Morozov AN, Fraaije JGEM (2001) Phase behavior of ring diblock copolymer melt in equilibrium and under shear. Macromolecules 34:1526–1628
50. Olvera de la Cruz M, Sanchez IC (1986) Theory of multiphase separation in graft and star copolymers. Macromolecules 19:2501–2508

51. Vilgis T, Benmouna M, Benoit H (1991) Static scattering from multicomponent polymer systems: theoretical models. Macromolecules 24:4481–4488
52. Barrat JL, Fredrickson GH (1991) Collective and single-chain correlations near the block copolymer order–disorder transition. J Chem Phys 95:1281–1289
53. Almdal K, Koppi KA, Bates FS, Mortensen K (1992) Multiple ordered phases in a block copolymer melt. Macromolecules 25:1743–1751
54. Hajduk DA, Gruner SM, Rangarajan P, Register RA, Fetters LJ, Honeker C, Albalak RJ, Thomas EL (1994) Observation of a reversible thermotropic order–order transition in a diblock copolymer. Macromolecules 27:490–501
55. Hamley IW, Koppi KA, Rosedale JH, Bates FS, Almdal K, Mortensen K (1993) Hexagonal mesophases between lamellae and cylinders in a diblock copolymer melt. Macromolecules 26:5959–5970
56. Kim JK, Lee HH, Ree M, Lee KB, Park Y (1998) Ordering kinetics of cylindrical and spherical microdomains in an SIS block copolymer by synchrotron SAXS and rheology. Macromol Chem Phys 199:641–653
57. Kim JK, Lee HH, Gu Q, Chang T, Jeong YH (1998) Determination of order–order and order–disorder transition temperatures of SIS block copolymers by differential scanning calorimetry and rheology. Macromolecules 31:4045–4048
58. Kimishima K, Koga T, Hashimoto T (2000) Order-order phase transition between spherical and cylindrical microdomain structures of block copolymer. 1. Mechanism of the transition. Macromolecules 33:968–977
59. Lee HH, Jeong WY, Kim JK, Ihn KJ, Kornfield JA, Wang ZG, Qi S (2002) Orientational proliferation and successive twining from thermoreversible hexagonal-body-centered cubic transition. Macromolecules 34:785–794
60. Ryu CY, Lodge TP (1999) Thermodynamic stability and anisotropic fluctuations in the cylinder–sphere transition of a block copolymer. Macromolecules 32:7190–7201
61. Ryu CY, Vigild ME, Lodge TP (1998) Fluctuation with cubic symmetry in a hexagonal copolymer microstructure. Phys Rev Lett 81:5354–5357
62. Sakamoto N, Hashimoto T, Han CD, Kim D, Vaidya NY (1997) Order–order, order–disorder transitions in a polystyrene-*block*-polyisoprene-*block*-polystyrene copolymer. Macromolecules 30:1621–1632
63. Sakurai S, Kawada H, Hashimoto T, Fetters LJ (1993) Thermoreversible morphology transition between spherical and cylindrical microdomains of block copolymers. Macromolecules 26:5796–5802
64. Brazovskii SA (1975) Phase transition of an isotropic system to a nonuniform state. Sov Phys (JETP) 41:85–89
65. Burger C, Ruland W, Semenov AN (1990) Polydispersity effects on the microphase-separation transition in block copolymers. Macromolecules 23:3339–3346 16:545–553
66. Han CD, Baek DM, Kim J, Kimishima K, Hashimoto T (1992) Viscoelastic behavior, phase equilibria, and microdomain morphology in mixtures of a block copolymer and a homopolymer. Macromolecules 25:3052–3067
67. Han CD, Baek DM, Kim JK, Ogawa T, Sakamoto N, Hashimoto T (1995) Effect of volume fraction on the order–disorder transition in low molecular weight polystyrene-*block*-polyisoprene copolymers. 1. Order–disorder transition temperature determined by rheological measurements. Macromolecules 28:5043–5062
68. Floudas G, Vlassopoulos D, Pitsikalis M, Hadjichristidis N, Stamm M (1996) Order–disorder transition and ordering kinetics in binary diblock copolymer mixtures of styrene and isoprene. J Chem Phys 104:2083–2088
69. Lin CC, Jonnalagadda SV, Kesani PK, Dai HJ, Balsara NP (1994) Effect of molecular structure on the thermodynamics of block copolymer melts. Macromolecules 27:7769–7780
70. Mai SM, Fairclough PA, Terrill NJ, Turner SC, Hamley IW, Matsen MW, Ryan AJ, Booth C (1998) Microphase-separation in poly(oxyethylene)-poly(oxybuthylene) diblock copolymers. Macromolecules 31:8110–8116

71. Mai SM, Mingvanish W, Turner SC, Chaibundit C, Fairclough PA, Heatley F, Matsen MW, Ryan AJ, Booth C (2000) Microphase-separation behavior of triblock copolymer melts: comparison with diblock copolymer melts. Macromolecules 33:5124–5130

72. Rosedale JH, Bates SF, Almdal K, Mortensen K, Wignall GD (1995) Order and disorder in symmetric diblock copolymer melts. Macromolecules 28:1429–1443

73. Schulz MF, Khandpur AK, Bates FS, Almdal K, Mortensen K, Hajduk DA, Grune SM (1996) Phase behavior of polystyrene–poly(2-vinylpyridine) diblock copolymers. Macromolecules 29:2857–2867

74. Hong KM Noolandi J (1981) Theory of inhomogeneous multicomponent polymer systems. Macromolecules 14:727–736

75. Hong KM, Noolandi H (1983) Theory of phase equilibria in systems containing block copolymers. Macromolecules 16:1083–1093

76. Matsen MW, Bates FS (1996) Unifying weak- and strong-segregation block copolymer theories. Macromolecules 29:1091–1098

77. Sakurai S, Irie H, Umeda H, Nomura S, Lee HH, Kim JK (1998) Gyroid structures and morphological control in binary blends of polystyrene-*block*-polyisoprene diblock copolymers. Macromolecules 31:336–343

78. Sakurai S, Umeda H, Furukawa C, Irie H, Nomura S, Lee HH, Kim JK (1998) Thermally induced morphological transition from lamella to gyroid in a binary blend of diblock copolymers. J Chem Phys 108:4333–4339

79. Cochran EW, Garcia-Cervera CJ, Fredrickson GH (2006) Stability of the gyroid phase in diblock copolymers at strong segregation. Macromolecules 39:2449–2451

80. Hashimoto T, Tsukahara Y, Kawai H (1980) Analysis of segmental interdiffusion in phase-separated block copolymers and polymer blends by small-angle X-ray scattering. J Polym Sci Polym Lett Ed 18:585–592

81. Hashimoto T, Shibayama M, Kawai H (1980) Domain-boundary structure of styrene-isoprene block copolymer films cast from solution. 4. Molecular-weight dependence of lamellar microdomains. Macromolecules 13:1237–1247

82. Hashimoto T, Shibayama M, Kawai H, Watanabe H, Kotaka T (1983) Ordered structure in block polymer solutions. 2. Its effect on rheological behavior. Macromolecules 16:361–371

83. Hashimoto T, Kowsaka K, Shibayama M, Kawai H (1986) Time-resolved small-angle X-ray scattering studies on the kinetics of the order-disorder transition of block polymers. 2. Concentration and temperature dependence. Macromolecules 19:754–762

84. Hashimoto T, Ijichi Y, Fetters LJ (1988) Order-disorder transition of starblock copolymers. J Chem Phys 89:2463–2472

85. Roe RJ, Fishkis M, Chang JC (1981) Small-angle X-ray diffraction study of thermal treatment in styrene-butadiene block copolymers. Macromolecules 14:1091–1103

86. Shibayama M, Hashimoto T, Kawai H (1983) Ordered structure in block copolymer solutions. 1. Selective solvents. Macromolecules 16:16–28

87. Shibayama M, Hashimoto T, Kawai H (1983) Ordered structure in block copolymer solutions. 5. Equilibrium and nonequilibrium aspects of microdomain formation. Macromolecules 16:1434–1443

88. Zin WC, Roe RJ (1984) Phase equilibria and transitions in mixtures of a homopolymer and a block copolymer. 1. Small-angle X-ray scattering study. Macromolecules 17:183–188

89. Bates FS, Hartney MA (1985) Block copolymers near the microphase-separation transition. 3. Small-angle neutron scattering study of the homogeneous melt state. Macromolecules 18:2478–2486

90. Roe RJ (2000) Methods of X-ray and neutron scattering in polymer science. Oxford University Press, New York

91. Hashimoto T, Todo A, Itoi H, Kawai H (1977) Domain-boundary structure of styrene-isoprene block copolymer films cast from solutions. 2. Quantitative estimation of the interfacial thickness of lamellar microphase systems. Macromolecules 10:377–384

92. Tanaka H, Hasegawa H, Hashimoto T (1991) Ordered structure in mixtures of a block copolymer and homopolymers. 1. Solubilization of low molecular weight homopolymers. Macromolecules 24:240–251

93. Ijichi Y, Hashimoto T, Fetters LJ (1989) Order–disorder transition of star block copolymers. 2. Effect of arm number. Macromolecules 22:2817–2824

94. Ogawa T, Sakamoto N, Hashimoto T, Han CD, Baek DM (1996) Effect of volume fraction on the order–disorder transition in low molecular weight polystyrene–*block*–polyisoprene copolymers. 2. Order–disorder transition temperature determined by small-angle X-ray scattering. Macromolecules 29:2113–2123

95. Russell TP, Hjelm RP, Seeger P (1990) Temperature dependence of the interaction parameter of polystyrene and poly(methyl methacrylate). Macromolecules 23:890–893

96. Sakamoto N, Hashimoto T (1995) Order-disorder transition of low molecular weight polystyrene-*block*-polyisoprene. 1. SAXS analysis of two characteristic temperature. Macromolecules 28:6825–6834

97. Sakurai S, Mori K, Okawara A, Kimishima K, Hashimoto T (1992) Evaluation of segmental interaction by small-angle X-ray scattering based on the random-phase approximation for asymmetric, polydisperse triblock copolymers. Macromolecules 25:2679–2691

98. Zha W, Han CD, Le DH, Han SH, Kim JK, Kang JH, Park C (2007) Origin of the difference in order–disorder transition temperature between polystyrene-*block*-poly(2-vinylpyridine) and polystyrene-*block*-poly(4-vinylpyridine) copolymers Macromolecules 40:2109–2119

99. Bodycomb J, Yamaguchi D, Hashimoto T (1996) Observation of a discontinuity in the value of $I_{m^{-1}}$ at the order–disorder transition in diblock copolymer/homopolymer and diblock copolymer/diblock copolymer blends. Polym J 28:821–824

100. Koga K, Koga K, Hashimoto T (1999) Ultra-small-angle X-ray scattering studies on order-disorder transition in diblock copolymers. J Chem Phy 110:11076–11086

101. Sakamoto N, Hashimoto T (1998) Ordering dynamics of cylindrical and spherical microdomains in polystyrene-*block*-polyisoprene-*block*-polystyrene. 1. SAXS and TEM observations for the grain formation. Macromolecules 31:8493–8502

102. Stühn B (1992) The relation between the microphase-separation transition and the glass transition in diblock copolymers. J Polym Sci Polym Phys Ed 30:1013–1019

103. Ehlich D, Takenaka M, Hashimoto T (1993) Forced Rayleigh scattering study of diffusion of block copolymers. 2. Self-diffusion of block copolymer chains in lamellar microdomains and disordered melts. Macromolecules 26:492–498

104. Adams JL, Graessley WW, Register RA (1994) Rheology and the microphase-separation transition in styrene-isoprene block copolymers. Macromolecules 27:6026–6032

105. Balsara NP, Garetz BA, Chang MY, Dau HJ, Newstein MC, Goveas JL, Krishnamoorti R, Rai S (1998) Identification of the molecular parameters that govern ordering kinetics in a block copolymer melt. Macromolecules 31:5309–5315

106. Bates FS (1984) Block copolymers near the microphase-separation transition. 2. Linear dynamic mechanical properties. Macromolecules 17:2607–2613

107. Bates FS, Rosedale JH, Fredrickson GH (1990) Fluctuation effects in a symmetric diblock copolymer near the order-disorder transition. J Chem Phys 92:6255–6270

108. Chung CI, Lin MI (1978) Butadiene-styrene block copolymer. J Polym Sci Polym Phys Ed 16:545–553

109. Floudas G, Hadjichristidis N, Iatrou H, Pakula T, Fischer EW (1994) Microphase-separation in model 3-miktoarm star copolymers (simple graft) and terpolymers. 1. Statics and kinetics. Macromolecules 27:7735–7746

110. Floudas G, Pispas S, Hadjichristidis N, Pakula T, Erukhimovich I (1996) Microphase-separation in star block copolymers of styrene and isoprene. Theory, experiment, and simulation. Macromolecules 29:4142–4154

111. Futamura S, Meinecke E (1977) Effect of center block structure on the physical and rheological properties of ABA block copolymers. Part II. Rheological properties. Polym Eng Sci 17:563–569

112. Gehlsen MD, Bates FS (1993) Heterogeneous catalytic hydrogenation of polystyrene: thermodynamics of poly(vinylcyclohexane) containing diblock copolymers. Macromolecules 26:4122–4127

113. Gouinlock EV, Porter RS (1997) Linear dynamic mechanical properties of an SBS block copolymer. Polym Eng Sci 17:535–543

114. Modi MA, Krishnamoorti R, Tse MF, Wang HC (1999) Viscoelastic characterization of an order-order transition in a mixture of di- and triblock copolymers. Macromolecules 32: 4088–4097
115. Morrison FA, Winter HH, Gronski W, Barnes J (1990) Effects of unidirectional shear on the structure of triblock copolymers. 2. Polystyrene-polyisoprene-polystyrene. Macromolecules 23:4200–4205
116. Patel SS, Larson RG, Winey KI, Watanabe H (1995) Shear orientation and rheology of a lamellar polystyrene-polyisoprene block copolymer. Macromolecules 28:4313–4318
117. Phatak A, Macosko CW, Bates FS, Hahn SF (2005) Extrusion of triblock and pentablock copolymers: evolution of bulk and surface morphology. J Rheol 49:197–214
118. Rosedale JH, Bates FS (1990) Rheology of ordered and disordered symmetric poly(ethylenepropylene)-poly(ethylethylene) diblock copolymers. Macromolecules 23:2329–2338
119. Wang Z, Dormidontova EE, Lodge TP (2002) The order-disorder transition and the disordered micelle regime for poly(ethylenepropylene-*b*-dimethylsiloxane) spheres. Macromolecules 35:9687–9697
120. Winey KI, Gobran DS, Xu Z, Fetters LJ, Thomas EL (1994) Dynamics of block copolymer micelles. Macromolecules 27:2392–2397
121. Winter HH, Scott DB, Gronski W, Okamoto S, Hashimoto T (1993) Ordering by flow near the disorder-order transition of a triblock copolymer styrene-isoprene-styrene. Macromolecules 26:7236–7244
122. Yurekli K, Krishnamoorti R (2002) Dynamics of block copolymer micelles. Macromolecules 35:4075–4083
123. Ferry JD (1980) Viscoelastic properties of polymers, 3rd edn. Wiley, New York
124. Han CD, Kim J (1987) Rheological technique for determining the order–disorder transition temperature of block copolymers. J Appl Polym Sci 25:1741–1764
125. Choi S, Lee KM, Han CD, Sota N, Hashimoto T (2003) Phase transitions in sphere-forming polystyrene-*block*-polyisoprene-*block*-polystyrene copolymer and its blends with homopolymer. Macromolecules 36:793–803
126. Choi S, Vaidya NY, Han CD, Sota N, Hashimoto T (2003) Effects of sample preparation method and thermal history on phase transition in highly asymmetric block copolymers: comparison with symmetric block copolymers. Macromolecules 36:7707–7720
127. Han CD, Vaidya NY, Kim D, Shin G, Yamaguchi D, Hashimoto T (2000) Lattice order/disordering and demicellization/micellization transitions in highly asymmetric polystyrene-*block*-polyisoprene copolymers. Macromolecules 33:3767–3780
128. Kim JK, Lee HH, Sakurai S, Aida S, Masamoto J, Nomura S, Kitagawa Y, Suda Y (1999) Lattice disordering and domain dissolution transitions in polystyrene-*block*-poly(ethylene-*co*-but-1-ene)-*block*-polystyrene copolymer having a highly asymmetric composition. Macromolecules 32:6707–6717
129. Balsara NP, Perahia D, Safinaya CR, Tirrell M, Lodge TP (1992) Birefringence detection of the order-to-disorder transition in block copolymer liquids. Macromolecules 25:3896–3901
130. Kasten H, Stühn B (1995) Density discontinuity at the microphase-separation transition of a symmetric diblock copolymers. Macromolecules 28:4777–4778
131. Stühn B, Mutter R, Albrecht T (1992) Direct observation of structure formation at the temperature-driven order-to-disorder transition in diblock copolymers. Europhys Lett 18:427–432
132. Voronov VP, Buleiko VM, Podneks VE, Hamley IW, Fairclough JPA, Ryan AJ, Mai SM, Liao BX, Booth C (1997) A high resolution calorimetry study of the order-disorder transition in a diblock copolymer melt. Macromolecules 30:6674–6676
133. Ryu DY, Lee DJ, Kim JK, Lavery KA, Russell TP, Han YS, Seong BS, Lee CHH, Thiyagarajan P (2003) Effect of hydrostatic pressure on closed-loop phase behavior of block copolymers. Phys Rev Lett 90:235501–1–235501–4
134. Dudowicz J, Freed KF (1991) Effect of monomer structure and compressibility on the properties of multicomponent polymer blends and solutions. 2. Application to binary blends. Macromolecules 24:5096–5111

135. Dudowicz J, Freed KF (1991) Effect of monomer structure and compressibility on the properties of multicomponent polymer blends and solutions. 3. Application to PS(D)/PVME blends. Macromolecules 24:5112–5123
136. Freed KF, Dudowicz J (1992) On the large entropic contribution to the effective interaction parameter of polystyrene-poly(methyl methacrylate) diblock copolymer systems. J Chem Phys 97:2105–2109
137. Dudowicz J, Freed KF (1993) Relation of effective interaction parameters for binary blends and diblock copolymers: lattice cluster theory predictions and comparison with experiment. Macromolecules 26:213–220
138. Maurer WW, Bates FS, Lodge TP, Almdal K, Mortensen K, Fredrickson GH (1998) Can a single function for χ account for block copolymer and homopolymer blend phase behavior? J Chem Phys 108:2989–3000
139. Sakamoto N, Hashimoto T (1998) Ordering dynamics of a symmetric polystyrene-*block*-polyisoprene. 1. Ordering mechanism from the disordered state. Macromolecules 31:3292–3302
140. Segalman RA, Hexemer A, Hayward RC, Kramer EJ (2003) Ordering and melting of block copolymer spherical domains in 2 and 3 dimensions. Macromolecules 36:3272–3288
141. Abuzaina FM, Patel AJ, Mochrie S, Narayanan S, Sandy A, Garetz BA, Balsar NP (2005) Structure and phase behavior of block copolymer melts near the sphere–cylinder boundary. Macromolecules 38:7090–7097
142. Han CD (1988) The influence of molecular weight distribution on the linear viscoelastic properties of polymer blends. J Appl Polym Sci 35:167–213
143. Han CD, Jhon MS (1986) Correlations of the first normal stress difference with shear stress and of the storage modulus with loss modulus for homopolymers. J Appl Polym Sci 32:3809–3840
144. Han CD, Kim JK (1993) On the use of time-temperature superposition in multicomponent/multiphase polymer systems. Polymer 34:2533–2539
145. Dormidontova EE, Lodge TP (2001) The order–disorder transition and the disordered micelle regime in sphere-forming block copolymer melts. Macromolecules 34:9143–9155
146. Matsen MW (2002) The standard Gaussian model for block copolymer melts. J Phys Condens Matter 44:R21–R47
147. Wang J, Wang ZG, Yang Y (2005) Nature of disordered micelles in sphere-forming block copolymer melts. Macromolecules 38:1979–1988

Editor: K.-S. Lee

New Class Materials of Organic–Inorganic Hybridized Nanocrystals/Nanoparticles, and Their Assembled Micro- and Nano-Structure Toward Photonics

Hidetoshi Oikawa, Tsunenobu Onodera, Akito Masuhara, Hitoshi Kasai, and Hachiro Nakanishi

Abstract A π-conjugated organic and polymer nanocrystal (NC) is an intermediate state between a single molecule and the corresponding bulk crystals, the size of which is usually in the range of several tens of nanometers to sub-micrometer. According to the development of so-called "reprecipitation method," well-defined organic and polymer NCs could be fabricated conveniently, and are expected to exhibit peculiar optoelectronic and photonic properties, depending on size and shape. Actually, linear optical properties such as visible (VIS) absorption (or extinction) and fluorescence emission spectra were found to be remarkably dependent on crystal size, due to thermal softening of crystal lattice in NCs, being different from so-called quantum confinement effect in semiconductor nanoparticles (NPs). Polydiacetylene (PDA) noted in the present research is well known to be one of the most promising candidate organic materials for nonlinear optics (NLO). The apparent enhancement of NLO was confirmed in the layered thin film of PDA NCs. Hybridization of π-conjugated polymer NCs with noble metals on a nanometer scale, i.e., core/shell type hybridized NCs, would open a novel scientific paradigm in optoelectronics, photonics, and so on. In the present chapter, the fabrication techniques of core/shell type hybridized NCs, their characterization, and the evaluation of physical properties are first described, and subsequently ordered array structure of polymer microspheres and spherically encapsulated PDA NCs on a patterned substrate are introduced toward photonic device application. Finally, the future scope in the relevant field will be discussed.

H. Oikawa (✉), T. Onodera, A. Masuhara, H. Kasai, and H. Nakanishi
Institute of Multidisciplinary Research for Advanced Materials (IMRAM),
Tohoku University, Katahira 2–1–1, Aoba-ku, Sendai 980–8577 Japan
email: oikawah@tagen.tohoku.ac.jp

Keywords Hetero nano-interface · Localized surface plasmon · Ordered array structure · Organic core/shell type hybridized nanocrystals · Reprecipitation method

Contents

Abbreviations

ADA	10,12-Heptacosadiynoic acid
Ag	Silver
$AgNO_3$	Silver nitrate
AIST	National Institute of Advanced Industrial Science and Technology, Japan
Au	Gold
BL15XU	Beam line of NIMS in SPring-8
CB	Conduction band
ccp	Cubic-closest packed
CdS	Cadmium sulfide
D	Diameter of PSMS
DA	Diacetylene
DAST	$4'$-Dimethylamino-N-methylstilbazolum p-toluenesulfonate

DCHD	1,6-Di(*N*-carbazoylyl)-2,4-hexadiyne
DOS	Density of state
DTMAC	*n*-Dodecyltrimetylammonium chloride
DVB	Divinylbenzene, crosslink agent
EAP	Excitonic absorption peak
EB	Electron beam
ED	Electron diffraction
EDTA	Ethylenediaminetetraacetic acid
EL	Electroluminescence
EPMA	Electron probe microanalysis
fcc	Face-centered cubic
$HAuCl_4$	Tetrachloroauric acid
HCHO	Formaldehyde
HSt	1-(4-Vinylphenyl)ethane-1,2-diol, hydrophilic styrene derivative
K_2PtCl_4	Potassium tetrachloroplatinate
KPS	Potassium peroxodisulfide, initiator
L	Size of dimple
LSP	Localized surface plasmon
MC	Microcrystal
mL	Milliliter
mM	Millimolar
MP	Microparticle
MS	Microsphere
Na_2PdCl_4	Sodium tetrachloropalladate
$NaBH_4$	Sodium borohydride
NC	Nanocrystal
NH_2OH	Hydroxylamine
NIMS	National Institute for Materials Science, Japan
NLO	Nonlinear optics
NP	Nanoparticle
P	Pitch between dimples
PAT	Poly(3-alkylthiophene)
PAT-4	Poly(3-butylthiophene)
PAT-6	Poly(3-hexylthiophene)
PAT-8	Poly(3-octylthiophene)
PCP	Polymer colloidal particle
Pd	Palladium
PDA	Polydiacetylene
PS	Polystyrene
PSMS	Polystyrene microsphere
Pt	Platinum
PVP	Poly(vinylpyrrolidone)
SDS	Sodium dodecylsulfate
SEM	Scanning electron microscopy
SERS	Surface enhanced Raman scattering

SHE   Standard hydrogen electrode
Si   Silicon
SPring-8   Super Photon ring-8 GeV in Japan
SR   Synchrotron radiation
St   Styrene monomer
TEM   Transmission electron microscopy
TFT   Thin film transistor
THF   Tetrahydrofuran
TPB   1,1,4,4-Tetraphenylbutadiene
UV   Ultraviolet
VB   Valence band
VIS   Visible
WF   Work function
XANES   X-ray absorption near-edge structure
XPS   X-ray photoelectron spectroscopy
XRD   X-ray diffraction
ZnS   Zinc sulfide

1 Introduction

A π-conjugated organic and polymer nanocrystal (NC) may occupy an intermediate phase between a single molecule and the corresponding bulk crystals [1–3]. These polymer NCs could be fabricated successfully by developing the so-called "reprecipitation method" [4]. The crystal size is usually in the range of several tens of nanometers to sub-micrometer, which is controlled conveniently by suitably changing the used good and poor solvents, the concentration and amount of the injected solution, temperature and stirring rate for poor solvent, the added surfactant, and so on [5–15]. Polymer NCs are expected to provide a new physical property, depending on crystal size, and to exhibit peculiar optoelectronic and photonic functions [1–3, 13, 14, 16–22]. So far, the following research projects mainly concerned with polydiacetylene (PDA) NC [23], which is one of the most candidate organic materials for nonlinear optics (NLO) [24–26], have been performed: (1) improvement of reprecipitation method [2, 27–35]; (2) analysis of nanocrystallization process to obtain more well-defined polymer NCs [12, 36, 37]; (3) size-dependence of linear optical properties [1, 19, 20, 22]; (4) preparation of layered thin films of PDA NCs, and their enhanced NLO properties [1, 38–40]; (5) "liquid and crystal" system induced by the applied electric- or magnetic-field [21, 41–43]; (6) hybridization of PDA NCs with a noble metal [44–54]; and (7) arrangement-control of PDA NCs on a substrate [55–61]. In particular, item (3) concerns specific behavior in organic and polymer NCs. Namely, the absorption (or extinction) and fluorescence emission spectra were clearly shifted, depending on crystal size. These facts were considered to be due to thermal softening of crystal lattice in organic and polymer NCs.

The recent progress in organic–inorganic hybridized NCs regarding the above-mentioned items (6) and (7) will be introduced in detail in the present chapter.

Hybridization is one of the most important objectives in current material science and technology [62–66]. There are mainly two categories of hybridized polymer materials: the one is polymer blends or alloys, and polymer nanocomposites [67], and the other is core/shell type hybridized NCs or nanoparticles (NPs) [68–76]. In the former, some useful fabrication techniques such as mechanical mixing, sol-gel reaction in polymer matrix, in situ polymerization in the co-existence of inorganic fillers, and surface-modification of loaded fillers are usually performed to provide many kinds of function to polymer "bulk" matrix. The latter case, however, should obviously be distinguished from the former. Undoubtedly, core/shell type hybridized NCs and NPs are on a nanometer scale, and their properties are strongly influenced by size (or total volume), core/shell volume ratio, and components [71–73]. In particular, the delocalized electronic state and/or exciton resulted from π-conjugation in polymer component, localized surface plasmon (LSP) originated in a noble metal [77–79], and a certain mutual interaction such as exciton and LSP coupling through core/shell hetero interface have attracted great interest on the nanometer scale [74, 75, 80–85] because of the appearance of novel nanomaterials with excellent optoelectronic, photonic, redox, conductive, and catalytic properties and functions. However, polymer (π-conjugation) and noble metal (LSP) hetero nano-interface interaction are unexpectedly still not understood [86], although many discussion on hetero-junction have been reported previously in the semiconductor field.

Well now, the proposed "co-reprecipitation method" [45] and "visible-light-driven photocatalytic reduction method" [53] have been established for the purpose of these kinds of core/shell type hybridized NCs composed of PDA NC and noble metal NP, and both processes have been further improved to extend to another type hybridized NCs, respectively [50, 54]. Typical core/shell type hybridized NPs were first reported by Halas and Caruso research groups [70, 71, 73, 84, 87]. A great number of fine gold (Au) NPs as Au shell were deposited densely on the surface of silica NPs, which are spherical and uniform size. The LSP spectra were continuously blue-shifted with increasing the thickness of Au shell, and some optoelectronic applications have been now presented such as a substrate for surface enhanced Raman spectrum (SERS) measurement, chemical- and bio-sensors, etc. Silica NPs, however, are core as a template to fabricate core/shell type hybridized nanostructure, and there is no something like optoelectronic interaction through core/shell hetero nano-interface in this case.

In addition, it is very important to arrange, align, orientate, and integrate these polymer and/or hybridized NCs exactly and selectively on a substrate [55–59, 61, 87], and one should keep such kinds of NCs in mind in order to input and output optical- and electric-signals and/or information for device application. Here, encapsulation of polymer NCs and their arrangement by the use of a lithographically patterned substrate have been proposed to solve the above-mentioned problems [61]. As a typical example, the assembled structure of polymer microspheres (MSs) having mono-dispersed size is well known in the applications of some photonic crystal devices [87]. In contrast, the proposed fabrication procedures seem to be much more extensive and superior to the previous ones.

In the present chapter, the fabrication techniques of core/shell type hybridized NCs and their structure and properties are first described. Next, the ordered array structure of polymer MSs and spherically encapsulated PDA NCs on a patterned substrate will be introduced. Finally, the future scope will be discussed in the relevant fields.

2 Reprecipitation for Preparation of Polymer Nanocrystals

Techniques such as vacuum evaporation method, melting process in a glass matrix, and so on [88], basically fundamental fabrication techniques for inorganic NPs and semiconductor quantum dots, would not be expected to be applied to organic and polymer compounds and materials because of their thermal instability [89, 90]. In contrast, the so-called "reprecipitation method" [1–4] is a useful and convenient procedure to prepare organic and polymer NCs. This method has been further improved as the "supercritical reprecipitation method" [1–3, 28, 29], "reprecipitation-microwave irradiation method" [1–3, 30–34], and "inverse-reprecipitation method" [1–3, 27, 42, 43], being closely related to the physicochemical properties of the target compound and materials.

In the conventional reprecipitation method [1–4], a target compound is first dissolved in a water-miscible organic solvent, e.g. alcohol, acetone, tetrahydrofuran (THF), etc., so that the concentration is on the order of milli-molar (mM). Next, a few microliters of this diluted solution should be injected into 10 mL of vigorously stirred water as a poor solvent at a given temperature by using a microsyringe, and then the target compound is immediately reprecipitated and nanocrystallized in an aqueous dispersion liquid. As a result, one can obtain organic and polymer NCs dispersed in water, for example, π-conjugated PDA [6, 8, 9], and low-molecular weight aromatic compounds like perylene and fullerene [7, 10–12]. The crystal size is usually in the range of several tens of nanometers to sub-micrometer [1–4]. The resulting polymer NCs dispersion liquid looks like an ordinary solution, owing to too low scattering loss caused by the crystal size being less than the wavelength of visible (VIS) light. Actually, PDA is a special case, because diacetylene (DA) monomer is first nanocrystallized by the reprecipitation method, and then the formed DA monomer NCs are further solid-state polymerized in an aqueous dispersion liquid by ultraviolet (UV) irradiation ($\lambda = 254$ nm) to convert to the corresponding PDA [91–93]. We have already revealed the main nanocrystallization processes in the reprecipitation method [12, 36, 37], and could control experimentally the crystal size and shape by changing the reprecipitation conditions: concentration and amount of the injected solution, temperature of poor medium, injection pressure and speed, and addition of surfactant [1–4]. The concentration and the added surfactant may greatly influence the crystal size and shape.

Microwave irradiation (2.45 GHz, 500 W, for a given time) after injection in the reprecipitation-microwave irradiation method could greatly promote rapidly nanocrystallization [1–3, 30–34] due to quick removal of the used organic solvent

by heating, so as to fabricate almost mono-dispersed 1,1,4,4-tetraphenylbutadiene (TPB) NCs within 20 s. TPB is a useful organic electroluminescence (EL) material, being aggregated and not nanocrystallized by the ordinary reprecipitation method without microwave irradiation. As described in Sect. 3, this microwave irradiation is also a very important process for the preparation of metal-core/polymer-shell hybridized NCs.

In addition, the supercritical reprecipitation method [1–3, 28, 29] is available for sparingly soluble compounds in a water-miscible organic solvent, e.g., titanyl-phthalocyanine and fullerene. After dissolving titanyl-phthalocyanine in supercritical acetone fluid, this fluid was cooled by a mixture of acetone and water at room temperature to nanocrystallize titanyl-phthalocyanine. We could control successfully the crystal size and forms of titanyl-phthalocyanine NCs by changing the temperature of supercritical acetone and the volume ratio of the mixed refrigerant of acetone with water. In particular, the γ-form of titanyl-phthalocyanine NCs obtained is noted in the industrial field of Xerography [94].

On the other hand, water-soluble organic compounds, that is to say, organic ionic functional dyes such as merocyanine and pseudoisocyanine, are successfully nanocrystallized by the inverse-reprecipitation method [1–3, 27, 42, 43], in which the poor solvent is a hydrocarbon such as n-hexane and decalin. As a typical example, 4′-dimethylamino-N-methylstilbazolum p-toluenesulfonate (DAST) NCs were fabricated by injecting ethanol solution of DAST into vigorously stirred decalin (10 mL) containing a surfactant n-dodecyltrimethylammonium chloride (DTMAC) to avoid aggregation of formed DAST NCs. DAST presently exhibits the highest performance for organic second-order NLO material [95]. The crystal size was varied from about 200 to 600 nm by adding a small amount (ca. 0.3 wt%) of poly(ester acrylate) (Acrydic A1381, DIC Inc.). DAST NCs dispersion liquid was evaluated in detail as a "Liquid and Crystal" system [1, 2].

3 Metal-Core/Polymer-Shell Hybridized Nanocrystals

In our research group, this kind of metal-core/polymer-shell type hybridized NCs have been first prepared by the "co-reprecipitation method" [45], and it was found that LSP dramatically damped without changing its resonance frequency. We have investigated the damping mechanism in detail, and the revealed reasons have provided a novel material design to avoid the LSP damping [47, 49].

3.1 Co-Reprecipitation Method

Co-reprecipitation method [45] is one of the improved reprecipitation method to prepare a metal-core/polymer-shell type hybridized NCs, in which silver (Ag) NPs aqueous dispersion liquid was employed as a poor medium, instead of water in the

conventional reprecipitation method. Actually, the diluted acetone solution (7.5 mM, 200 μL) of 1,6-di(*N*-carbazolyl)-2,4-hexadiyne (DCHD) [96], which is a kind of DA monomer, was injected into vigorously stirred Ag NPs aqueous dispersion liquid [97]. It was desirable that Ag NPs act as a nucleus and a core, which would be covered with solid-state polymerizable DCHD NCs as a shell, which was subsequently converted into poly(DCHD) shell by UV-irradiation [91–93]. The color of hybridized NCs dispersion liquid changed from pale yellow to bluish purple during solid-state polymerization of DCHD.

3.2   Ag Core/Poly(DCHD)-Shell Hybridized Nanocrystals

Figure 1 shows the scanning electron microscopy (SEM) and transmission electron microscopy (TEM) images of the resulting Ag core/poly(DCHD)-shell hybridized NCs [45]. There are two types, "Type I and Type II," in the SEM image. Type I corresponds to most hybridized NCs. The shape is roughly spherical, and the diameter became clearly larger than bare Ag NPs which was ca. 15 nm in size. That is to say, Ag core could be successfully covered with poly(DCHD) shell, which is also confirmed by the TEM image. The black area, corresponding to Ag NPs, is obviously surrounded by the gray poly(DCHD) shell. On the other hand, Type II is likely to be aggregates of hybridized NCs, in which Ag NPs were partially embedded.
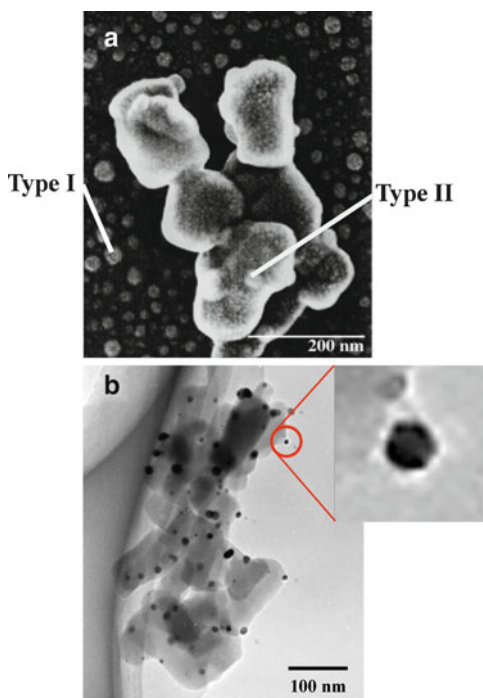
Fig. 1   (a) Scanning electron microscopy (SEM). **(b)** Transmission electron microscopy (TEM) images of Ag core/poly(DCHD)-shell hybridized NCs

3.2.1 Linear Optical Properties During Solid-State Polymerization

Figure 2 exhibits VIS absorption spectral changes during solid-state polymerization [45]. The excitonic absorption peak (EAP) from π-conjugated main chain of poly(DCHD) shell appeared and grew at ca. 655 nm with UV-irradiation time [23], while the LSP from Ag core at around 395 nm was reduced continuously and disappeared at the same time. There are the two characteristic points in the spectral changes [45]: (1) LSP damped without changing the resonance frequency, and (2) the disappearance of LSP may be closely connected with the growth of EAP. The resonance frequency or the peak position of LSP usually changes or shifts when the intensity of LSP is reduced, for example, in bi-metal alloy and metal NPs in an inorganic matrix [98, 99]. In addition, no LSP damping was observed in the case of UV-irradiated mixture of Ag NPs and DCHD NCs dispersion liquids, and the measured VIS absorption spectrum indicates additives of both spectra from Ag NPs and poly(DCHD) NCs [45]. In other words, these facts suggest that a specific electronic and optical interaction may occur at the core/shell hetero nano-interface in hybridized NCs.

On the other hand, the EAP position in Fig. 2 was remarkably red-shifted [23, 45]. As already described in Sect. 1, PDA NCs like poly(DCHD) NCs exhibit the blue-shift of the EAP position with decreasing crystal size [1–3]. The present EAP position, ca. 655 nm, may approximately correspond to poly(DCHD) NCs with above 200 nm in crystal size, which is considerably different from the actual crystal size of Type I as shown in Fig. 1.

This characteristic LSP damping without changing resonance frequency was qualitatively speculated to occur by the following experimental conditions at that time [45]: (1) the energy level of LSP of metal core is near the exciton level (or between band gap) of PDA shell, (2) metal core should be in direct contact with PDA shell at hetero nano-interface in hybridized NCs, and (3) the core/shell volume ratio should also be optimized experimentally.
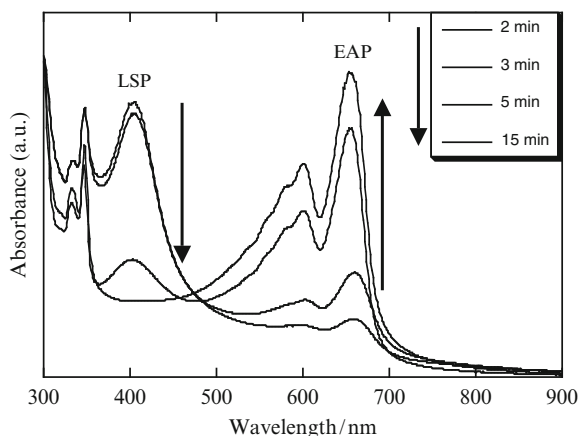
Fig. 2 VIS absorption spectral changes during solid-state polymerization for Ag core/DCHD-shell hybridized NCs

3.2.2   Synchrotron Radiation X-Ray Photoelectron Spectroscopy, and the Speculated Mechanism of LSP Damping

To discuss further the specific interaction at hetero nano-interface in hybridized NCs such as LSP damping, synchrotron radiation X-ray photoelectron spectroscopy (SR-XPS), and X-ray absorption near-edge structure (XANES) were performed in SPring-8 (BL15XU) [47, 49], which is a constant beam line of National Institute for Materials Science (NIMS), Japan. BL15XU has a revolver-type (planar or helical) undulator X-ray source and Si double crystal monochromator, and the energy resolution is about $\delta E/E = 10^{-4}$. XPS analyzer is the modified type based on ULVAC-PHI 10–360 model hemispherical analyzer. SR energy was set to be 4.75 keV, and high energy XPS is necessary to measure an electronic state over the long observation depth in core/shell type hybridized NCs. The binding energy was calibrated not with Fermi edge but the corresponding $C(1s) = 284.8$ eV, since there might not be good metallic contact between PDA shell and specimen holder. The intensity of $L_3M_{4,5}M_{4,5}$ Auger process from Ag core was monitored as a function of X-ray energy with XANES measurement by using a sensitively special mode for thin PDA shell.

Figure 3 indicates the XANES of Ag core in Ag core/poly(DCHD)-shell hybridized NCs [49]. The $L_3M_{4,5}M_{4,5}$ Auger intensity in L_3-absorption edge grew sharply above 3.35 keV, which corresponds to Fermi edge. There was scarcely any difference in XANES before and after solid-state polymerization for PDA shell, these spectra being in fair agreement with that of Ag in the bulk state [100], and clearly different from that of silver oxide. Specifically, no physicochemical changes such as oxidation were brought out in Ag core during solid-state polymerization to
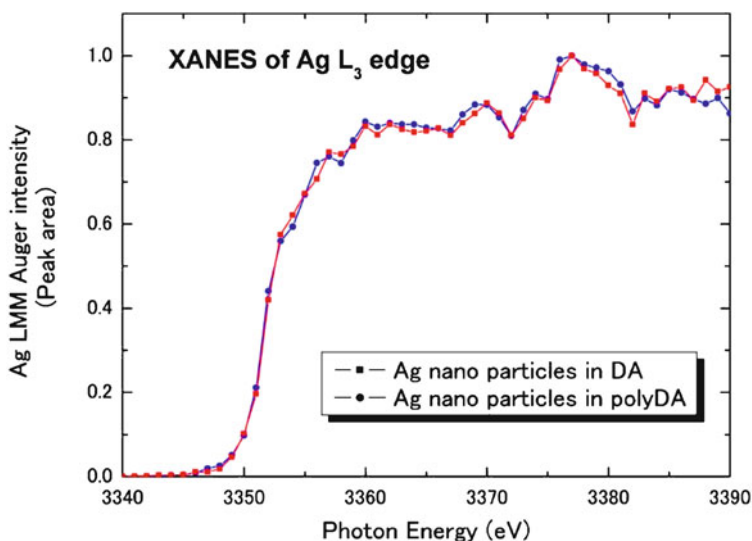
Fig. 3 X-ray absorption near-edge structure (XANES) of Ag core/poly(DCHD) hybridized NCs
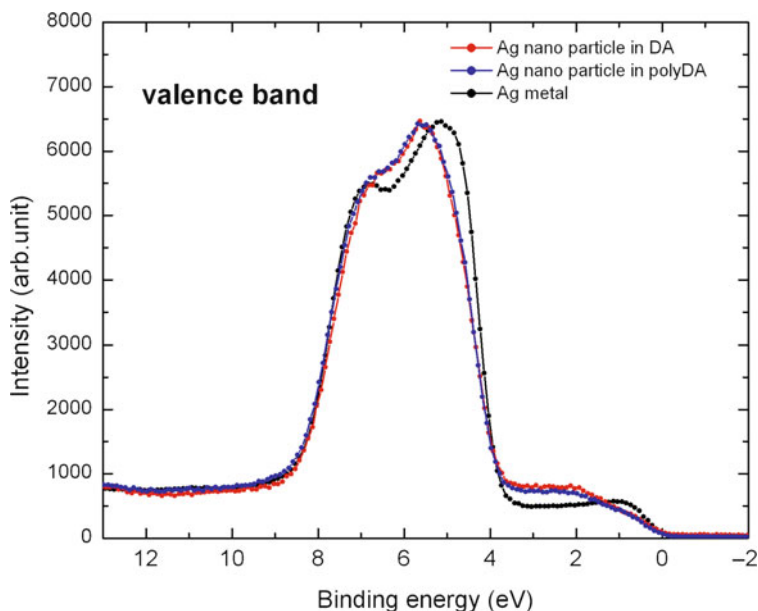
Fig. 4 X-ray photoelectron spectroscopy (XPS) spectra of Ag core in hybridized NCs and bulk Ag

form poly(DCHD) shell. That is to say, Ag core still remains metallic in hybridized NCs. The XPS spectra of Ag core, Ag(5s) and Ag(4d) bands, in hybridized NCs, and bulk Ag are shown in Fig. 4 [47, 49]. Ag(4d) and Ag(5s) bands often form the hybrid valence band (VB) in bulk Ag [101]. The slope at Fermi edge was relatively more gentle than bulk Ag [102], and the intensity of Ag(5s), corresponding to the density of state (DOS), also became higher than that of bulk Ag. In addition, Ag(4d) band at around 4–6 eV was obviously shifted by ca. 0.4 eV to the high binding energy region, and Ag(4d) band width became narrow, compared with bulk Ag. Probably, the hybrid band of Ag(4d) and Ag(5s) in hybridized NCs is different from that of bulk Ag [47]. In particular, the narrowing of Ag(4d) band suggests that the "electronic conductive domain" inside Ag core is less than ca. 5 nm [49], which is obviously smaller than the overall size of the hybridized NCs as shown in Fig. 1. This domain might be a kind of resistive boundary in Ag core, and becomes difficult to keep the intensity of LSP, since LSP originates in a collective oscillation of the conduction electrons in VB and is closely related to mean-free-path of conduction free electrons [47, 103].

On the other hand, the main peak of C(1s) band (284.8 eV) from poly(DCHD)-shell was accompanied by the satellite peak (ca. 292 eV), due to π–π* transition along π-conjugated poly(DCHD) shell [104]. The spectra of C(1s) were independent of observation depth, using SR energy = 4.5 and 3.0 keV, which may lead to the almost uniformity in depth of poly(DCHD) shell. Under a certain circumstance, the main peak of C(1s) band was broadened and tailed asymmetrically to the high binding energy region [47]. This type of tailing was not observed in poly(DCHD) NCs without Ag core.

In addition, the MVV Auger peak (kinetic energy = 351.6 eV) from Ag core, corresponding to short observation depth, appeared in the hybridized NCs, which suggests the existence of interspace between poly(DCHD)-shell and some part of Ag core [49]. The present interspace is due to difficulty in stacking poly(DCHD) shell closely on a steeply curved surface of Ag core, because poly(DCHD) is one-dimensional conjugated and rigid chain in the crystal state of PDA shell [91–93].

One can imagine from these experimental results that PDA chains inside poly(DCHD)shell may contact with some points on the surface of Ag core [47, 49]. These contact points at hetero nano-interface might be anchors to disturb and depress the plasma oscillation, and then diminish the mean-free-path of conduction free electrons in VB of Ag core. In other words, the LSP of Ag core would damp simply without changing the resonance frequency, owing to the reduction of electronic conductive domain induced by locally and strongly physicochemical interaction at the core/shell interface in the hybridized NCs [103, 105].

3.3 Ag Core/Poly(ADA)-Shell Hybridized Nanocrystals

LSP damping as discussed in Sect. 3.2.2 is basically an interesting behavior in core/shell type hybridized NCs. However, this kind of LSP damping describes an undesirable result for potential application as plasmonic nanomaterials. We have to and would like to control LSP behavior by optimizing the hetero nano-interface structure. There exists the two factors to avoid LSP damping: (1) enlargement of Ag core, relating to the size of electronic conductive domain and (2) indirect contact at hetero nano-interface to reduce specific physicochemical interaction between core and shell [50]. Instead of DCHD monomer, 10,12-heptacosadiynoic acid (ADA) monomer was used in the present section. ADA is a kind of amphiphilic DA having $R_1 = -(CH_2)_{13}CH_3$ and $R_2 = -(CH_2)_6COOH$.

3.3.1 Co-Reprecipitation and Microwave-Irradiation Method

The improved co-reprecipitation and microwave-irradiation method is an effective process to fabricate Ag core/poly(ADA)-shell hybridized NCs [30, 45, 50]. Ag NPs in an aqueous dispersion liquid were prepared by reducing silver nitrate (AgNO$_3$) with trisodium citrate [106]. The size of the resulting Ag NPs was ca. 45–50 nm, which is larger than that in Sect. 3.2.

The acetone solution (5 mM, 200 μL) of ADA was injected into vigorously stirred Ag NPs dispersion liquid at room temperature. Afterwards, the mixed dispersion liquid was poured into a Teflon vessel, sealed-up, irradiated by microwave (2.45 GHz, 500 W, 40 s), and then was cooled down again to room temperature. After UV-irradiation for solid-state polymerization to convert ADA into poly(ADA) [91–93], the resulting dispersion liquid was centrifuged for 15 min at 8,000 rpm to remove residual poly(ADA) NCs having no Ag core.
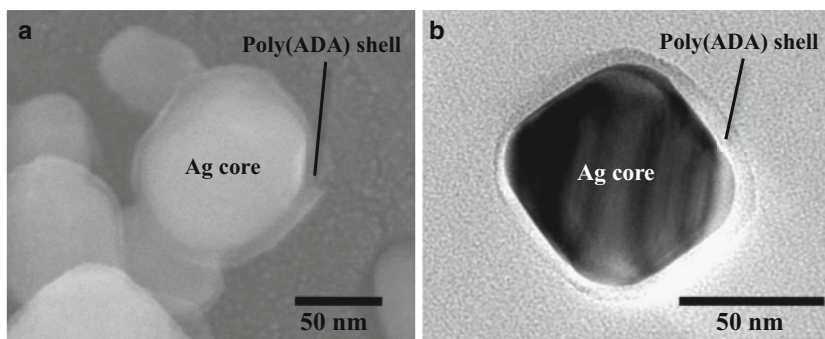
Fig. 5 SEM (**a**) and TEM (**b**) images of Ag core/poly(ADA)-shell hybridized NCs

Figure 5 displays the SEM and TEM images of Ag core/poly(ADA)-shell hybridized NCs [50]. Actually, Ag core was clearly covered with almost uniform poly(ADA) shell. The thickness of the shell was about 5 nm, and the morphology of the core/shell nanostructure in the present hybridized NCs was dependent remarkably on microwave irradiation conditions [50]. For example, the above-mentioned microwave irradiation condition is the most desirable, and the core/shell nanostructure could not be formed successfully when the irradiation condition was 500 W, 20 s or 200 W, 40 s. After co-reprecipitation, the dispersion liquid is considered to be a mixture of Ag NPs and ADA NCs. The heated ADA NCs were probably partially melted by microwave irradiation, and may easily collide and fuse with Ag NPs at the elevated temperature. As a result, molten ADA monomer could adsorb effectively on the surface of Ag core, and was then recrystallized to form solid-state polymerizable ADA shell during the cooling process after microwave irradiation [50]. The present co-reprecipitation and microwave-irradiation method is available for the fabrication of another type of metal-core/π-conjugated polymer-shell hybridized NCs [107].

3.3.2 Extinction Spectrum of Hybridized Nanocrystals

The extinction spectrum of Ag core/poly(ADA)-shell hybridized NCs dispersion liquid is shown in Fig. 6 [50]. The main peak at ca. 450 nm is assigned to LSP of Ag core [108], and was red-shifted and broadened because of the large size and its distribution of Ag core [109–111]. The small shoulder peak at 540 nm may come from the EAP of poly(ADA) shell [112], and the inset in Fig. 6 also displays the differential spectrum before and after solid-state polymerization. The obtained extinction spectrum could be reproduced by spectrum simulation on the basis of Mie scattering theory [113], assuming spherical Ag core (radius = 45 nm)/poly(ADA) shell (thickness = 5 nm) type hybridized NC. In Fig. 7, both main peaks around 450–500 nm is attribute to LSP (Fröhlich mode) of Ag core, and the two sharp peaks at 380 and 400 nm are the quadrupole mode of LSP [108].

Fig. 6 Extinction spectra of
(**a**) bare Ag core and
(**b**) Ag core/poly(ADA)-shell
hybridized NCs. The *inset* is
differential spectrum
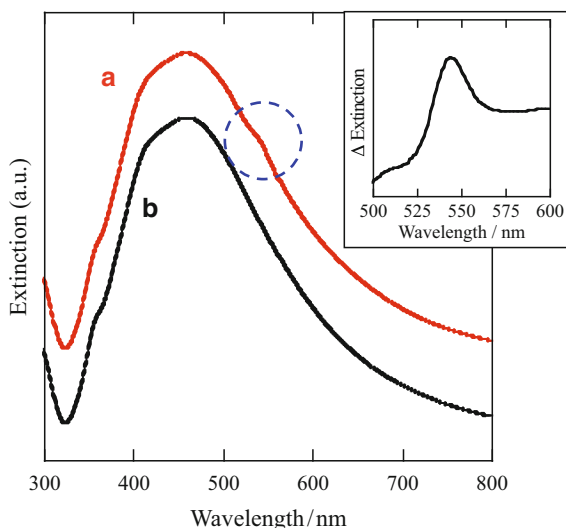
Fig. 7 Simulated extinction
spectra of (**a**) spherical Ag
core (radius = 45 nm) and
(**b**) Ag core (radius =
45 nm)/poly(ADA)-shell
(thickness = 5 nm)
hybridized NCs by Mie
scattering theory
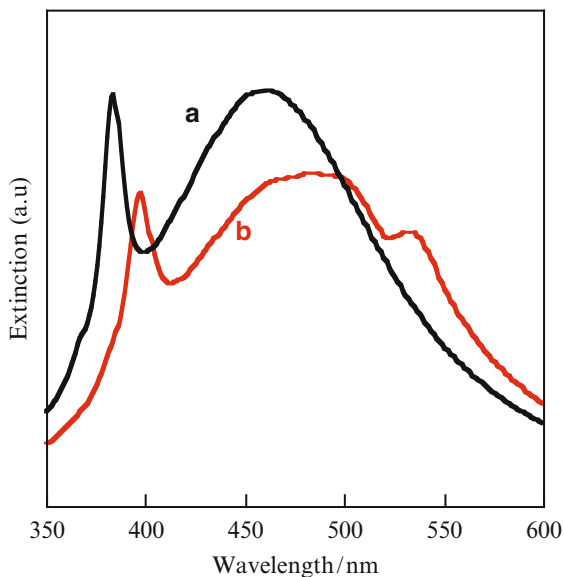
One can see the EAP at 540 nm [112], which is due to the red-phase of poly(ADA) [114, 115]. In comparison with the previous poly(DCHD), the polymer backbone of poly(ADA) is relatively not rigid but flexible, and then there exist the two kinds of excitonic states from red-phase ($\lambda = 540$ nm) and blue-phase ($\lambda = 630$ nm), relating to the effective π-conjugation length. An average molecular weight, temperature, strain of crystal lattice, and so on may greatly affect the effective π-conjugation length in a solid state of PDA. Namely, poly(ADA) shell in the present hybridized NCs was reasonably assigned to red-phase, corresponding to

shorter π-conjugation length. As shown in TEM image of Fig. 5b, the surface of Ag core consists of some facets, which are not completely plane but curved surface. On the other hand, ADA monomers are solid-state polymerizably arranged inside the shell, but one end of ADA monomer is adsorbed and fixed on the curved surface of Ag core. These factors presumably lead to the difficulty in releasing lattice strain during solid-state polymerization of ADA shell [91–93]. In the end, the backbone of the resulting poly(ADA) is disordered and perturbed in the shell, and then the effective π-conjugation length becomes shorter [50].

Anyway, the LSP still appears in Ag core/poly(ADA)-shell hybridized NCs, which will be one of the promising nanomaterials for photonic device application in the near future.

4 Polymer-Core/Metal-Shell Hybridized Nanocrystals

This polymer-core/metal-shell type of the hybridized NCs has an inverse nanostructure of Sect. 3. Our research group has recently established the unique fabrication process, "visible-light-driven photocatalytic reduction method" [53], to PDA-core/metal-shell hybridized NCs.

4.1 Ag-Coated Poly(DCHD) Nanocrystals Prepared by Using Surfactant as a Binder

The following fabrication process was first proposed. By the reprecipitation method [1–4], poly(DCHD) NCs as a core were commonly prepared by injecting acetone solution of DCHD monomer containing a certain surfactant into vigorously stirred water [51, 52], and then UV-irradiation was performed for solid-state polymerization [91–93]. Subsequently, aqueous solutions of $AgNO_3$ and the reducing agents like sodium borohydride ($NaBH_4$) and hydroxylamine (NH_2OH) were added into poly(DCHD) NCs dispersion liquid for the purpose of in-site reducing Ag^+ in the presence of poly(DCHD) NCs [51, 52]. We found that Ag NPs deposited on the surface of poly(DCHD) NCs by the SEM observation [51, 52]. As previously discussed in [14], poly(DCHD) NCs are coated with the surfactant, this ionic moiety being exposed to the water phase in the present case. It was found that sodium dodecylsulfate (SDS) was the most effective in ordinary anionic or cationic surfactant [52]. It was speculated that Ag^+ was first caught by the anionic moiety of SDS adsorbed on the surface of poly(DCHD) core, and then Ag NPs were deposited subsequently by reducing the trapped Ag^+ in situ [51, 52]. The coverage of the deposited Ag NPs as Ag shell would be necessarily high (roughly 50%), and strongly dependent on concentration of added SDS. For example, the coverage becomes low when SDS concentration is too low. On the other hand, Ag NPs were produced in an aqueous medium as well as on the surface of poly(DCHD)

core, due to non-adsorbed SDS, when SDS concentration is too high. Namely, it is necessary and difficult to appropriately optimize the concentration of added SDS, which is also in connection with to the surface area and dispersion concentration of poly(DCHD) core. Moreover, if a surfactant would give an unexpected influence to hetero nano-interface interaction and function, the existence of surfactant is not desirable in the present case.

4.2 Visible-Light-Driven Photocatalytic Reduction Method to Fabricate Poly(DCHD)-Core/Ag-Shell Hybridized Nanocrystals

To overcome the above-mentioned subject matter in Sect. 4.1, "visible-light-driven photocatalytic reduction method" [53] (hereinafter, called "photocatalytic reduction method") has been newly established by utilizing that poly(DCHD) core may absorb VIS light because of excitonic absorption along π-conjugation polymer backbone [23]. In this method, aqueous solutions of $AgNO_3$ and ammonia are first added into poly(DCHD) NCs dispersion liquid, and then VIS light should be irradiated for a given time, commonly 30 min, using a xenon lamp (USHIO, 500 W) equipped with an attenuator and UV-cut filter ($\lambda > 420$ nm). The reaction temperature was fixed at 40°C in the present case. Namely, poly(DCHD) NCs may act as a photocatalysis and substrate as later discussed in detail [53].

Figure 8 indicates the SEM and TEM images of the obtained poly(DCHD)-core/Ag-shell hybridized NCs [53]. Actually, Ag shell is composed of a great number of Ag NPs of size 5–15 nm, densely deposited "only" on the surface of
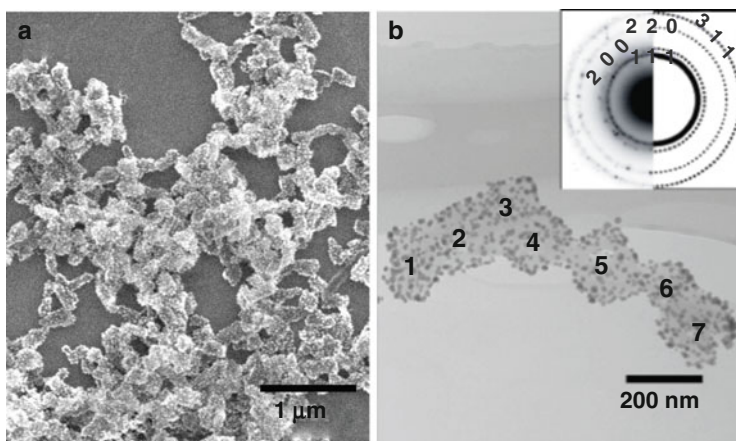
Fig. 8 SEM (**a**) and TEM (**b**) images of poly(DCHD)-core/Ag-shell hybridized NCs. The *inset* is electron diffraction (ED) patterns of Ag nanoparticles on poly(DCHD) NCs
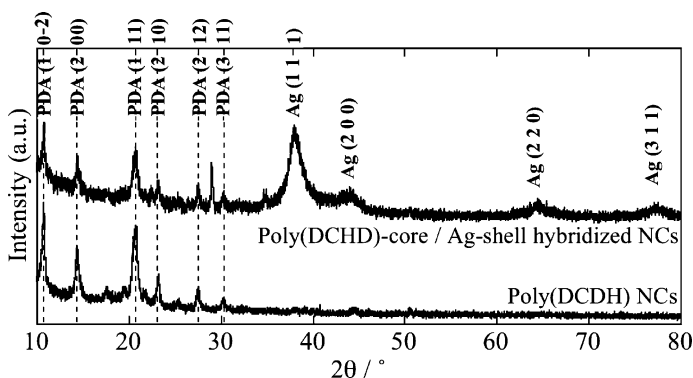
Fig. 9 Powder-XRD patterns of bare poly(DCHD) NCs and poly(DCHD)-core/Ag-shell hybridized NCs

Fig. 10 Electron probe microanalysis (EPMA) spectrum of poly(DCHD)-core/Ag-shell hybridized NCs
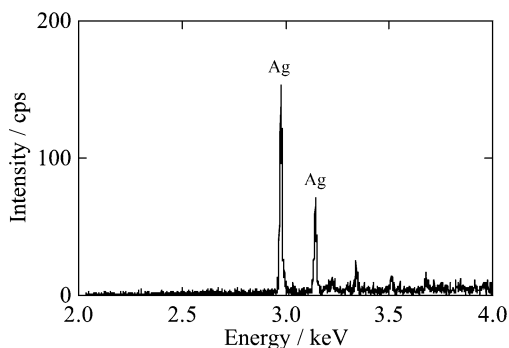
poly(DCHD) core. No isolated Ag NPs were observed in both SEM and TEM images. All the data measured with electron diffraction (ED) pattern, displayed in the inset of TEM image [Debye-Scherrer rings, i.e., ED from (111), (200), (210), and (311) planes in the face-centered cubic (fcc) crystal lattice of bulk Ag (JCPDS: 4–783)], powder X-ray diffraction (XRD) pattern (Fig. 9), and electron probe microanalysis (EPMA) (Fig. 10) evidently supported that the deposited material on the surface of poly(DCHD) core is not anything like silver oxide but truly Ag at the hetero nano-interface.

4.2.1 Extinction Spectrum of Hybridized Nanocrystals

Figure 11 exhibits the extinction spectra of poly(DCHD)-core/Ag-shell hybridized NCs [53]. The LSP in the hybridized NCs was red-shifted ($\lambda = 448$ nm) and broadened, compared with the LSP ($\lambda = 395$ nm) of bare Ag NPs [108] of the same size as the deposited ones on the surface of poly(DCHD) core. The red-shift of LSP is mainly caused by the increase in the dipole–dipole interaction [109], owing to

Fig. 11 Extinction spectra of (**a**) bare poly(DCHD) NCs, (**b**) isolated Ag nanoparticles (ave. diameter = 10 nm), and (**c**) poly(DCHD)-core/Ag-shell hybridized NCs
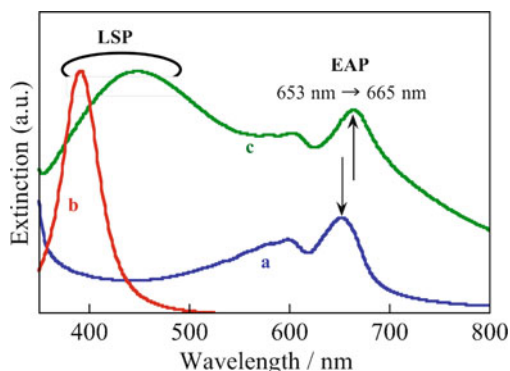
the shortening of average distance among the deposited Ag NPs, as the reduction and deposition proceeded during photocatalytic reduction process. The broadening is not understood so clearly. Probably, this is due to imhomogeneous size distribution of the deposited Ag NPs and the dephasing effect of LSP in grown Ag NPs deposited on the surface of poly(DCHD) core [109–111].

On the other hand, the EAP ($\lambda = 653$ nm) [23] was also red-shifted a little, because of changes in surrounding dielectric properties around the poly(DCHD) core. These spectral changes also support the formation of poly(DCHD)-core/Ag-shell hybridized NCs. The tailing of LSP spectrum is overlapped enough on excitonic absorption [74, 75, 80–85], which would be expected to be a interaction between plasmon and exciton for a novel optoelectronic application.

4.2.2 Mechanism of Photocatalytic Reduction Method (1)

Interestingly, the reduction did not proceed when only one factor was lacking in the above-mentioned experimental conditions [53]. For example, Ag^+ from $AgNO_3$ was not reduced entirely by VIS light in the absence of poly(DCHD) NCs as a core. In addition, this reduction also did not take place completely, when unpolymerized DA NCs were used [53], these not undergoing absorption in the VIS light region. In fact, the photocatalytic reduction seems to be specific on the surface of poly(DCHD) core. To our knowledge, Ag^+ cannot be directly reduced to Ag^0 by irradiating VIS light.

Figure 12 demonstrates the typical band structure of PDA [116]: normally, conduction band (CB) $= -3.44$ eV and VB $= -5.77$ eV, and the band gap, which is not an excitonic absorption band, is 2.33 eV, corresponding to $\lambda = 530$ nm in the VIS light region. On the other hand, the redox potential of $[Ag(NH_3)_2]^+$ is 0.373 V vs standard hydrogen electrode (SHE) [53], which is located in the band gap between CB and VB for PDA. Therefore, the electrons excited to CB of PDA by absorbing VIS light are capable of specifically reducing $[Ag(NH_3)_2]^+$ on the surface PDA core. In the present case, an aqueous solution of ammonia was added to form silver-amine complex, and the pH in the dispersion liquid was ca. 9 at the initial stage. After finishing the reduction and the subsequent deposition of Ag NPs,
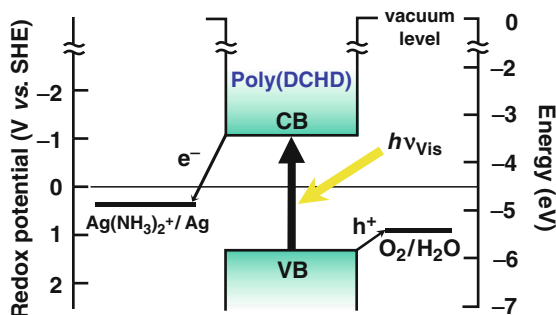
Fig. 12 Energy diagram of photocatalytic reduction process. The conduction band (CB) and valence band (VB) for poly(DCHD) are, respectively, -3.44 and -5.77 eV vs the vacuum level, corresponding to -1.06 and 1.27 V vs SHE. The redox potentials of $[Ag(NH_3)_2]^+$ as a major component of the Ag cations in the present system and H_2O are 0.373 and 1.23 V vs SHE, respectively

the pH became low at ca. 6 [53]. These facts suggest the possibility of oxidation of water molecules in the surrounding aqueous dispersion liquid by the holes generated in VB of VIS light-irradiated PDA NCs as shown in Fig. 12. In other words, the following oxidation process of water molecules may quench the holes:

$$2H_2O + 4h^+ \rightarrow O_2 + 4H^+ \tag{1}$$

In general, the pH-dependence of redox potential for the water molecule is given by [117]

$$E_{redox}(H_2O) = 1.23 - 0.059 \times pH (V\,vs.\,SHE) \tag{2}$$

Actually, the present reduction did not occur under acidic conditions. In a word, it becomes difficult to oxidize water molecules at low pH for hole scavenging [53].

In addition, there are some advantageous factors in surface-specific reduction of Ag^+ on PDA core. The first is the electrostatic adsorption between $[Ag(NH_3)_2]^+$ and PDA-core having negative ζ-potential (ca. -40 mV) [14], the second is the self-catalytic property [118] of already-deposited Ag NPs to reduce $[Ag(NH_3)_2]^+$, and the final is the suppression of electron-hole recombination, because of rapid carrier separation at hetero nano-interface.

4.3 Extension of Photocatalytic Reduction Method, and the Post Chemical Reduction Treatment to Form Metal Nanoshell Structure

The most important point in the present photocatalytic reduction method is that the redox potential of metal ion should be located between CB and VB for π-conjugated polymer core, and that the generated holes in the VB should be quenched at once through an oxidation of scavenger [53]. In other words, the photocatalytic

reduction method could proceed, regardless of the size, shape, and morphology of the polymer core [53]. Thus, by using the post chemical reduction treatment together [54], one can expectedly apply and expand this method to various combinations of π-conjugated polymer core and noble metal shell for highly potential applications [119], e.g., novel electronic and photonic devices, polymer/metal hetero-junction for integrated circuits in organic transistors, and a new type of hybridized system such as meta-materials [120].

4.3.1 Poly(DCHD)-Core/Pt-Shell Hybridized Nanocrystals

Figure 13 shows the SEM and TEM images of the resulting poly(DCHD)-core/platinum (Pt)-shell hybridized NCs prepared by using potassium tetrachloro-platinate (K_2PtCl_4) [54]. The redox potential of $[PtCl_4]^-$ is 0.73 mV vs SHE, and is also located fairly in the band gap of poly(DCHD) core [53]. The fabrication conditions are basically similar to those in Sect. 4.2. A large number of Pt NPs were homogeneously and very densely deposited on the surface of poly(DCHD) core, and the average size of deposited Pt NPs were very fine and estimated to be below 5 nm from the TEM image. As a result, the SEM image of hybridized NCs provided clearer contrast, compared with that of bare poly(DCHD) NCs.

4.3.2 Mechanism of Photocatalytic Reduction Method (2)

As shown in Figs. 8 and 13, the difference in size of the deposited Ag NPs and Pt NPs seems to be attributable to work function (WF) of Ag and Pt. We now summarize the values of redox potential and WF [54]. The redox potential of $Ag[(NH_3)_2]^+$ is 0.373 mV vs SHE $= -4.873$ eV, and WF(Ag) is -4.26 eV. On the other hand, the same quantity of $[PtCl_4]^-$ is 0.73 mV vs SHE $= -5.23$ eV, and WF(Pt) is -5.64 eV, respectively.

According to these numerical data, we could perform the following discussion. The WF(Ag) is higher than the redox potential of $[Ag(NH_3)_2]^+$. The reduction of $[Ag(NH_3)_2]^+$ by electrons excited to CB of PDA-core may preferentially take place
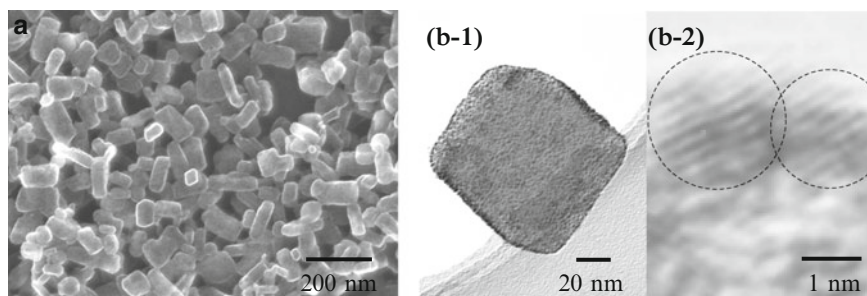
Fig. 13 SEM (**a**) and TEM (**b-1**, **b-2**) images of poly(DCHD)-core/Pt-shell hybridized NCs

on the surface of Ag NPs already-deposited on PDA core, and then the preformed Ag NPs principally grow up. In contrast, the reduction of Pt-complex may proceed mainly on the surface of PDA core, since the WF(Pt) is lower than the redox potential of $[PtCl_4]^-$. In other words, electrons excited to CB of PDA core by VIS light irradiation may move rapidly to WF level of Ag or to the redox potential level of Pt in each case. Therefore, the size of the deposited Ag NPs is relatively large, and the coverage becomes low, compared with the case of deposition of Pt NPs. The relative correlation between WF and redox potential may also considerably affect the morphology of metal/shell nanostructure [54].

Actually, the following experimental conditions should be optimized to fabricate the present type well-defined hybridized NCs, except for selected combination of π-conjugated polymer and a noble metal, concentration of metal-salt solution, initial pH control by adding base like ammonia, reaction temperature and time, stirring method, and VIS light intensity [53,54]. Recently, it has become apparent that ultrasonic wave irradiation is much more effective than mechanical stirring [121].

4.3.3 Post-Chemical Reduction Treatment to Form Metal Nanoshell Structure

Perhaps, it becomes difficult to deposit gold (Au) NPs directly, as Au shell, on the surface of poly(DCHD) core by means of the photocatalytic reduction method [60], since the redox potential of $[AuCl_4]^-$, precursor of Au, is 1.002 mV vs SHE. This value is close to the redox potential of water given by (2) as well as VB for PDA as shown in Fig. 12. In addition, $[AuCl_4]^-$ may absorb some VIS light, which is also undesirable in the present preparation procedure. However, already-deposited Ag NPs on poly(DCHD) core can be regarded as both a catalyst and a substrate for electroless plating with other kinds of metals. Thus, we could prepare metal nanoshell structure by means of post-chemical reduction treatment.

So, a certain amount of tetrachloroauric acid (HAuCl$_4$) aqueous solution and ascorbic acid (reducing agent) were added into the aqueous dispersion liquid of poly(DCHD)-core/Ag-shell hybridized NCs, and then the mixture was stirred at room temperature for a given time. Figure 14 demonstrates the SEM images before and after the post-chemical reduction treatment. A large number of metal NPs were deposited selectively only on the surface of the poly(DCHD) core, i.e., Au(–Ag)-deposited poly(DCHD) NCs. As shown in Fig. 15, the composition of metal-shell could be confirmed to be Au by the measurement with EPMA. The powder XRD method was not measured, because the fcc lattice constant of Au is $a = 0.408$ nm, almost the same as that of Ag (fcc: $a = 0.409$ nm) [54]. Figure 16 shows the extinction spectral changes with post-chemical reduction treatment [54]. The LSP peak of Ag NPs was reduced gradually, while the LSP from Au NPs appeared around 560 nm. Since both deposited Ag NP and Au NP domains formed inside the metal shell are much smaller than the wavelength in VIS region, the effective dielectric constant of the metal shell may correspond to an alloy of Ag and Au [122, 123]. Namely, the extinction spectra in Fig. 16 may reflect the effective dielectric constant of Ag-Au
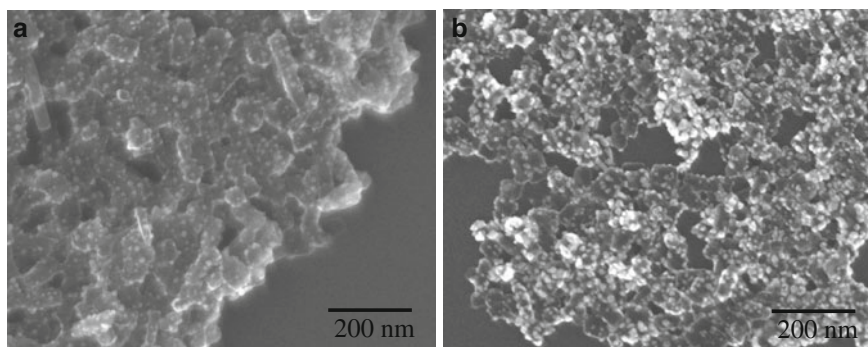
Fig. 14 SEM images (**a**) before and (**b**) after the post-chemical reduction treatment: (**a**) Ag- and (**b**) Au(–Ag)-deposited poly(DCHD) NCs

Fig. 15 EPMA spectrum of Au(–Ag)-deposited poly(DCHD) NCs
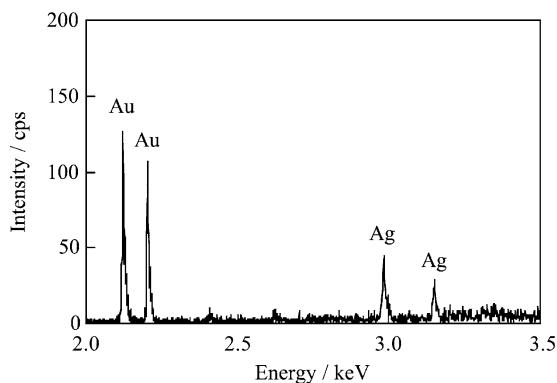
Fig. 16 Extinction spectral changes with the post-chemical reduction treatment: (**a**) Ag- and (**b**) Au(–Ag)-deposited poly(DCHD) NCs
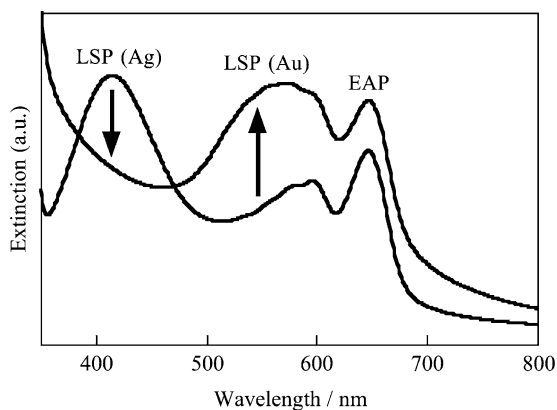
alloy and poly(DCHD) core, not being simply the additive extinction spectra from individual Ag NPs and Au NPs [54].

In addition, Fig. 17a, b indicates the SEM images in the cases of Pt and palladium (Pd) [54]: Pt(–Ag)-deposited, and Pd(–Ag)-deposited poly(DCHD) NCs, which
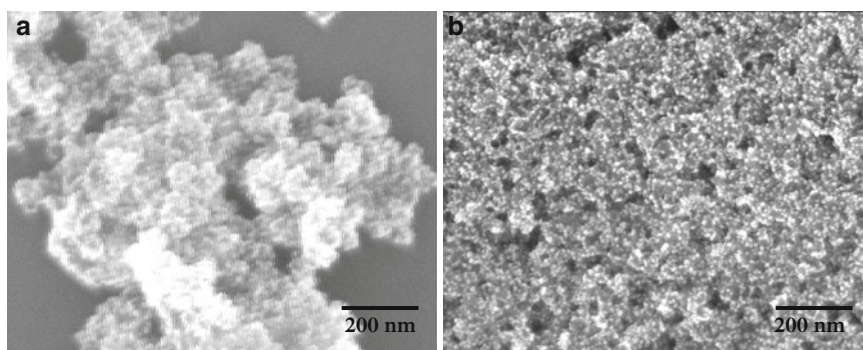
Fig. 17 SEM images of (**a**) Pt(–Ag)- and (**b**) Pd(–Ag)-deposited poly(DCHD) NCs
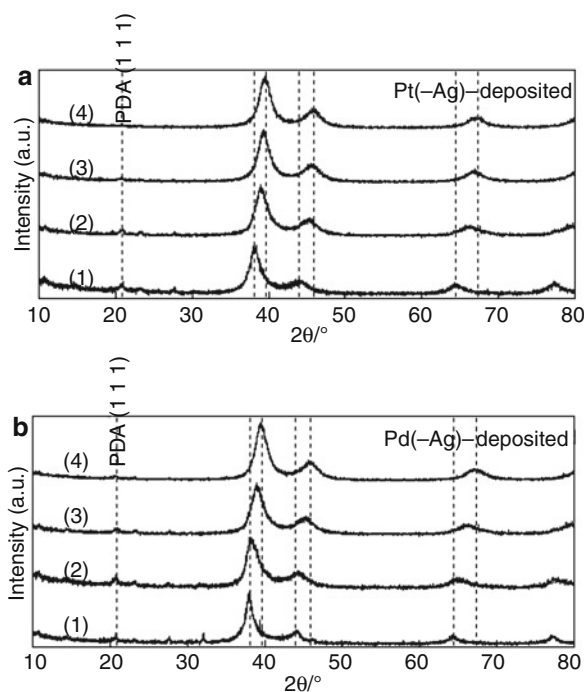
Fig. 18 Powder-XRD patterns of (**a**) Pt(–Ag)- and (**b**) Pd(–Ag)-deposited poly(DCHD) NCs: Added amount of Pt or Pd salt aqueous solution; (1) 0, (2) 20, (3) 50, and (4) 100 μL

were, respectively, fabricated by the reduction of aqueous solutions of K_2PtCl_4 and sodium tetrachloropalladate (Na_2PdCl_4) using ascorbic acid. Figure 18 displays the powder XRD patterns of these hybridized NCs prepared with different amounts of K_2PtCl_4 or Na_2PdCl_4 aqueous solution. Interestingly, the XRD peaks were shifted from the original peak position of Ag to that of Pt or that of Pd with increasing the

amount of added Pt or Pd salt. Perhaps the present shells of Pt(–Ag) and Pd(–Ag) were a metal-alloy (nano)structure [124–126].

On the other hand, Pt NPs preformed on poly(DCHD) core (see Sect. 4.3.1) were also used as both self-catalyst and substrate. That is to say, when K_2PtCl_4 aqueous solution and ascorbic acid is further added into the dispersion liquid of poly(DCHD)-core/Pt-shell hybridized NCs, one could successfully fabricate the thicker and self-grown Pt shell [54], i.e., Pt(-Pt)-deposited poly(DCHD) NCs, as shown in the TEM images of Fig. 19. Figure 20 exhibits the powder XRD pattern of poly(DCHD)-core/Pt-shell hybridized NCs and Pt(-Pt)-deposited poly(DCHD) NCs. The average size of deposited Pt NPs was evaluated to be 3.1 nm by applying the Scherrer equation [127] to the (111) diffraction peak, which was almost the same as the average size from the TEM images as described in Sect. 4.3.1. In Fig. 20 there are no diffraction peaks from deposited Pt NPs before post-chemical reduction treatment, owing to too small a size. On the contrary, the broad (111) diffraction

Fig. 19 TEM image of Pt(-Pt)-deposited poly(DCHD) NCs

100 nm
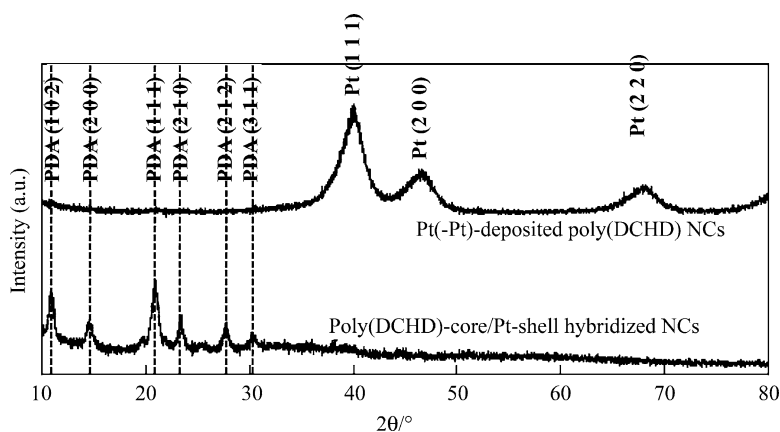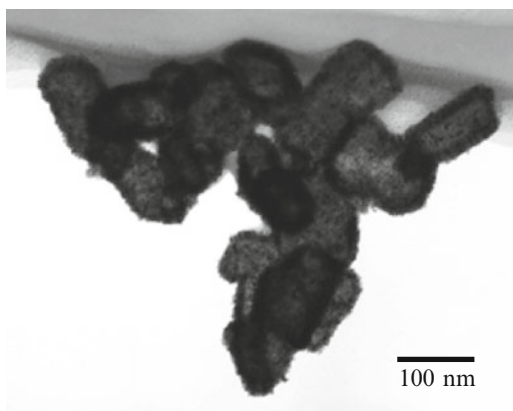
Fig. 20 Powder-XRD patterns of poly(DCHD)-core/Pt-shell hybridized NCs and Pt(-Pt)-deposited poly(DCHD) NCs

peak of Pt NPs appeared after post chemical reduction treatment. The XRD from poly(DCHD) core apparently disappeared at the same time. This fact also supported the formation of a thicker Pt shell [54].

4.4 Poly(alkylthiophene)-Core/Pt-Shell Hybridized Nanocrystals Fabricated by Visible-Light-Driven Photocatalytic Reduction Method

Poly(3-alkylthiophene) (PAT) is also a kind of π-conjugated polymer, which is soluble in common organic solvents, and one of the most remarkable polymer materials for polymer devices such as the organic thin film transistor (TFT) and EL, photovoltaic cell, etc. [128].

PAT used in the present study was regioregular, and the alkyl chain lengths were butyl (PAT-4), hexyl (PAT-6), and octyl (PAT-8), respectively. Figure 21 indicates the SEM images of PAT NPs, which were fabricated conveniently by the reprecipitation method, using THF and water as good and poor solvents [121, 129]. The size of the formed PAT NPs increased in general with the concentration of THF solutions of PAT, and the shape was also turned from spherical to rectangular-like. The VIS absorption (or extinction) spectra for THF solutions of PAT showed the maximum absorption peaks at around 430 nm, interestingly being independent of alkyl chain lengths, and these peaks were distinctly red-shifted to the range of about 480–510 nm in PAT NPs. This behavior indicates the extension of effective π-conjugation along PAT backbone [130], compared with the random coiled configuration of PAT chain in the solution state. In particular, PAT-6 and PAT-8 NPs provided the small absorption shoulder at ca. 630 nm, due to ordered π–π stacking structure induced by long alkyl chains.

As shown in the TEM images of Fig. 22, PAT-core/Pt-shell hybridized NPs were similarly prepared by adding K_2PtCl_4, ammonia, and a small amount of formaldehyde (HCHO) as a hole scavenger into an aqueous dispersion liquid of PAT NPs, and
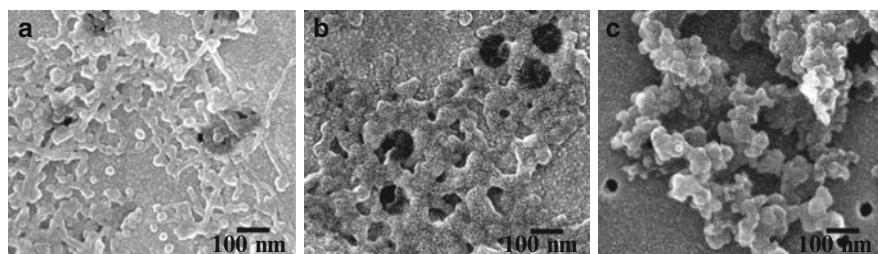
Fig. 21 SEM images of (**a**) PAT-4, (**b**) PAT-6, and (**c**) PAT-8 NPs

Fig. 22 TEM image
of PAT-8-core/Pt-shell
hybridized NPs
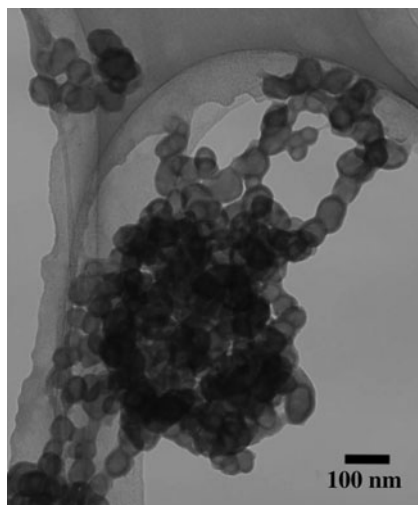
Fig. 23 EPMA spectrum
of PAT-8-core/Pt-shell
hybridized NPs
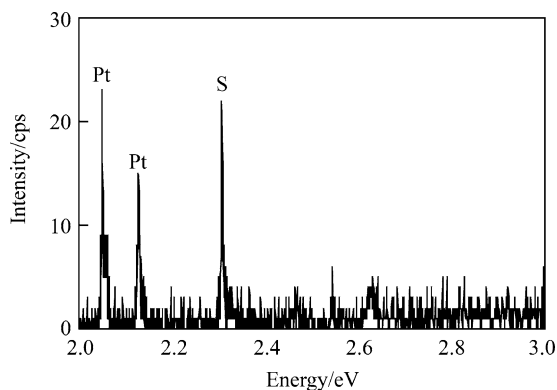
then VIS light was irradiated for a given time [121, 129]. The thickness of Pt shell is about 5–10 nm. Figure 23 represented the typical EPMA data. The band structure of PAT is shallow: CB = −2.85 eV and VB = −5.25 eV [131] by comparison with PDA. Namely, the oxidation of water to quench the hole, as discussed in Sects. 4.2.2 and 4.3.2, is ineffective, and then HCHO (E_{redox} = 0.197vs SHE) was employed as follows [117]:

$$HCHO_{aq.} + 2H_2O + 4h^+ \rightarrow CO_3^{2-} + 6H^+ \tag{3}$$
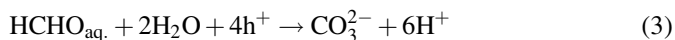
In addition, Pt shell, i.e., Pt(-Pt)-deposited PAT NPs, could be fabricated successfully through the post-chemical reduction treatment by adding K_2PtCl_4, a small amount of poly(vinylpyrrolidone) (PVP) as a dispersion stabilizer, and formic acid (reducing agent) [121, 129]. Figure 24 indicates the SEM image of Pt shell formed on the surface of PAT NPs.
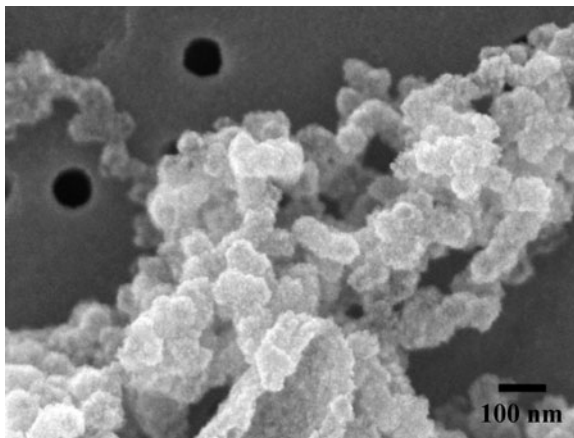
Fig. 24 SEM image of PAT-8-core/Pt-shell hybridized NPs after the post-chemical reduction treatment

5 Ordered Array Structure of Polymer Microspheres on Patterned Substrate, and Arrangement of Encapsulated Polymer Nanocrystals

For optoelectronic or photonic device application using polymer NCs (or NPs) including hybridized ones, it should be necessary to integrate and assemble high ordered nanostructure on a substrate [87], and should be possible to control input and output information signals by accessing polymer NCs electronically (or electrically) and/or optically [132–134]. In other words, the dispersion liquids of the present polymer NCs and hybridized ones are not directly available for device application, except for a so-called "Liquid and Crystal" system like DAST NCs dispersion liquid as described in Sect. 2 [21, 41–43]. Specifically, one has to array, align, and orientate polymer NCs selectively on a substrate. However, ordinary polymer NCs are not spherical but cubic or rectangular, and unfortunately have a size distribution [61].

To overcome these problems, our attention is now intently focused on encapsulation of polymer NCs and the use of lithographically patterned substrate [59–61]. Encapsulation could provide some advantages [61]: pseudo-monodisperse in size of polymer NCs, spherical shape, and passivation effect for stable dispersion. In addition, a patterned substrate seems to be very useful in order to control the selectivity of position and location on a substrate and to construct ordered array and integrated nanostructure [59, 135, 136].

Actually, self-assembly micro-structure and nano-structure of colloidal particles have generated much interest for developing photonic device application [59, 87]. The large area and regular micro-structure and nano-structure made of polymer or silica colloidal crystal on a substrate could be realized by means of some preparation techniques, for example, sedimentation at the gravitational field [137], crystallization induced by capillary force [138], and dewetting processes [139]. On

the other hand, a patterned substrate is often employed as a template to control precisely the position of colloidal particles or as a field to induce nucleation of organic NCs [55, 56, 135, 136].

First, some ordered structure of mono-dispersed polystyrene microspheres (PSMSs) is demonstrated on a lithographically patterned substrate by means of the tapered cell method [59]. Next, we encapsulate poly(DCHD) NCs, that is poly(DCHD) core, with polystyrene (PS) shell by seed-emulsion polymerization method, and encapsulated poly(DCHD) core will also be arrayed on a patterned substrate [61].

5.1 Ordered Array Structure of Polymer Colloidal Particles on a Patterned Substrate

5.1.1 Lithographically Patterned Substrate and Tapered Cell Method

As shown in Fig. 25, a patterned silicon (Si) (100) substrate was fabricated by electron beam (EB) lithography and the subsequent anisotropic wet etching [59]. The dimple formed has a square-pyramidal shape, and are equally spaced with hexagonal or tetragonal symmetry, being defined as the size of dimple (L) and the pitch between dimples (P). Si substrate used has the advantage of allowing colloidal crystal to integrate with the present Si-based optoelectronic devices.

Figure 26 illustrates the set-up and schematic procedures of the tapered cell method [140, 141], where a cover glass was slightly tilted (angle = 1–2°) on the patterned Si substrate. An aqueous dispersion liquid of polymer colloidal particles
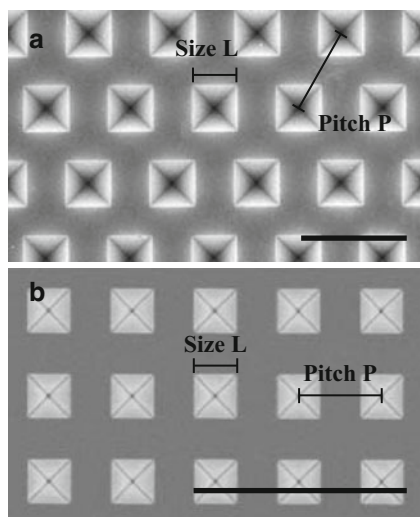
Fig. 25 SEM images of (**a**) hexagonally and (**b**) tetragonally patterned silicon (Si) (100) substrates. The dimple has a square-pyramidal shape, and its size and pitch are defined as L and P, respectively. The *scale bars* are 5 μm long

Fig. 26 Schematic
illustration of the tapered cell
method
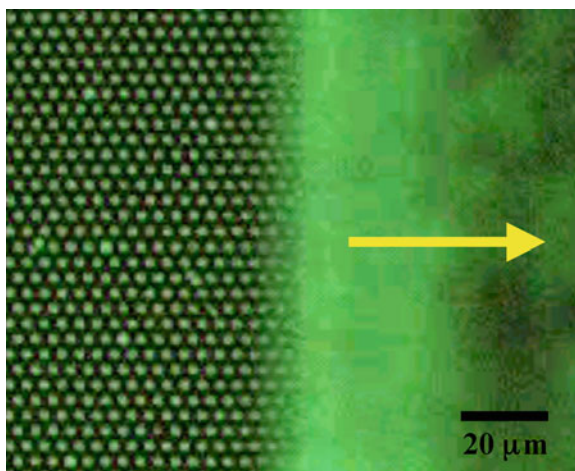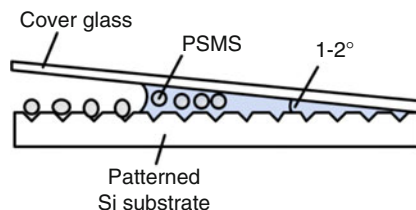
Fig. 27 Fluorescence microscopy image of the fluorescent polystyrene microspheres (PSMSs) on
hexagonally patterned substrate during the deposition process. The *arrow* indicates the movement
direction of the meniscus front inside the tapared cell. $L = 1.0\,\mu m, P = 2.0\,\mu m$, and $D = 1.9\,\mu m$

(PCPs) should be injected inside the tapered cell, and then slowly evaporated under
controlled conditions: surface treatment, e.g., the immersion in piranha solution,
temperature (ca. 20°C), and humidity (about 40%) [59]. The concentration of the
dispersion liquid is also an important factor. Consequently, PCPs would be trapped
within the dimples with stepping back of the meniscus. In addition, the above pro-
cess could be repeated to deposit further PCPs by utilizing the first ordered array
structure as a template [59]. Figure 27 displays the fluorescence microscopy image
of green fluorescent PSMSs trapped within the dimples on hexagonally patterned
substrate [59]. The arrow corresponds to the direction of step back of the meniscus.
That is, the image at the right area is still a wet region, while the left area has already
been dried up, and the middle area at the border of the meniscus is bright, due to
condensed fluorescent PSMSs. One can obviously see the ordered array structure of
fluorescent PSMSs trapped "only" within the dimples at the left area. As described
again in Sect. 5.1.2, the residual PSMSs, not trapped by the dimples, were com-
pletely dragged and swept with moving the meniscus. In other words, no PSMSs
are on the terrace [59].

5.1.2 Array Structure Ordered on Patterned Substrate

PSMS was used as a PCP in the present case [59]. Ordered array structure could be designed by optimizing the parameters of L and P, the diameter of PSMS (D), and pattern symmetry.

Figure 28a exhibits the SEM image of ordered array structure where each PSMS was trapped within the individual dimple on the hexagonal patterned substrate ($L = 2.1\,\mu m$ and $P = 4.0\,\mu m$) in a large-scale area [59]. Namely, all the dimples were perfectly filled with PSMS ($D = 2.0\,\mu m$). Since $L = 2.1\,\mu m$, the trapped PSMS partly protruded from the substrate terrace as shown in Fig. 28b, and the height of the protrusion was calculated to be about $1.2\,\mu m$ from the schematic cross-section view illustrated in Fig. 28c. In addition, Fig. 28d displays the ordered array structure of PSMSs ($D = 2.0\,\mu m$) on the tetragonally patterned substrate ($L = 1.0\,\mu m$ and $P = 2.0\,\mu m$).

When $D = 300$ or $350\,nm$, all the PSMSs were also trapped within the dimple on the patterned substrate as shown in Fig. 28e [$L = 2.1\,\mu m$ and $P = 4.0\,\mu m$] and f[$L = 1.0\,\mu m$ and $P = 2.0\,\mu m$]. No PSMSs were left on the terrace within the observed SEM images. PSMS colloidal crystal formed in the dimple is defined as the dimension of the dimple, which took cubic-closest packed (ccp) structure. The facet, (100) plane, is evidently parallel to the substrate surface. In other words, the present dimple may act as a template to produce PSMS colloidal crystals, the nucleation and growth of which would be confined and controlled by the four sidewalls inside the dimples [132, 133]. Namely, the deposition process of PSMSs on patterned substrate
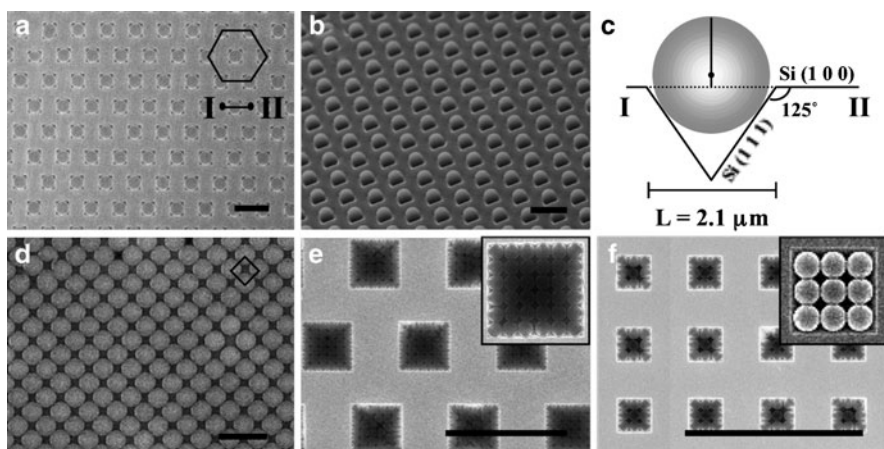
Fig. 28 SEM images and the schematic cross-sectional view of two-dimensional ordered arrays of PSMSs on patterned Si (100) substrates. Hexagonal pattern [(**a**), (**b**) and (**e**)]: $L = 2.1\,\mu m$ and $P = 4.0\,\mu m$; tetragonal pattern [(**d**) and (**f**)]: $L = 1.0\,\mu m$ and $P = 2.0\,\mu m$. The tilt angle is 45° in (**b**). The cross-sectional view (**c**) corresponds to (**a**) and (**b**). The diameter of the PSMS (**D**) used is 2.0 μm in (**a**), (**b**), and (**d**), 350 nm in (**e**), and 300 nm in (**f**). The *scale bars* are 5 μm long

seems to be a kind of colloidal epitaxy process in this case [132]. Moreover, Fig. 28e, f may provide the two types of hierarchical micro-structure and nano-structures by the combination of the pattern symmetry with the dimple geometry.

5.1.3   Repeated Procedures in Tapered Cell Method

The same procedure was further repeated, and PSMSs were subsequently deposited on the PSMS-filled hexagonally patterned substrate, which means the first layer of ordered array structure of PSMSs can be employed as a new template [59], because PSMSs protruded by 60% from the substrate surface as shown in Fig. 28c.

Figure 29a illustrates schematically the cross section view, when $D = 2.0\,\mu m$, $L = 2.0\,\mu m$, and $P = 4.0\,\mu m$ in the hexagonal patterned substrate. As expected, the second layer of ordered array structure was obtained successfully on the first layer as shown in Fig. 29b, which can be regarded as so-called "Kagome structure" [142]. The Kagome structure composed of dielectric rods or wire network has been theoretically investigated and expected to have a large flat band rather than Honeycomb structure [143–145]. In contrast, the same structure based upon polymer microspheres has scarcely been reported until now. The present fabrication method
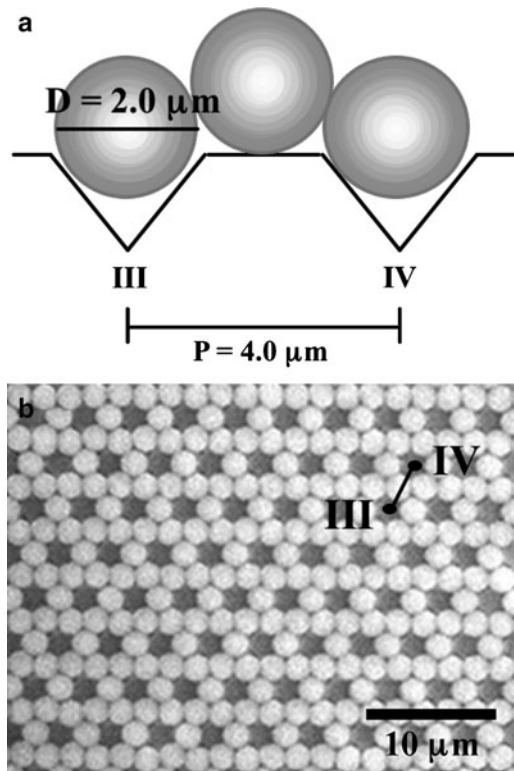
Fig. 29 Cross-sectional view (**a**) and SEM image (**b**) of Kagome sturucture on hexagonally patterned substrate: $L = 2.0\,\mu m$, $P = 4.0\,\mu m$, and $D = 2.0\,\mu m$
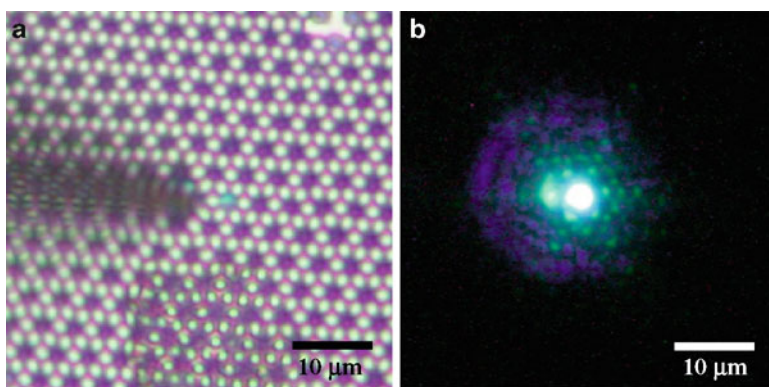
Fig. 30 Topography (**a**) and the corresponding fluorescence images (**b**) by the measurement with far-field optical microscopy

will open new research fields associated with photonic bands and magnetic properties in the present Kagome structure, and moreover would present the possibility that microspheres having different physical properties could in turn be incorporated or integrated repeatedly [146].

For example, the Kagome structure is said to exhibit the confinement effect of light propagation. In order to reveal this phenomenon, the Kagome structure, containing a small amount of fluorescent PSMSs with the same size ($D = 2.0\,\mu m$), was fabricated by the same procedure. Figure 30 represents the topography and the corresponding fluorescence images from measurements with far-field optical microscopy. It seems that light propagation would be confined clearly, in comparison with the ordinary hexagonal-close-packed structure of PSMS on a flat substrate [147].

5.2 Encapsulation of Polymer Nanocrystals and Their Arrangement on Patterned Substrate

5.2.1 Encapsulation of Semiconductor Nanoparticles and Their Ordered Array Structure

Before performing the encapsulation of PDA NCs, we have attempted to fabricate encapsulated semiconductor microparticles (MPs) like cadmium sulfide (CdS) and zinc sulfide (ZnS), which were previously produced by the gel–sol method [148].

A gelatin aqueous solution (1%, 20 mL), which contains cadmium hydroxide, EDTA-2Na, ammonium acetate, and ammonia, was mixed with a gelatin aqueous solution (1%, 5 mL) of thioacetamide as a source of S^{2-} at 60°C for about 10 h. After removing gelatin and by-products, the resulting CdS NPs were re-dispersed in an aqueous dispersion medium. In contrast, ZnS NPs aqueous dispersion liquid was also prepared through the same procedure by using zinc hydroxide.
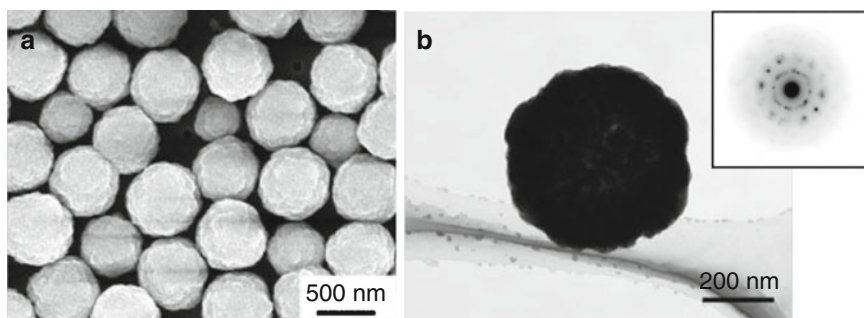
Fig. 31 SEM (**a**) and TEM (**b**) images of CdS NPs. The *inset* is ED patterns
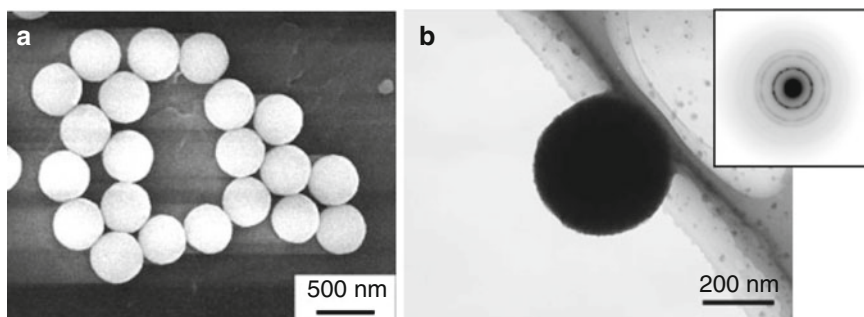
Fig. 32 SEM (**a**) and TEM (**b**) images of ZnS NPs. The *inset* is ED patterns

Figures 31 and 32 indicate the SEM and TEM images of CdS and ZnS NPs, respectively [149]. The shape is spherical, and the diameter is about 450 nm and almost mono-dispersed in both cases. From SEM images, the surface of CdS NPs is a little rough, while ZnS NPs have a smooth surface. In addition, the ED patterns suggest polycrystalline state in any case of CdS and ZnS NPs.

These CdS or ZnS NPs were encapsulated by a seed-emulsion polymerization process [149]. After adding styrene monomer (St), divinylbenzene (DVB: crosslink agent), potassium peroxodisulfide, initiator (KPS), and a small amount of SDS, CdS NPs, or ZnS NPs, the dispersion liquid was refluxed at 80°C in a nitrogen atmosphere. The obtained dispersion liquids were purified by the centrifugation method, re-dispersed in an aqueous dispersion medium. The encapsulated CdS or ZnS NPs having transparent and weakly crosslinked PS shell was obtained successfully as shown in Fig. 33 [149]. Actually, the bright area in the SEM images and the black region in the TEM images correspond to CdS or ZnS NPs, and the thickness of PS shell (or the total diameter of the encapsulated MPs) could be suitably controlled by repeating a series of seed-emulsion polymerization processes. However, CdS NP was not located at the center of the encapsulated MPs, but ZnS NP was roughly centered. In addition, SDS was not necessarily effective for encapsulation in the case of ZnS NPs. From these experimental results, the present seed-emulsion
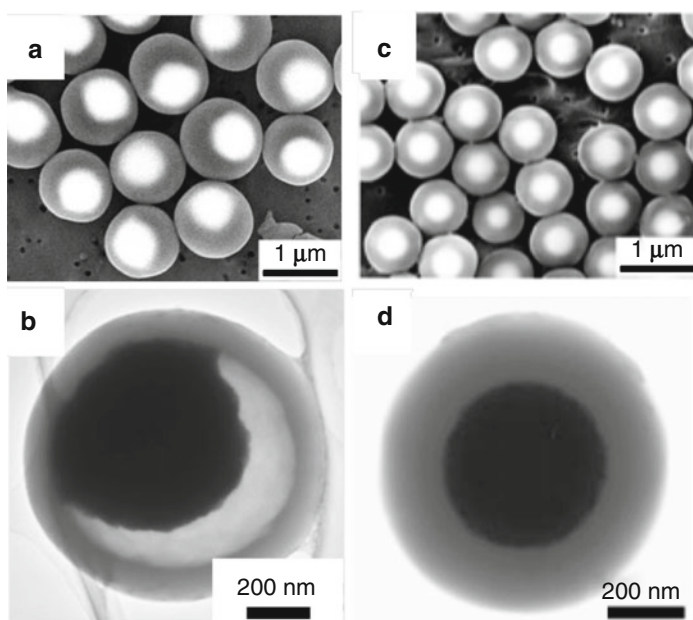
Fig. 33 SEM (**a,c**) and TEM (**b,d**) images of PS-encapsulated CdS (**a,b**) and ZnS (**c,d**) MPs
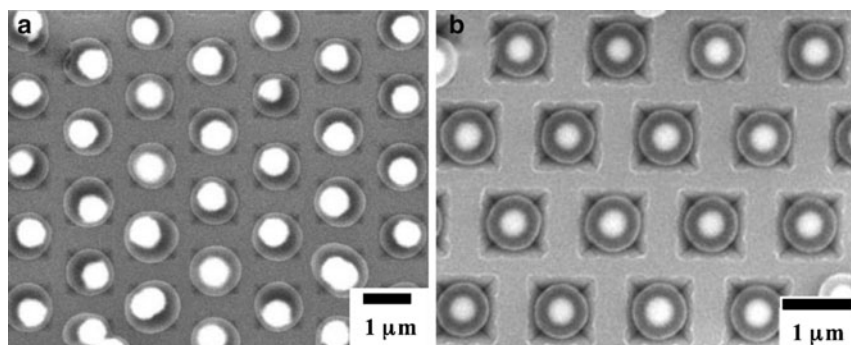
Fig. 34 SEM images of hexagonally ordered array structure in PS-encapsulated CdS (**a**) and ZnS (**b**) MPs

polymerization seems to be a very complicated phenomenon, and the resulting encapsulated semiconductors MPs may be considerably influenced by the differences in affinity among St, the formed PS, SDS, and semiconductor NPs.

Anyway, the encapsulated CdS or ZnS MPs are clearly spherical, and the size is almost uniform. So it was also possible to arrange these MPs easily on the patterned substrate by means of the tapered cell method. Figure 34 exhibits the SEM images of hexagonally ordered array structure in PS-encapsulated CdS and/or ZnS MPs, which occupied only pits on the patterned substrate within the SEM observation [149]. However, the total area of ordered array structure was unfortunately not so

large in any case, compared with PSMS case. Probably, the rate of stepping back of the meniscus should be optimized, because CdS or ZnS NPs have a greater specific gravity than PSMS.

5.2.2 Encapsulation of Polydiacetylene Nanocrystals with Polystyrene

In principle, PDA NCs were successfully encapsulated by PS shell in the following manner [61]. Poly(DCHD) NCs dispersion liquid previously fabricated by the reprecipitation method was condensed and used without dialysis treatment for the subsequent encapsulation process [150, 151]. The concentrated poly(DCHD) NCs dispersion liquid is $0.63\,mg\,mL^{-1}$ and 10 mL. The conductivity was over $1,000\,\mu S$. Poly(DCHD) NCs were encapsulated by seed-soap-free emulsion co-polymerization of St and hydrophilic styrene derivative 1-(4-vinylphenyl)ethane-1,2-diol, hydrophilic styrene derivative (HSt) (see Fig. 35) using KPS as an initiator. That is to say, SDS was not added in the present case [61]. After nitrogen bubbling, the co-polymerization for encapsulation was performed at 80°C and 1,000 rpm, when the added weight ratio was St:HSt = 99:1. The thickness of PS shell could be controlled by repeatedly adding St and HSt. Co-polymerization was confirmed from ^{1}H-NMR and IR spectra [61].

Figure 36a, b displays the SEM images of poly(DCHD) NCs encapsulated with only PS or with poly(St-*co*-HSt), respectively [61]. When encapsulated with PS, the shape was not spherical but irregular. A number of isolated PS NPs, not containing poly(DCHD) NCs, were observed in the SEM image. The dialysis treatment of PDA NCs dispersion liquid for several days is usually said to be an essential process to produce mono-dispersed encapsulation [150, 151], since high ion strength would induce undesirable aggregation and/or segregation during seed-emulsion polymerization. As shown in Fig. 36b, however, the encapsulation of poly(DCHD) NCs proceeded promptly without the dialysis treatment in the co-polymerization of St and HSt [61]. The apparent shape evidently changed from rectangular-like to spherical, and the size increased to about 200 nm, when poly(DCHD) NCs were approximately 95 nm in size. In addition, the ζ-potential increased from -23 to $-66\,mV$ after encapsulation [61]. The dispersion stability of encapsulated poly(DCHD) NCs was clearly raised, because sulfo-residual fragments from
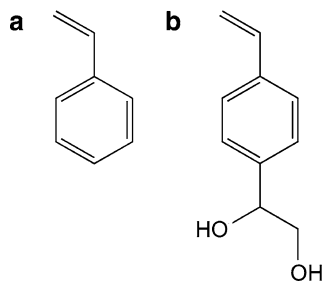
Fig. 35 Chemical structures of (**a**) St and (**b**) HSt, (1-4-vinylphenyl)ethane-1,2-diol
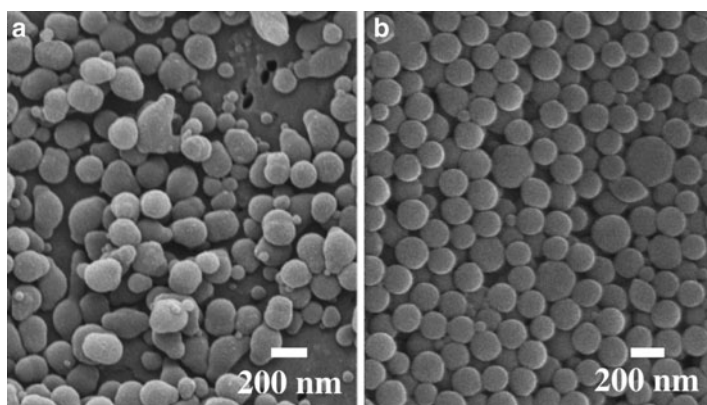
Fig. 36 SEM images of encapsulated poly(DCHD) NCs (**a**) with only PS and (**b**) with poly(St-*co*-HSt)

Fig. 37 TEM image of encapsulated poly(DCHD) NCs with poly(St-*co*-HSt)
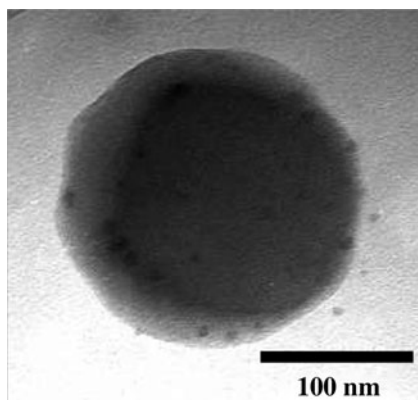
decomposed KPS and the hydroxyl moiety from HSt may be located on the surface of the encapsulated poly(DCHD) NCs and exposed to a water phase [61]. This is very important to construct an ordered array structure on a patterned substrate by means of the tapered cell method. Figure 37 shows the TEM image of encapsulated poly(DCHD) NCs, corresponding to Fig. 36b [61]. Rectangular poly(DCHD) NCs was completely covered with spherical poly(St-*co*-HSt) shell.

As discussed in Sect. 5.2.1, encapsulation would be strongly dependent on affinity between PDA core and poly(St-*co*-HSt) shell. Probably there are the two main schemes of encapsulation mechanism as shown in Fig. 38 [61]. (1) At the initial stage St oligomers co-polymerized with HSt are first produced, which may have a higher affinity to poly(DCHD) NCs than only St oligomers. As the polymerization proceeds, poly(St-*co*-HSt) formed may adsorb on the surface of poly(DCHD) NCs, because of the lowering of solubility in a water phase, and then nucleation, and encapsulation may take place on the surface of poly(DCHD) NCs. (2) On the other hand, it is assumed that there exist initially St fine droplets, which contain HSt to
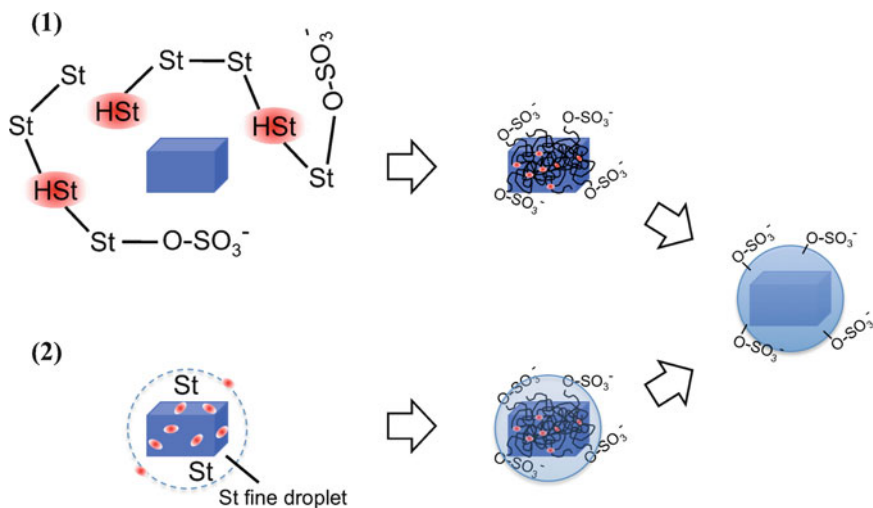
Fig. 38 Schematic illustrations of proposed mechanisms for encapsulation by soap-free emulsion polymerization with poly(St-*co*-HSt). In both cases, HSt serves as a kind of surfactant

some extent, at the surrounding poly(DCHD) NCs. The fine droplets may be ther-modynamically stabilized by the surface activity of HSt, and then co-polymerization starts in or on the surface of St fine droplets in the presence of poly(DCHD) NC. Anyway, HSt is considered to be a kind of surfactant, and may enhance the affinity and stability between formed PS and poly(DCHD) NC [61]. As a result, PS-encapsulation PDA NCs may proceed smoothly. Actual encapsulation is probably intermediate between the above-mentioned (1) and (2) processes.

In contrast, ionic St derivatives, e.g., cationic *p*-styrene ammonium chloride and anionic sodium *p*-styrenesulfonate, were completely inappropriate for encap-sulation rather than HSt. The resulting encapsulated NCs were aggregated and irregularly shaped in these cases [61].

5.2.3 Ordered Array Structure of Polystyrene-Encapsulated Polydiacetylene Nanocrystals

We have similarly attempted to arrange PS-encapsulated poly(DCHD) NCs on a patterned substrate by means of the tapered cell method [61]. As shown in Fig. 39, it has become apparent that the concentration of PS-encapsulated poly(DCHD) NCs dispersion liquid should be optimized. In the present case, all the dimples were occu-pied at 0.61 wt% [61]. The proper concentration is influenced by the number density of the dimples as well as preparation conditions such as temperature, humidity, and the affinity between encapsulated NC and substrate.

Moreover, the repeated tapered cell method was performed successfully to construct a heterogeneously ordered array structure as shown in Fig. 40a [61].
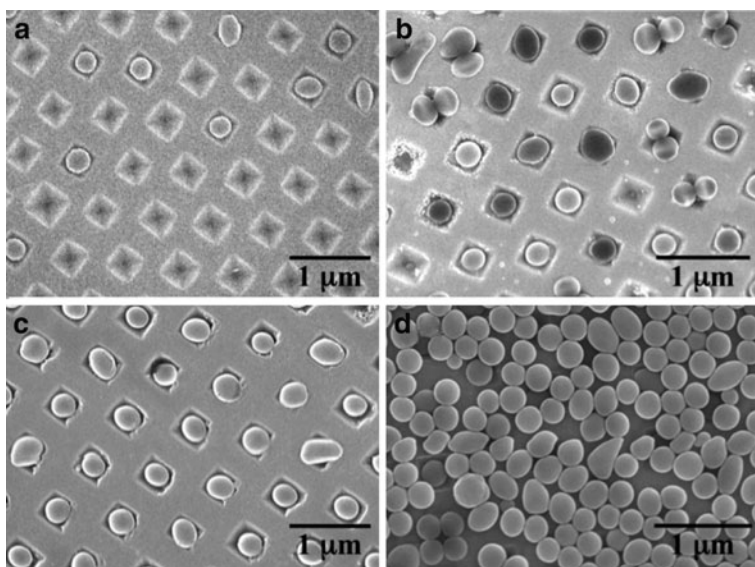
Fig. 39 SEM images of poly(St-*co*-HSt)-encapsulated poly(DCHD) NCs on a hexagonally pat-terned substrate using the tapered cell method: (**a**) 0.15, (**b**) 0.31, (**c**) 0.61, and (**d**) 0.90 wt%
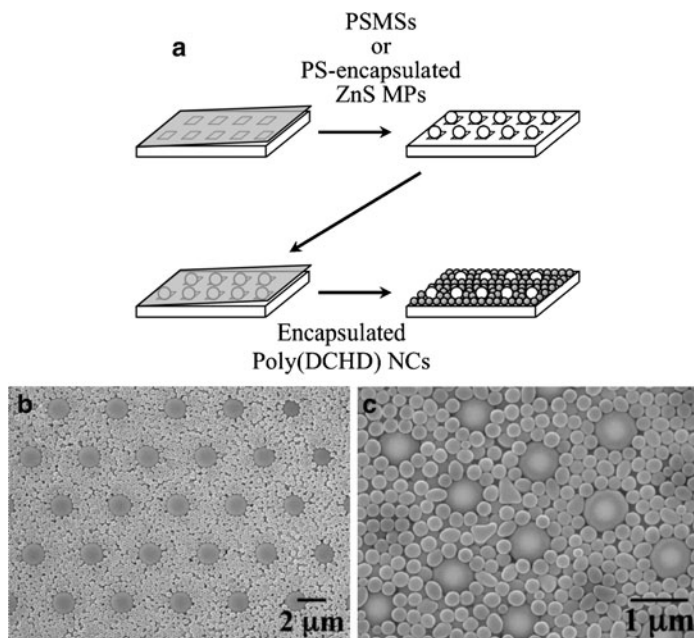
Fig. 40 Schematic illustration (**a**) of step-by-step deposition and SEM images (**b**,**c**) of step-by-step arrangement; (**b**) PSMSs in the dimple and poly(St-*co*-HSt)-encapsulated poly(DCHD) NCs on the terrace and (**c**) PS-encapsulated ZnS MPs in the dimple and poly(St-*co*-HSt)-encapsulated poly(DCHD) NCs on the terrace

Figure 40b, c demonstrates, respectively, the heterogeneous hexagonally ordered array structures: (a) PSMS in the dimple and the PS-encapsulated PDA NCs on the terrace; (b) PS-encapsulated ZnS MPs in the dimple (see Sect. 5.2.1) and PS-encapsulated PDA NCs on the terrace [61].

It became possible to array and arrange selectively non-spherical and irregular-shaped polymer NCs by encapsulation on a patterned substrate using the tapered cell method. In addition, this repeated procedures may produce a heterogeneously ordered array structure composed of encapsulated NCs and/or MPs having different optoelectronic, photonic, and magnetic properties, which may lead to integrated device application such as functional photonic crystals and super-lattice structure [61].

6 Conclusions and Future Scope

We have also already prepared successfully the different types of hybridized NCs and microcrystals (MCs) by further developing the fabrication techniques, e.g., Pt-coated phthalocyanine NCs [152], Au NPs deposited fullerene MCs [153], J-aggregated chromospheres-adsorbed noble metal NPs core [154], and so on. On the other hand, our attention is now focused on the present visible-light-driven photocatalytic reduction process for novel applications to the two-dimensional surface of π-conjugated polymer substrate and film [121].

Considering the above-mentioned research potential and background, these hybridized NCs and the corresponding encapsulated NPs (or MPs) can be regarded as new and promising building blocks in bottom-up fabrication processes. In addition, the improved fabrication technique and process superior to the tapered cell method and the use of a patterned substrate are freely available to produce ordered and regularly integrated array structure. Considering nano-plating, highly integrated nano- or micro-structure [155] for NLO and photonics devices, and meta-material [120], these next-generation organic and polymer devices should be further developed in the near future, and will probably be extremely useful to solve resource, energy, and environmental problems on a global scale.

References

1. Oikawa H, Kasai H, Nakanishi H (2001) Fabrication of organic microcrystals and their optical properties (Chapter 11); Some applications of organic microcrystals (Chapter 12). In: Glaser R, Kaszynski P (eds) Anisotropic organic materials –approaches to polar order. ACS symposium series 798. ACS, Washington, pp 158, 169

2. Oikawa H, Nakanishi H (2003) Reprecipitation method for organic nanocrystals (Chapter 2); Optical properties of polymer nanocrystals (Chapter 14); Particle-based optical devices (Chapter 29). In: Masuhara H, Nakanishi H, Sasaki K (eds) Nano science and technology −single organic nanoparticles. Springer, Berlin, pp 17, 169, 382

3. Oikawa H, Masuhara A, Kasai H, Mitsui T, Sekiguchi T, Nakanishi H (2004) Organic and polymer nanocrystals: their optical properties and function (Chapter 13). In: Masuhara H, Kawata S (eds) Handai nanophotonics –nanophotonics: integrating photochemistry, optics and nano/bio materials studies. Elsevier, Amsterdam, p 205

4. Kasai H, Nalwa HS, Oikawa H, Okada S, Matsuda H, Minami N, Kakuta A, Ono K, Mukoh A, Nakanishi H (1992) Jpn J Appl Phys 31:L1132

5. Kamatani H, Kasai H, Okada S, Matsuda H, Oikawa H, Minami N, Kakuta A, Ono K, Mukoh A, Nakanishi H (1994) Mol Cryst Liq Cryst 252:233

6. Katagi H, Kasai H, Okada S, Oikawa H, Matsuda H, Liu ZF, Nakanishi H (1996) Jpn J Appl Phys 35:L1364

7. Kasai H, Kamatani H, Okada, S, Oikawa H, Matsuda H, Nakanishi H (1996) Jpn J Appl Phys 35:L1221

8. Katagi H, Kasai H, Kamatani H, Okada S, Oikawa H, Matsuda H, Nakanishi H (1997) J Macromol Sci Pure Appl Chem A34:2013

9. Matsuda H, Yamada S, Keuren EV, Katagi H, Kasai H, Kamatani H, Okada S, Oikawa H, Nakanishi H, Smith EC, Kar AK, Wherrett S (1997) SPIE Proc 2998:241

10. Kasai H, Yoshikawa Y, Seko T, Okada S, Oikawa H, Matsuda H, Watanabe A, Ito O, Toyotama H, Nakanishi H (1997) Mol Cryst Liq Cryst 294:173

11. Fujitsuka M, Kasai H, Masuhara A, Okada S, Oikawa H, Nakanishi H, Watanabe A, Ito O (1997) Chem Lett 1211

12. Kasai H, Oikawa H, Okada S, Nakanishi H (1998) Bull Chem Soc Jpn 71:2597

13. Oikawa H, Oshikiri T, Kasai H, Okada S, Tripathy SK, Nakanishi H (2000) Polym Adv Technol 11:783

14. Onodera T, Oshikiri T, Katagi H, Kasai H, Okada S, Oikawa H, Terauchi M, Tanaka M, Nakanishi H (2001) J Cryst Growth 229:586

15. Alargova RG, Deguchi S, Tdujii K (2001) J Am Chem Soc 123:10460

16. Takahashi S, Miura H, Kasai H, Okada S, Oikawa H, Nakanishi H (2002) J Am Chem Soc 124:10944

17. An BK, Kwon SK, Jung SD, Park SY (2002) J Am Chem Soc 124:14410

18. Xiao D, Xi L, Yang W, Fu H, Shuai Z, Fang Y, Yao J (2003) J Am Chem Soc 125:6740

19. Oikawa H, Mitsui T, Onodera T, Kasai H, Nakanishi H, Sekiguchi T (2003) Jpn J Appl Phys 42:111

20. Volkov VV, Asahi T, Masuhara H, Masuhara A, Kasai H, Oikawa H, Nakanishi H (2004) J Chem Phys B 108:7674

21. Kaneko Y, Shimada S, Fukuda T, Kimura T, Yokoi H, Matsuda H, Onodera T, Kasai H, Okada S, Oikawa H, Nakanishi H (2005) Adv Mater 17:160

22. Asahi T, Sugiyama T, Masuhara H (2008) Acc Chem Res 41:1790 and references cited therein

23. Wegner G, Bässler H, Sixl H, Enkelmann V (1984) Polydiacetylene. In: Cantow HJ (ed) Advances in polymer science, vol 63, Springer, Berlin

24. Bloembergen N (1996) Nonlinear optics. World Science, Singapore

25. Charra F, Agranovich VM, Kajzar F (eds) (2003) Organic nanophotonics. Kluwer Academic, London

26. Prasad PN (2004) Nanophotonics. Willey, Hoboken

27. Nakanishi H, Kasai H (1997) ACS Symp Ser 672:183

28. Komai Y, Kasai H, Hirakoso H, Hakuta Y, Okada S, Oikawa H, Adschiri T, Inomata H, Arai K, Nakanishi H (1998) Mol Cryst Liq Cryst 322:167
29. Komai Y, Kasai H, Hirakoso H, Hakuta Y, Okada S, Oikawa H, Adschiri T, Inomata H, Arai K, Nakanishi H (1999) Jpn J Appl Phys 38:L81
30. Baba K, Kasai H, Okada S, Oikawa H, Nakanishi H (2000) Jpn J Appl Phys 39:L1256
31. Baba K, Kasai H, Okada S, Nakanishi H, Oikawa H (2006) Mol Cryst Liq Cryst 445:161
32. Ishii KU, Baba K, Wei Z, Kasai H, Nakanishi H, Okada S, Oikawa H (2006) Mol Cryst Liq Cryst 445:177
33. Baba K, Kasai H, Masuhara A, Okada S, Oikawa H, Nakanishi H (2007) Jpn J Appl Phys 46:7558
34. Baba K, Kasai H, Shinohara Y, Okada S, Oikawa H, Nakanishi H (2008) Jpn J Appl Phys 47:3769
35. Ishii KU, Kwon E, Kasai H, Nakanishi H, Oikawa H (2008) Cryst Growth Des 8:369
36. Chung HR, Kwon E, Oikawa H, Kasai H, Nakanishi H (2006) J Cryst Growth 294:459
37. Tachikawa T, Chung HR, Masuhara A, Kasai H, Oikawa H, Nakanishi H, Fujitsuka M, Majima T (2006) J Am Chem Soc 128:15944
38. Tripathy SK, Katagi H, Kasai H, Balasubramanian S, Oshikiri H, Kumar J, Oikawa H, Okada S, Nakanishi H (1998) Jpn J Appl Phys 37:L343
39. He JA, Yang K, Kumar J, Tripathy SK, Samuelson LA, Oshikiri T, Katagi H, Kasai H, Okada S, Oikawa H, Nakanishi H (1999) J Phys Chem B 103:11050
40. Yang K, He JA, Samuelson LA, Oshikiri T, Katagi H, Kasai H, Okada S, Oikawa H, Nakanishi H, Tripathy SK (2005) J Opt Soc Am B Opt Phys 22:623
41. Fujita S, Kasai, H, Okada S, Oikawa H, Fukuda T, Matsuda H, Tripathy SK, Nakanishi H (1999) Jpn J Appl Phys 38:L659
42. Oikawa H, Fujita S, Kasai H, Okada S, Tripathy SK, Nakanishi H (2000) Colloids Surf A169:251
43. Okazoe S, Fujita S, Kasai H, Okada S, Oikawa H, Nakanishi H (2001) Mol Cryst Liq Cryst 367:11
44. Katagi H, Kasai H, Okada S, Oikawa H, Matsuda H, Nakanishi H (2000) Adv Polym Tech 11:778
45. Masuhara A, Kasai H, Okada S, Oikawa H, Terauchi M, Tanaka M, Nakanishi H (2001) Jpn J Appl Phys 40:L1129
46. Masuhara A, Oshikiri S, Kasai H, Okada S, Oikawa H, Nakanishi H (2004) J Nonlinear Opt Phys Mater 13:587
47. Oikawa H, Vlaicu AM, Kimura M, Yoshikawa H, Tanuma S, Masuhara A, Kasai H, Nakanishi H (2005) Nonlinear Opt Quantum Opt 34:275
48. Matsumoto A, Ishikawa T, Odani T, Oikawa H Okada S, Nakanishi H (2006) Macromol Chem Phys 207:361
49. Yoshikawa H, Vlaicu AM, Kimura M, Masuhara A, Tanuma S, Nakanishi H, Oikawa H (2009) J Surf Sci 7:711
50. Yokoyama T, Masuhara A, Onodera T, Kasai H, Oikawa H (2009) Synth Met 159:897
51. Onodera T, Oikawa H, Kasai H, Nakanishi H, Sekiguchi T (2005) Mater Res Soc Symp Proc 846:257
52. Onodera T, Tan Z, Masuhara A, Oikawa H, Kasai H, Nakanishi H, Sekiguchi T (2006) Jpn J Appl Phys 45:379
53. Onodera T, Oikawa H, Masuhara A, Kasai H, Sekiguchi T, Nakanishi H (2007) Jpn J Appl Phys 46:L336
54. Onodera T, Ujita J, Ishikawa D, Masuhara A, Kasai H, Oikawa H (2009) ECS Trans 16:1
55. Wakayama Y, Mitsui T, Onodera T, Oikawa H, Nakanishi H (2005) Chem Phys Lett 417:503
56. Wakayama Y, Mitsui T, Onodera T, Oikawa H, Nakanishi H (2006) J Surf Sci Nanotech 4:69
57. Mitsui T, Wakayama Y, Onodera T, Takaya Y, Oikawa H (2008) Nano Lett 8:853
58. Mitsui T, Wakayama Y, Onodera T, Takaya Y, Oikawa H (2008) Opt Lett 33:1189
59. Onodera T, Takaya Y, Mitsui T, Wakayama Y, Oikawa H (2008) Jpn J Appl Phys 47:1404
60. Wei Z, Ishii KU, Masuhara A, Kasai H, Okada S, Matsune H, Asahi T, Masuhara H, Nakanishi H (2005) J Nanosci Nanotech 5:937

61. Onodera T, Nakamura M, Takaya Y, Masuhara A, Wakayama Y, Nemoto N, Nakanishi H, Oikawa H (2009) J Phys Chem 113:11647
62. Peng X, Schlamp MC, Kadavanich AV, Alivisatos AP (1997) J Am Chem Soc 199:7019
63. Valden M, Lai X, Goodman DW (1998) Science 281:1674
64. Peng X, Manna L, Yang W, Wickham J, Scher E, Kadavanich A, Alivisatos AP (2000) Nature 404:59
65. Lu Y, Yang Y, Selinger A, Lu M, Huang J, Fan H, Haddad R, Lopez G, Burns AR, Sasaki DY, Shelnutt J, Brinker CJ (2001) Nature 410:913
66. Liz-Marzán LM (2006) Langmuir 22:32 and references cited therein
67. Mai YW, Yu ZZ (eds) (2006) Polymer nanocomposites. Woodhead, Cambridge
68. Kraeutler B, Bard AJ (1978) J Am Chem Soc 100:4317
69. Sellinger A, Weiss PM, Nguyen A, Lu Y, Assink RA, Gong W, Brinker CJ (1998) Nature 394:256
70. Oldenburg SJ, Averitt RD, Westcott SL, Halas NJ (1998) Chem Phys 288:243
71. Caruso F (2001) Adv Mater 13:11
72. Thomas KG, Kamat PV (2003) Acc Chem Res 36:888
73. Prodan E, Radloff C, Halas NJ, Nordlander P (2003) Science 302:419
74. Wiederrecht GP, Wurtz GA, Hranisaljevic J (2004) Nano Lett 4:2121
75. Wurtz GA, Evans PR, Hendren W, Atkinson R, Dickson W, Pollard RJ, Zayats AV (2007) Nano Lett 7:1297
76. Ni W, Yang Z, Chen H, Li L, Wang J (2008) J Am Chem Soc 130:6692
77. Jin R, Cao Y, Mirkin CA, Kelly KL, Schatz GC, Zheng JG (2001) Science 294:1901
78. Murphy CJ, Jana NR (2002) Adv Mater 14:80
79. Loo C, Lowert A, Halas NJ, West J, Drezek R (2005) Nano Lett 5:709
80. Yoshida A, Yonezawa Y, Kometani N (2009) Langmuir DOI:10.1021/la901431n
81. Sugawara Y, Kelf TA, Baumberg JJ, Abdelsalam ME, Bartlett PN (2006) Phys Rev Lett 97:266808
82. Bonnand C, Bellessa J, Plénet JC (2006) J Non-Cryst Solids 352:1683
83. Bellessa J, Bonnand C, Plénet JC (2004) Phys Rev Lett 93:036404–1
84. Fofang NT, Park TH, Neumann O, Mirin NA, Nordlander P, Halas NJ (2008) Nano Lett 8:3481
85. Hranisavljevic J, Dimitrijevic NM, Wurtz GA, Wiederrecht GP (2002) J Am Chem Soc 124:4536
86. Ishii H, Seki K (2002) Energy level alignment at organic-metal interfaces (Chapter 10). In: Salaneck WR, Seki K, Kahn A, Pireaux JJ (eds) Conjugated polymer and molecular interfaces. Marcel Dekker, New York, p 293
87. Caruso F (ed) (2004) Colloids and colloid assemblies. Wiley-VCH Verlag GmbH & KGaA, Weinheim
88. Leonard D, Krishnamurthy M, Reaves CM, Denbaars SP, Petroff PM (1993) Appl Phys Lett 63:3203
89. Toyotama H (1987) Kinozairyo (Funct Mater) 6:44 (in Japanese)
90. Yase K, Inoue T, Okada M, Funada T, Hirano J (1898) Hyomen Kagaku (Surf Sci) 8:434 (in Japanese)
91. Yee KC, Chance RR (1978) J Polym Sci 16:431
92. Enkelmann V, Leyrer R, Schleier G, Wegner G (1980) J Mater Sci 15:168
93. Enkelmann V, Werz G, Müller MA, Schmidt M, Wegner G (1984) Mol Cryst Liq Cryst 105:11
94. Watanabe K, Kinoshita A, Hirasa N, Itami A (1990) Konica Tech Rept 3:108
95. Nakanishi H, Matsuda H, Okada S, Kato M (1989) MRS Int Mtg Adv Mater 1:97
96. Yee KC, Chance RR (1978) J Polym Sci Polym Phys Ed 16:431
97. Vlckova B, Matejka P, Simonova J, Cemakova K, Pancoska P, Baumruk V (1993) J Phys Chem 97:9719
98. Kreibig U, Gartz M, Hilger A (1997) Ber Bunsenges Phys Chem 101:1593
99. Hirakawa K, Toshima N (2003) Chem Lett 32:78
100. Czyzyk MT, de Groot RA, Dalba G, Fornasini P, Kisiel A, Rocca F, Burattini E (1989) Phys Rev B39:9831

101. Wertheim GK, DiCenzo SB, Buchanan DNE (1986) Phys Rev B33:5384
102. Tanaka A, Takeda Y, Nagasawa T, Sasaki H, Kuriyama Y, Suzuki S, Sato S (2003) Surf Sci 532/535:281
103. Mulvaney P (1996) Langmuir 12:788
104. Dilks A (1981) X-ray photoelectron spectroscopy for the investigation of polymeric materials. In: Brundle CR, Baker AD (eds) Electron spectroscopy –theory, techniques and application, vol 4, Academic, London, p 277
105. Louie SG, Chelikowsky JR, Cohen ML (1977) Phys Rev B15:2154
106. Pyatenko A, Yamaguchi M, Suzuki M (2005) J Phys Chem B 109:21608
107. Matsuda Y (2008) Studies on hybridization between conjugated polymers and metal nanoparticles. Master Thesis
108. Kerker M (1985) J Colloid Interface Sci 105:297
109. Westcott SL, Oldenburg SJ, Lee TR, Halas NJ (1999) J Chem Phys Lett 300:651
110. Peceros KE, Xu X, Bulcock SR, Cortie MB (2005) J Phys Chem B 109:21516
111. Pileni MP, Taleb A, Petit C (1998) J Dispersion Sci Technol 19:185 and references cited therein
112. Kuriyama K, Kikuchi H, Oishi Y, Kajiyama T (1995) Langmuir 11:3536
113. Van de Hulst HC (1981) Light scattering by small particles. Dover Pub, New York
114. Huo Q, Russell KC, Leblanc RM (1999) Langmuir 15:3536
115. Itoh K, Nishizawa T, Yamagata J, Fujii M, Osaka N, Kudryashov I (2005) J Phys Chem B 109:264
116. Spannring W, Bässler H (1981) Chem Phys Lett 84:54
117. Hoare JP (1985) Oxygen. In: Bard AJ, Parsons R, Jordan J (eds) Standard potentials in aqueous solution. Marcel Dekker, New York
118. Brown KR, Natan MJ (1998) Langmuir 14:726
119. Neeves AE, Birnboim MH (1989) J Opt Soc Am B 6:787
120. Ishikawa A, Tanaka T (2006) Opt Commun 258:300
121. Ishikawa D (2008) Studies on hybridized nanostructure of polymer/metal fabricated by photocatalytic reduction method and its properties. Master Thesis
122. Link S, Wang ZL, El-Sayed MA (1999) J Chem Phys B 103:3529
123. Hodak JH, Henglein A, Giersig M, Hartland GV (2000) J Phys Chem B 104:11708
124. Patel K, Kapoor S, Dave DP, Mukherjee T (2005) J Chem Sci 117:311
125. Vasan HN, Rao CNR (1995) J Mater Chem 5:1755
126. Torigoe K, Nakajima Y, Esumi K (1993) J Phys Chem 97:8304
127. Klig HP, Alexander LE (1974) X-ray diffraction procedures for polycrystalline and amorphous materials. Wiley, New York, p 687
128. Salaneck WR, Seki K, Kahn A, Pireaux JJ (eds) (2002) Energy level alignment at organic-metal interfaces (Chapter 10). In: Conjugated polymer and molecular interfaces. Marcel Dekker, New York
129. Ujita J (2006) Studies on hybridized nanocrystals of conjugated polymer and metal. Master Thesis
130. Kurokawa N, Yoshikawa H, Hirota N, Hyodo K, Masuhara H (2004) Chem Phys Chem 5:1609
131. Kymakis E, Alexandrou I, Amaratunga GAJ (2003) J Appl Phys 93:1764
132. Van Blaaderen A, Ruel R, Wiltzius P (1997) Nature 385:321
133. Ozin GA, Yang SM (2001) Adv Func Mater 11:95
134. Botzung-Appert E, Zaccaro J, Gourgon C, Usson Y, Baldeck PL, Ibanez A (2005) J Cryst Growth 283:444
135. Matsuo S, Fujine T, Fukuda K, Juodkazis S, Misawa H (2003) Appl Phys Lett 82:4283
136. Yin Y, Li ZY, Xia Y (2003) Langmuir 19:622
137. Everett DH (1988) Basic principles of colloid science. Royal Society of Chemistry, London
138. Denkov ND, Velev OD, Kralchevsky PA, Ivanov IB, Yoshimura H, Nagayama K (1992) Langmuir 8:3183
139. Karthaus O, Mikami S, Hashimoto Y (2006) J Colloid Interface Sci 301:703
140. Yamasaki T, Tsutsui T (1999) Jpn J Appl Phys 38:5916

141. Yin Y, Lu Y, Gates B, Via Y (2001) J Am Chem Soc 123:8718
142. Nielsen JB, Søndergaard T, Barkou SE, Bjarklev A, Broeng J, Nielsen MB (1999) Electron Lett 35:1736
143. Shiraishi K, Tamura H, Takayanagi H (2001) Appl Phys Lett 78:3702
144. Takeda H, Takashima T, Yoshino K (2004) J Phys Condens Mater 16:6317
145. Gaji'c R, Meisels R, Kuchar F, Hingerl K (2006) Phys Rev B 73:165310
146. Grego S, Jarvis TW, Stoner BR Lewis JS (2005) Langmuir 21:4971
147. Mitsui T, Onodera T, Takaya Y, Wakayama Y, Oikawa H Manuscript in preparation
148. Sugimoto T, Dirige GE, Muramatsu A (1996) J Colloid Interface Sci 180:305, 182:444
149. Takaya Y (2007) Studies on polymer-encapsulation of photo-functional microparticles and their arrangement. Master Thesis
150. Wei Z, Ishii KU, Masuhara A, Kasai H, Okasa S, Matsune H, Asahi T, Masuhara H, Nakanishi H (2005) J Nanosci Nanotech 5:937
151. Zou D, Derlich V, Grandhei K, Park M, Sun L, Kriz D, Lee YD, Kim G, Aklonis J (1990) J Polym Sci A 28:1909
152. Yaguchi Y (2006) Studies on hybridization of phthalocyanine nanocrystals with metal nanoparticles. Master Thesis
153. Masuhara A, Tan Z, Kasai H, Nakanishi H, Oikawa H (2008) Mol Cryst Liq Cryst 492:262
154. Masuhara A, Ohashi S, Kasai H, Okada S, Oikawa H, Nakanishi H (2004) J Nonlinear Opt Phys Mater 13:587
155. Horn D, Rieger J (2001) Angew Chem Int Ed 40:4330

Editor: S. Kobayashi

Poly(substituted Methylene) Synthesis: Construction of C–C Main Chain from One Carbon Unit

Eiji Ihara

Abstract This review describes recent progress in the preparation of C–C main chain polymers, where the main chain is constructed from one carbon unit. The first example for this strategy is polymerization of diazoalkanes and aryldiazomethanes, which were extensively explored in the period 1950–1970, despite the high explosiveness of the monomers. The metal surface-catalyzed polymerization of diazoalkanes has recently attracted much attention, as an efficient method for coating the surface with nanometer-scale polymethylene thin films, which can be regarded as a useful substitute for polyethylene films. Diazocarbonyl compounds such as diazoacetates, diazoketones, and diazoacetamides with a variety of substituents have been polymerized by Pd-complexes to give poly(substituted methylene)s with polar functional groups. Rh(diene) complexes polymerize ethyl diazoacetate in a stereospecific manner, giving high molecular weight polymers (M_n up to 270,000). Organoborane-initiated living polymerization of sulfoxonium methylides is remarkably effective as a method for preparing polymethylenes with a controlled chain length and a well-defined polymer architecture. Some polymerizations related to the above examples are also described.

Keywords Diazoalkane · Diazocarbonyl compound · Metal surface · Organoborane · Poly(substituted methylene) synthesis · Pd complex · Rh complex · Sulfoxonium ylide

E. Ihara (✉)
Department of Material Science and Biotechnology, Graduate School of Science and Engineering, Ehime University, 3 Bunkyo-cho, Matsuyama 790-8577, Japan
e-mail: ihara@eng.ehime-u.ac.jp

Contents

1   Introduction

Needless to say, vinyl polymerization is one of the most important methods for polymer synthesis. A variety of carbon–carbon (C–C) main chain polymers have been prepared by the vinyl polymerization of monomers with diverse substituents, via radical, cationic, anionic, or coordination mechanism. Furthermore, with the technological achievement such as living and stereoselective (or stereospecific) polymerizations, fine-tuning of the polymer structure with respect to molecular weight and tacticity has been realized in a number of examples. In particular, polymers obtained with vinyl polymerization (vinyl polymer) as represented by polyethylene, polypropylene, polystyrene, and poly(methyl methacrylate) have contributed to the progress of modern society in various aspects as useful synthetic materials.

However, even with technological development, there still exist some significant limitations in vinyl polymerization as a method for polymer synthesis. For example, because of the significant difference of reactivity between non-polar olefins (ethylene, propylene, etc.) and polar monomers (e.g., alkyl [meth]acrylate), random copolymerization of such a monomer combination as ethylene and alkyl acrylate

is very difficult, even though some palladium complexes have been discovered recently, which can conduct the copolymerization to some extent [1–6]. From the viewpoint of modifying physical properties of polyolefins, an efficient method for preparing such copolymers has been strongly desired for a long time. Thus, there still remain many technological objectives in vinyl polymerization that have yet to be attained. Or, instead, there could exist some alternative synthetic methods for C–C main chain polymers, which are totally different from vinyl polymerization.

Meanwhile, as a method for the synthesis of C–C main chain polymers, if we can construct the main chains from one carbon unit, a variety of new C–C main chain polymers can be prepared, including polymers which cannot be prepared by vinyl polymerization [7, 8]. Scheme 1 illustrates the general concept of such strategy, by which we can prepare polymers having substituents on all the main chain carbons or having the same composition as those of vinyl polymers with totally different distribution patterns of the substituents along the main chain. To realize such a method for polymer synthesis, we need to find a class of monomers which have an appropriate reactivity for the transformation (initiation and propagation) and hopefully to which introduction of various substituents is feasible. In comparison to vinyl polymerization, which can be called "poly(substituted ethylene) synthesis", we can call the method "poly(substituted methylene) synthesis (PSMS)." Furthermore, compared to vinyl polymerization, where the substituent is located at every other carbon atom, the structural flexibility of PSMS is larger than that of vinyl polymerization with respect to the distribution pattern of the substituent along the main chain.
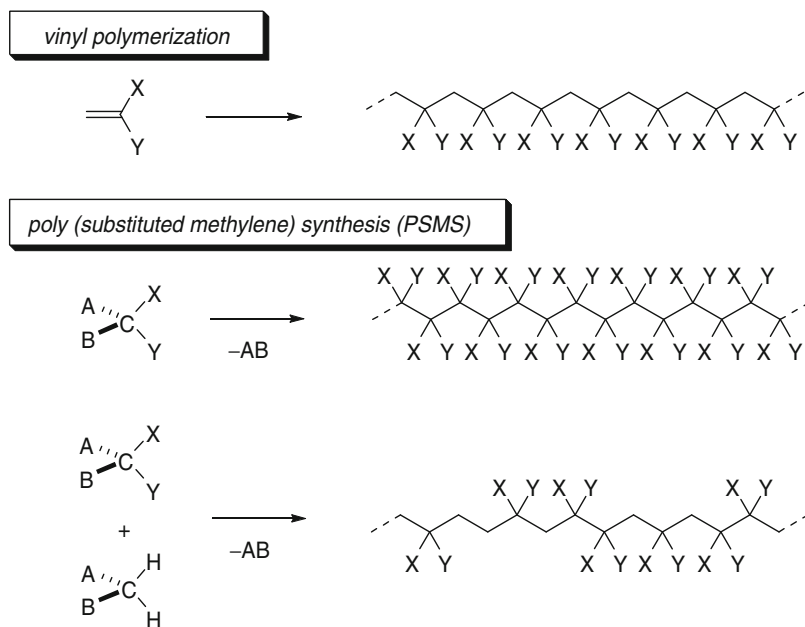
Scheme 1 Vinyl polymerization and poly(substituted methylene) synthesis (PSMS)

As a reported example for PSMS, polymerization of diazoalkanes and aryldiazomethanes was extensively investigated until 1970 [9–11], although the well known explosiveness of the monomers hampered its utilization as a general method for polymer synthesis. Whereas not much progress had been attained thereafter for almost three decades, there have been some new attempts for PSMS using rather more stable compounds such as sulfoxonium ylides and diazocarbonyl compounds since 1997. Thus, the main objective of this review is introducing these new investigations of PSMS. Although polymerization of isocyanides [12] and related compounds can also be regarded as a method for preparing C–C main chain polymers from one carbon unit, they are not included here because they do not afford sp^3 carbon main chains, which should be dealt with in this review, but sp^2-carbon main chains, instead.

2   Polymerization of Diazoalkanes and Aryldiazomethanes

Obviously, the first example of poly(substituted methylene) synthesis (PSMS) is polymerization of diazoalkanes and aryldiazomethanes, which was extensively studied in 1950–1970 [9–11] and whose importance as an alternative method for polyolefin synthesis was well recognized. In that period, in spite of the high explosiveness of the diazo compounds, many researchers were engaged in the polymerization and some unique and important characteristics for the process were revealed. Although some reviews of the polymerization were published [9–11], it is worthwhile to mention briefly some of the representative results, which are closely related to the contents of the later sections of this review. In addition, the unique character of surface-catalyzed polymerization of diazomethane has been utilized for surface modification recently, which is also described in this section. The efficient synthesis of nanometer-scale polymethylene thin films from diazomethane is quite remarkable, compared to the difficulty of polyethylene thin film formation because of the low solubility of the polymer.

2.1   Lewis Acid-Mediated and Transition Metal-Mediated Polymerization of Diazoalkanes and Aryldiazomethanes

Basically, boron-based Lewis acids and some transition metal complexes have been recognized to polymerize diazoalkanes and aryldiazomethanes to give polymethylenes and poly(substituted methylene)s. In particular, boron trifluoride (BF_3) has been most frequently employed as an initiator. One of the most striking features of the BF_3-initiated polymerization of the monomers is that polymers with very high molecular weights ($M_v > 1,000,000$) could be obtained in high yields in some cases, in spite of the poor solubility of the polymers. For example, in 1953, Kantor and Osthoff reported that a crystalline polymethylene (mp $= 132\,°C$) quantitatively obtained with BF_3/Et_2O at $0\,°C$ in ether had a viscosity-based molecular weight
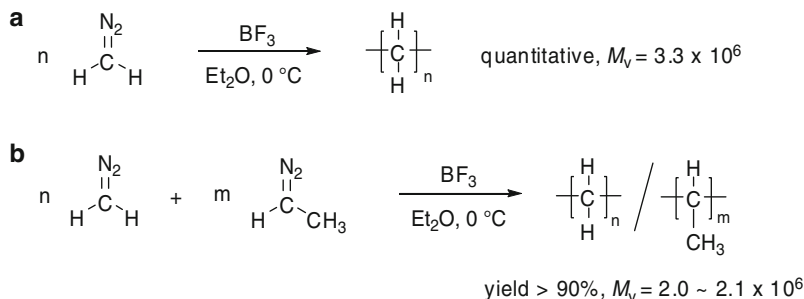
Scheme 2 BF$_3$-mediated polymerization of diazoalkanes

of 3.3×10^6 [13] (Scheme 2a). Furthermore, according to a report by Feltzin and coworkers in 1955, rubber-like copolymers obtained in high yields (>90%) by the initiator from a 4:1 mixture of diazomethane and diazoethane in ether at 0 °C had a viscosity-based molecular weight of ca. 2×10^6 [14] (Scheme 2b). Considering the high reactivity and volatility of the monomers and heterogeneity of the reaction due to the low product solubility, the high yields and molecular weights of the products were somewhat surprising.

As for the mechanism for the Lewis acid-initiated polymerization, while radical mechanism was ruled out by the progress of the polymerization in the presence of radical inhibitors such as hydroquinone, *tert*-butylcatechol, and α, α-diphenyl-β-picrylhydrazyl (DPPH) [14], two types of mechanism had been proposed. In one of the mechanism types proposed by the authors reporting the examples in Scheme 2, cationic propagating species, which should be either carbonium ion (Scheme 3a) or diazonium ion (Scheme 3b) depending on the structure of an actual initiating species, are proposed. In the former scenario, the propagating chain has a zwitter-ion type structure, in which cationic and anionic species are located at propagating and initiating chain ends, respectively (Scheme 3a). On the other hand, in the latter case described in Scheme 3b, the initiating borate should be generated by the reaction of BF$_3$ with acidic compound HX, such as H$_2$O, as often assumed in the initiation for cationic polymerization. Although such cationic propagating species seem to be too unstable to give high molecular weight polymers, Davies and coworkers argued that the ionic propagating species can be stabilized by being surrounded by the large amount of highly polar diazomethane molecules under the polymerization condition [15].

On the other hand, another proposed mechanism is so-called "insertion mechanism," where coordination (nucleophilic addition) of diazo-bearing carbon to the boron atom followed by 1,2-migration of fluoride or propagating alkyl chain constitutes the propagation steps [16, 17] (Scheme 4). On the assumption that the coordination of the monomer to the B-center is rate-limiting, the mechanism reasonably explains the experimental observation of the first-order dependence of the polymerization rate on diazomethane and BF$_3$ concentration and the increase of the molecular weight with the decrease of the initiator concentration.

a

b
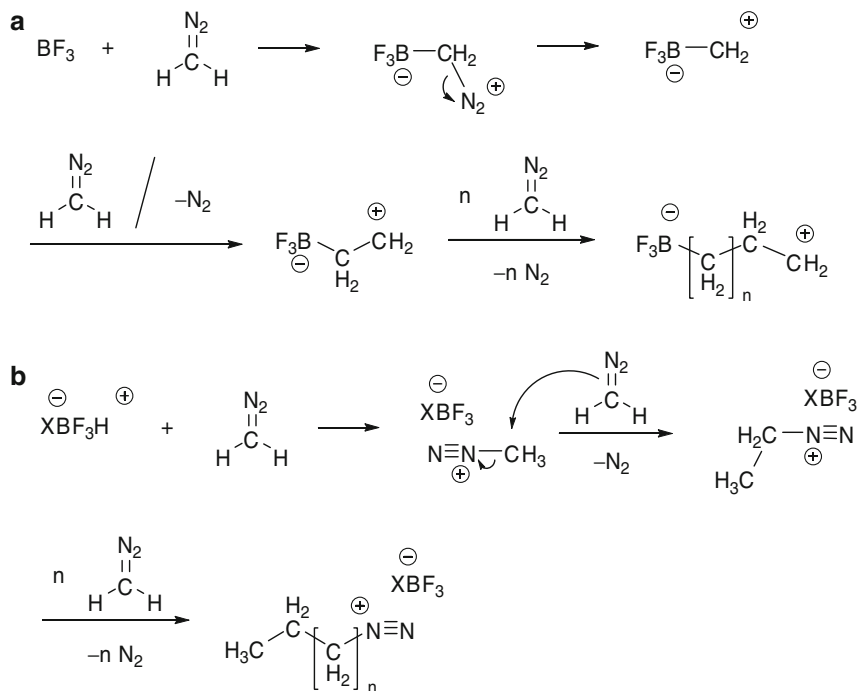
Scheme 3 Cationic mechanism for BF_3-mediated polymerization of diazomethane

observed at -40 ~ - 60 °C
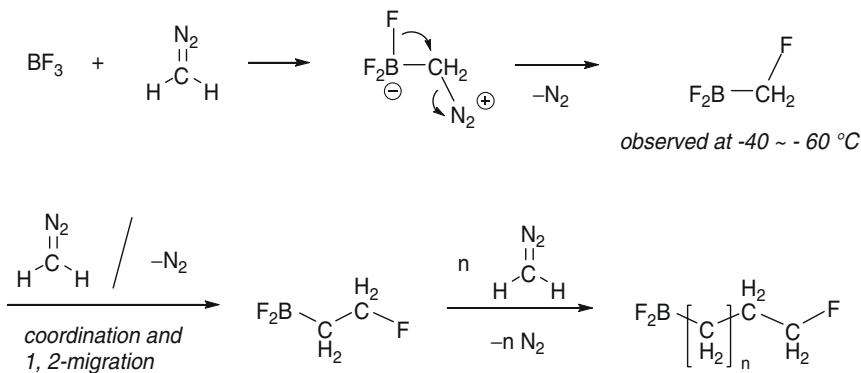
Scheme 4 Insertion mechanism for BF_3-mediated polymerization of diazomethane

The mechanism was also supported by the observation of quantitative formation of an insertion (initiation) product F_2B–CH_2-F as a result of the reaction of BF_3 with diazomethane at -40°C to around -60°C [18]. As described later in this review for the Pd-mediated polymerization of diazocarbonyl compounds and the B-mediated polymerization of dimethylsulfoxonium ylides, this type of mechanism is significant as a general one for PSMS with a combination of coordination (nucleophilic addition) and 1,2-migration for the metal-mediated reactions.

In contrast to diazomethane, homopolymerization of higher diazoalkanes and aryldiazomethanes have not been so successful, giving lower molecular weight polymers in lower yields in general. Recently, Wada, Morisaki, and Chujo applied the BF_3-initiated polymerization to paracyclophane-substituted diazomethanes, aiming at the synthesis of C–C main chain polymers, whose main chain is densely surrounded by cyclophane units [19]. The poly(cyclophane-substituted methylene)s with $M_n = 800 \sim 1,300$ were obtained in $5 \sim 20\%$ yields. As expected, absorption and emission spectra of the polymers exhibited characteristics derived from π-π stacking of the cyclophane units around the polymer main chain. Furthermore, when optically active monomers were employed, CD spectra of the resulting poly(cyclophane-substituted methylene)s suggested the presence of a higher-ordered structure supposedly induced by the expected tight packing of the chiral cyclophane units (Scheme 5).

In addition to boron-based Lewis acids, some transition metal complexes have been shown to be able to polymerize diazomethane [20, 21]. For example, Werner and Richards reported that nickelocene was highly active for polymerization of diazomethane, and proposed a polymerization mechanism where a propagating chain end contained a Ni–C bond as an active species [21]. On the other hand, when they examined a reaction of nickelocene with ethyl diazoacetate (EDA) in cyclohexene, no polymer was formed but diethyl fumarate, diethyl maleate, and ethyl norcaranecarboxylate were obtained in a 1.4:2.6:1.0 ratio (Scheme 6).

Looking back at the above-mentioned early investigations on PSMS from diazo compounds, we realize that the fundamental and significant part of the
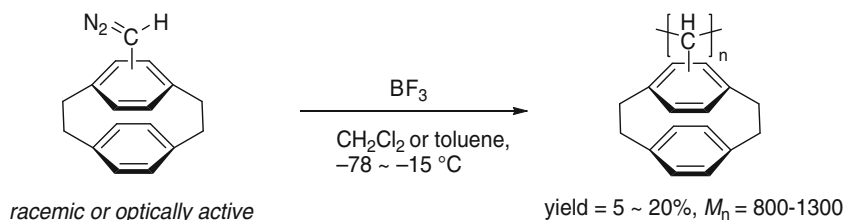
Scheme 5 BF_3-mediated polymerization of paracyclophane-substituted diazomethane
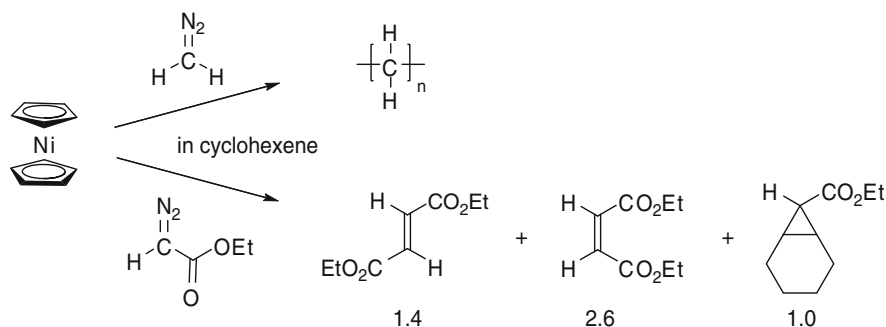
Scheme 6 Reactions of nickelocene with diazomethane and ethyl diazoacetate

polymerization has been already established in these periods. Actually, it was very unfortunate that the explosive nature of the monomers might have prevented their further application, in particular a large scale production of the polymers, even though the efficient synthesis of the high molecular weight polymers comparable to polyolefins should have seemed very promising from the viewpoint of producing useful polymeric materials.

2.2 Surface-Catalyzed Polymerization of Diazoalkanes

Along with the Lewis acid and transition metal-initiated polymerization described above, it has been reported that diazoalkanes can be polymerized to give polyalkylidenes by contact with the surface of various transition and main group metals. The metal surface-catalyzed polymerization was originally found when polymerization of diazoalkane was examined by using AuX_3 (X=Cl or Br) as a Lewis acid catalyst [22–24]. At the beginning of the reaction, diazoalkane reduced the Au complex to colloidal Au, which catalyzed the polymerization to give polyalkylidene. The results led the researchers to investigate catalytic activity of surfaces of evaporated metals toward polymerization of diazoalkanes, where the activity of various transition metal surfaces was revealed [25]. In particular, polymerization initiated by an Au-surface afforded crystalline polyethylidenes, which suggested stereoselective propagation at the metal surface.

The Au surface-catalyzed polymerization of diazoalkanes has recently been applied to the coating of Au-surfaces with nanometer-scale polymethylene thin films. Because of its high inertness and stability, polyethylene has been considered a desirable material for metal surface coating. However, the low solubility of the polymer has prevented the use of common film-forming methods such as spin coating and solution casting. Moreover, conditions required for ethylene polymerization is basically not suitable for applying to surface-initiated polymerization to prepare thin films. Thus, in 1997, instead of using polyethylene or ethylene monomer, Tao, Allara, and coworkers demonstrated that nanometer-scale polymethylene thin films can be efficiently coated onto Au surfaces by using the surface-catalyzed polymerization of diazomethane [26]. By exposing evaporated Au surfaces to an ether solution of diazomethane, crystalline polymethylene films in the thickness range of 1–100 nm were formed on the metal surface via the polymerization initiated at Au defect sites. As a mechanism for surface-catalyzed polymerization, the authors proposed a radical mechanism (Scheme 7), where Au on the surface decomposed diazomethane with release of N_2 to leave transient active CH_2 species absorbed on the surface by the interaction with the metal in a form of metal carbene, $Au = CH_2$. Then, the active CH_2 species collide with each other forming a biradical species, $\bullet CH_2–CH_2\bullet$, still absorbed on the metal surface. The propagation can proceed via reaction of an activated CH_2 with one of the radical chain ends, giving polymethylene on the surface.

By combining this technique with formation of a self assembled monolayer (SAM) of organothiol compounds, Tao and coworkers succeeded in making
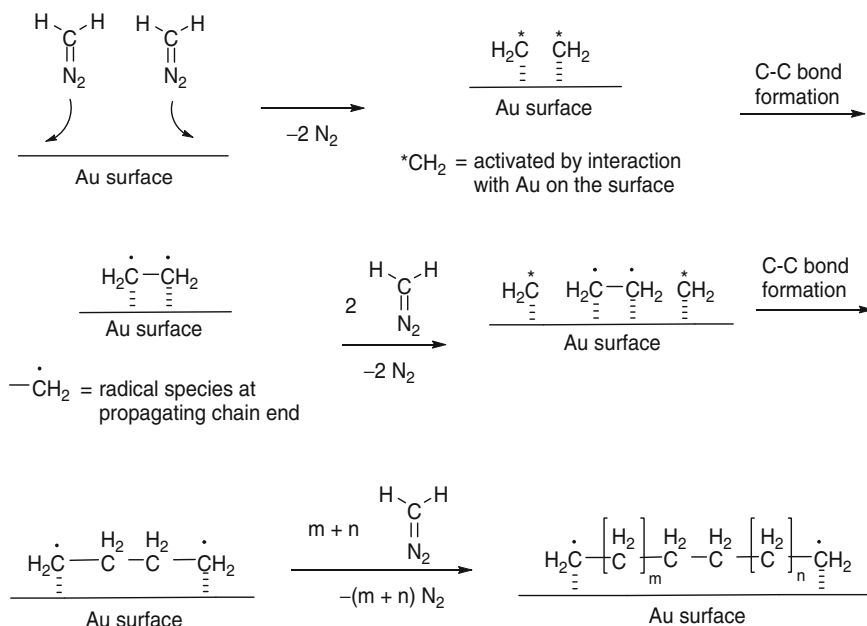
Scheme 7 Mechanism for Au surface-catalyzed polymerization of diazomethane
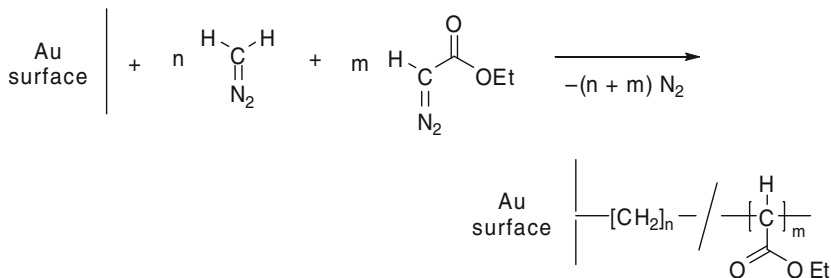
Scheme 8 Au surface-catalyzed copolymerization of diazomethane with ethyl diazoacetate

microscale patterns on Au-surfaces [27]. Jennings and coworkers have found that underpotentially deposited Cu (upd-Cu) and Ag (upd-Ag) layers on Au-surfaces accelerate and prevent the polymerization of diazomethane, respectively [28], and then, by combining the upd-Cu activation and upd-Ag deactivation, they also realized microscale patterning on Au-surfaces [29].

A particularly important breakthrough was achieved by Bai and Jennings in 2005 in the surface-catalyzed polymerization of diazomethane by using ethyl diazoacetate (EDA) as a comonomer [30] (Scheme 8). Although surface-catalyzed homopolymerization of EDA did not proceed, EDA can be incorporated into the resulting polymer chain when an ether solution of a mixture of diazomethane and EDA was contacted with an Au-surface. The resulting surface bound copolymer, poly(methylene-*co*-ethoxycarbonylmethylene), has the same structure as that of random copolymer of ethylene and ethyl acrylate. Whereas the incorporation efficiency

of EDA was not so high, the EDA composition can be controlled in a range of $0 \sim 4\%$ by changing the relative monomer concentration of diazomethane and EDA.

Most strikingly, they revealed that the propagation occurred not at the outer film-solvent interface, but at the film-metal interface, by designing sophisticated experiments, where the relative monomer concentration of diazomethane and EDA was changed in the middle of the polymerization to an extent that significantly affected the contact angle of the resulting polymer surface. As a result, the resulting surface exhibited the contact angle expected from the composition of the first stage polymerization, which meant that the polymer chain derived from the second stage polymerization inserted into the interface between the metal surface and the polymer chain derived from the first stage polymerization. Thickness of the copolymer film can be controlled by the polymerization period and increased at a constant rate during the polymerization, which suggests that the propagating species at the film-metal interface is rather stable. Another interesting point is that the rate of the polymerization increased with the increase of relative concentration of EDA, even after the incorporation efficiency of EDA reached a constant level and no longer increased.

From these experimental results, a polymerization mechanism has been proposed (Scheme 9). As was proposed by Tao, Allara, and coworkers in Scheme 7, the first step of the reaction is decomposition of diazo compounds releasing N_2 by the contact with an Au-surface, resulting in the formation of transient carbene-type species with interaction with Au on the surface. Because the propagation occurs at the metal-polymer interface, pushing the polymer chain outwardly, the presence of Au–C bond is postulated as an active chain end. Thus, the propagation should be an insertion of the activated CH_2 and $CHCO_2Et$ species into the Au–C bond, where the reactivity of the former is much higher than the latter. Then, the transient $CHCO_2Et$ species existing on the metal surface but not participating in the propagation should activate the Au atom in the propagating chain end by withdrawing electrons from the metal because of the electron withdrawing effect of the ester group.
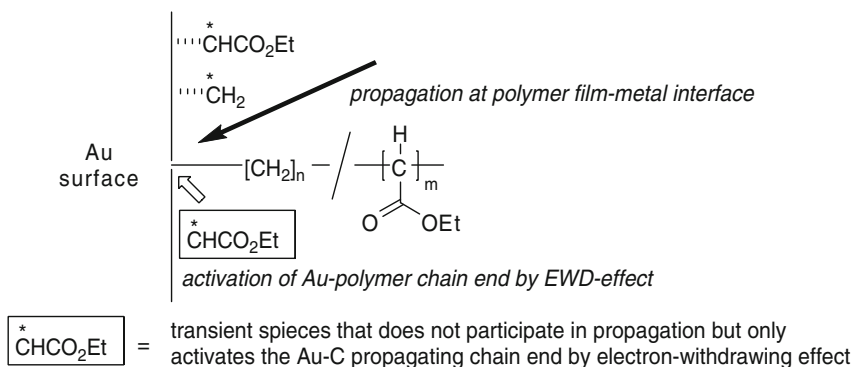
Scheme 9 Mechanism for Au surface-catalyzed copolymerization of diazomethane with ethyl diazoacetate

The use of EDA as a comonomer in the surface-catalyzed polymerization not only contributed to the efficient formation of polymer films, but can also be utilized for the modification of surface properties by using the incorporated ester groups. In particular, pH-responsive membranes have been achieved by hydrolysis of the ester group [30–33] or introduction of amino group via substitution at the ester group [34].

3   Polymerization of Diazocarbonyl Compounds

In contrast to the aforementioned diazoalkanes and aryldiazomethanes, whose instability and high explosiveness have diminished their general utility as a monomer for polymer synthesis, diazocarbonyl compounds have been known to be rather stable and frequently used as a reagent for organic synthesis [35, 36]. In particular, transition metal catalyzed cyclopropanation of diazocarbonyl compounds with C=C double bonds has been extensively investigated and established as a very useful method for the formation of cyclopropane frameworks, where application for asymmetric synthesis using various optically active ligands has been successfully achieved.

On the other hand, polymerization of diazocarbonyl compounds had not been reported until 2002, which seems somewhat strange considering the extensive studies of polymerization of diazoalkanes and the prevalence of diazocarbonyl compounds in synthetic organic chemistry. If the polymerization of diazocarbonyl compounds releasing N_2 proceeds in a similar manner as diazoalkanes, synthesis of poly(substituted methylene)s bearing carbonyl containing polar functional groups such as ester and ketone could be realized, extending the generality of PSMS considerably. For example, the combination with a monomer providing an unsubstituted CH_2 unit (one candidate = diazomethane) will result in the formation of a new polymer, whose composition is equal to poly(alkyl acrylate) or poly(vinyl ketone), but whose distribution pattern of the polar substituents along the main chain is random, being quite different from that derived from vinyl polymerization where the substituent is located on every other carbon atom (Scheme 10).
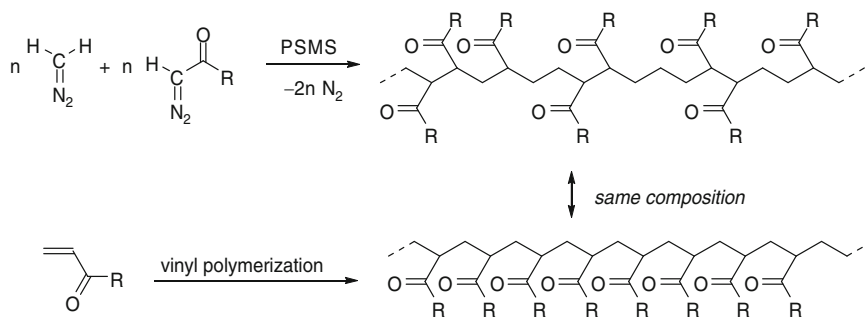
Scheme 10 Syntheses of polymers with a same composition by PSMS and vinyl polymerization
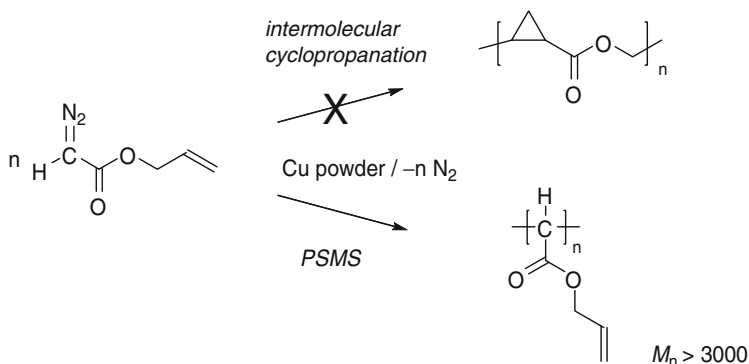
Scheme 11 Cu-mediated polymerization of allyl diazoacetate

3.1 Cu-Mediated Polymerization of Allyl Diazoacetate

In 2002, in an attempt to prepare poly(2-hydroxymethylcyclopropanecarboxylic acid) via intermolecular cyclopropanation of allyl diazoacetate catalyzed by Cu powder, Liu and co-workers found that the product was not the desired polymer with the cyclopropane-framework in the main chain, but poly(allyloxycarbonyl-methylene) as shown in Scheme 11 [37]. Although the polymer yield was not mentioned in the paper, the polymer structure was confirmed by ^{1}H and ^{13}C NMR and IR spectroscopy, and M_n of the product was reported to be over 3,000 by the estimation with GPC based on polystyrene standards. This is the first report for the polymerization of diazocarbonyl compounds.

3.2 Pd-Mediated Polymerization of Diazocarbonyl Compounds

3.2.1 Polymerization of Alkyl and Aryl Diazoacetates

Independent from Liu and coworkers, we have found and reported that alkyl and aryl diazoacetates can be polymerized by the initiation with palladium dichloride (PdCl$_2$) in the presence of amine such as pyridine and triethylamine [38]. Poly(ethoxycarbonylmethylene) and poly(methoxycarbonylmethylene) were obtained in 50 ∼ 100% yields by the polymerization of ethyl diazoacetate (EDA) and methyl diazoacetate, respectively (Scheme 12), and the ^{1}H NMR spectra of the former products are almost identical with those of polymers obtained by radical polymerization of diethyl fumarate and maleate [39]. Although GPC-estimated M_ns based on PMMA standards were rather low (<500), MALDI-TOF-MS spectra for the products exhibited signals in a range of $m/z = 1,000 \sim 10,000$, indicating that they were not mere mixtures of oligomers with degree of polymerization (DP) below 10, but actually polymers with higher DP (up to 100) were included even in small quantities.
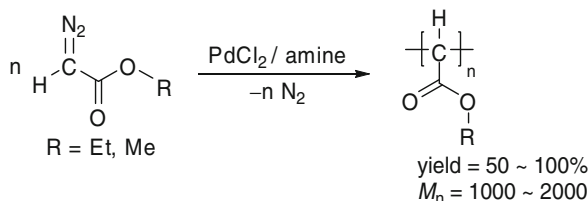
Scheme 12 PdCl$_2$-mediated polymerization of alkyl diazoacetates
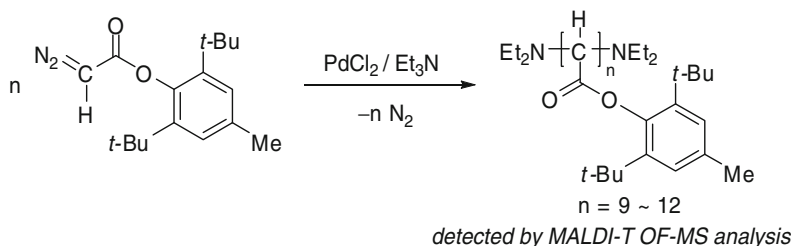
Scheme 13 PdCl$_2$-mediated polymerization of aryl diazoacetate
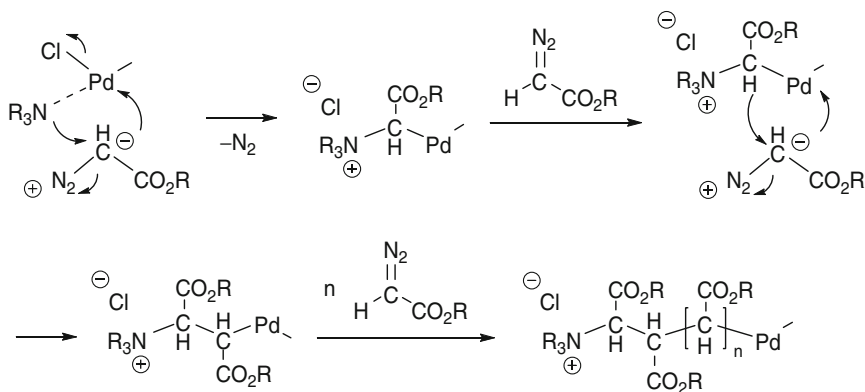
Scheme 14 Mechanism for PdCl$_2$-mediated polymerization of alkyl diazoacetate

When an aryl diazoacetate with bulky substituents on its phenyl ring was employed as a monomer and the product obtained by initiation with PdCl$_2$/Et$_3$N was analyzed by MALDI-TOF-MS in reflector mode, the result suggested the presence of diethylamino groups at both polymer chain ends [38] (Scheme 13).

On the assumption that the diethylamino group was derived from triethylamine used as an additive, a mechanism for the polymerization can be proposed as shown in Scheme 14. The initiation would be a nucleophilic attack of the amine coordinated on the Pd center to the diazo-bearing carbon atom of the monomer accompanied by the release of N$_2$, resulting in the formation of a Pd–C bond. Then, the propagation would be an analogous attack of the chain end carbon on the Pd center to the diazo-bearing carbon of another monomer with the release of N$_2$, resulting in the

insertion of an alkoxycarbonylmethylene repeating unit into the propagating Pd–C bond. The reductive elimination of two propagating chains from a divalent Pd center explains the formation of the attachment of amino groups at the both polymer chain ends. The observation of neutral diethylamino groups in the MALDI-TOF-MS spectrum indicates that the Hofmann type elimination of HCl from the ammonium ion occurred during work-up or the MS analysis.

In accord with the mechanism proposed above, elemental analysis of the thus obtained polymers indicated the presence of a small amount of nitrogen, which can be ascribed to the presence of N-containing groups at the chain ends. Calculation on the basis of the N-content shows that M_ns of the polymers are about 2,000, for the samples whose GPC-estimated M_n were below 500.

Because Pd complexes would catalyze dimerization of EDA to give diethyl fumarate and maleate, it might be possible that the polymers were obtained by radical polymerization of the diesters generated by the Pd-catalyzed dimerization. However, whereas the polymer obtained by AIBN-initiated radical polymerization of diethyl fumarate exhibited signals in MALDI-TOF-MS spectra with peak intervals of $m/z = 172$ ($CHCO_2Et \times 2$), the intervals of the spectra of polymers from EDA were $m/z = 86$, suggesting that the polymers were not obtained by the radical polymerization of the diesters [38] (Scheme 15).

Recently, we have found that a combination of Pd(0) complexes having an N-heterocyclic carbene (NHC) ligand and tetraarylborate [(NHC)Pd/borate system] is effective for affording relatively high molecular weight polymers from EDA [40] (Scheme 16). Poly(ethoxycarbonylmethylene)s with $M_n = 10,000 \sim 25,000$ were obtained in good yields. MALDI-TOF-MS analyses of the product suggested that a part of the polymer had H and C=C at its chain ends. Accordingly, one of the possible mechanisms for the polymerization is that initiation with Pd–H species and termination with β-H elimination as shown in Scheme 17. The initiating cationic divalent Pd species would be generated by the reaction of the zerovalent (NHC)Pd
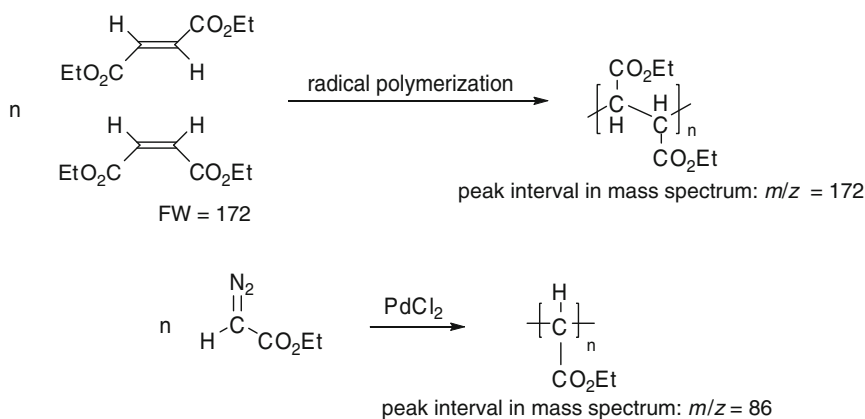
Scheme 15 Radical polymerization of diethyl fumarate and maleate vs. PdCl$_2$-mediated polymerization of ethyl diazoacetate
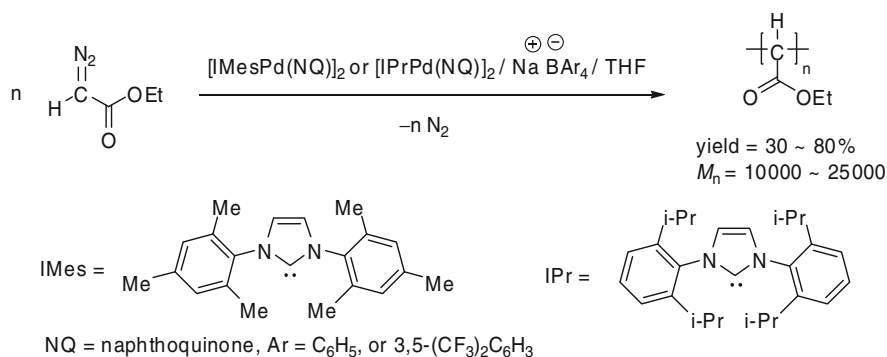
Scheme 16 Polymerization of ethyl diazoacetate initiated with (NHC)Pd/borate system
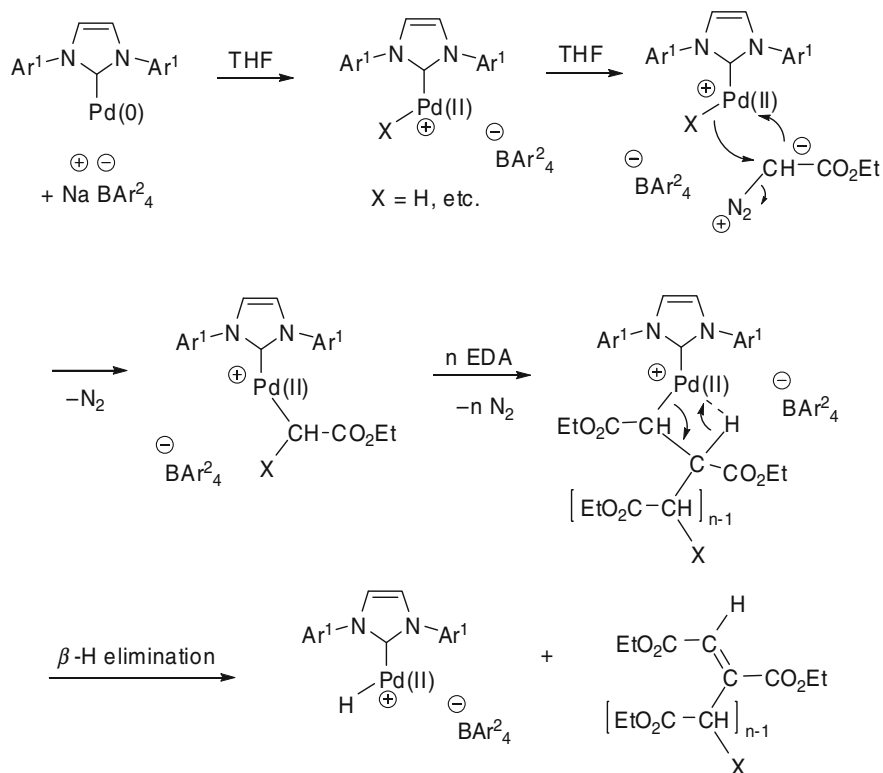
Scheme 17 Mechanism for (NHC)Pd/borate-initiated polymerization of ethyl diazoacetate

complex with THF in the presence of the borate, and the cationic (NHC)Pd(II) having tetraarylborate as a counter anion should remain as the propagating chain end during the polymerization.

Interesting to note with the (NHC)Pd/borate initiating system is that the tacticity of the resulting polymers estimated by the appearance of the main chain C*H* and
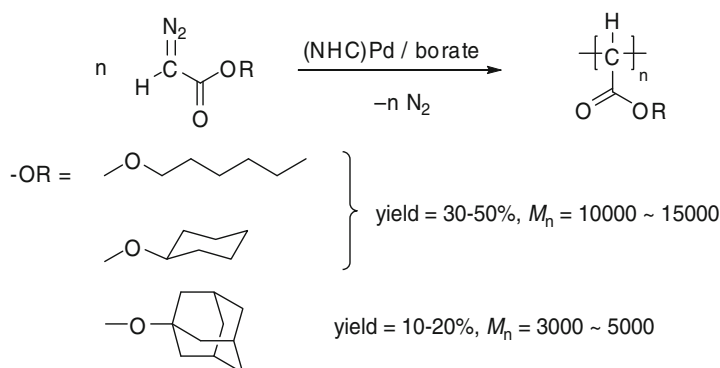
Scheme 18 (NHC)Pd/borate-initiated polymerization of primary-, secondary-, and tertiary-alkyl diazoacetates
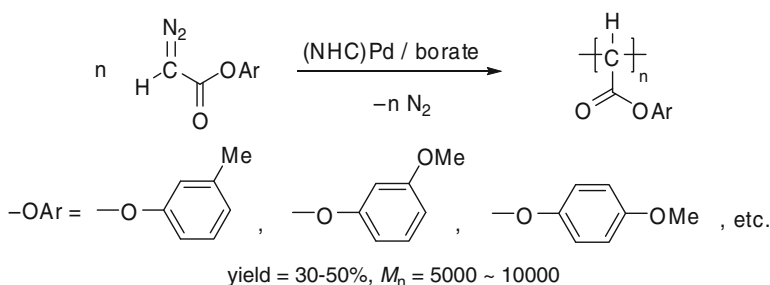
Scheme 19 (NHC)Pd/borate-initiated polymerization of aryl diazoacetates

carbonyl $C{=}O$ signals in their ^{1}H and ^{13}C NMR spectra, respectively, is dependent on the substituent on the NHC ligand. The results suggest that the stereocontrol of the polymerization would be possible by proper choice of the ligand structure.

The (NHC)Pd/borate system can be used for other alkyl diazoacetates than EDA. For example, n-hexyl and cyclohexyl diazoacetates can be transformed by the initiating system into the corresponding poly(alkoxycarbonylmethylene)s with $M_n > 10,000$ in moderate yields (Scheme 18). On the other hand, polymers with much lower yields and M_ns were obtained by the polymerization of adamantyl diazoacetate, which suggests that the bulkiness of the tertiary ester group prevents the efficient progress of the polymerization [41].

Although radical polymerization of diaryl fumarate and maleate does not proceed, Pd-mediated polymerization of aryl diazoacetates can afford polymers, whose main chain is densely surrounded by aromatic rings. As shown in Scheme 19, the (NHC)Pd/borate initiating system polymerized aryl diazoacetates to give poly(aryloxycarbonylmethylene)s with $M_n = 5,000$–$10,000$ in moderate yields [42]. Similar to the aforementioned poly(cyclophane-substituted methylene)s [19], the close packing of aromatic groups in the polymer is quite unique, especially in comparison with vinyl polymers such as polystyrene or poly(vinylnaphthalene), whose arrangement of the aromatic groups cannot be so dense because of the presence of an unsubstituted CH_2 unit at every other carbon atom in the main chain.

3.2.2 Polymerization of Diazoketones

When diazoketones instead of diazoacetates were used as monomers for the Pd-mediated polymerization, poly(acylmethylene)s having an acyl group on every main chain carbon atom can be prepared. α,β-Unsaturated diazoketones **1** and **2** can be polymerized to give polymers with $M_n = 1,500 \sim 2,500$ in good yields [43] (Scheme 20a). The presence of C=C in α,β-position of the carbonyl group is essential for the polymerization to proceed, because the diazoketones without the C=C such as **3**, **4**, and **5** gave polymers with lower M_ns in lower yields (Scheme 20b).

Even when the polymerization was conducted in the absence of amine, the results of elemental analysis of the obtained polymers indicated the presence of a small amount of nitrogen (ca. 1%), which could be ascribed to the incorporation of azo group (–N=N–) in the main chain. As shown in Scheme 21, the incorporation of azo group would occur, when the propagating chain end attacks the terminal nitrogen of the diazoketones instead of its diazo-bearing carbon. The presence of the azo group was confirmed by the observation of absorption at $1,560\,\mathrm{cm}^{-1}$ in a Raman spectrum for a polymer obtained by Pd-mediated polymerization of phenyldiazomethane [44]. The composition of the azo group in the polymers from **1** and **2** is 3–5 mol%, for example.
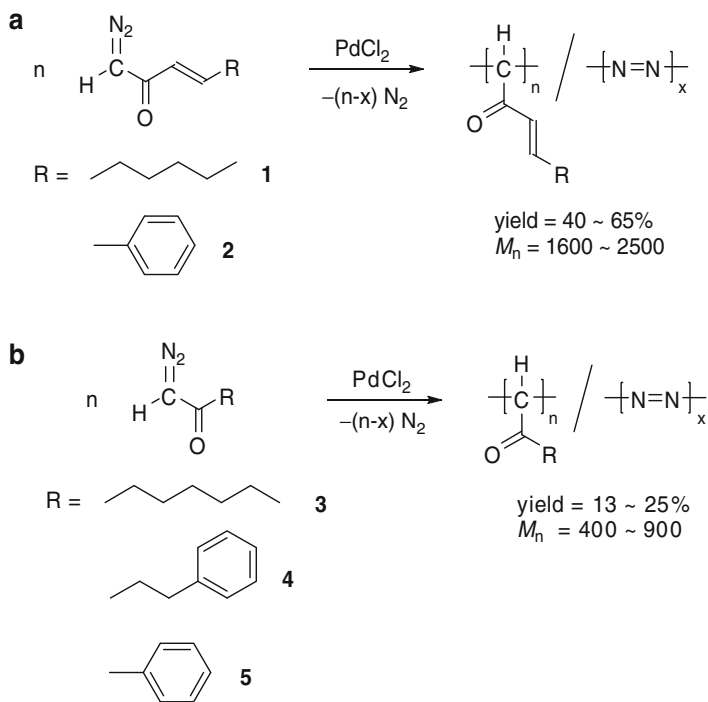
Scheme 20 PdCl$_2$-mediated polymerization of diazoketones
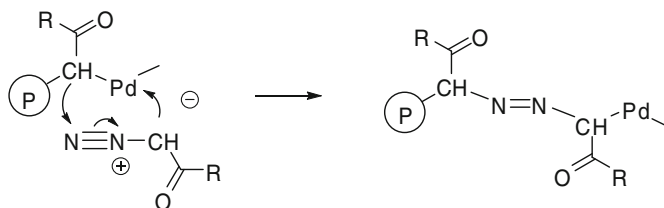
Scheme 21 Mechanism for azo group incorporation

R¹, R² = -CH=CH-n-C₅H₁₁ **1**, -CH=CH-Ph **2**, -OEt (EDA)
-n-C₆H₁₃ **3**, -CH₂CH₂-Ph **4**, -Ph **5**
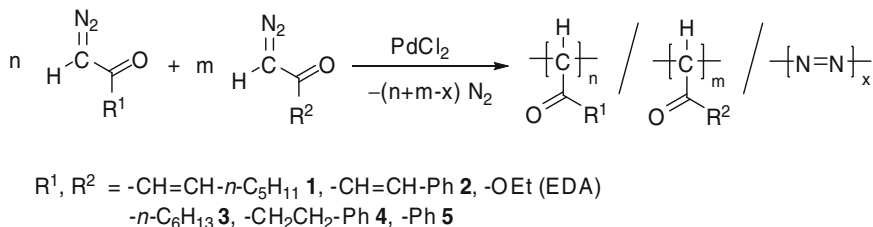
Scheme 22 PdCl₂-mediated copolymerization of various diazocarbonyl compounds

Despite the low polymerization efficiency of the diazoketones **3**, **4**, and **5** without C=C at α,β-position, they can be used as a comonomer for copolymerization with other polymerizable diazocarbonyl compounds including EDA (Scheme 22). Thus, copolymerization with a variety of monomer combinations are possible, affording poly(substituted methylene)s with various structures, and physical properties of the copolymers can be controlled by the proper choice of the monomers and their relative concentrations. For example, polymers derived from **1** with an alkyl chain are highly viscous oils, whereas those from **2** with a phenyl group are solid. By changing the initial relative concentrations of the monomers for the copolymerization, we can control the compositions of repeating units in the resulting copolymers, which significantly affect the physical properties of the copolymers.

As diazocarbonyl compounds bearing a substituent other than H on the diazo-bearing carbon, some cyclic diazoketones were applied to the Pd-mediated polymerization. The α,β-unsaturated cyclic diazoketone **6** derived from cyclohexenone can be transformed into polymers with a unique structure, where the main chain carbon is one of carbon atoms of a six-membered ring [45] (Scheme 23). In addition, the C=C bond conjugated with C=O would be directed outward from the main chain, which may render an attack of nucleophiles (1,4-conjugate addition) feasible. As expected, the addition of nucleophiles such as organolithium and sodium salt of diethyl malonate occurred by the reaction with the polymer.

Although homopolymerization of α,β-unsaturated cyclic diazoketones with substituents on the six-membered ring or α,β-saturated cyclic diazoketones do not proceed efficiently, they can be used as a comonomer for copolymerization with polymerizable diazoketones **1** and **2**, providing poly(substituted methylene)s with a variety of structures [45] (Scheme 24). These results indicate that diazocarbonyl compounds bearing substituents other than H on the diazo-bearing carbon can be used as monomers for the Pd-mediated polymerization.

yield = 24%, M_n = 1400

nucleophile = RLi / CuI (R = n-Bu, Ph), NaCH(CO$_2$Et)$_2$
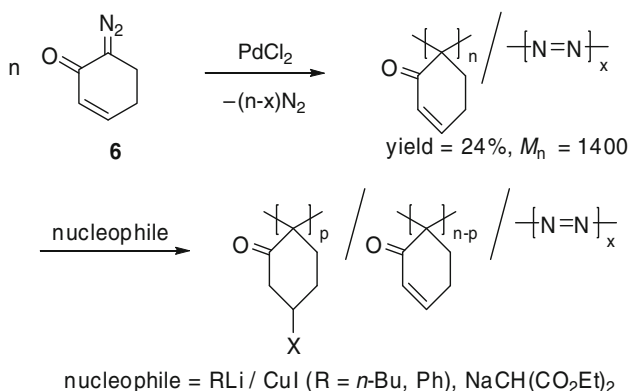
Scheme 23 PdCl$_2$-mediated polymerization of cyclic diazoketones

R= n-C$_5$H$_{11}$ **1**, Ph **2**

yield = 25 ~ 50%, M_n = 700 ~ 2500
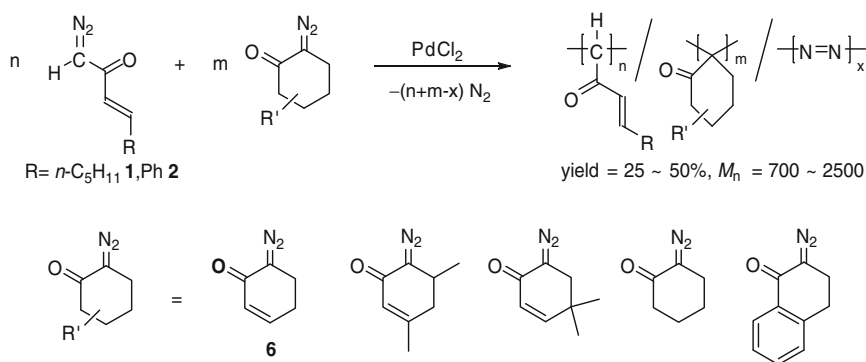
Scheme 24 PdCl$_2$-mediated copolymerization of cyclic diazoketones with acyclic diazoketones

3.2.3 Polymerization of Diazoacetamides

Diazoacetamide is another important class of diazocarbonyl compounds. We investigated Pd-mediated polymerization of N-substituted diazoacetamides, which could afford poly(N-substituted carbamoylmethylene)s after polymerization [46]. The structure of the polymer can be regarded as a poly(substituted methylene) analogue of poly(N-substituted acrylamide)s, whose interesting physical properties such as thermo-responsiveness are well known. In addition, preparation of poly(N,N-dimethylcarbamoylmethylene) by transformation of poly(di-*tert*-butyl fumarate) and its unique miscibility with commodity polymers have been reported [47]. Among the monomers we examined, only **7** and **8** can be homopolymerized by the initiation with PdCl$_2$, affording polymers in low yields (Scheme 25a). On the other hand, all the diazoacetamides can be used as a comonomer with diazoketone **2**, and copolymers containing acyl and carbamoyl groups on the main chain were obtained (Scheme 25b).

a

R = -*n*-C$_6$H$_{13}$ **7**,
      -C$_6$H$_4$-*n*-C$_8$H$_{17}$ **8**

yield = ~10%, M_n = 1000 ~ 2000

b

yield = 30 ~ 55%, M_n = 700 ~ 1500
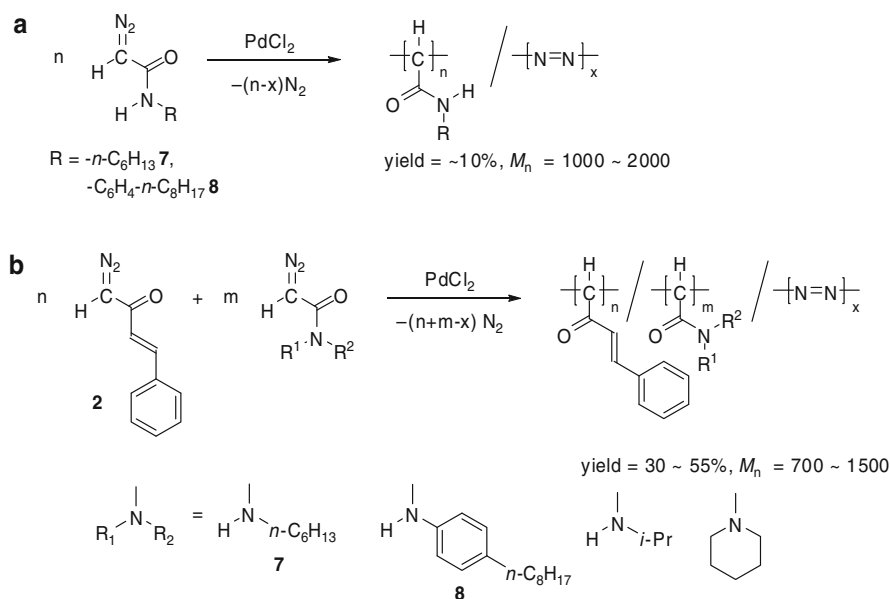
Scheme 25 PdCl$_2$-mediated (co)polymerization of *N*-substituted diazoacetamides

PdCl$_2$ → cross-linked polymer

R = -CH=CH-*n*-C$_5$H$_{11}$ **1**,
      -CH=CH-Ph **2**,
      -OEt (EDA)

—X—   =   **9**

 10
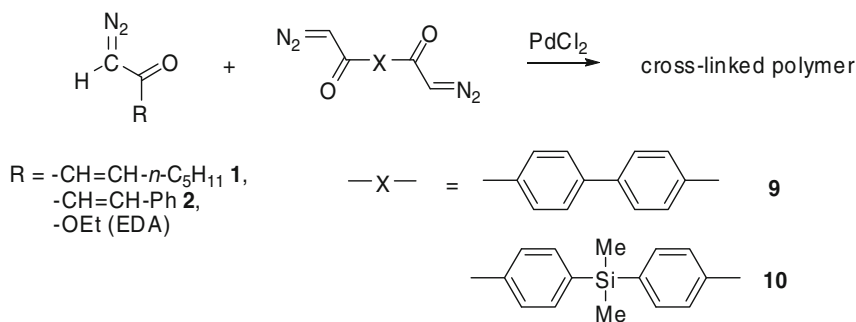
Scheme 26 Synthesis of cross-linked polymers by PSMS

3.2.4 Polymerization of Bis(diazocarbonyl) Compounds

In vinyl polymerization, the use of bifunctional monomers such as divinylbenzene and *N*,*N*′-methylene-bis(acrylamide) with monofunctional vinyl monomers is a very common and useful method for the synthesis of cross-linked polymers. The same strategy was examined with the use of some bis(diazocarbonyl) compounds as shown in Scheme 26 [48]. The copolymerization of bis(diazocarbonyl) compounds **9** and **10** with monofunctional monomers **1**, **2**, and EDA with feed ratios of [**9** or **10**]/[**1**, **2**, or EDA] = 0.2 ~ 0.33 afforded soluble products with M_n = 10,000 ~ 50,000, which would have hyperbranch structures. Further increasing the feed ratio of [**9** or **10**]/[**1**, **2**, or EDA] to >0.5 in the copolymerization resulted in the formation of insoluble products, which should be cross-linked polymers. These products

should have higher densities of substituents (functional groups) in each lattice of their cross-linked structure than those obtained by analogous vinyl copolymerization, and the characteristic can be utilized for preparing useful polymeric materials.

3.3 Rh-Initiated Polymerization of Ethyl Diazoacetate

In 2006, de Bruin and coworkers reported that some Rh(diene) complexes with N,O-ligands initiated the polymerization of EDA, giving high molecular weight polymers with M_n up to 270,000 [49–51] (Scheme 27). Although the initiation efficiency of the Rh complexes is low ($<5\%$), the polymerization proceeds through a rather stable propagating chain end as demonstrated by the linear relationship between molecular weight and polymer yield. Because the kind of the N,O-ligand does not affect the polymerization behavior with respect to M_n and M_w/M_n of the products, the propagating chain end is assumed to have Rh(diene) moiety as an active species. In contrast to poly(ethoxycarbonylmethylene)s obtained by the Pd-mediated polymerization, very sharp signals were observed in the ^{1}H and ^{13}C NMR spectra of polymers obtained by the Rh complexes, indicating that the polymerization proceeded in a highly stereoselective manner. Comparison of the ^{13}C NMR with that of poly(diethyl fumarate) obtained by radical polymerization suggested that the polymers have a predominantly syndiotactic structure. In accord with the highly stereoregulated main chain structure, the polymers show higher T_g than atactic poly(diethyl fumarate).

yield = 10 ~ 50%,
M_n = 22000 ~ 270000,
syndiotactic

diene =

N, O-ligand =
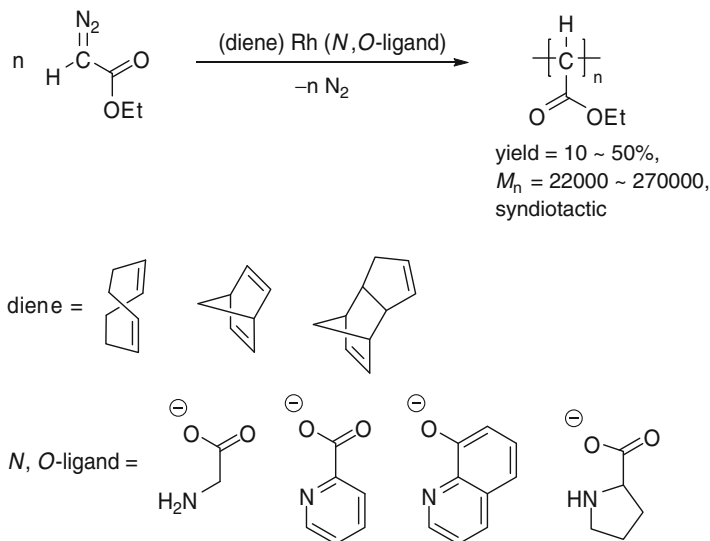
Scheme 27 Rh-initiated polymerization of ethyl diazoacetate
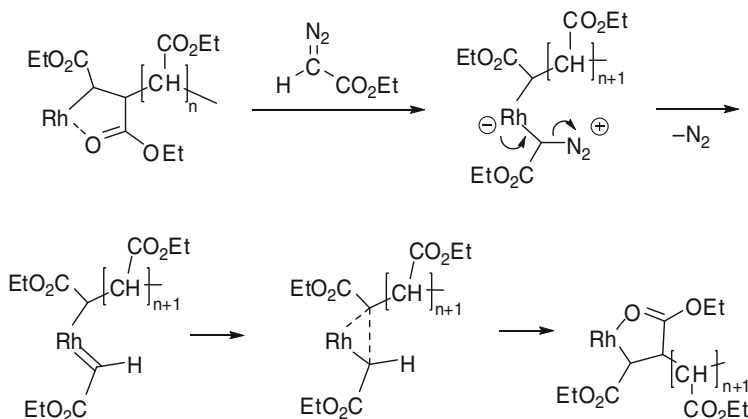
Scheme 28 Mechanism for Rh-initiated polymerization of ethyl diazoacetate
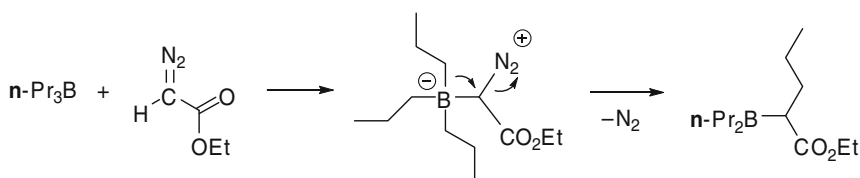
Scheme 29 Homologation of trialkylborane with ethyl diazoacetate

The polymerization is assumed to proceed via (1) nucleophilic attack of diazo-bearing carbon of EDA to the Rh(I)-center of propagating chain end, (2) formation of Rh(III)-carbene complex after elimination of N_2, and (3) insertion of the carbene into Rh–C bond regenerating the Rh(I) propagating species (Scheme 28). DFT calculation following this mechanism indicated the preference for the syndioselective insertion step in chain end control.

3.4 B-Mediated Polymerization of Ethyl Diazoacetate

It was reported that the reaction of trialkylborane with EDA proceeded via nucleophilic attack of the diazo-bearing carbon of EDA to the boron center followed by 1,2-migration of an alkyl group from boron to carbon with elimination of N_2, resulting in the homologation of trialkylborane [52–54] (Scheme 29).

Although the reaction can be extended to polymerization of EDA if it occurs consecutively, it does not proceed further than single insertion as long as trialkylborane was used. On the other hand, in 2007 Shea and coworkers reported that reaction of borane (BH_3) instead of trialkylborane with EDA afforded oligomers, as a result of multiple insertions of the diazo-bearing carbon of EDA into B–C bond accompanied by elimination of N_2 [55]. The reaction of EDA with BH_3 in 3:1 ratio furnished oligomers ($M_n < 480$) in a 34% yield along with products resulting from single
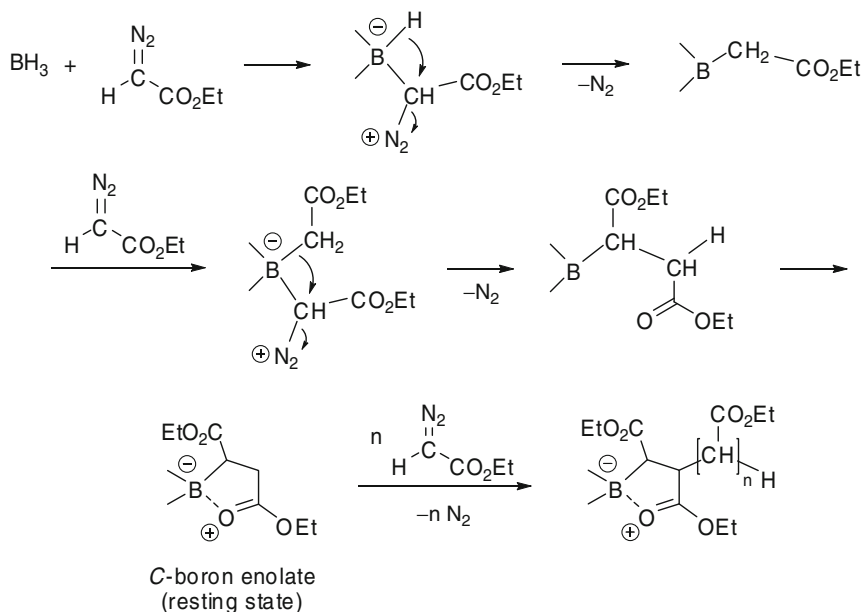
Scheme 30 Mechanism for BH_3-mediated polymerization of ethyl diazoacetate

(11%), double (38%), and triple (8%) insertions. Interestingly, in the reaction of EDA with BH_3 in a 1:1.2 feed ratio, 22 mol% of EDA was transformed into a five-membered cyclic *C*-boron enolate, which was characterized by ^1H, ^{13}C, and ^{11}B NMR and whose relative stability compared to the corresponding *O*-enolate was supported by theoretical calculation. Accordingly, the BH_3 initiated polymerization should proceed with the *C*-boron enolate as a resting state, as shown in Scheme 30.

As demonstrated by the observation that only single insertion of EDA occurs from trialkylborane, the polymerization would stop once three propagating chains exist on the B center. Accordingly, as the theoretical calculation suggested that there is not much difference between activation energies for the 1,2-migration of H and alkyl group, the use of a large excess of EDA to BH_3 did not afford high molecular weight polymers, but only oligomers in low conversion along with unreacted EDA.

3.5 Al-Mediated Polymerization of Diazoketones

When organoaluminum compounds were used as initiators for polymerization of di-azoketone **1**, polymers with $M_n=2,000 \sim 3,000$ were obtained in a similar manner as the Pd-mediated polymerization [56] (Scheme 31). However, elemental analysis of the polymers obtained by organoaluminums exhibited a higher N content than those of polymers obtained by the Pd-mediated polymerization, corresponding to
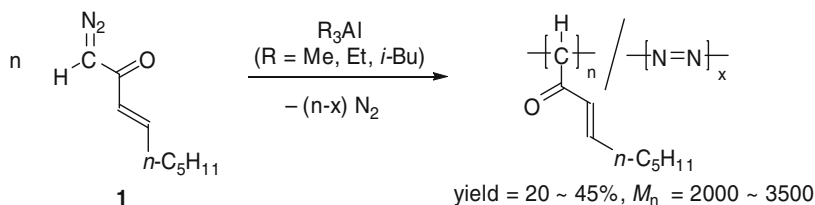
Scheme 31 Al-mediated polymerization of diazoketone **1**
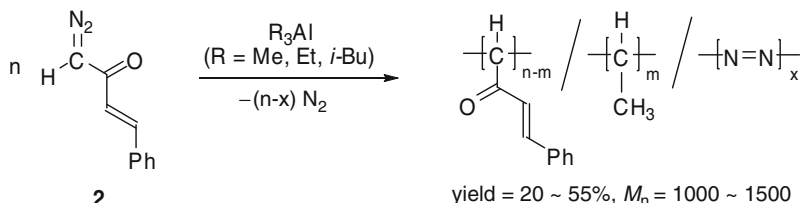
Scheme 32 Al-mediated polymerization of diazoketone **2**

an azo group content of about 33 mol%. On the assumption that the propagating chain end has an Al–C bond, these results suggest that the Al–C bond has a higher tendency for the attack on the terminal nitrogen of the monomer than the corresponding Pd–C bond.

Similarly, the organoaluminum initiated polymerization of Ph-substituted diazoketone **2** also proceeded to give rather low molecular weight polymers, which have ethylidene repeating units as a result of reductive transformation of a part of the acyl group to methyl group [56] (Scheme 32). The presence of ethylidene repeating unit was confirmed by the appearance of a broad methyl signal at $0.3 \sim 1.2$ ppm in the ^{1}H HNR spectrum. The reduction also proceeded when a polymer of **2** obtained by the Pd-mediated polymerization was reacted with the organoaluminum reagent.

3.6 Copolymerization of Diazocarbonyl Compounds with Other Monomers

3.6.1 Copolymerization with Phenyldiazomethane

Pd-mediated copolymerization of diazocarbonyl compounds with phenyldiazomethane proceeded, affording poly(substituted methylene)s with phenyl group directly attached on the main chain carbons [44] (Scheme 33).
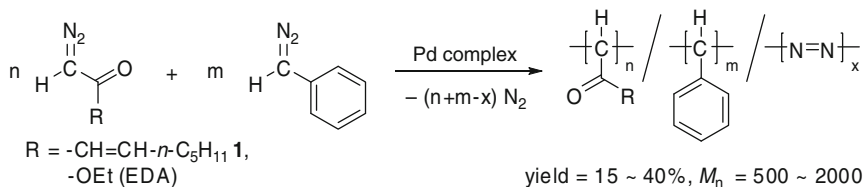
Scheme 33 Pd-mediated copolymerization of diazocarbonyl compounds with phenyldiazomethane
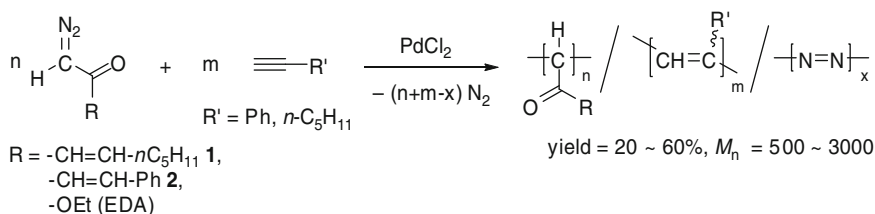
Scheme 34 PdCl$_2$-mediated copolymerization of diazocarbonyl compounds with alkynes

3.6.2 Copolymerization with Alkynes

Because C≡C triple bond can insert into Pd–C bond, which is assumed to be a propagating chain end of the Pd-mediated polymerization of diazocarbonyl compounds, copolymerization of diazocarbonyl compounds with alkynes would be expected to proceed. Actually, copolymerization of diazocarbonyl compounds **1**, **2**, and EDA with phenylacetylene and 1-heptyne proceeded to give copolymers with unique structures as shown in Scheme 34 [57].

3.6.3 Copolymerization with Styrene

It was found that diazoketones **1** and **2** can be polymerized by heating alone without addition of any initiator [58] (Scheme 35). Although ^{1}H NMR spectra of the products of the thermally-induced polymerization were identical with those of the products of the Pd-mediated polymerization, elemental analyses revealed that the azo contents in the former products were much higher than those in the latter, being about 33 mol%. In addition, interesting to note for the thermally-induced polymerization was that the molecular weights of the polymers increased significantly up to $M_n = 8,400$, when benzoquinone was used as an additive. Thus, a proposed propagation mechanism for the polymerization includes radical coupling of biradical species generated from the monomer with a propagating radical chain end. The benzoquinone might stabilize the propagating radical by forming a C–O bond, which can be reversibly cleaved by heating, enabling the synthesis of polymers with relatively high molecular weights.

On the basis of the mechanism proposed above, radical copolymerization of diazoketone **1** with styrene was examined to give copolymers [58]. As a result,
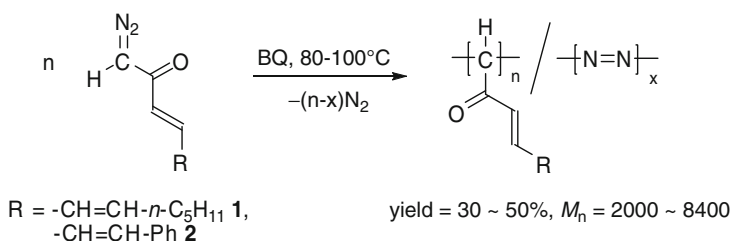
Scheme 35 Thermally-induced polymerization of diazoketones
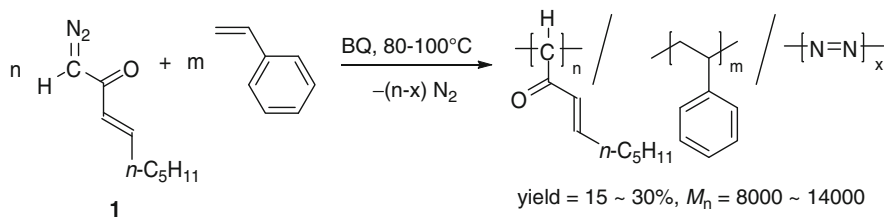
Scheme 36 Thermally-induced copolymerization of diazoketone with styrene

thermally-induced copolymerization proceeded in the presence of benzoquinone, giving copolymers with relatively high molecular weight (Scheme 36).

4 Polymerization of Sulfoxonium Ylides

In 1997, Shea and coworkers reported polyhomologation, which applies homologation of organoborane with dimethylsulfoxonium ylide to polymer synthesis [7, 59]. This new polymerization is a highly effective method for polymethylene synthesis, which proceeds in a living fashion and can afford high molecular weight polymethylenes with a very narrow molecular weight distribution (MWD) in a high yield. Furthermore, by utilizing the living nature of the polymerization, quantitative functionalization of the chain ends is possible, thus enabling preparation of a variety of molecular architecture based on the polymethylene chain with a controlled chain length.

4.1 Living Polymerization of Dimethylsulfoxonium Methylide

Homologation of organoborane with dimethylsulfoxonium methylide **11** was developed by Tufariello and co-workers, where nucleophilic addition of the ylide-carbon to boron center followed by 1,2-migration of one of the alkyl groups of organoborane with elimination of dimethylsulfoxide (DMSO) resulted in the elongation of the alkyl group by a CH$_2$ unit on the boron center [60–62] (Scheme 37). Because the product has a similar structure with CH$_2$–B bonds as that of the starting alkylborane,

R
\
B−CH$_2$

+

$\ominus$ $\oplus$ O
H$_2$C−S$^{\prime\prime\prime}$Me
|
Me **11**

⟶

R
|
CH$_2$
$\ominus$ |
B
|
CH$_2$
|
Me$^{\prime\prime\prime}$S$=$O
$\oplus$
Me

− DMSO ⟶

CH$_2$−R
\
B−CH$_2$
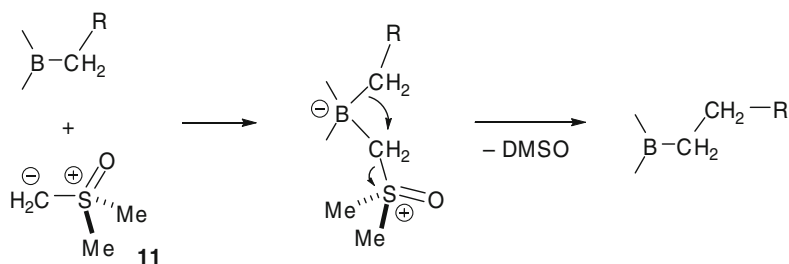
Scheme 37 Mechanism for homologation of alkylborane with dimethylsulfoxonium methylide **11**

$\ominus$ $\oplus$ O
H$_2$C−S$^{\prime\prime\prime}$Me
|
Me **11**

$[n\text{-}C_6H_{13}]_3$B ⟶ NaOH / H$_2$O$_2$ ⟶

$n\text{-}C_6H_{13}OH$ 69%

+

$n\text{-}C_7H_{15}OH$ 25% *single insertion product*

+

$n\text{-}C_8H_{17}OH$ 6% *double insertion product*
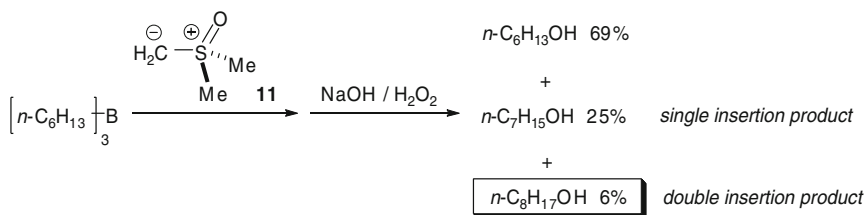
Scheme 38 Homologation of tri-*n*-hexylborane with dimethylsulfoxonium methylide **11**

employing a large excess of **11** would result in polymerization (polyhomologation), as suggested by the observation of a product resulting from double insertions in the reaction of tri-*n*-hexylborane with **11** (Scheme 38).

When a large excess of **11** was reacted with trialkylborane, the expected propagation occurred from all three C–B bonds, giving a three-arm star polymer, which was oxidized with HOOH/NaOH or trimethylamine-*N*-oxide (TMA-*O*) to give hydroxyl-terminated polymethylenes. As the polymerization proceeds in a living manner, polymethylenes with a very narrow MWD were obtained in high yields and the M_n of the products corresponds to the feed ratio of monomer to initiator ([**11**]/[alkylborane]/3) [59, 63]. In spite of the low solubility of polymethylenes, the polymerization in a mixture of 1,2,4,5-tetrachlorobenzene and toluene at 120 °C afforded high molecular weight polymers with $M_n > 100{,}000$ and $M_w/M_n < 1.10$. The propagation is very fast with turnover frequency of 6×10^6 g polymethylene (mol boron)$^{-1}$ h^{-1} at 120 °C in the mixed solvent (Scheme 39).

Kinetic study shows that the propagation is first-order in organoborane and zero-order in the monomer **11** under the condition of a large excess of the monomer, and thus indicates that fast formation of borate from organoborane and **11** is followed by a rate-limiting 1,2-migration of one of the three alkyl groups on B to the CH$_2$ derived from **11** with the elimination of a DMSO molecule as described in Scheme 37. Furthermore, 1:1 complexes of BF$_3$ and B(C$_6$F$_5$)$_3$ with the ylide **11** corresponding to the intermediate in the propagation was isolated and characterized by X-ray crystallographic analyses [64]. Although F and C$_6$F$_5$ groups do not migrate easily in these complexes, the crystal structures revealed that one of the F and C$_6$F$_5$ groups is located in the anti-periplanar position to the carbon-sulfur bond, demonstrating the presence of orbital interaction favorable for the 1,2-migration (Scheme 40).
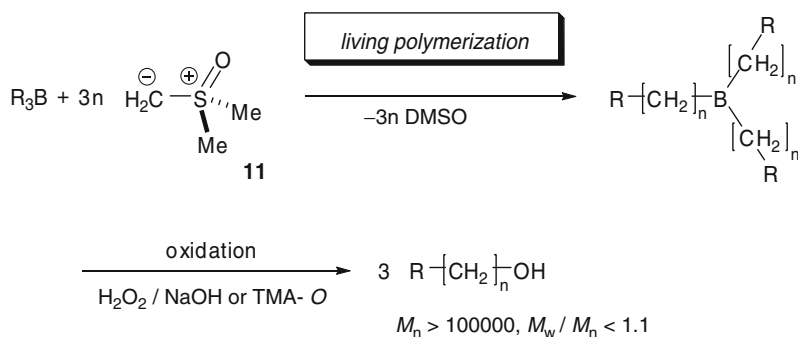
Scheme 39 R$_3$B-initiated polymerization of dimethylsulfoxonium methylide **11**

characterized by X-ray analysis
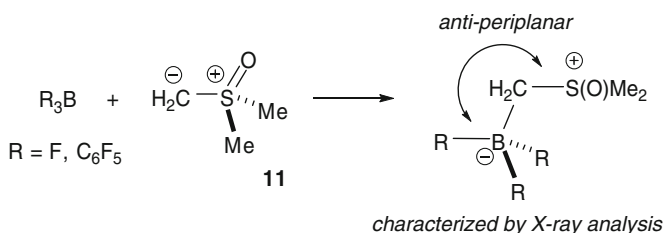
Scheme 40 Structure of 1:1 complexes of BF$_3$ and B(C$_6$F$_5$)$_3$ with dimethylsulfoxonium methylide **11**
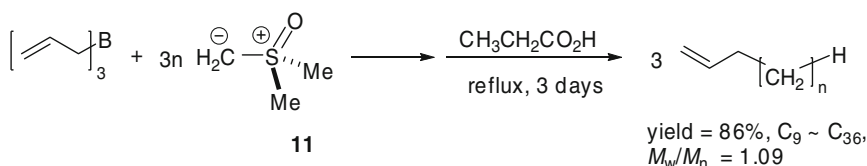
Scheme 41 Synthesis of linear α-olefin oligomer by polymerization of dimethylsulfoxonium methylide **11**

In addition to the quantitative introduction of a hydroxyl group at the terminating chain end by the oxidation, methyl-terminated polymethylene can be obtained by protolysis with propionic acid [65]. The termination combined with the initiation by triallylborane successfully afforded an oligomeric (C$_9$ ~ C$_{36}$) α-vinyl-ω-methylpolymethylene with a narrow MWD in a high yield (Scheme 41). This transformation can be a useful method for preparing well-defined linear α-olefin (LAO) oligomers, which would be valuable as a starting material for olefin polymerization.

Similarly, quantitative introduction of a variety of functional groups into the initiating chain end was achieved by using trialkylboranes bearing the corresponding functional groups as initiators [66] (Scheme 42). The initiators can be prepared by hydroboration of compounds having the functional group (X) and C=C with BH$_3$. Polymerization of **11** with the initiators can provide telechelic polymethylenes with a narrow MWD bearing the functional group and a hydroxyl group at α and ω chain ends, respectively.
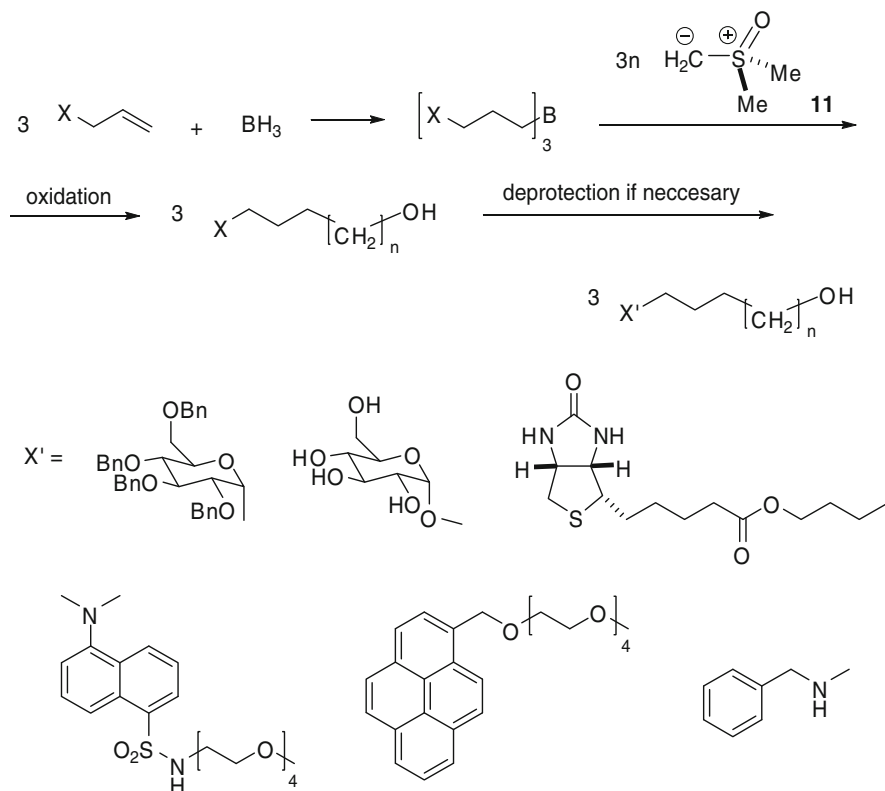
Scheme 42 Synthesis of polymethylenes with various functional groups at initiating chain end
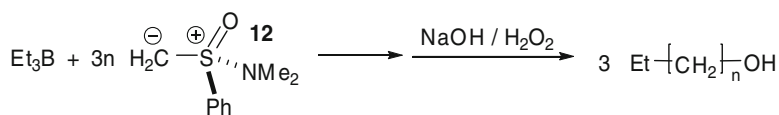
Scheme 43 Et$_3$B-initiated polymerization of (dimethylamino)phenyloxosulfonium methylide **12**

4.2 Synthesis of Substituted Carbon Backbone Polymers Based on Polymerization of Sulfoxonium Ylides

In a similar manner as that of **11**, (dimethylamino)phenyloxosulfonium methylide **12** can be polymerized in a living manner to give polymethylene with a narrow MWD [67] (Scheme 43).

In contrast to dimethylsulfonium ylide, for which introduction of substituents into the ylide carbon is difficult, the ylide carbon in (dimethylamino)phenyloxosulfonium ylide can be modified to have a substituent. For example, methylsubstituted (ethylide) analogue, (dimethylamino)phenyloxosulfonium ethylide **13**,
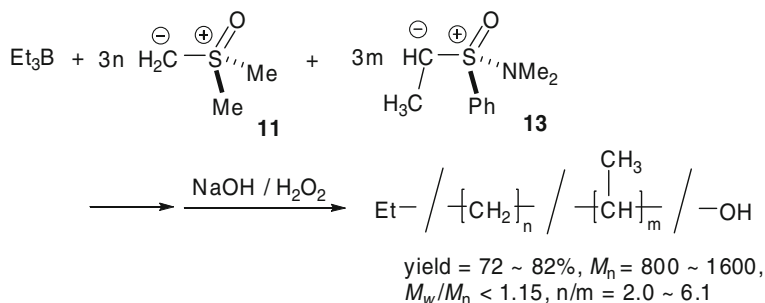
Scheme 44 Et$_3$B-initiated copolymerization of **11** with (dimethylamino)phenyloxosulfonium ethylide **13**
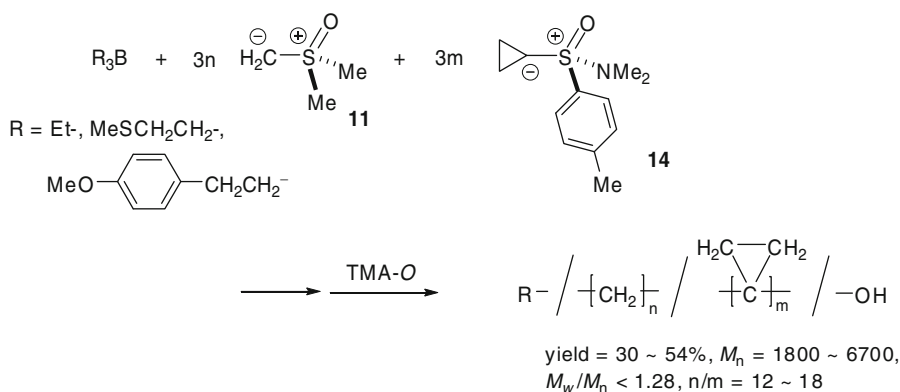
Scheme 45 R$_3$B-initiated copolymerization of **11** with cyclopropyl-substituted ylide **14**

was prepared and its organoborane-initiated polymerization was examined (Scheme 44). Whereas homopolymerization of **13** did not proceed because of steric congestion around the boron center during propagation, copolymerization of **13** with **11** proceeded to give random copolymers, whose composition is the same as those of copolymers of ethylene and propylene. As the polymerization proceeds in a living manner, the molecular weight and composition of the copolymer can be controlled by the feed ratio of [organoborane]/[**11**]/[**13**] and the products have a narrow MWD.

Similarly, cyclopropyl-substituted ylide **14** was prepared and subjected to organoborane-initiated polymerization [68]. Although **14** again cannot be homopolymerized for steric reasons in a similar manner as **13**, copolymerization of **14** with **11** proceeds in a living fashion to give polymers with a unique main chain structure, where some of the main chain carbon atoms constitute a cyclopropyl ring as shown in Scheme 45. Compared to the case with **13**, the copolymerization of bulkier and less stable **14** is less efficient, giving lower incorporation of **13** than that expected from the comonomer feed ratio.
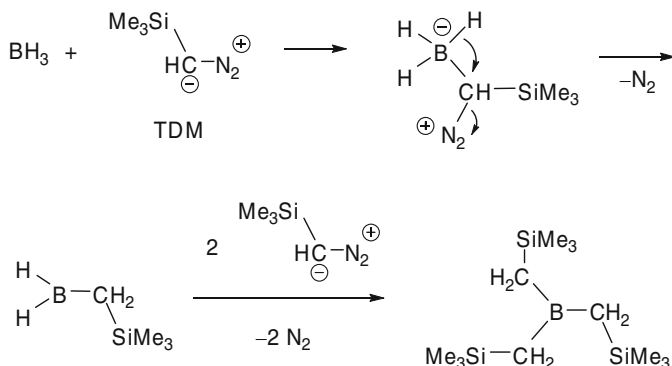
Scheme 46 Reaction of BH$_3$ with trimethylsilyldiazomethane

yield = 26 ~ 99%, M_n = 380 ~ 1100,
M_w/M_n 1.02 ~ 1.57, n/m = 15 ~ 42
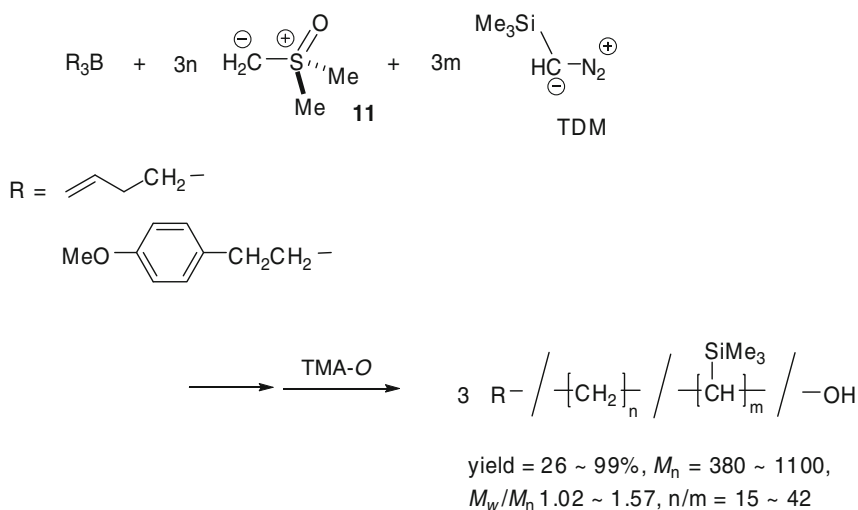
Scheme 47 R$_3$B-initiated copolymerization of **11** with trimethylsilyldiazomethane

When borane BH$_3$ was reacted with 2 equiv. of trimethylsilyldiazomethane (TDM), insertion of TDM into B–H with release of N$_2$ occurred to give tris(trimethylsilylmethyl)borane in a high yield [69] (Scheme 46). However, addition of an excess of TDM to borane did not lead to polymerization of TDM.

On the other hand, because TDM and dimethylsulfoxonium methylide **11** react with organoborane in a similar mechanism (formation of borate followed by 1,2-migration), organoborane-initiated copolymerization of TMD with **11** proceeded to give poly(TMSmethylidene-*co*-methylene), which is a partially TMS-substituted polymethylene [69]. Although the composition of TMSCH in the products was lower than that expected from the feed ratio of [TDM]/[**11**], oligomers with a relatively narrow MWD were obtained as shown in Scheme 47.

4.3 Synthesis of Polymethylene Architecture Based on Polymerization of Dimethylsulfoxonium Methylide

By utilizing transformations of C–B bonds in tris(polymethylene)boranes, synthesis of unique molecular architecture is realized based on the well-defined polymethylene backbones prepared by the organoborane-initiated polymerization of **11**. Telechelic polymethylenes with hydroxyl groups at both chain ends and cyclic ketones were obtained from the products of polyhomologation of *B*-thexylborocane **15** with **11** as shown in Scheme 48 [70]. These transformations take advantage of inertness of thexyl group on **15** towards 1,2-migration due to the steric bulkiness of the thexyl group, which brings about the propagation only from two CH$_2$–B bonds in **15**.

Similarly, synthesis of a linear ketone was achieved by combining two polymethylene chains on a thexyl-bearing organoborane [70] (Scheme 49). Analogous
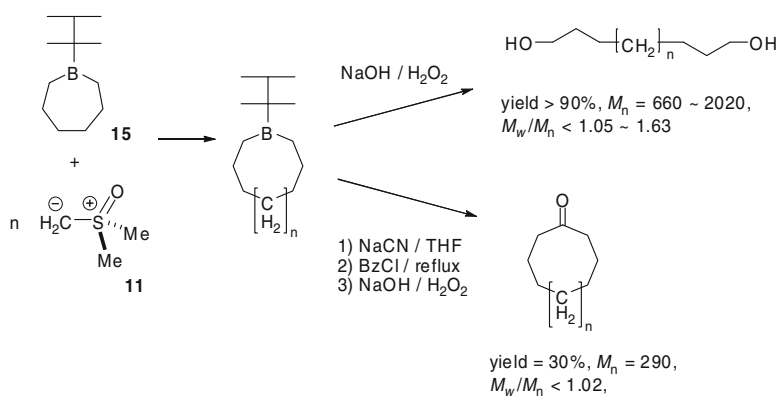
Scheme 48 Syntheses of α, ω-dihydroxypolymethylene and cyclic ketone by polymerization of **11** initiated with *B*-thexylborocane **15**
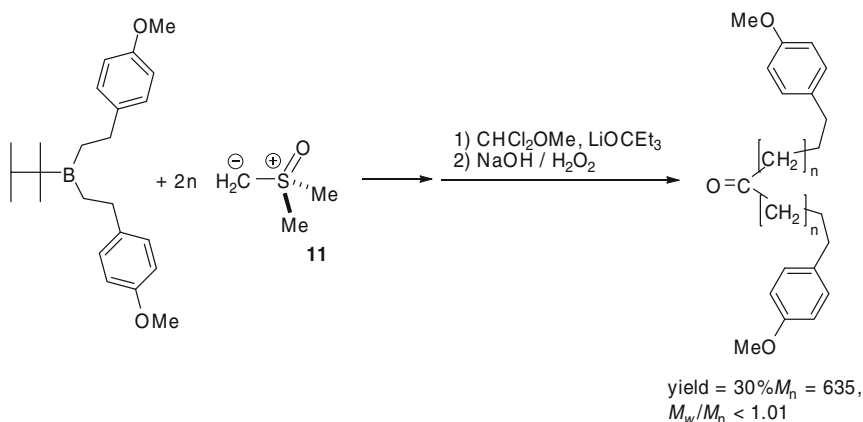
Scheme 49 Synthesis of linear ketone by polymerization of **11** initiated with thexyl-bearing organoborane

$R = Et-,\ MeO\!-\!\langle\ \rangle\!-\!CH_2CH_2-$

$M_n = 530 \sim 2780,$
$M_w/M_n = 1.02 \sim 1.20$
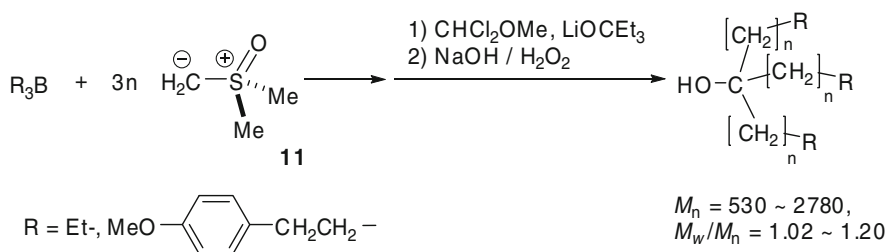
Scheme 50 Synthesis of three armed star polymethylene by R_3B-initiated polymerization of **11**

yield = 80 ~ 90%, $M_n = 680 \sim 10700,$
$M_w/M_n < 1.11,$
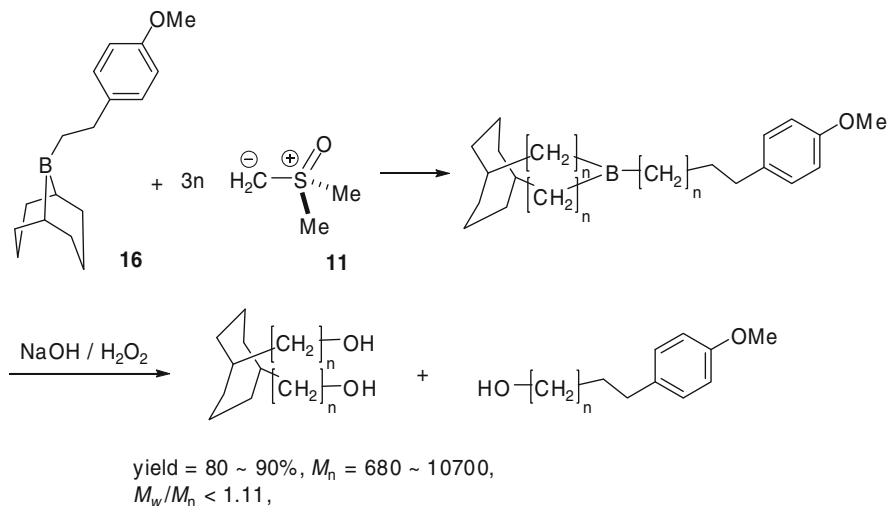
Scheme 51 Synthesis of polymethylene-substituted cyclooctane by polymerization of **11**

transformation was applied for the synthesis of three armed star polymethylene having hydroxyl group at the center carbon atom [71] (Scheme 50).

When 9-BBN-based cyclic organoborane **16** was employed as an initiator, two hydroxyl-terminated polymethylene chains can be attached to 1,5-positions in a cyclooctane framework [71] (Scheme 51). On the other hand, three polymethylene chains can be attached to 1,3,5-positions in a cyclohexane framework by using 1-boraadamantane **17** as an initiator [72, 73] (Scheme 52).

4.4 Synthesis of Block Copolymers Based on Polymerization of Dimethylsulfoxonium Methylide

Since it is generally difficult to prepare block copolymers containing a polyethylene block with a controlled molecular weight, it is quite significant to demonstrate that a well-defined polymethylene block generated by polymerization of **11** can be incorporated into block copolymers. This strategy can be very useful

$$M_n = 2400 \sim 19600, \; M_w/M_n < 1.09$$
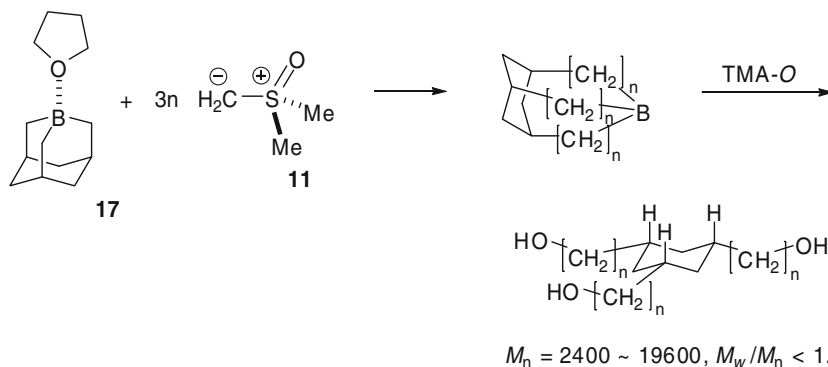
Scheme 52 Synthesis of polymethylene-substituted cyclohexane by polymerization of **11** initiated with 1-boraadamantane **17**
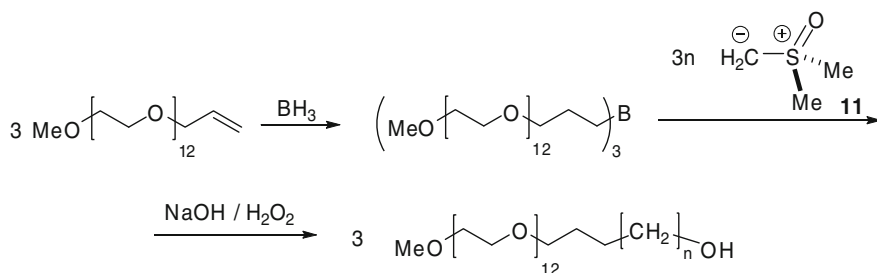
Scheme 53 Synthesis of poly(methylene-*b*-ethyleneglycol)

as a synthetic route for providing substitutes of polyethylene-containing block copolymers. The first example for such block copolymer synthesis was preparation of poly(methylene-*b*-ethyleneglycol) and poly(methylene-*b*-dimethylsiloxane-*b*-methylene) [74]. The former block copolymer was prepared by polyhomologation of a boron-terminated poly(ethyleneglycol), which was prepared by the hydroboration of an allyl-terminated poly(ethyleneglycol) (Scheme 53). On the other hand, the latter ABA-type triblock copolymer was prepared by polyhomologation of a poly(dimethylsiloxane) precursor, which was prepared by hydroboration of a poly(dimethylsiloxane) bearing vinyl groups at both chain ends with thexylborane. Homologation of the precursor polymer with **11** followed by oxidation afforded the ABA-type triblock copolymer with controlled polymethylene blocks (Scheme 54).

Another example for block copolymer synthesis is the preparation of poly (methylene-*b*-styrene), which was achieved by using a hydroxyl-terminated living polystyrene obtained by TEMPO-mediated living radical polymerization [75] (Scheme 55). The chain end hydroxyl group was transformed into an allyl ether moiety, which was subjected to hydroboration with BH$_3$ to afford polystyrene macroinitiator for the polymerization of **11**. After chain elongation with **11**, oxidation of the C–B chain ends furnished poly(methylene-*b*-styrene) bearing TEMPO and hydroxyl group at chain ends.
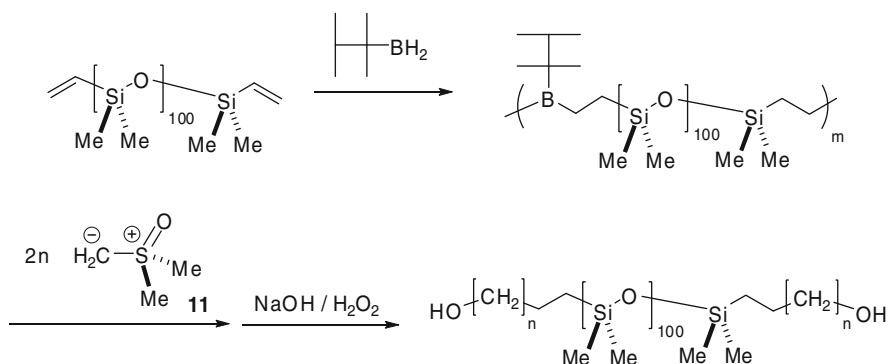
Scheme 54 Synthesis of poly(methylene-*b*-dimethylsiloxane-*b*-methylene)
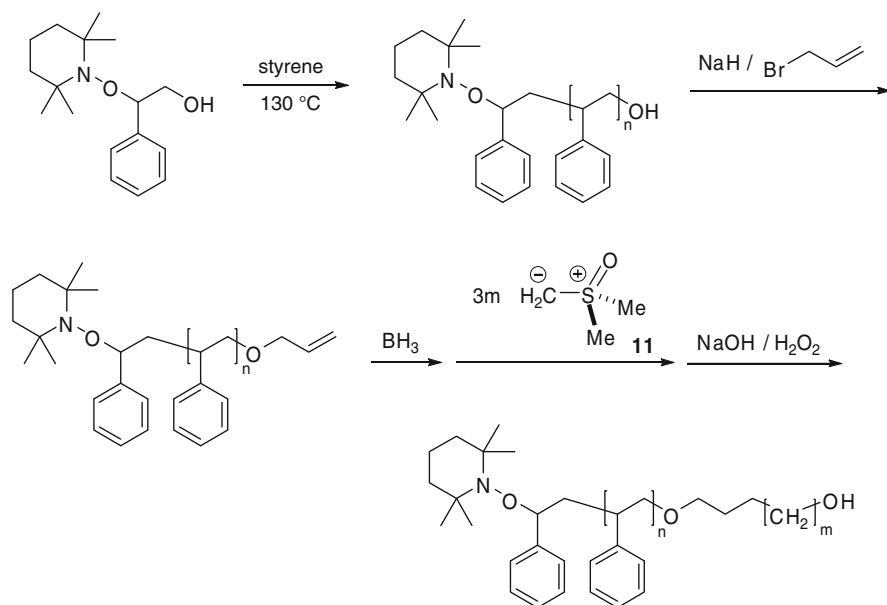
Scheme 55 Synthesis of poly(methylene-*b*-styrene)

4.5 Organoborane-Initiated Polymerization of Allylic Arsonium Ylides

In 2005, Gall, Mioskowski, and coworkers reported the organoborane-initiated polymerization of allylic arsonium ylides, which proceeds in a mechanism closely related to that of **11** [76]. However, in this process the polymer main chain is not constructed from one carbon unit but three carbon unit, which results in the formation of a series of poly(2-substituted-1-propenylene)s. When 2-substituted allylic arsonium ylide generated by the reaction of the corresponding arsonium salt with base

R = Me, Et, hexyl, tBuMe$_2$SiOCH$_2$CH$_2$–
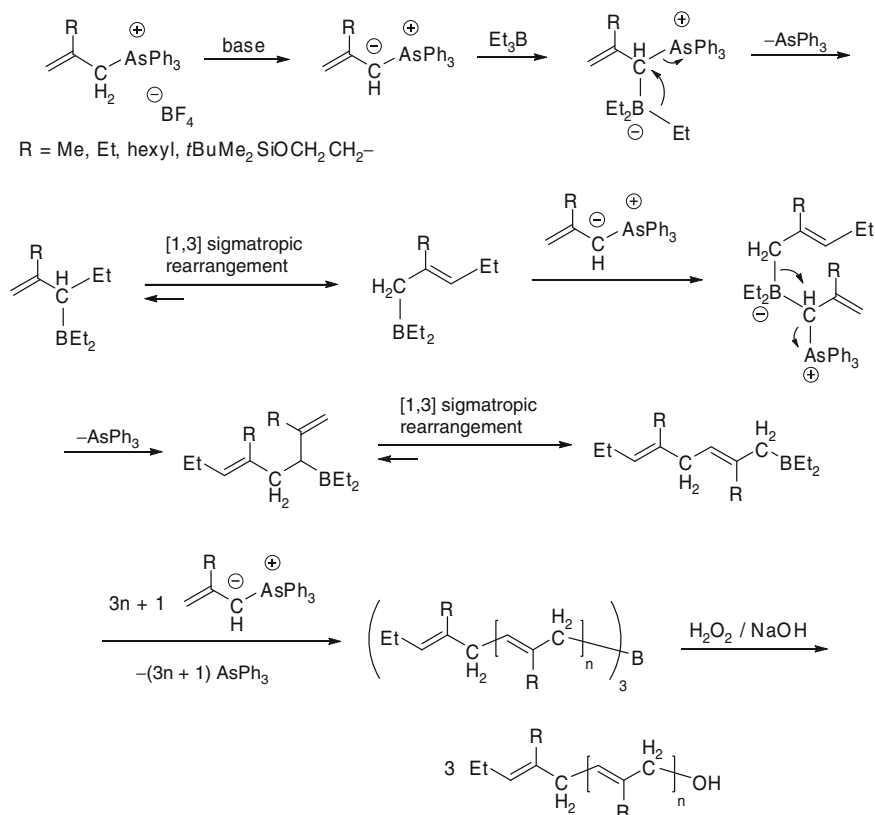
yield = 37 ~ 85%, M_n = 600 ~ 2400, M_w/M_n < 1.21 ~ 1.80

Scheme 56 Et$_3$B-initiated polymerization of allylic arsonium ylides

(t-BuLi or lithium hexamethyldisilazide) was reacted with triethylborane, addition of the ylide carbon to the boron center gave a borate, where 1,2-migration of one of ethyl groups followed by elimination of triphenylarsine results in the formation of insertion product (Scheme 56), in a similar manner as observed in the polymerization of **11**. However, in contrast to the case of **11**, [1,3] sigmatropic rearrangement occurs after the 1,2-migration, giving 2-substituted-1-propenylene framework as a repeating unit. After monomer consumption, oxidation of the C–B chain ends with hydrogen peroxide under an alkaline condition introduced a hydroxyl group at the chain end.

5 Polymerization of Sulfonium Ylide

Related to the aforementioned polymerization of sulfoxonium ylides, a unique polymerization of sulfonium ylide was reported by Bai and Shea in 2006 [77]. The monomer generated in situ by the reaction of trimethylsilylmethyldimethylsulfonium

iodide **18** with *n*-BuLi or *t*-BuLi was a mixture of three ylides, dimethylsulfonium trimethylsilylmethylide **19**, trimethylsilylmethylmethylsulfonium methylide **20**, and dimethylsulfonium methylide **21**. Polymerization of the mixture was initiated with $BF_3 \cdot OEt_2$, affording a copolymer consisting of trimethylsilylmethylene (CHTMS) and methylene repeating units, whose composition ([CHTMS]/[CH$_2$]) was dependent on the reaction condition, ranging from 0.45 to 1.75 (Scheme 57). Thus, the relatively high incorporation of TMS group exceeded the value for a homopolymer of vinyltrimethylsilane ([CHTMS]/[CH$_2$] = 1.0).

Cationic polymerization is assumed to proceed, where propagation is a nucleophilic attack of a negatively charged ylide-carbon to a carbon bearing the sulfonium cation at the propagating chain end (Scheme 58).

Even when the isolated **19** was used as a monomer, the resulting polymer had predominantly unsubstituted methylene units ($M_n = 31,540$, [CHTMS]/[CH$_2$] = 0.12), which suggested that the interconversion between **19** and **20** occurred during polymerization. This polymerization is unique in a sense that a copolymer is formed from a single monomer precursor.
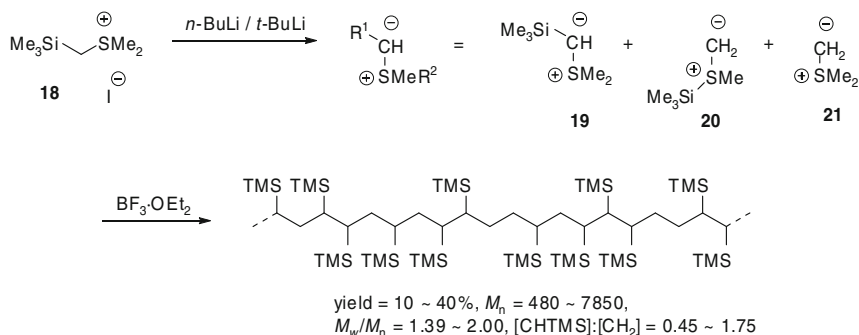
Scheme 57 BF_3-initiated polymerization of sulfonium ylide
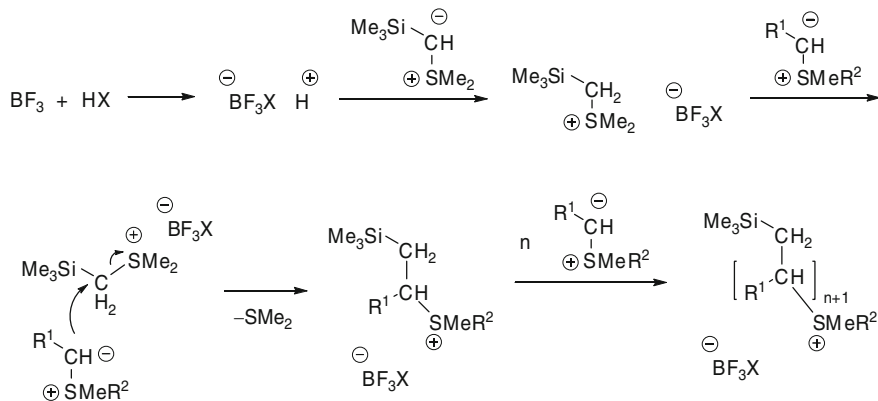
Scheme 58 Cationic mechanism for polymerization of sulfonium ylide

6 Polymerization of Arylaziridine Hydrazones of Aldehydes

In 1996, Yamamoto and coworkers reported that organolithium (*t*-BuLi, *n*-BuLi, PhLi)-initiated oligomerization of hydrocinnamaldehyde *trans*-1-amino-2,3-diphenylaziridine hydrazone **22** afforded oligo(phenylpropylidene) with $M_n = 1,500 \sim 2,500$ in 43~67% yield [78]. The polymerization proceeded as shown in Scheme 59, where the nucleophilic attack of a carbanion to C = N bond in **22** followed by elimination of N_2 and stilbene generated a secondary carbanion as a propagating chain end.

Interesting to note is that when benzaldehyde 1-amino-2-phenylaziridine hydrazone **23** was used as a monomer in place of **22**, eliminated styrene participated as a comonomer in the anionic polymerization in THF, to give a copolymer with a structure illustrated in Scheme 60.

On the other hand, when the oligomerization of **23** was conducted in toluene, azo-containing oligomer was obtained via generation of an azo-containing propagating carbanion as shown in Scheme 61.
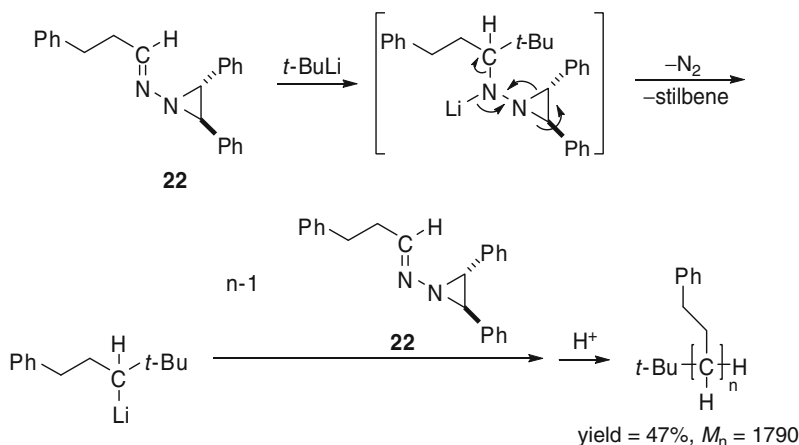
Scheme 59 Anionic polymerization of hydrocinnamaldehyde *trans*-1-amino-2,3-diphenyl-aziridine hydrazone **22**
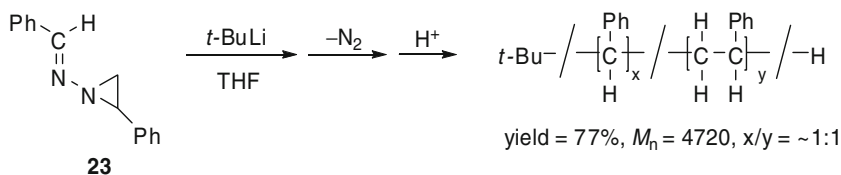
Scheme 60 Anionic polymerization of benzaldehyde 1-amino-2-phenylaziridine hydrazone **23** in THF

yield = 43%, M_n = 4790, x/y = ~1.5:1
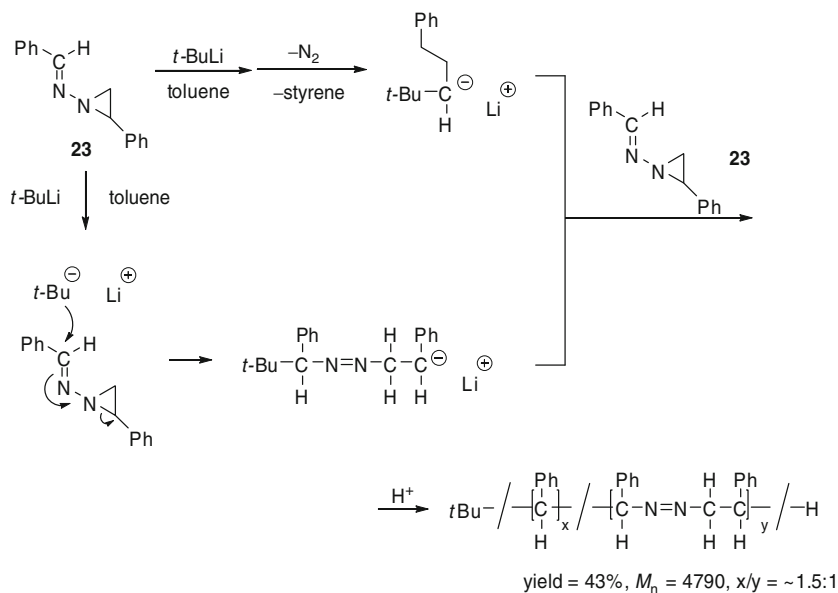
Scheme 61 Anionic polymerization of **23** in toluene

7 Concluding Remarks

Polymerization of diazoalkanes and aryldiazomethanes, which was once expected to be a method for preparing substitutes for polyolefins, has again attracted much attention recently, as a highly efficient method for metal surface coating with hydrocarbon-based polymer thin films. For this purpose, the remarkable utility compared to the alternative method using corresponding vinyl monomers or polymers would overwhelm the drawback of necessity of handling the explosive monomers. In addition, surface coating with nanometer-scale thin films may not generally need the monomers in large scale. In particular, introduction of polar functional groups into the thin film attained by employing EDA as a comonomer is highly promising for future applications in this field.

On the other hand, recent progress of organoborane-initiated polymerization of sulfoxonium ylides and transition metal mediated polymerization of diazocarbonyl compounds have opened up new possibilities for PSMS as a general method for polymer synthesis. In particular, it is worthwhile to note that important general objectives in polymer synthesis such as living polymerization, high molecular weight (M_n > 100,000) polymer synthesis, and stereospecific polymerization have been realized in some cases as described in this review. The relative safety and ease in handling these monomers are also important advantages of these polymerizations.

With further development of the polymerizations described in this review and the finding of totally new classes of monomer for this strategy, PSMS would become an important synthetic method for C–C main chain polymers, comparable or supplementary to vinyl polymerization, in the future.

References

1. Drent E, van Dijk R, van Ginkel R, van Oort B, Pugh RI (2002) Chem Commun 744
2. Luo S, Vela J, Lief GR, Jordan RF (2007) J Am Chem Soc 129:8946
3. Kochi T, Noda S, Yoshimura K, Nozaki K (2007) J Am Chem Soc 129:8948
4. Weng W, Shen Z, Jordan RF (2007) J Am Chem Soc 129:15450
5. Chen C, Luo S, Jordan RF (2008) J Am Chem Soc 130:12892
6. Guironnet D, Roesle P, Rünzi T, Göttker-Schnetmann I, Mecking S (2009) J Am Chem Soc 131:422
7. Shea KJ (2000) Chem Eur J 6:1113
8. Noels AF (2007) Angew Chem Int Ed 46:1208
9. Bawn CEH, Ledwith A (1970) Encyc Polym Sci Technol 10:337
10. Cowell GW, Ledwith A (1970) Quart Rev 24:119
11. Imoto M, Nakaya T (1972) J Macromol Sci Revs Macromol Chem C7:1
12. Suginome M, Ito Y (2004) Adv Polym Sci 171:77
13. Kantor SW, Osthoff RC (1953) J Am Chem Soc 75:931
14. Feltzin J, Restaino AJ, Mesrobian RB (1955) J Am Chem Soc 77:206
15. Davies AG, Hare DG, Khan OR, Sikora J (1963) J Chem Soc 4461
16. Bawn GEH, Ledwith A, Matthies P (1959) J Polym Sci 34:93
17. Mucha M, Wunderlich B (1974) J Polym Sci 12:1993
18. Goubean J, Rohwedder KH (1957) Justus Liebigs Ann Chem 604:168
19. Wada N, Morisaki Y, Chujo Y (2009) Macromolecules 42:1439
20. Mango FD, Dvoretzky I (1966) J Am Chem Soc 88:1654
21. Werner H, Richards JH (1968) J Am Chem Soc 90:4976
22. Saini G, Campi E, Parodi S (1957) Gazz Chim Ital 87:342
23. Saini G, Nasini AG (1955–1956) Atti Accad Sci Torino 90:586
24. Redwith A (1956) Chem Ind 1310
25. Nasini AG, Trossarelli L, Saini G (1961) Makromol Chem 44/46:550
26. Seshadri K, Atre SV, Tao YT, Lee MT, Allara DL (1997) J Am Chem Soc 119:4698
27. Tao YT, Pandian K, Lee WC (1998) Langmuir 14:6158
28. Guo W, Jennings GK (2002) Langmuir 18:3123
29. Guo W, Jennings GK (2003) Adv Mater 15:588
30. Bai D, Jennings GK (2005) J Am Chem Soc 127:3048
31. Bai D, Habersberger BM, Jennings GK (2005) J Am Chem Soc 127:16486
32. Bai D, Elliott SM, Jennings GK (2006) Langmuir 18:5167
33. Bai D, Hardwick CL, Berron BJ, Jennings GK (2007) J Phys Chem B 111:11400
34. Bai D, Ibrahim Z, Jennings GK (2007) J Phys Chem C 111:461
35. Doyle MP, Mckervey MA, Ye T (1998) Modern catalytic methods for organic synthesis with diazo compounds. Wiley-Interscience, New York
36. Zhang Z, Wang J (2008) Tetrahedron 64:6577
37. Liu L, Song Y, Li H (2002) Polym Int 51:1047
38. Ihara E, Haida N, Iio M, Inoue K (2003) Macromolecules 36:36
39. Toyoda N, Yoshida M, Otsu T (1983) Polym J 15:255
40. Ihara E, Ishiguro Y, Yoshida N, Hiraren T, Itoh T, Inoue K (2009) Macromolecules 42:8608
41. Takahashi H, Itoh T, Ihara E, Inoue K (2009) Polym Prepr Jpn 58:2221
42. Asano T, Itoh T, Ihara E, Inoue K (2009) Polym Prepr Jpn 58:2220
43. Ihara E, Fujioka M, Haida N, Itoh T, Inoue K (2005) Macromolecules 38:2101
44. Ihara E, Kida M, Fujioka M, Haida N, Itoh T, Inoue K (2007) J Polym Sci Part A Polym Chem 45:1536
45. Ihara E, Hiraren T, Itoh T, Inoue K (2008) J Polym Sci Part A Polym Chem 46:1638
46. Ihara E, Hiraren T, Itoh T, Inoue K (2008) Polym J 40:1094
47. Oyama T, Fukui T, Naka K, Chujo Y (1999) Polym Bull 43:183
48. Ihara E, Goto Y, Itoh T, Inoue K (2009) Polym J 41:1117

49. Hetterscheid DGH, Hendriksen C, Dzik WI, Smits JMM, van Eck ERH, Rowan AE, Busico V, Vacatello M, Castelli VVA, Segre A, Jellema E, Bloemberg TG, de Bruin B (2006) J Am Chem Soc 128:9746
50. Jellema E, Budzelaar PHM, Reek JNH, de Bruin B (2007) J Am Chem Soc 129:11631
51. Rubio M, Jellema E, Siegler MA, Spek AL, Reek JNH, de Bruin B (2009) Dalton Trans 8970
52. Hooz J, Linke S (1968) J Am Chem Soc 90:6891
53. Hooz J, Gunn DM (1969) Tetrahedron Lett 10:3455
54. Pasto DJ, Wojtkwski PW (1970) Tetrahedron Lett 11:215
55. Bai J, Burke LD, Shea KJ (2007) J Am Chem Soc 129:4981
56. Ihara E, Kida M, Itoh T, Inoue K (2007) J Polym Sci Part A Polym Chem 45:5209
57. Ihara E, Nakada A, Itoh T, Inoue K (2006) Macromolecules 39:6440
58. Nishida H, Itoh T, Ihara E, Inoue K (2008) Polym Prepr Jpn 57:405
59. Shea KJ, Walker JW, Zhu H, Paz M, Greaves J (1997) J Am Chem Soc 119:9049
60. Tufariello JJ, Lee LTC (1966) J Am Chem Soc 88:4757
61. Tufariello JJ, Wojtkowski P, Lee LTC (1967) J Chem Soc Chem Commun 88:505
62. Tufariello JJ, Lee LTC, Wojtkowski P (1967) J Am Chem Soc 89:6804
63. Busch BB, Paz MM, Shea KJ, Staiger CL, Stoddard JM, Walker JR, Zhou XZ, Zhu H (2002) J Am Chem Soc 124:3636
64. Stoddard JM, Shea KJ (2003) Organometallics 22:1124
65. Wagner CE, Rodriguez AA, Shea KJ (2005) Macromolecules 38:7286
66. Busch BB, Staiger CL, Stoddard JM, Shea KJ (2002) Macromolecules 35:8330
67. Zhou XZ, Shea KJ (2000) J Am Chem Soc 122:11515
68. Sulc R, Zhou XZ, Shea KJ (2006) Macromolecules 39:4948
69. Bai J, Shea KJ (2006) Macromol Rapid Commun 27:1223
70. Shea KJ, Lee SY, Busch BB (1998) J Org Chem 63:5746
71. Shea KJ, Busch BB, Paz MM (1998) Angew Chem Int Ed 37:1391
72. Wagner CE, Shea KJ (2001) Org Lett 3:3063
73. Wagner CE, Kim JS, Shea KJ (2003) J Am Chem Soc 125:12179
74. Shea KJ, Staiger CL, Lee SY (1999) Macromolecules 32:3157
75. Zhou XZ, Shea KJ (2001) Macromolecules 34:3111
76. Mondière R, Goddard JP, Carrot G, Gall TL, Mioskowski C (2005) Macromolecules 38:663
77. Bai J, Shea KJ (2006) Macromolecules 39:7196
78. Maruoka K, Oishi M, Yamamoto H (1996) Macromolecules 29:3328

Editor: S. Kobayashi

Index